

ALMA MATER STUDIORUM - UNIVERSITÀ DI BOLOGNA

DOTTORATO DI RICERCA

in

MECCANICA E SCIENZE AVANZATE DELL'INGEGNERIA

Ciclo 31°

Settore Concorsuale di afferenza 09/A2

Settore Scientifico disciplinare ING-IND/13

DYNAMICALLY FEASIBLE TRAJECTORIES
OF FULLY-CONSTRAINED
CABLE-SUSPENDED PARALLEL ROBOTS

Presentata da: **Giovanni Mottola**

Coordinatore Dottorato Supervisore

Prof. **Marco Carricato** Prof. **Marco Carricato**

Esame Finale anno 2019

Alma Mater Studiorum - Università degli Studi di Bologna

DYNAMICALLY FEASIBLE TRAJECTORIES
OF FULLY-CONSTRAINED
CABLE-SUSPENDED PARALLEL ROBOTS

A dissertation submitted in partial fulfillment
of the requirements for the degree of Doctor of Philosophy
in Mechanics and Advanced Engineering Sciences

Giovanni Mottola

Bologna, Italy
February 13, 2019

But remember this, Japanese boy. . .
airplanes are not tools for war.
They are not for making money.
Airplanes are beautiful dreams.
Engineers turn dreams into reality.
HAYAO MIYAZAKI, *The wind rises* (2013)



This work is licensed under the Creative Commons Attribution-NonCommercial-ShareAlike 4.0 International License. To view a copy of this license, visit <http://creativecommons.org/licenses/by-nc-sa/4.0/> or send a letter to Creative Commons, PO Box 1866, Mountain View, CA 94042, USA.

Abstract

CABLE-Driven Parallel Robots employ multiple cables, whose lengths are controlled by winches, to move an end-effector (EE). In addition to the advantages of other parallel robots, such as low moving inertias and the potential for high dynamics, they also provide specific advantages, such as large workspaces and lower costs. Thus, over the last 30 years, they have been the object of academic research; also, they are being employed in industrial applications. The main issue with cable actuation is its unilaterality, as cables must remain in tension: if they become slack, there is a risk of losing control of the EE's pose. This complicates the control of cable-driven robots and is among the most studied topics in this field. Most previous works resort to extra cables or rigid elements pushing on the EE to guarantee that cables remain taut, but this complicates robot design. An alternative is to use the gravitational and inertial forces acting on the EE to keep cables in tension. This thesis shows that the robot's workspace can be greatly increased, by considering two model architectures. Moreover, practical limits to the feasibility of a motion, such as singularities of the kinematic chain and interference between cables, are considered. Even if a motion is feasible, there is no guarantee that it can be performed with an acceptable precision in the end-effector's pose, due to the inevitable errors in the positioning of the actuators and the elastic deflections of the structure. Therefore, a set of indexes are evaluated to measure the sensitivity of the end-effector's pose to actuation errors. Finally, the stiffness of one of the two architectures is modeled and indexes to measure the global compliance of the robot due to the elasticity of the cables are presented.

Riassunto

I ROBOT paralleli a cavi impiegano cavi, la cui lunghezza è controllata da argani, per muovere un elemento terminale o end-effector (EE). Oltre ai vantaggi degli altri robot paralleli, come basse inerzie in movimento e la possibilità di raggiungere velocità e accelerazioni elevate, possono anche fornire vantaggi specifici, come ampi spazi di lavoro e costi inferiori. Pertanto, negli ultimi 30 anni, questi robot sono stati oggetto di ricerche accademiche e stanno trovando applicazione anche in campo industriale. Il problema principale dell'azionamento mediante cavi è che è unilaterale, poiché i cavi possono essere tesi ma non compressi: quando diventano laschi, si rischia di perdere il controllo della posa dell'EE. Questo complica il controllo dei robot ed è uno dei temi più studiati nel settore. Gli studi compiuti sinora ricorrono prevalentemente a cavi addizionali o a elementi rigidi che spingono sull'EE per garantire che i cavi rimangano tesi, ma questo complica la progettazione dei robot. Un'alternativa è sfruttare le forze gravitazionali e inerziali che agiscono sull'EE per mantenere i cavi in tensione. Questa tesi dimostra che, in questo caso, lo spazio di lavoro del robot può essere notevolmente aumentato, applicando questo concetto a due architetture modello. Inoltre, vengono considerati i limiti imposti all'effettiva realizzabilità di un movimento, come le singolarità della catena cinematica e l'interferenza tra i cavi. Anche se un movimento è fattibile, non è garantito che si possa eseguire con precisione accettabile, a causa degli inevitabili errori di posizionamento degli attuatori e delle deformazioni elastiche della struttura. Si valutano quindi alcuni indici per misurare la sensibilità della posizione dell'elemento terminale agli errori di azionamento. Infine, è modellata la rigidità di una delle due architetture proposte e sono presentati indici per misurare la cedevolezza globale del robot dovuta all'elasticità dei cavi.

Contents

1	Introduction	1
1.1	Prologue	1
1.2	Motivations and goals	5
1.3	State of the art	8
1.3.1	Parallel Robotics	8
1.3.2	Cable-Driven Parallel Robots	8
1.3.2.1	Classification	10
1.3.2.2	Applications	12
1.3.2.3	Theoretical issues	14
1.3.2.4	Translational motion	19
1.4	Thesis Outline	21
1.5	Robot architectures	22
1.5.1	Point-mass robot	23
1.5.2	Translational robot	24
1.5.2.1	Special architecture \mathcal{L}	27
1.5.2.2	Special architecture \mathcal{R}	27
1.5.2.3	Special architecture \mathcal{LR}	27
2	Kinetostatic model	29
2.1	Dynamics of CSPRs: state of the art	29
2.2	Model for a point-mass EE	31
2.3	Model for a finite-size EE	32

Contents

2.3.1	Special architecture \mathcal{L}	37
3	Dynamical trajectories	41
3.1	Introduction	41
3.2	General trajectories	43
3.3	Natural frequency	45
3.4	Generic frequency	47
3.5	Variable frequency	52
3.6	Transition trajectories	57
3.6.1	Variable amplitudes	57
3.6.2	Variable center	61
3.7	Experimental results	65
3.7.1	Experimental results: point-mass EE	66
3.7.2	Experimental results: finite-size EE	67
3.8	Summary of the chapter	74
4	Practically feasible motions	77
4.1	Introduction	77
4.2	Singularities	80
4.2.1	Two \mathbf{d}_{ij} 's are parallel	85
4.2.2	All \mathbf{d}_{ij} 's are parallel to plane II	87
4.3	Reachable workspace	88
4.4	Cable interference	89
4.5	Summary of the chapter	91
5	Kinematic performance indexes	93
5.1	Introduction	93
5.2	Definition of sensitivity indexes	97
5.3	Properties of sensitivity indexes	100

5.4	Application to translational robot	104
5.5	Parallelogram planarity error	112
5.6	Summary of the chapter	116
6	Stiffness modeling and measuring	119
6.1	Stiffness modeling	119
6.1.1	Stiffness matrix	122
6.2	Stiffness indexes	126
6.3	Application to robot A: stiffness maps	128
6.4	Summary of the chapter	130
7	Conclusions	133
7.1	Conclusions	133
7.2	Future work	134
Appendix A	Proofs	137
A.1	Proof of properties in Sec. 3.2.	137
A.2	Proof of properties in Sec. 3.3	138
A.3	Proof of properties in Sec. 3.5	139
A.4	Proof of properties in Subsec. 3.6.1	142
A.5	Proof of properties in Sec. 5.3	143
A.6	Full expressions of quantities in Sec. 5.4	146
A.7	Proof of properties in Sec. 5.4	148
List of figures		153
List of video attachments		157
List of symbols and acronyms		159
List of Symbols	159

Contents

List of Acronyms	159
Acknowledgments	161
References	165

1

Introduction

in which the goals of this thesis are presented, the state of the art on cable-driven robots is described, and the thesis structure is outlined. Relevant robot architectures are also presented, that will be used throughout the thesis as examples.

1.1 Prologue

In the last 50 years, an important shift has been taking place in the field of automation: thanks to advancements principally in power electronics and control systems, automated machines designed to perform repeatedly a certain operation, with little room for adjustments to accommodate for different tasks, have faced growing competition from *flexible automation* systems: this has led to the birth of the field of *robotic automation*.

The word “*robot*” was coined in 1920 by Czech novelist Karel Capek: in one of his plays, robots are “artificial people” built to substitute human work. More recently, in 1979, the Robot Institute of America provided a practical definition of a robot as “a reprogrammable, multifunctional manipulator designed to move material, parts, tools, or specialized devices through various programmed motions for the performance of a variety of tasks”.

After the first prototypes produced in the '50s, starting from the latter half of the '70s the first commercial robots to find widespread use in automated

1. Introduction

production cells were released, such as the Cincinnati Milacron T³, UNIMATE and PUMA robots. Since then, robotics market has boomed and found wider and wider application in industrial production: just in the years from 2009 to 2016, the annual worldwide supply of industrial robots grew from 60000 to 294000 units and a growth of about 15% a year is forecast for years 2017-2020 (source: IFR World Robotics 2017).

This success is justified by the advantages that robotic automation systems provide: the main one is their flexibility, in that they can be easily reprogrammed depending on the task at hand. Robots can thus substitute humans in tasks that are either tedious, stressful or dangerous, while allowing their programming to be adapted to best suit our needs. At the same time, robots maintain the advantages of non-flexible, *hard automation*, such as reduced production times and increased accuracy and repeatability of the finished product.

Moreover, robots are starting to find their way outside the manufacturing industry: for example, robots for care and assistance to elderly, disabled or injured people have found increased acceptance by institutional and private users. The class of *service* robots, that are to work in direct contact with people, is thought to be close to a breakthrough of a similar scale to the one seen by industrial robots in the '80s.

Broadly speaking, robots are generally composed of:

- *links*, the components that form the physical structure of the robot;
- *joints*, that connect the links and allow them to move with respect to one another;
- a *base* that is fixed and provides an immovable reference frame*;
- an *End-Effector (EE)*, which is generally the terminal element of the robot and the one whose motion is directly defined by the task to be executed: for example, a spray-painting robot in a car-manufacturing

* There are also *mobile* robots, such as *drones* and *Automated Guided Vehicles (AGVs)*, which are defined by having no fixed base. Such robots, however, are outside the scope of this thesis.

line will have a spray-paint nozzle whose motion must follow the profile of the vehicle's chassis;

- *sensors* that measure the operational parameters of the robot during operation (such as the position and orientation of the EE with their time derivatives, the forces/torques applied on the structure, etc.);
- a *user interface* where one can define the desired operation to be performed;
- a *control system* that compares the current parameters of the robot (as detected by the sensors) and compares them with the target ones to execute the task at hand as desired;
- a set of *actuators* that act directly or indirectly on the joints and links of the robot and provide the necessary actuation forces/torques to move the EE as requested: their motion is controlled by the control system.

The independent parameters that are required to completely define a general mechanism's configuration are commonly called its Degrees of Freedom (DoFs). For example, most industrial manipulators have 6-DoFs, to control the *pose* (that is, the position and orientation) of a rigid-body EE, since a rigid body in space has 6 DoFs (3 translational and 3 rotational ones). Usually, a robot has a number n_D of DoFs equal to the number n_A of actuators, in what is commonly defined a *fully-actuated* architecture. However, various architectures of *under-actuated* and *redundantly-actuated* robotic systems have been proposed: these are defined by having respectively $n_D < n_A$ or $n_D > n_A$. Each of these architectures offers specific advantages and disadvantages: for instance, redundant robots offer in general a superior dexterity and flexibility, but are also more complicated to control and more expensive due to their higher number of actuators. This thesis will concern fully-actuated systems.

In a general robotic architecture one can further define *kinematic chains* as a set of links connected by joints. A fundamental distinction is then made depending on the robot architecture (see Fig. 1.1), which can be either

- *serial* or *open-loop*, if there is only one kinematic chain connecting any

1. Introduction

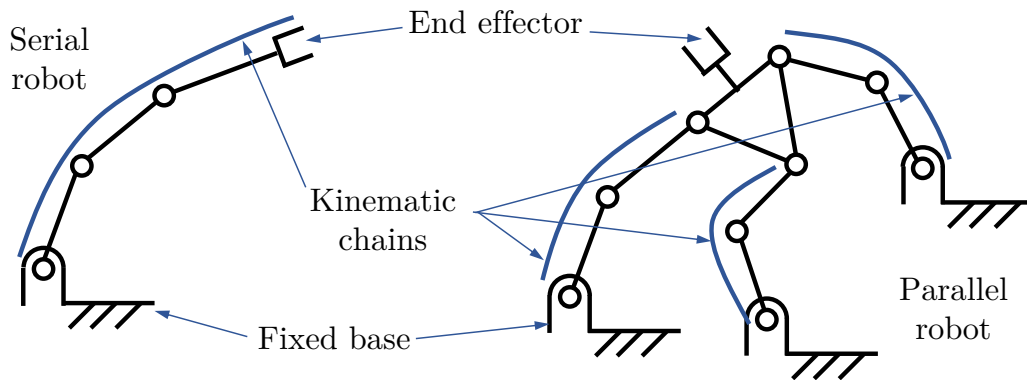


Figure 1.1: A comparison of serial (left) and parallel (right) robots.

two given links;

- *parallel* or *closed-loop*, if every couple of links is connected by (at least) two paths;
- *hybrid*, if there are both closed- and open-loop chains.

Since their appearance, parallel robots have shown strong advantages in industrial applications for their superior stiffness and payload-to-robot-weight-ratio with respect to traditional serial robots; however, their workspace is limited by the interference between multiple kinematic chains.

This thesis is concerned with the analysis of a particular class of robots where the actuation is obtained through flexible cables. *Cable-Driven Parallel Robots (CDPRs)* are a subset of parallel robots where the EE is not moved by rigid-body kinematic chains, but instead by flexible cables. Thus, cable robots operate like multiple-DoF, high-flexibility cranes controlled by several cables.

Due to their peculiar architecture, cable robots increase the classical advantages of parallel robots over serial ones, such as

- reduced mass and inertia;
- a high payload-to-robot-weight ratio;
- superior dynamic performance in terms of velocities and accelerations (see [101], where a cable robot able to reach accelerations up to 400 m/s^2)

was presented);

- smaller and cheaper actuators.

Cables, which are both lightweight and high-resistance, are readily available on the market, having a wide application in civil engineering [93]. Moreover, cables work under pure axial tension, which is the optimal stress condition.

Besides the classical advantages of parallel manipulators, CDPRs also provide characteristic advantages of their own. For instance:

- they can operate in a large workspace, potentially a very large one, by employing long cables. In this, they represent a vast improvement over standard parallel manipulators (see the CDPR presented in [145, 214], which has a 500-meter wide workspace);
- they have generally reduced costs, both for manufacturing and maintenance, as cables are relatively inexpensive;
- they are easier to assemble, disassemble and transport where needed;
- finally, they offer superior modularity and reconfigurability, as their design makes it easier to change the number of cables and the placement of their attachment points (either on the fixed frame [64] or on the EE [11]) according to the user's needs.

A subclass of CDPRs that is of particular interest are *Cable-Suspended Parallel Robots (CSPRs)*, where cables are kept in tension mainly by the gravity force pulling the EE downward. This architecture gives greater accessibility to the robot working area below the EE itself.

Cable robots, for the reasons listed before, are attracting intense interest from both academic and industrial researchers.

1.2 Motivations and goals

One of the main downsides of cable actuation is in that it is *unilateral*: cables can only pull, but cannot push, and when subjected to compressive forces they

1. Introduction

become slack and thus unable to properly control the robot motion. This is the main issue in the control and development of such robots, for which different approaches have been proposed:

- (a) some robots employ more cables than DoFs, thus being redundantly-actuated. In this way, the cables remain taut by pulling on each other;
- (b) others use hybrid cable/rigid-link actuation systems, where the rigid elements guarantee that cables are kept in tension;
- (c) finally, some rely on external forces to maintain positive tensions. For example, CSPRs generally use the own weight of the EE, which is dangling from the cables pulling it upwards, to keep the cables taut.

Most previous works on cable robots employ strategies (a) and (b), but it is apparent that these complicate the robot design and ultimately increase its cost.

In recent years, researchers have given more attention to option (c); specifically, it was proposed to apply *inertial* effects to maintain the cables in tension. First proposed by the group led by C. Gosselin in Canada [59, 60, 98] and further expanded by the team of S. Cong in China [210–212], this idea has proven fruitful, in that it was empirically proved that it allows the workspace of the robot to be greatly expanded. This can be helpful especially when the robot footprint is limited due to space reasons, as dynamic motions allow the EE to reach a much wider workspace.

Also, dynamic motions can be used to recover a robot in case of a cable breakdown [21, 29]; if a cable robot undergoes a sudden cable break, it could be brought back to a safe zone by using dynamic trajectories.

Finally, there is an intrinsic interest in studying the dynamics of cable robots: given that CDPRs can move with very high accelerations, it becomes necessary to take into account the inertial forces acting on them.

Once a feasible trajectory has been defined, to be able to actually perform it, one must verify other conditions for feasibility, such as avoiding kine-

matically indeterminate configurations and interference between the robot's components.

Moreover, even if a robot can move along a dynamic motion as desired, there is in general no guarantee that it will be able to do so with an acceptable precision: the effect of unavoidable control errors and the elastic deflections of the manipulator will result in a displacement between the desired and the real pose of the robot. A common method to tackle this problem is to define *performance indexes* that capture this complex behavior with a set of scalar, real-valued numbers which can be defined for every pose of the robot. These indexes can then be used to verify whether the performance remains acceptable during the motion; also, they can be used to compare different robot architectures and optimize the robot's geometrical parameters.

The goals of this thesis are thus threefold:

- (I) to define new *dynamic trajectories* that guarantee positive cable tensions throughout the motion, thereby increasing the “library” of available dynamic motions for CSPRs;
- (II) to consider practical issues that limit the application of said trajectories, such as *singularities* and *interference* between cables, and show how these influence the workspace available for dynamic motions;
- (III) to give measures of the *sensitivity to errors* and of the *elastic compliance* of CSPRs that may aid the designer in choosing the optimal architecture; these indexes ought to be physically significant and have a clear practical interpretation.

These goals were carried out by focusing on two model robots: a first, simpler one with point-mass EE and a second one with a finite-size EE. The latter is designed with the goal of having a purely-translational motion. In fact, most of the previous works on dynamically-feasible trajectories for CSPRs considered only robots like the former model defined above; in this thesis, it will also be shown how to apply previous work on point-mass robots to a translational cable robot such as the second model considered, which is more

1. Introduction

realistic and can thus find a greater application.

Part of the work in this thesis has been published by the author in [136–138].

1.3 State of the art

Robotics is now a mature research field, on which a vast literature is available. Even on the relatively recent topic of cable robotics, it is speculated that around 1000 journal and conference papers might exist [161, p. 7]. This section will thus provide a very brief introduction to parallel robots (serial architectures are beyond the scope of the present work) and focus on cable robots, specifically on their dynamics.

1.3.1 Parallel Robotics

Using the distinction between serial and parallel architectures introduced in Sec. 1.1, the first truly parallel robotic systems were proposed in the early '60s by Gough [76] and Stewart [182] working independently: the robotic architecture they developed is thus called the *Gough-Stewart platform*. This robotic mechanism was based on a 6-DoF EE connected to the fixed frame through 6 U \bar{P} S legs; here, U denotes a *universal* joint, while \bar{P} is a *prismatic* joint (the overline denotes the fact that the joint is actuated). The original Gough-Stewart platform employed rigid links; later, cable-robots were designed based on this architecture (see Sec. 1.3.2.4 and Refs. [2, 13, 89, 164, 195]).

1.3.2 Cable-Driven Parallel Robots

Some of the first robots to employ cables for their actuation were called *tensegrity* robots [152], so named after the work of architect Buckminster Fuller on tensegrity structures (the name was coined as a combination of “tension” and “integrity”). These robots employ both rigid links (struts) and flexible cables, all under pure axial loads, where no compressed struts are directly connected

to each other [9]; the tensegrity condition requires that in any configuration the nature of loading remains the same in each link, so that cables are always under tension.

It is also worth mentioning *tendon mechanisms* as predecessors of cable-driven robots: these are mechanisms with open-loop architectures where the actuation is obtained with cables that are routed from the fixed base, allowing the designer to place all motors on the frame, which makes the design compact and reduces the total weight [95]. The first designs were proposed in the '80s and early '90s and were mainly applied to actuate the fingers of robotic hands [94, 125, 176]. Here, these systems are not considered as purely cable-driven, as the terminal element of the mechanism is connected to the fixed frame by rigid links; however, it must be mentioned that the nomenclature is not completely settled [161, p. 15] and some include CDPRs in the class of tendon-driven systems [195]. For coherence, the expression “cable-robot” or its acronym CDPR will be used throughout this thesis, as these are the most commonly used terms.

The team of J. Albus at NIST is generally credited for the development of the first cable-driven robot, the ROBOCRANE [2, 55], which was designed as a flexible crane for large-scale robotic operations, such as painting and welding of ships and planes; working independently, a cable-actuated system was also proposed by Landsberger [112] to operate under water or in space. A cable-suspended camera had also been proposed for the recording of sports events in stadiums [52], taking advantage of the large workspaces of CSPRs and the fact that cable actuation is less obtrusive than traditional alternatives: this robot, called SkyCam, remains so far the main industrial application of CDPRs. Another early design was Charlotte [41], a light-weight, compact robot developed by McDonnell Douglas Corp. for space applications, which was tested during a Space Shuttle/MIR joint mission. In one of the first patents in this field [116], a cable robot was proposed as a cargo transfer system from ship to dock or vice versa.

1. Introduction

For general surveys on the state of the art, the reader can refer to [72, 131, 135, 143, 161, 165, 190] and [129, pp. 68–70].

1.3.2.1 Classification

As seen in Sec. 1.1, robots can be characterized depending on the number n_D of DoFs and the number n_A of actuators. With cable robots, however, another classification is introduced that is more relevant in this field, depending on the number of constraints n_C (which is given by the number of *taut* cables and the number of constraints set by rigid joints):

- (A) *over-constrained* (or redundantly-restrained) robots where $n_C > n_D$: the kinematic and static analyses of the robot are completely *decoupled*, that is, one can separately study the pose of the robot and the cable tensions. In this case there are infinitely many possible combinations of positive cable tensions that balance a given external wrench \mathbf{W}_e . The “best” combination is then usually found through an optimization algorithm [63, 85];
- (B) *fully-constrained* (or completely-restrained) robots for whose $n_C = n_D$; the kinematics and statics are still fully decoupled, but in this case there is one and only one possible set of cable tensions to balance an external \mathbf{W}_e ;
- (C) *under-constrained* (or incompletely-restrained) robots, where $n_C < n_D$: these cannot control all DoFs of the EE, whose motion depends not only on the actuators’ motion but also on the \mathbf{W}_e applied to the EE: the *twist space* (the subspace of all EE velocities that are compatible with the kinematic constraints) has dimension greater than zero even when all actuators are locked. The kinematic and static problems must then be solved simultaneously [44–46], which leads to a *geometrico-static problem* (see Subsec. 1.3.2.3). These robots have proven to be useful when the consequent reduction in dexterity is acceptable in exchange for a simpler design with an easy-to-access working area [91].

With this classification, a given robot can be under-, fully- or over-constrained

depending on its pose and on the applied wrench \mathbf{W}_e , as the number of cables in tension (and thus the number of constraints n_C) might change.

The number of cables is generally—but not necessarily, see for instance [13]—equal to n_A . Therefore, a robot can be at the same time fully- or redundantly-actuated but under-constrained: see the CABLEV robot [87] developed at the University of Rostock, which has seven independent actuators and a 6-DoF EE. Since this CSPR has only three cables attached to the EE, the robot can move even when all actuators are locked.

It is however necessary to mention that this terminology is far from settled, especially when applied to CSPRs. As proven by Ming and Higuchi in [134], the number of cables n_C should be at least equal to $n_D + 1$ if one wants to have at least n_D taut cables for any \mathbf{W}_e (at least in some robot poses); the results in [134], valid for robots having one rigid body (the EE), were later extended to multi-body cable-driven systems [142]. Therefore, CDPRs architectures are sometimes classified as under-, fully- or over-constrained respectively if $n_C \leq n_D$, $n_C = n_D + 1$ or $n_C > n_D + 1$ [161, pp. 19–20]. This classification however appears potentially misleading if compared with the definitions of full constraining from classical mechanics; therefore, this thesis will use the classification outlined in cases (A) to (C) above, coherently with Refs. [22, 44–46].

In this thesis, the models of cable robots used to study the dynamic feasibility of trajectories are all cable-suspended (see Subsecs. 1.5.1 and 1.5.2) and will be denoted as fully-constrained and fully-actuated.

CDPRs are also frequently classified depending on their actuation system. The cables are usually coiled and uncoiled on fixed *cable winches*: these are composed of actuated drums and pulley systems guiding the cables. The drums have helical grooves to ensure that the cables are properly wound at a (usually) constant radius r_D , without overlapping [163]. Avoiding overlapping has two main advantages: it increases cable lifetime (as wear and fatigue are reduced) and leads to a much greater accuracy in the estimation of the cable lengths, by using the data from the motor encoders. However, using winches also brings

1. Introduction

about an increase in complexity and cost; moreover, the length of the cables that can be used is limited by the length of the drum, which must be machined with high precision. For these reasons, the prototypes presented in the experimental parts of this thesis (Subsecs. 3.7.1 and 3.7.2) do not use winches, but instead simple pulleys (directly connected to the actuators) where the cables wrap freely. This is acceptable for non-fully-engineered prototypes, which are meant to be proofs-of-concept of the feasibility of dynamic motions; in any case, in Subsecs. 3.7.1 and 3.7.2 it will also be shown that the accuracy thus obtained is acceptable for the goals of the current work.

Beside the winches previously mentioned, there are other cable actuation designs worth mentioning: for example, some authors use linear actuators [184], in some cases with a system of sliding pulleys to multiply the velocity of the cable [130]. The CABLEV robot also uses linear actuators, that move the winches on the fixed frame [87]. In [179], Shoham first applies twisting wire actuation (an ancient technique, used for instance in Roman artillery) to cable robots: here, a rotary motion applied to two parallel wires is transformed into a linear motion as the wire pair shortens: this provides high forces and precise motions with small friction, but the workspace is reduced. Yet other authors place the cable exit points directly on rotary links [123], to maintain the actuation system as simple and low-cost as possible. It is also worth mentioning the hybrid cable actuation system in [215], based on a five-bar parallel mechanism, to increase the admissible payload.

A final classification could be based on whether the robot is fixed or mobile. Most CDPRs fall into the first category, as is commonly the case for industrial robots. However, mobile cable robots have also been proposed: the mobile base can either be aerial [133, 150] or terrestrial [31, 166].

1.3.2.2 Applications

Cable robots were first proposed for industrial, heavy-duty applications, as was the case of the NIST's ROBOCRANE [2]. Later, various industrial applications were proposed for CDPRs:

- maintenance and assembly of large scale naval [34] and aerospace [148] structures;
- loading and unloading of cargo containers for the shipping industry [68, 116, 149];
- remediation of radioactive waste storage tanks [35];
- storage retrieval in automated warehouses [39];
- large-scale 3D printing [13].

Cable robots have found their way also as service robots. For instance:

- haptic interfaces (either attached to the user's hands [140] or feet [157]);
- upper-limb [169] or lower-limb [184] rehabilitation;
- virtual reality simulation [187];
- simulation of sport activities [216];

There are various applications of CDPRs in *field robotics*: this sector is defined by dynamic, unstructured environments, such as farms, construction areas, in the air or under water. See the following examples:

- search and rescue operations [31] in disaster-struck areas;
- large-scale construction [33];
- assembly of solar power plants [162];
- actuated marine platforms [89];
- flying cable robots, attached to either single [150] or multiple [133] aerial platforms;
- fruit harvesting in farms [146].

Finally, CDPRs were proposed in various other sectors, such as:

- motion of telescope reflectors [144, 145, 214];
- scanning of sculpted artifacts [27];
- motion systems for wind tunnels [111];
- measurement devices of the inertial properties of an object [66] or of its pose [198]; see also [96, 163], where cable-driven parallel mechanisms were used to calibrate a robot by measuring its pose.

1. Introduction

1.3.2.3 Theoretical issues

Kinematics

One of the main issues to consider in any robot architecture is its *kinematics*, that is, the relationship between the motion of the n_A actuated joints and the corresponding motion of the EE. Kinematics considers the movement of a mechanism from a purely geometric viewpoint, disregarding the effect of any wrenches applied to said mechanism: if $\boldsymbol{\theta}$ denotes the $n_A \times 1$ vector of the actuated joints' positions and by \mathbf{x} the pose of the EE (defined by n_D DoF), the general relationship between the two vectors can be written as $\mathbf{F}(\boldsymbol{\theta}, \mathbf{x}) = \mathbf{0}$. Here, \mathbf{F} is a vector-valued function (dependent on the robot pose), derived by analyzing the robot geometry, that defines the relationship between the input (the joints' position) and the output (the EE pose) of the mechanism: this position relationship is also denoted as the *0th-order kinematics*. Differentiating with respect to time, one obtains the relationship

$$\mathbf{F}_x \dot{\mathbf{x}} + \mathbf{F}_\theta \dot{\boldsymbol{\theta}} = \mathbf{0} \quad (1.1)$$

(see [74]) where $\mathbf{F}_x = \partial \mathbf{F} / \partial \mathbf{x}$ and $\mathbf{F}_\theta = \partial \mathbf{F} / \partial \boldsymbol{\theta}$ are called *Jacobian matrices* of the robot. The relationship (1.1) between the joint velocities $\dot{\boldsymbol{\theta}}$ and the derivatives of the robot pose $\dot{\mathbf{x}}$ defines the *1st-order kinematics* of the system; the *2nd-order kinematics*, that concerns the accelerations, is obtained in a similar way.

One can further define the *Direct-Kinematics Problem (DKP)* that requires obtaining \mathbf{x} for a known $\boldsymbol{\theta}$ and the *Inverse-Kinematics Problem (IKP)*, where one needs to find $\boldsymbol{\theta}$ as \mathbf{x} is known: clearly, both the direct and the inverse kinematics are required to properly control the robot. It is well known that in general for serial architectures the DKP is easier to solve than the IKP, while for parallel architectures such as those considered in this thesis the opposite is true [129, Ch. 3–4].

The kinematics of cable-driven robots is generally approached with the tools of classical robot analysis, assuming that all cables are either under tension (so the free cable length is equal to the one set by the actuators, if cable

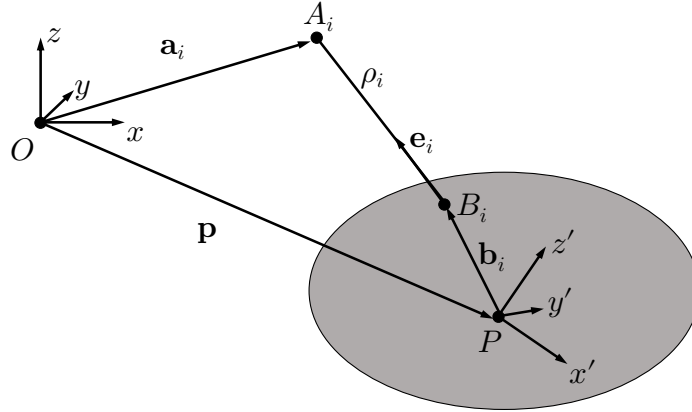


Figure 1.2: Schematic of the robot: the i -th cable, of length ρ_i and direction \mathbf{e}_i , is attached to the frame at point A_i and to the EE (in gray) at point B_i .

elasticity is disregarded) or slack, in which case they apply no constraint on the EE motion. This is the modeling approach used in this thesis, unless otherwise specified. Here, the notation of Fig. 1.2 will be used, where \mathbf{p} is the position vector of P , the *Operation Point (OP)* on the EE (that is, the point that defines the robot position), \mathbf{a}_i is the position of the cable attachment point A_i on the frame and \mathbf{b}_i the vector connecting P to the cable attachment point B_i on the EE (expressed in the base frame $Oxyz$): the kinematic constraint set by the i -th cable is thus

$$\rho_i \mathbf{e}_i = \mathbf{p} + \mathbf{b}_i - \mathbf{a}_i \quad (1.2)$$

where ρ_i and \mathbf{e}_i respectively denote the length and direction of the cable. The input joint position for cable robots is usually ρ_i , which is set by the corresponding actuator (this does not apply for CDPR with constant-length cables such as [19, 123, 133]).

As for most parallel architectures, the IKP of fully-actuated cable-based platforms is generally fairly easy to solve [168] both analytically and numerically; moreover, it can be seen from Eq. (1.2) that the solution always exists and is unique. The kinematic model presented here has been generalized to CDPR with multiple rigid links in [114]. Also, the pulley mechanism changes the kinematic model, as shown in [160], since in this case the cable attachment

1. Introduction

point on the frame A_i is no longer fixed. In this thesis, however, the simpler model of Fig. 1.2 will be employed, as it is sufficient to gather the essential properties of the dynamic trajectories under study.

When considering the DKP, the situation is significantly more complicated: even for standard parallel robots, there is no guarantee that a given input joint position will give a unique solution. In fact, for the Gough-Stewart platform mentioned in 1.3.1, it has been proven that up to 40 solutions may exist [58]. To further complicate the situation, Eq. (1.2) is valid under the assumption that cable i is in tension, which could be not true. If the number of taut cables is lower than the number of EE DoFs (which is the case for an under-constrained robot, see case (C) in Sec. 1.3.2.1), a pure kinematic analysis is not sufficient to fully determine the robot pose: the static equilibrium conditions must then be taken into account and thus the Direct Geometrico-static Problem (DGP) is obtained. Assuming that m of the n_C cables are under tension, the DGP gives a system of equations that can have multiple solutions: for instance, it has been shown in [1, 44, 45] that the DGP for a robot with 3, 4 or 5 cables in tension can have respectively up to 156, 216 and 140 solutions. The solutions which have at least one negative tension in the cables are then discarded as unfeasible [46]. Common numerical algorithms used to obtain the full set of possible solution are obtained by *homotopy continuation* [1] and *interval analysis* [22]: this latter method is especially interesting as it is known to be robust (that is, insensitive to small changes in the data) and safe, as it guarantees that all solutions can be found in a reasonably short time. The union of all feasible solutions, for m going from 1 to n_C , gives the full solution set for the robot pose [131].

The results above are valid under the assumption of massless, infinitely stiff cables that form a straight line segment as in Fig. 1.2. These concepts can be generalized by using the classical model from [93] of a cable with both mass (uniformly distributed along the cable length) and finite stiffness: the cable will then sag under its own weight and form what is called an *elastic catenary* curve. The IKP for this case was also studied [109].

Workspaces

A number of *workspaces* have been defined for cable robots, that define the CDPR region where the robot can operate while respecting a number of constraints due to its actuation, kinematics, and so on.

By taking into account the necessity of avoiding intersection between the cables, the *interference-free* workspace has been defined in [127, 158]; in [25], the authors also take into account the effects of cable sagging and elasticity. The interference of cables with obstacles in their environment of known shape and position was considered in [124, 212]. It is also worth noting that cable interference is generally less dangerous than interference between the rigid legs of a classical parallel robot, and it has been shown [201] that a CDPR can retain functionality even when two cables collide.

Another kinematic constraint is given by the limits on the cable lengths: indeed, for each cable there will be a maximum length ρ_{max} given by the span of the cable that can be accommodated on the winch. One can also set a lower limit ρ_{min} to ensure that the EE remains far enough from the winches, a situation that could be dangerous both for the risk of collisions and the fact that is usually leads to very high cable tensions. The Reachable Workspace (RW) can then be defined [132] as the set of positions that can be reached by the EE (with any orientation) while respecting the kinematic constraints on the joints $\rho_i \in [\rho_{min}, \rho_{max}]$, $i = 1, \dots, 6$. This workspace can then be found by using the tools of classical robot analysis [129, Ch. 7], for both planar [132] and spatial robots [105, 126], under the assumption that all cables remain in tension.

It has been shown in Subsec. 1.3.2.1 that, for over-constrained robots, there are poses where any external wrench applied on the EE can be balanced by positive cable tensions; the set of all such poses is called the *Wrench-Closure Workspace (WCW)* [77]. This concept has been studied for both single-link robots (either planar [77] or spatial [78]) and multiple-link mechanisms [113]. The WCW becomes especially important for dynamic motions: if a robot tra-

1. Introduction

jectory is entirely within the WCW, then it surely can be described by the EE while keeping positive cable tensions. However, the WCW leads in many cases to unnecessarily strict conditions and is not defined for under or fully-constrained robots.

For CSPRs specifically, it is customary to define a Static Equilibrium Workspace (SEW) as the set of positions where the EE can remain in equilibrium with positive tensions under the sole effect of gravity, either for point-mass EEs [167] or EEs having finite extension [164, 183] assuming a constant orientation of the EE. In particular, [164] considers a 6–6 cable spatial robot conceptually similar to a Gough-Stewart platform, while [183] considers both planar and spatial robots. A CSPR can then move anywhere in its SEW, provided that the motion is slow enough to be *quasi-static*, so that dynamic effects can be disregarded, and no disturbance forces are applied on the EE.

The requirement for a pose to be in the WCW is sometimes relaxed: one can define thus the *available wrench set* [30] as the set of all possible wrenches that can be applied on the EE under given constraints on the cable tensions $\boldsymbol{\tau}_{max} \succeq \boldsymbol{\tau} \succeq \mathbf{0}$, where $\boldsymbol{\tau}$ denotes the $n_C \times 1$ vector of cable tensions and $\boldsymbol{\tau}_{max}$ is the vector of the upper cable tension limits (depending on the maximum safe load provided by the cable manufacturer and the peak torque of the motors)[†].

If the manipulator is to withstand wrenches in a given set, the Wrench-Feasible Workspace (WFW) is then defined [61] as the set of all poses where this set of required wrenches is entirely contained within the available wrench set: in other words, the WFW is the set of poses where any of the required wrenches can be exerted by the robot on its surroundings while respecting the limits on cable tensions. Clearly, if the set of required wrenches is the full vector space of forces and torques in the motion space of the robot and $\tau_{max} \rightarrow +\infty$, the WFW coincides with the WCW; if the only element of the required wrench set is instead a pure gravitational force (and if, again, upper

[†] Here, as in the rest of this thesis, the symbol \succeq denotes *component-wise* inequality, so for instance $\boldsymbol{\tau} \succeq \mathbf{0}$ means that every element of $\boldsymbol{\tau}$ is ≥ 0 .

cable tension limits tend to infinity), then the WFW coincides with the SEW. A method to find the WFW for either planar CDPRs or spatial fully-constrained robots with point-mass EE was presented in [32]; later, in [36], the method was extended to consider both fully- and over-actuated robots, either planar or spatial and with a generic lower bound $\boldsymbol{\tau}_{min} \succeq \mathbf{0}$ on the cable tensions. Interval analysis has proven useful also for obtaining the WFW with reduced computation times [79] and at the same time handle small uncertainties in the design parameters. The WFW is less restrictive than the WCW, however it requires defining beforehand a set of required wrenches, a decision that can often be arbitrary.

The results on the workspaces described above can be used as a guide during the design phase: for example, the selection of an optimal robot geometry, under the constraint of a required workspace, was presented in [80].

1.3.2.4 Translational motion

Many robotic applications do not require a full control of the EE pose, but only of the EE position while its orientation remains constant. There are numerous architectures of conventional, rigid-link robots that fulfill this requirement, such as the 3-UPU [194], the Tripteron [47, 108] and the *Delta* robot [50]; a classification and a synthesis method of such manipulators was proposed in [47]. The *Delta* robot architecture in particular is based on three “legs”, each composed of a parallelogram linkage connected to a rotating lever: the actuation is provided by a motor fixed on the base which rotates the lever.

Various cable robots have also been proposed with purely translational motion. Some of the simplest models [28, 68, 71, 136, 137, 167] simply use a *point-mass* EE, that is, one whose dimensions are compact enough that all the mass can be considered concentrated in the Center of Mass (CoM): the rotational DoFs can thus be disregarded and the robot has only three translational DoFs (this is the first architecture considered in this thesis, see Subsec. 1.5.1). However, this is only a crude approximation, as point masses do not exist in nature, and has limited applications.

1. Introduction

A number of cable-driven mechanisms with translational motion has been proposed whose legs are based on a *parallelogram* structure: that is, each leg is composed of two cables that at all times must have the same length and remain parallel. If three or more parallelograms of this kind are employed, it can be shown that the orientation of the EE remains fixed.

One of the first robots of this kind was presented in [31], a CSPR with 6 cables: this robot is conceptually analogous to the Delta [50], with the difference that here the parallelograms are *extensible* (being composed of cables that can be coiled and uncoiled on winches) while the Delta had fixed-length kinematic chains. The robot in [31] was designed for search-and-rescue operations: in this paper, the authors showed how the DKP can be reduced to a *trilateration* problem, that is to say finding the intersection of three spheres of known centers and radii. In [31] the authors also found the SEW through a numerical procedure and defined a calibration method.

This concept was extended in [33] to a robot devised for the construction sector with over-constrained architecture, having 4 parallelogram cable pairs and 4 extra tensioning cables: in [33], the authors showed how to find the WFW with a numerical procedure, while in a later work [199] the robot dynamics was considered by simulating various trajectories and a control scheme was proposed.

Another translational robot with an over-constrained architecture was proposed in [174]: here, the authors use 3 *active* cables (that is, directly connected to cable winches) with a common attachment point on the EE to control its position, while 6 other *passive* cables (which are not actuated, but kept in tension by springs) set in a parallelogram fashion to maintain a constant platform orientation. The authors also showed the design of a gripper attached to the EE, as the proposed application was for pick-and-place operations; later, in [173], they also studied the wrench-feasibility conditions.

Numerous other cable-based, parallelogram-actuated manipulators have been proposed, where the cables were kept in tension by either antagonis-

tic jacks (see for instance the DeltaBot [19] and BetaBot [15, 16] robots developed by Behzadipour et al. or [213]) or by antagonistic additional cables [4, 5, 115, 172]; over-constrained robots are more complicated to design and more expensive to build compared to the simpler, fully-constrained architecture in [31].

Proposed applications for 3-DoF cable robots were in service robotics to help disabled people in navigating around architectural barriers [49] or for large-scale 3D printing [13].

CSPRs with parallelogram actuation have thus proven useful in a number of potential applications; however, they were usually assumed to move quasi-statically and the potential advantages of dynamic motions were not studied.

1.4 Thesis Outline

The remainder of this thesis is structured as follows. To show how dynamical trajectories can be realized (aim (I) in Sec. 1.2), two CSPR architectures will first be developed, that will be used throughout this work: a 3-cable robot with point-mass EE (Subsec. 1.5.1) and a 6-cable robot with a finite-size platform (Subsec. 1.5.2); both models have only translational DoFs. These are models that are simple enough to give an immediate sense of the properties of dynamic motions for cable robots, while at the same time being able to capture the behavior of real cable-driven systems. Special architectures will also be presented (Subsecs. 1.5.2.1 to 1.5.2.3) that are particular cases of the most general 6-cable model and which provide useful features.

In Ch. 2, the state of the art on the dynamic modeling of CDPRs will be presented and the kineto-static model of the two reference robots will be derived.

In Ch. 3, then, new dynamic trajectories will be presented and applied to the two model robots; also, the results from experimental tests will be presented (Subsecs. 3.7.1 and 3.7.2) that confirm the theoretical work.

1. Introduction

For the 6-cable robot in particular, there are practical limits on the motions that can be realized: even if a trajectory is feasible (that is, it can be described with all cables taut) the robot can pass through a singularity pose. Also, the cable lengths might reach their limits or have interference between them. Therefore, in Ch. 4 the singularity loci (Sec. 4.2), the reachable workspace RW (Sec. 4.3) and the interference-free workspace (Sec. 4.4) will be presented. This covers the second goal of the present work (point (II) in Sec. 1.2).

In Ch. 5, indexes will be introduced to provide a physically coherent measure of the behavior of a spatial parallel robot in terms of its sensitivity to control errors: if said sensitivity is excessively high, even small errors on the actuators' positions could lead to a large error on the robot pose. Said indexes will be calculated for the 6-cable robot model defined in Subsec. 1.5.2 to show how they vary throughout the robot's RW.

Ch. 6 will show how to model the stiffness properties of the 6-cable manipulator and prove that, for the special architecture in 1.5.2.1, this can be expressed in a particularly simple form. Indexes that measure the global stiffness properties of a parallel manipulator will be presented: these indexes, like the ones presented in Ch. 5, are shown to be meaningful for the designer. Ch. 6 is concluded by presenting the variation of these indexes across the robot workspace. Together, Chapters 5 and 6 fulfill goal (III) in Sec. 1.2.

The conclusions in Ch. 7 highlight the advantages of the work in this thesis and outline possible future work on the topic.

The proofs of some theorems in the Thesis are reported in Appendix A.

1.5 Robot architectures

For all robot models presented in this section, the following assumptions will be used:

- cables are modeled as infinitely stiff and massless, with negligibly small

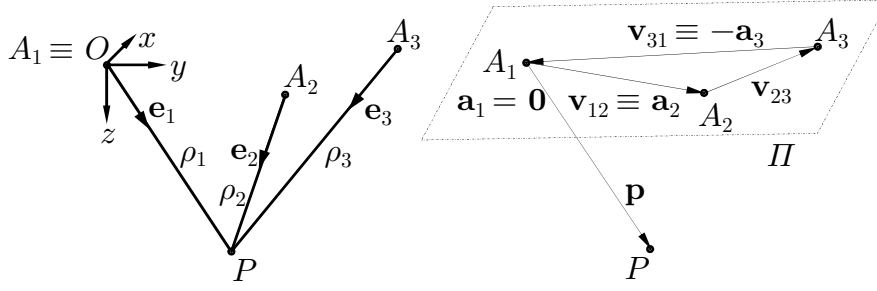


Figure 1.3: (Left) Schematic of a spatial C SPR with point-mass EE and 3 DoFs.
 (Right) Auxiliary vectors and plane Π .

diameter; therefore, they are represented as straight line segments;

- the EE is an ideal rigid body of mass m ;
- an OP P is chosen on the EE that defines the robot's position; having defined a fixed coordinate system on the frame $Oxyz$, the position of P is given by $\mathbf{p} = P - O = [x, y, z]^T$. For convenience, the OP is chosen to coincide with the CoM;
- the only wrenches acting on the EE are due to the cables' tensions, gravity and dynamic inertial effects;
- cables have fixed attachment points A_i on the frame; the position vectors of said attachment points are $\mathbf{a}_i = A_i - O = [x_{ai}, y_{ai}, z_{ai}]^T$. Without loss of generality, it is convenient to set $O \equiv A_1$ (see Figs. 1.3 and 1.4).
- the attachment points on the EE are modeled as perfect spherical joints in points B_i having positions (with respect to the OP) $\mathbf{b}_i = B_i - P$; when the robot has a point-mass EE, all points B_i coincide in P and thus $\mathbf{b}_i = \mathbf{0}$ for all i .
- the cables are always assumed to be at a strictly positive length $\rho_i = \|\mathbf{a}_i - \mathbf{p} - \mathbf{b}_i\| > 0$.

1.5.1 Point-mass robot

The first robot model considered in this thesis is a spatial C SPR whose EE is modeled as a point mass P . It is also useful to define some auxiliary vectors:

$$\mathbf{v}_{jk} = [x_{ajk}, y_{ajk}, z_{ajk}]^T = \mathbf{a}_k - \mathbf{a}_j \quad (j, k \in \{1, 2, 3\}) \quad (1.3)$$

1. Introduction

Also, it is useful to define the plane Π that passes through points A_i 's, which has equation

$$ax + by + cz + d = 0 \quad (1.4)$$

The coefficients in Eq. (1.4) depend on vectors \mathbf{a}_i as follows:

$$\begin{aligned} a &= \begin{vmatrix} 1 & y_{a1} & z_{a1} \\ 1 & y_{a2} & z_{a2} \\ 1 & y_{a3} & z_{a3} \end{vmatrix}, & b &= \begin{vmatrix} x_{a1} & 1 & z_{a1} \\ x_{a2} & 1 & z_{a2} \\ x_{a3} & 1 & z_{a3} \end{vmatrix} \\ c &= \begin{vmatrix} x_{a1} & y_{a1} & 1 \\ x_{a2} & y_{a2} & 1 \\ x_{a3} & y_{a3} & 1 \end{vmatrix}, & d &= - \begin{vmatrix} x_{a1} & y_{a1} & z_{a1} \\ x_{a2} & y_{a2} & z_{a2} \\ x_{a3} & y_{a3} & z_{a3} \end{vmatrix} \end{aligned} \quad (1.5)$$

In this case, the unit vectors along the cables are $\mathbf{e}_i = (\mathbf{p} - \mathbf{a}_i) / \rho_i$ for $i \in \{1, 2, 3\}$ (compare with Fig. 1.2). For the 3-cable robot, it is convenient to define the unit vectors from A_i to P , to maintain a coherent notation with [71, 137]; for the same reason, the z axis in the reference frame chosen is oriented downwards.

1.5.2 Translational robot

The second robot model used in this thesis is a spatial robot with finite-size EE having a purely translational motion as described in Subsec. 1.3.2.4. This CSPR is a 6-cable robot having three parallelogram “legs”: therefore, its orientation remains constant.

The robot is conceptually analogous to the ones presented in [13, 31, 196]; however, while the cited references considered special architectures, this thesis will consider the most general case, thereby including all the robots from [13, 31, 196] in the analysis.

One interesting feature of this architecture is that it allows using just as many actuators as DoFs, thereby reducing the total cost and the design complexity: indeed, since the two cables in a given parallelogram ought to remain at the same length at all times, they can be actuated by the same motor.

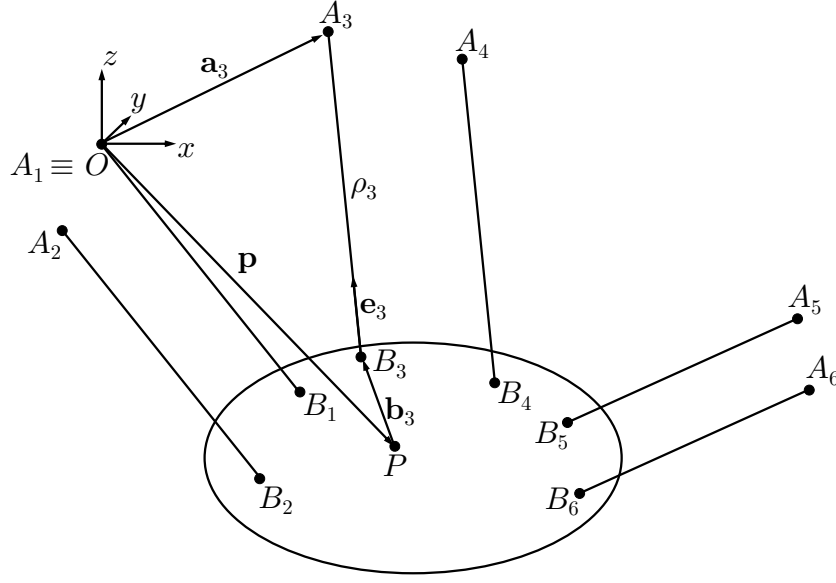


Figure 1.4: A 6-cable CDRP with 3 translational DoFs.

Also, the robot is controlled by the minimum number of cables needed for a fully-constrained CDRP, without introducing tensioning devices such as passive spines [16, 19].

In this case, the cable directions are given by $\mathbf{e}_i = (\mathbf{a}_i - \mathbf{p} - \mathbf{b}_i) / \rho_i$, which are the unit vectors from B_i to A_i (again, compare with Fig. 1.2); also, the z -axis of the fixed coordinate frame is oriented upwards.

In the “start” position, the cables are pairwise parallel and at equal lengths, so that $\rho_1 = \rho_2$, $\rho_3 = \rho_4$, $\rho_5 = \rho_6$, $\mathbf{e}_1 = \mathbf{e}_2$, $\mathbf{e}_3 = \mathbf{e}_4$, and $\mathbf{e}_5 = \mathbf{e}_6$. Moreover, the placement of points A_i and B_i is chosen in such a way that $\|\mathbf{a}_2 - \mathbf{a}_1\| = \|\mathbf{b}_2 - \mathbf{b}_1\|$, $\|\mathbf{a}_4 - \mathbf{a}_3\| = \|\mathbf{b}_4 - \mathbf{b}_3\|$, and $\|\mathbf{a}_6 - \mathbf{a}_5\| = \|\mathbf{b}_6 - \mathbf{b}_5\|$. Therefore, the 6 cables define 3 parallelograms $A_1B_1B_2A_2$, $A_3B_3B_4A_4$, and $A_5B_5B_6A_6$ at the start of the motion; since the motors control the cables in pairs, this condition remains true at all times, assuming that the cables remain taut and that the EE does not rotate. In this case, the parallelogram defined by cables i and j , which is contained in plane Π_{ij} , blocks the rotation of the EE in a direction \mathbf{n}_{ij} ; this is defined as the unit vector normal to Π_{ij} . Unless the three vectors \mathbf{n}_{12} , \mathbf{n}_{34} and \mathbf{n}_{56} are coplanar, no rotation is allowed: therefore, the EE will

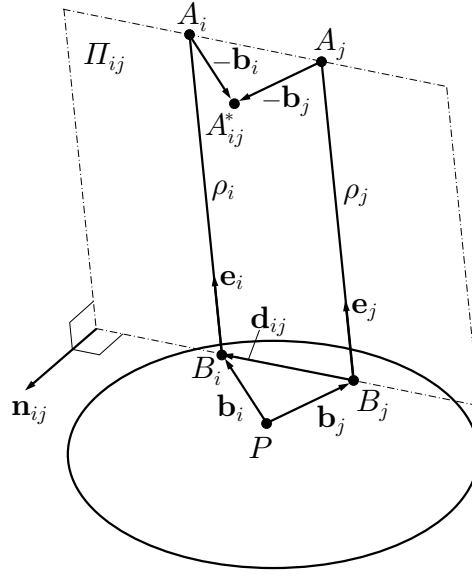


Figure 1.5: The planar parallelogram formed by cables i and j .

only have a translational motion. Note that vectors \mathbf{b}_i 's ($i = 1, \dots, 6$), which depend only on the EE's orientation, will remain constant throughout any purely-translational movement. This architecture is similar to that of the Delta robot [31, 48].

Here, some auxiliary elements can be usefully introduced:

- auxiliary points A_i^* ($i = 1, \dots, 6$) are defined by position vector $\mathbf{a}_i^* = \mathbf{a}_i - \mathbf{b}_i$. Note that, if the i -th and j -th cables form a parallelogram, $\mathbf{a}_i^* = \mathbf{a}_i - \mathbf{b}_i = (\mathbf{a}_j - \mathbf{b}_j + \mathbf{b}_i) - \mathbf{b}_i = \mathbf{a}_j - \mathbf{b}_j = \mathbf{a}_j^*$, since $\mathbf{a}_i - \mathbf{a}_j = \mathbf{b}_i - \mathbf{b}_j$ and thus $\mathbf{a}_i = \mathbf{a}_j - \mathbf{b}_j + \mathbf{b}_i$ (Fig. 1.5). Therefore, there is actually one such point for each pair $A_{ij}^* = A_i^* = A_j^*$, whose position is $\mathbf{a}_{ij}^* = \mathbf{a}_i^* = \mathbf{a}_j^*$; these positions are constant, as vectors \mathbf{a}_i and \mathbf{b}_i do not depend on the robot pose.
- auxiliary vectors $\mathbf{d}_{ij} = \mathbf{b}_i - \mathbf{b}_j$, which go from B_j to B_i ; these vectors are also constant.
- plane Π is the one passing through points A_{12}^* , A_{34}^* and A_{56}^* .

It is now convenient to introduce some special architectures, that are sub-

cases of the most general schematic shown in Fig. 1.4 which will be useful later in this work. A general schematic of the various robot sub-cases is presented in Fig. 1.6 on page 28.

1.5.2.1 Special architecture \mathcal{L}

The first special architecture \mathcal{L} (on the left of Fig. 1.6) is defined by point P , the CoM of the EE, being on the intersection of segments $\overline{B_1B_2}$, $\overline{B_3B_4}$, and $\overline{B_5B_6}$.

Further specializations of \mathcal{L}

A special case \mathcal{L}_1 of architecture \mathcal{L} is found if P is exactly in the midpoint of segments $\overline{B_iB_j}$. A further restriction is obtained by requiring that the three segments $\overline{B_iB_j}$ are of equal length: this gives the special architecture \mathcal{L}_2 .

1.5.2.2 Special architecture \mathcal{R}

The second special architecture \mathcal{R} (on the right of Fig. 1.6) is defined by having vectors \mathbf{d}_{ij} all parallel to Π .

Further specializations of \mathcal{R}

Architecture \mathcal{R}_1 is defined by having all A_i 's coplanar, on a plane Γ . This is a special case of \mathcal{R} : indeed, since $\mathbf{a}_i - \mathbf{a}_j = \mathbf{b}_i - \mathbf{b}_j = \mathbf{d}_{ij}$, one can see that vectors \mathbf{d}_{ij} will all be parallel to Γ and thus points B_i will also be coplanar, on a plane parallel to Γ . Then, Π will also be parallel to Γ^\ddagger .

1.5.2.3 Special architecture \mathcal{LR}

This special architecture is given by the intersection of the conditions for \mathcal{R}_1 and \mathcal{L}_2 : therefore, all A_i 's are coplanar and P is in the middle of segments $\overline{B_iB_j}$, which are of equal length. This “final” architecture is the one actually used to build the prototype for the experimental tests (Subsec. 3.7.2).

\ddagger P does not have to be in the plane through points B_i 's; if it is so, then $\Pi \equiv \Gamma$.

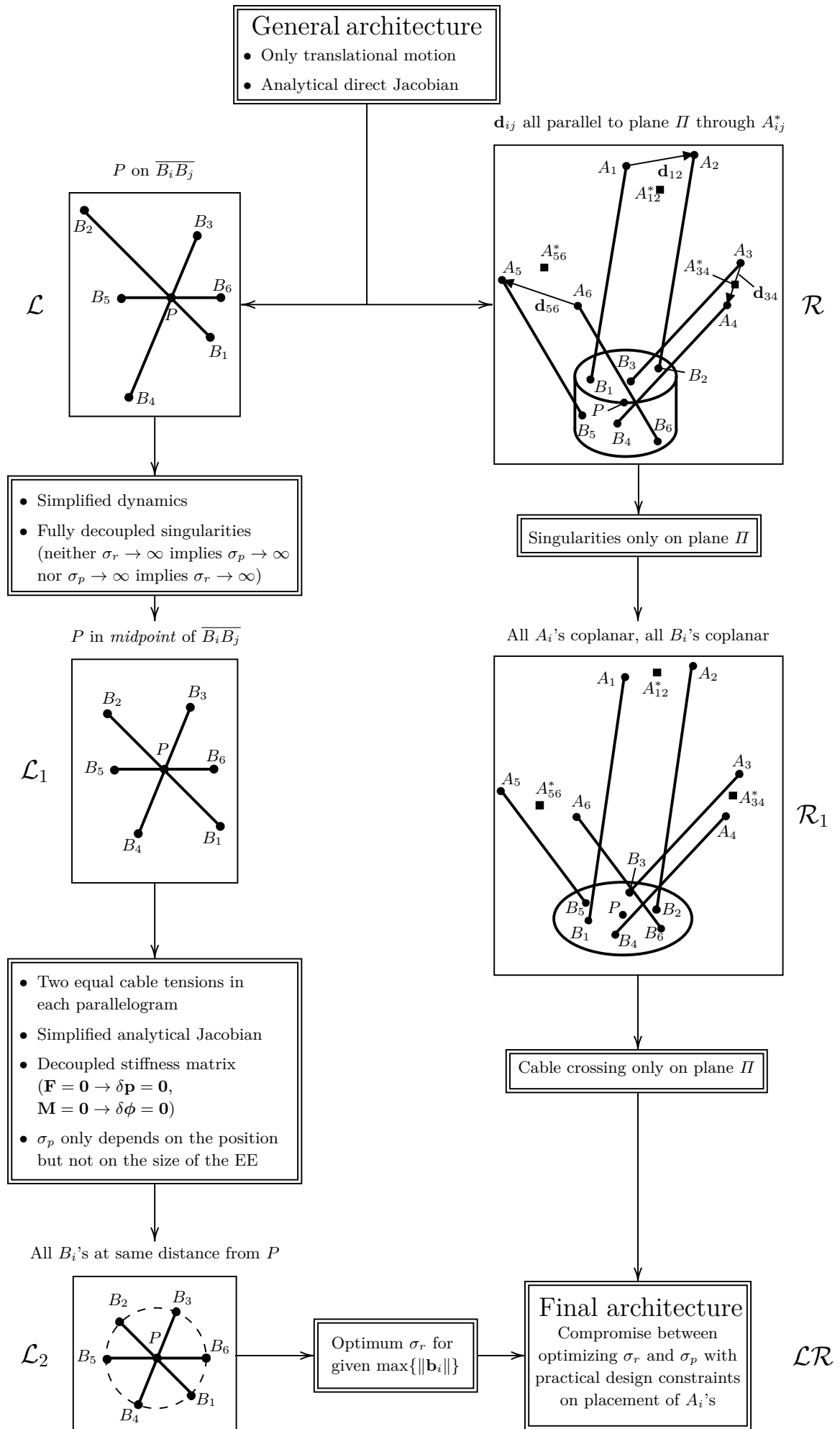


Figure 1.6: A general schematic of the possible special architectures for the translational robot.

2

Kinetostatic model

in which the dynamics of CSPRs is introduced with the kinetostatic model of two classes of robots, with a point-mass EE and with a finite-size EE, respectively.

2.1 Dynamics of CSPRs: state of the art

CSPRs are usually considered to move quasi-statically, so their accelerations (and, correspondingly, the inertial forces on the EE) are negligible. In this case, as seen in Subsec. 1.3.2.3, the robot can only move within its SEW.

However, one of the most interesting advantages of cable robots is their ability to reach very high accelerations (see Sec. 1.1), thanks to their parallel architecture and the low inertias of the cables. If the cable weight is neglected, as is usually done, the effect of dynamic actions on the robot amounts to a wrench acting on the EE which is composed of the inertia force and the inertia moment.

Here, a first necessary distinction must be made between under-constrained and fully- or over-constrained CSPRs: for the latter, the pose can be directly derived by solving the DKP, while for the former one must also consider the force and moment equilibrium conditions. Therefore, the dynamic analysis of under-constrained cable robots is more challenging.

One of the earliest studies on the dynamics of fully-actuated robots con-

2. Kinetostatic model

cerned a 3-cable robot with a point-mass EE [68], like the one presented in Subsec. 1.5.1. Later, dynamic models of 6-cable, 6-DoF CSPRs were proposed in [144, 214], which studied robots designed respectively for the LAR telescope (in Canada) and for the FAST telescope (in China); these works were among the first to include the effect of the cable mass in the dynamic model. The dynamics of over-actuated cable robots is studied in [199], specifically for a translational CSPR conceptually similar to the one in Subsec. 1.5.2.

An interesting generalization is the study of the dynamics of *multi-stage* cable robots. For instance, [150] presents an aerial mobile robot composed of two stages, a helicopter carrying a cable-actuated crane, while in [149], the stages are two mobile platforms connected to the fixed frame and to each other by cables. The exchange of forces between multiple stages makes the dynamic analysis especially complex.

One of the first studies about the dynamic modeling of an under-constrained (and under-actuated) system was presented in [203], for a 3-cable robot with a 6-DoF EE: the authors developed an inverse dynamics model and proposed a feedback control method to keep the sway motion under control while performing a desired trajectory. Another example was presented in [10]: here, the authors derived the dynamic equations of a hybrid serial-parallel robot (with a serial arm composed of two rigid links carried by a parallel, cable-actuated platform) using both a Newtonian and Lagrangian approach. In [91], the goal was to move an under-constrained CSPR along a given trajectory between two endpoints—both at rest—where a suitable subset of the EE generalized coordinates was set (the remaining generalized coordinates, along with the cable tensions, were then defined by the Inverse Geometrico-static Problem (IGP)); the authors showed how to apply general results about under-constrained robotic systems to reduce sway at the endpoints.

An approach that sometimes can be used to simplify the analysis and control of under-constrained cable robots is *differential flatness* which offers a framework to plan feasible trajectories for kinematically undetermined sys-

tems, by defining *flat outputs* that can be arbitrarily controlled: this approach has been successfully applied to some planar [12] and spatial [87] cable-driven robots.

One issue that is sometimes included in the dynamic modeling of CSPRs is the *vibration analysis*: since cables are flexible, their oscillations might become a source of concern, especially for robots with long cable spans. A complete vibration model of a generic cable-driven robot was presented in [57]: it was shown through a numerical investigation that the vibration of the EE is mostly due to axial flexibility of the cables. In [104] the effect of longitudinal vibrations in cables was thus assumed to be their dominant dynamic effect, a control system was designed specifically to reduce elastic effects and the conditions for stability of the closed-loop system were found.

The *dynamic workspace* of CSPRs (and of CDPRs in general) has been introduced in [14] for planar manipulators and is defined as the set of all poses where the EE can be in dynamic equilibrium, that is, with all cables in tension under some combination of velocity/acceleration. This is a generalization of the SEW, which is thus strictly contained in the dynamic workspace. The interest of studying the dynamic workspace, indeed, is especially in the fact that it allows greater freedom in planning the movements of the robot.

In the rest of this chapter, the dynamic models of the two architectures presented in Subsecs. 1.5.1 and 1.5.2 will be derived, according to the modeling method outlined in Sec. 1.5. For the translational cable robot, the advantages of the special architecture \mathcal{L} introduced in Subsec. 1.5.2.1 (and of its sub-cases \mathcal{L}_1 and \mathcal{L}_2) will be presented: it is found that these architectures lead to an especially simple dynamic model.

2.2 Model for a point-mass EE

The first model will now be considered (see Fig. 1.3). The forces applied to the EE are the following:

2. Kinetostatic model

- the cable tensions τ_i , directed along vectors \mathbf{e}_i ;
- the EE's own weight $m\mathbf{g}^*$;
- the inertia force $-m\ddot{\mathbf{p}}$.

By Newton's equation, the dynamic equilibrium is given by:

$$m\mathbf{g} - \sum_{i=1}^3 \tau_i \mathbf{e}_i = m\ddot{\mathbf{p}} \quad (2.1)$$

which can be rewritten in matrix form as

$$m(\mathbf{g} - \ddot{\mathbf{p}}) = \mathbf{M}[\tau_1, \tau_2, \tau_3]^T \quad (2.2)$$

by introducing the *structure matrix* $\mathbf{M} = [\mathbf{e}_1 \ \mathbf{e}_2 \ \mathbf{e}_3]$.

It has been proven in [71, Eqs. (17)–(19)] that $\tau_i > 0$ is equivalent to

$$\mu_i = [\mathbf{p} \times (\mathbf{a}_k - \mathbf{a}_j) + \mathbf{a}_k \times \mathbf{a}_j]^T (\ddot{\mathbf{p}} - \mathbf{g}) > 0 \quad (2.3)$$

as long as $\det \mathbf{M} < 0$; here, indexes j and k depend on index i , as follows:

$$\begin{cases} i = 1 \rightarrow j = 3, k = 2 \\ i = 2 \rightarrow j = 1, k = 3 \\ i = 3 \rightarrow j = 2, k = 1 \end{cases} \quad (2.4)$$

Inequality $\det \mathbf{M} < 0$ holds true if the following conditions are respected: the cable exit points A_i must be clockwise numbered when observed from above (along the positive z direction) and the EE must remain below plane Π as in Fig. 1.3. Note that the EE could actually move above Π by applying dynamic trajectories designed specifically to safely pass through a singularity condition [212]; this possibility, however, will not be explored here.

2.3 Model for a finite-size EE

For the kineto-static model of the 3-parallelogram robot introduced in Subsec. 1.5.2 the first step is to consider two cables i and j in a parallelogram pair;

* Note that, as in Subsec. 1.5.1 the reference frame was chosen with the z axis pointing downwards, the gravitational acceleration is given by $\mathbf{g} = [0, 0, g]^T$.

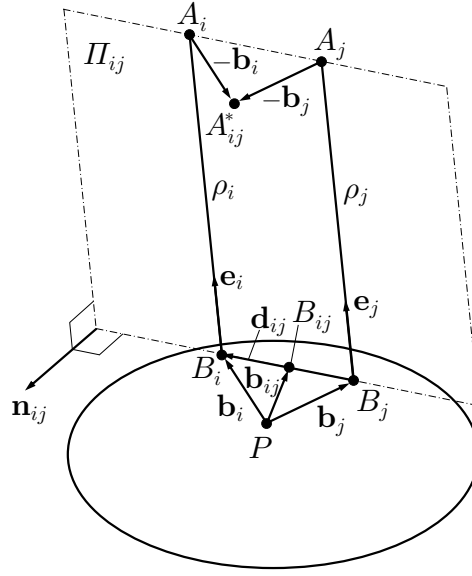


Figure 2.1: The planar parallelogram formed by cables i and j (cf. Fig. 1.5).

these exert two forces $\mathbf{F}_i = \tau_i \mathbf{e}_i$ and $\mathbf{F}_j = \tau_j \mathbf{e}_j = \tau_j \mathbf{e}_i$ on the EE (see Fig. 2.1). Therefore, the resultant wrench is given by a force \mathbf{F}_{tot} and a moment \mathbf{M}_{tot} about P , namely

$$\mathbf{F}_{tot} = \mathbf{F}_i + \mathbf{F}_j = (\tau_i + \tau_j) \mathbf{e}_i \quad (2.5a)$$

$$\mathbf{M}_{tot} = \mathbf{b}_i \times \mathbf{F}_i + \mathbf{b}_j \times \mathbf{F}_j = (\tau_i \mathbf{b}_i + \tau_j \mathbf{b}_j) \times \mathbf{e}_i \quad (2.5b)$$

One can define here the *total* tension given by $\tau_{tot,ij} = \tau_i + \tau_j$ and the *tension ratios* σ_i, σ_j as

$$\sigma_i = \frac{\tau_i}{\tau_{tot,ij}}, \quad \sigma_j = \frac{\tau_j}{\tau_{tot,ij}} = 1 - \sigma_i \quad (2.6)$$

It is thus found that the wrench $[\mathbf{F}_{tot}^T, \mathbf{M}_{tot}^T]^T$ is equivalent to the wrench given by a single force $\mathbf{F}_{ij} = \mathbf{e}_i \tau_{tot,ij}$ applied in point B_{ij} whose position is given by $\mathbf{p} + \mathbf{b}_{ij}^\dagger$, where \mathbf{b}_{ij} is the position vector

$$\mathbf{b}_{ij} = \frac{\tau_i \mathbf{b}_i + \tau_j \mathbf{b}_j}{\tau_{tot,ij}} = \sigma_i \mathbf{b}_i + \sigma_j \mathbf{b}_j = \sigma_i \mathbf{b}_i + (1 - \sigma_i) \mathbf{b}_j \quad (2.7)$$

[†] Eqs. (2.6) and (2.7) are defined only for $\tau_{tot,ij} \neq 0$. The case $\tau_{tot,ij} = 0$ is disregarded since it would necessarily imply either that $\tau_i = \tau_j = 0$ or that one of τ_i, τ_j is negative. In both cases the cables are no longer taut, against the original assumptions.

2. Kinetostatic model

From the definition of \mathbf{b}_{ij} in Eq. (2.7), point B_{ij} is on the straight line through B_i and B_j ; it coincides with B_i (respectively, B_j) if $\sigma_i = 1$ and thus $\tau_j = 0$ (resp. if $\sigma_i = 0$ and $\tau_i = 0$). If otherwise $\tau_i, \tau_j \in [0, \tau_{tot,ij}]$, then $\sigma_i, \sigma_j \in [0, 1]$: in this case B_{ij} lies on the segment through B_i and B_j .

The dynamic equations read in this case[‡]

$$\sum_{i=1}^6 \mathbf{e}_i \tau_i = m\ddot{\mathbf{p}} - m\mathbf{g} = -\mathbf{F}_e \quad (2.8a)$$

$$\sum_{i=1}^6 \mathbf{b}_i \times \mathbf{e}_i \tau_i = \mathbf{0} \quad (2.8b)$$

$\mathbf{F}_e = m(\mathbf{g} - \ddot{\mathbf{p}})$ is the total force due to inertia and to the EE's own weight: since it is applied in P , the CoM of the platform, the external moment around P (due to \mathbf{F}_e) is zero. Eqs. (2.8) can be expressed in matrix form as

$$\tilde{\mathbf{M}}\boldsymbol{\tau} = \mathbf{W}_e \quad (2.9)$$

where $\boldsymbol{\tau} = [\tau_1, \dots, \tau_6]^T$ is the vector of cable tensions, $\mathbf{W}_e = [-\mathbf{F}_e^T, \mathbf{0}^T]$ is the wrench due to gravity and inertia acting on the platform and

$$\tilde{\mathbf{M}} = \begin{bmatrix} \mathbf{e}_1 & \mathbf{e}_1 & \cdots & \mathbf{e}_5 & \mathbf{e}_5 \\ \mathbf{b}_1 \times \mathbf{e}_1 & \mathbf{b}_2 \times \mathbf{e}_1 & \cdots & \mathbf{b}_5 \times \mathbf{e}_5 & \mathbf{b}_6 \times \mathbf{e}_5 \end{bmatrix} \quad (2.10)$$

$\tilde{\mathbf{M}}$ is a 6×6 wrench matrix; here, the property of cables being pairwise parallel has been used, so $\mathbf{e}_1 = \mathbf{e}_2$ and so on.

Eq. (2.9) is a system of 6 equations in 6 unknowns, namely, cable tensions τ_1, \dots, τ_6 ; however, this system can be simplified by introducing \mathbf{F}_{ij} (applied in B_{ij} , as seen before) to replace the cable forces \mathbf{F}_i and \mathbf{F}_j in a cable pair. Eq. (2.9) then becomes

$$\mathbf{M}\boldsymbol{\tau}_{tot} = \mathbf{W}_e \quad (2.11)$$

Here, the total cable tensions are in vector $\boldsymbol{\tau}_{tot} = [\tau_{tot,12}, \tau_{tot,34}, \tau_{tot,56}]^T$, while the 6×3 matrix \mathbf{M} is defined by

$$\mathbf{M} = \begin{bmatrix} \mathbf{e}_1 & \mathbf{e}_3 & \mathbf{e}_5 \\ \mathbf{b}_{12} \times \mathbf{e}_1 & \mathbf{b}_{34} \times \mathbf{e}_3 & \mathbf{b}_{56} \times \mathbf{e}_5 \end{bmatrix} = \begin{bmatrix} \mathbf{M}_{sup} \\ \mathbf{M}_{inf} \end{bmatrix} \quad (2.12)$$

[‡] Here, with the notation from Subsec. 1.5.2 where z points upwards, $\mathbf{g} = [0, 0, -g]^T$.

This approach simplifies the dynamic equilibrium equations: one still obtains 6 equations in 6 unknowns, however this system is *decoupled*. Indeed, the first three unknowns (namely, the total tensions $\tau_{tot,ij}$) can be obtained by solving the first three equations; solving the remaining three equations yields the other three unknowns (the ratios σ_i 's, which define vectors \mathbf{b}_{ij} 's).

The first three equations in Eq. (2.11) are $\mathbf{M}_{sup}\boldsymbol{\tau}_{tot} = -\mathbf{F}_e = -m(\mathbf{g} - \ddot{\mathbf{p}})$. Then, $\boldsymbol{\tau}_{tot}$ is obtained from the inverse of \mathbf{M}_{sup} (the upper block of \mathbf{M}) as:

$$\boldsymbol{\tau}_{tot} = -\mathbf{M}_{sup}^{-1}\mathbf{F}_e \quad (2.13)$$

Calculating \mathbf{M}_{sup}^{-1} requires $\mathbf{M}_{sup} = [\mathbf{e}_1 \ \mathbf{e}_3 \ \mathbf{e}_5]$ to be non-singular: therefore, vectors \mathbf{e}_1 , \mathbf{e}_3 and \mathbf{e}_5 cannot be linearly dependent. This issue will be dealt with in Sec. 4.2; for now, \mathbf{M}_{sup} will be assumed non-singular. Note that the unit cable direction \mathbf{e}_i is $\mathbf{e}_i = (\mathbf{a}_i - \mathbf{b}_i - \mathbf{p}) / \|\mathbf{a}_i - \mathbf{b}_i - \mathbf{p}\|$ (Subsec. 1.5.2): substituting the definition $\mathbf{a}_{ij}^* = \mathbf{a}_i - \mathbf{b}_i$, one obtains $\mathbf{e}_i = (\mathbf{a}_{ij}^* - \mathbf{p}) / \|\mathbf{a}_{ij}^* - \mathbf{p}\| = \mathbf{e}_j$.

Given the similarity between (2.2) and the first three equations of (2.11), one can introduce an *equivalent* robot having three cables (attached in points A_{ij}^*) which move a point-mass EE: this equivalent robot has cable tensions $\tau_{tot,12}$, $\tau_{tot,34}$ and $\tau_{tot,56}$. If the cables of the real (6-cable) robot are all taut, the three total tensions must be positive:

$$\boldsymbol{\tau}_{tot} \succeq \mathbf{0} \quad (2.14)$$

From this equivalent model, one can derive the conditions for the $\tau_{tot,ij}$ to be positive, which are conceptually the same as those in (2.3):

$$\mu_{ij} := [\mathbf{p} \times (\mathbf{a}_{mn} - \mathbf{a}_{kl}) + \mathbf{a}_{mn} \times \mathbf{a}_{kl}]^T (\ddot{\mathbf{p}} - \mathbf{g}) > 0 \quad (2.15)$$

where indexes k , l , m and n depend on indexes i and j as follows:

$$\begin{cases} i = 1, j = 2 \rightarrow k = 5, l = 6, m = 3, n = 4 \\ i = 3, j = 4 \rightarrow k = 1, l = 2, m = 5, n = 6 \\ i = 5, j = 6 \rightarrow k = 3, l = 4, m = 1, n = 2 \end{cases} \quad (2.16)$$

2. Kinetostatic model

For Eqs. (2.15) to hold, P must remain below Π , and points A_{12}^* , A_{34}^* and A_{56}^* must be numbered clockwise (when seen along the positive z direction), analogously to the conditions seen in Sec. 2.2.

Requiring $\boldsymbol{\tau}_{tot}$ to be component-wise positive is a necessary, but not sufficient condition to guarantee that cable tensions in the translational CSPR are positive, since it might be the case that $\tau_{tot,ij} > 0$ with $\tau_i > 0$ and $\tau_j < 0$ (or vice versa). A second condition to satisfy emerges from the last three equations in Eq. (2.11), namely

$$(\mathbf{b}_{12} \times \mathbf{e}_1)\tau_{tot,12} + (\mathbf{b}_{34} \times \mathbf{e}_3)\tau_{tot,34} + (\mathbf{b}_{56} \times \mathbf{e}_5)\tau_{tot,56} = \mathbf{0} \quad (2.17)$$

By considering the expression of \mathbf{b}_{ij} in Eq. (2.7) and recalling the definition of auxiliary vectors $\mathbf{d}_{ij} = \mathbf{b}_i - \mathbf{b}_j$ on page 26, Eq. (2.17) can be rewritten as

$$\mathbf{A}\boldsymbol{\sigma}_{135} = -\mathbf{b}_{246} \quad (2.18)$$

where

$$\mathbf{A} = \begin{bmatrix} (\mathbf{d}_{12} \times \mathbf{e}_1)\tau_{tot,12} & (\mathbf{d}_{34} \times \mathbf{e}_3)\tau_{tot,34} & (\mathbf{d}_{56} \times \mathbf{e}_5)\tau_{tot,56} \end{bmatrix} \quad (2.19)$$

$$\boldsymbol{\sigma}_{135} = \begin{bmatrix} \sigma_1 & \sigma_3 & \sigma_5 \end{bmatrix}^T \quad (2.20)$$

and

$$\mathbf{b}_{246} = (\mathbf{b}_2 \times \mathbf{e}_1)\tau_{tot,12} + (\mathbf{b}_4 \times \mathbf{e}_3)\tau_{tot,34} + (\mathbf{b}_6 \times \mathbf{e}_5)\tau_{tot,56} \quad (2.21)$$

Eq. (2.18) is a system of 3 equations in the unknowns $\sigma_1, \sigma_3, \sigma_5$, which can be solved once one knows the total tensions $\boldsymbol{\tau}_{tot}$. The second and final condition for positive tensions in all cables is, thus[§]:

$$\mathbf{0} \preceq \boldsymbol{\sigma}_{135} \preceq \mathbf{1} \quad (2.22)$$

[§] Note that one could also solve Eq. (2.17) for the other three tension ratios as

$$\mathbf{A}\boldsymbol{\sigma}_{246} = \mathbf{b}_{135}$$

with

$$\boldsymbol{\sigma}_{246} = \begin{bmatrix} \sigma_2 & \sigma_4 & \sigma_6 \end{bmatrix}^T$$

$$\mathbf{b}_{135} = (\mathbf{b}_1 \times \mathbf{e}_1)\tau_{tot,12} + (\mathbf{b}_3 \times \mathbf{e}_3)\tau_{tot,34} + (\mathbf{b}_5 \times \mathbf{e}_5)\tau_{tot,56}$$

In this case, condition (2.22) could equivalently be set as $\mathbf{0} \preceq \boldsymbol{\sigma}_{246} \preceq \mathbf{1}$.

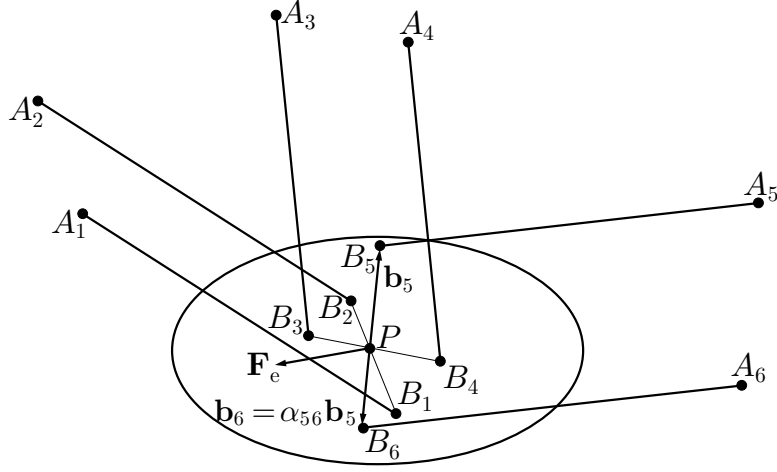


Figure 2.2: Scheme of the special architecture: the external force \mathbf{F}_e acts on P , which is the intersection of segments $\overline{B_1B_2}$, $\overline{B_3B_4}$ and $\overline{B_5B_6}$.

2.3.1 Special architecture \mathcal{L}

In this subsection the general kineto-static model developed in the previous section will be applied to the special architecture \mathcal{L} introduced in Subsec. 1.5.2.1. It will be shown that said architecture allows the user to define global conditions on a given trajectory so that condition (2.22) is always satisfied.

Let P lie at the intersection of lines B_1B_2 , B_3B_4 , and B_5B_6 (Fig. 2.2). Vectors \mathbf{b}_i and \mathbf{b}_j are then aligned, so $\mathbf{b}_j = \alpha_{ij} \mathbf{b}_i$, where α_{ij} is a generic scalar, and thus $\mathbf{d}_{ij} = \mathbf{b}_i(1 - \alpha_{ij})$. Substituting these expressions in Eqs. (2.19) and (2.21), one obtains that the column vectors of matrix \mathbf{A} have the form $(\mathbf{b}_i \times \mathbf{e}_i) \tau_{tot,ij} (1 - \alpha_{ij})$ and that vector \mathbf{b}_{246} is given by a sum of vectors $(\mathbf{b}_i \times \mathbf{e}_i) \tau_{tot,ij} \alpha_{ij}$. Eq. (2.18) then becomes

$$\sum_{ij} (\mathbf{b}_i \times \mathbf{e}_i) \tau_{tot,ij} (1 - \alpha_{ij}) \sigma_i = - \sum_{ij} (\mathbf{b}_i \times \mathbf{e}_i) \tau_{tot,ij} \alpha_{ij} \quad (2.23)$$

which after rearranging becomes

$$\sum_{ij} (\mathbf{b}_i \times \mathbf{e}_i) \tau_{tot,ij} [(1 - \alpha_{ij}) \sigma_i + \alpha_{ij}] = 0 \quad (2.24)$$

where the indexes in the summations on both sides take values $(i, j) \in \{(1, 2), (3, 4), (5, 6)\}$.

2. Kinetostatic model

It can now be seen that Eq. (2.24) always holds if $(1 - \alpha_{ij})\sigma_i = -\alpha_{ij}$, namely

$$\boldsymbol{\sigma}_{135} = \left[\frac{\alpha_{12}}{\alpha_{12}-1} \quad \frac{\alpha_{34}}{\alpha_{34}-1} \quad \frac{\alpha_{56}}{\alpha_{56}-1} \right]^T \quad (2.25)$$

Since the problem is linear, this is the only solution to Eq. (2.23), and it depends on neither the position \mathbf{p} nor the external force \mathbf{F}_e .

It can be easily shown that the condition required for positive cable tensions, namely $0 \leq \sigma_i \leq 1$, becomes in this case $\alpha_{ij} \leq 0$. This in turn means that P , the CoM of the robot, must lie on segment $\overline{B_i B_j}$ between points B_i and B_j .

In summary, if the three segments $\overline{B_1 B_2}$, $\overline{B_3 B_4}$, and $\overline{B_5 B_6}$ pass through the CoM P and the external wrench \mathbf{W}_e has zero moment about P (in this case because \mathbf{W}_e is only due to gravity and inertia), then the tension ratios are constant, and in order to verify that cable tensions are positive one can simply check the total tensions $\tau_{tot,ij}$, namely condition (2.14).

It is worth observing that this result also leads to a very simple formulation of the SEW which can be analytically defined for architecture \mathcal{L} (cf. other translational cable-driven systems, such as those in [31, 33], where the SEW was only numerically found).

Indeed, for the most general geometry of the translational robot (Subsec. 1.5.2), the SEW is the set of poses for which, when $\mathbf{F}_e = m\mathbf{g}$, $\boldsymbol{\tau}_{tot} \succeq \mathbf{0}$ (Eq. (2.14)) and $\mathbf{0} \preceq \boldsymbol{\sigma}_{135} \preceq \mathbf{1}$ (Eq. (2.22)). In general, these conditions define a complex volume in space: for instance, it may be proven that $\boldsymbol{\sigma}_{135} \succeq \mathbf{0}$ defines a 3rd-degree variety in x, y, z . However, for the special architecture \mathcal{L} , condition (2.22) is always satisfied, and only condition (2.14) must be checked. Due to the equivalence between this robot and the 3-cable robot with point-mass EE, it can immediately be seen that $\boldsymbol{\tau}_{tot} \succeq \mathbf{0}$ defines a vertical triangular prism having its upper vertices in A_{12}^* , A_{34}^* and A_{56}^* [167].

A virtual 3-cable robot with a point-mass EE has thus been obtained, that is dynamically equivalent to the original robot. By this result, the feasibility

conditions for dynamic trajectories of 3-cable point-mass robots [137] can be fully reused here.

A particular design of special architecture \mathcal{L} was proposed in [196] (special architecture \mathcal{L}_1): in the latter article, P lies in the *midpoint* of the three segments $\overline{B_1B_2}$, $\overline{B_3B_4}$, and $\overline{B_5B_6}$, so that $\alpha_{ij} = -1$ and $\boldsymbol{\sigma}_{135} = [1/2, 1/2, 1/2]^T$. Hence, the two cables in each parallelogram always have the same tension.

The result obtained in this section is analogous to the one found in [121] for a *planar* case, where the authors study a 3-cable planar CSPR with a finite-size EE, and with cables 2 and 3 defining a parallelogram, so that the EE motion is purely translational. The authors of [121] found that, if the external forces (gravity and inertia) are applied in a point P lying on the segment through the attachment points of cables 2 and 3, and cable 1 is attached to P , this robot is dynamically equivalent to a 2-cable point-mass robot: this case is conceptually similar to the translational *spatial* robot seen in this section, where again the CoM is in the intersection of the segments between points B_i .

3

Dynamical trajectories

in which dynamical trajectories that allow the robot to move outside the SEW are presented. Experiments that confirm the theoretical results are also described.

3.1 Introduction

In this chapter, the kineto-static models from Ch. 2 will be applied to define dynamic trajectories that allow a CSPR to move beyond its SEW by taking advantage of the inertial forces to keep cables in tension, thus fulfilling goal (I) from Sec. 1.2.

State of the art

As seen in Ch. 2, the dynamic motion of CSPRs is radically dependent on whether the robot is under- or fully-constrained [1, 22, 46]. As far as the former are concerned, one of the first works on dynamically feasible trajectories focused on a 2-DoF 1-cable robot moving in a plane [54]. The authors used a pendular motion to pump energy in the system and progressively increase the oscillation amplitude. Dynamic point-to-point motions of under-actuated CSPRs were also studied in [91, 117, 209, 218].

Regarding fully constrained CSPRs, reference [73] focused on a 2-DoF, fully-actuated planar robot. Here, the authors defined harmonic trajectories whose feasibility can be verified by checking if the motion frequency falls

3. Dynamical trajectories

within an admissible range, without the necessity to solve the inverse dynamics problem; furthermore, they found a special motion frequency, which is always within this range and is similar to the natural frequency of a pendulum. In later works, these results were applied to harmonic trajectories of 3-DoF spatial point-mass robots [71, 210] and 3-DoF planar robots [97]; later, point-to-point motions [60, 75, 98, 211] were also considered. For 3-DoF spatial robots in particular, some authors defined static-to-dynamic motions [59, 71] so that the robot can reach a dynamic condition when starting from rest; also, a method was recently proposed [212] to allow such robots to move beyond their singularity loci (a potentially dangerous condition, as one might lose control of the robot), again by using dynamic movements. More recently, 6-DoF robots (with a finite-size EE) were also considered, performing dynamic motions in space where both the orientation and the position are varied [99, 100].

Finally, some authors considered redundantly-actuated robots, either planar [189] or spatial [178]. The work presented in [191–193] is also worth mentioning, which focused on the dynamical trajectories of CSPRs with a passive serial support composed of rigid links.

Chapter description

In this chapter, elliptical dynamic trajectories for a spatial CSPR with 3 DoFs and a point-mass EE will be defined (Sec. 3.2). For these trajectories a special frequency will be found, akin to the one found in [71], which allows the EE to achieve arbitrarily large oscillations (Sec. 3.3). A range of frequencies will also be defined (Sec. 3.4) that guarantee that cable tensions remain always positive (hereafter, this property will be referred to as *feasibility condition*). The trajectories presented in [71], [210] and [211] are special cases of the ellipses studied here. In Sec. 3.4, results provided by computer simulations will be shown and the trajectories presented in this chapter will be compared with previous works. The possibility of changing the oscillation frequency along a given ellipse will also be studied (Sec. 3.5).

In Subsec. 3.6.1, transition motions will be defined to connect a state of

rest to a dynamic trajectory and vice versa. In the same way, yet another kind of transition motions will be shown, that connects two identical ellipses laying on parallel planes, but having different centers (Subsec. 3.6.2).

In the rest of this chapter, unless otherwise specified, the robot with point-mass EE will be considered. These trajectories can also be applied to the translational robot with architecture \mathcal{L} from Sec. 2.3.1, since in this case the finite-size robot is dynamically equivalent to the point-mass one. For this architecture, all harmonic and transition trajectories from [137] and point-to-point motions from [98] (for instance) can also be re-used, and the total tensions are guaranteed to be always positive.

The theoretical results will then be experimentally verified for both the robot with point-mass EE (Subsec. 3.7.1) and the one with finite-size EE (Subsec. 3.7.2).

Finally, the results presented in this chapter will be reviewed in Sec. 3.8.

3.2 General trajectories

Consider a point P moving along a trajectory Γ and having a position \mathbf{p} defined by three sine functions (Fig. 3.1):

$$\mathbf{p} = \begin{bmatrix} x \\ y \\ z \end{bmatrix} = \underbrace{\begin{bmatrix} x_C \\ y_C \\ z_C \end{bmatrix}}_{\mathbf{p}_C} + \underbrace{\begin{bmatrix} x_A \sin(\psi + \phi_x) \\ y_A \sin(\psi + \phi_y) \\ z_A \sin(\psi + \phi_z) \end{bmatrix}}_{\mathbf{p}_d} \quad (3.1)$$

where

- x_C, y_C, z_C are the coordinates of the center C of Γ ;
- x_A, y_A, z_A are the amplitudes of oscillation;
- ϕ_x, ϕ_y, ϕ_z are phase angles;
- $\psi = \psi(t)$ gives the position of P along Γ ;
- \mathbf{p}_d is the displacement of point P from point C .

3. Dynamical trajectories

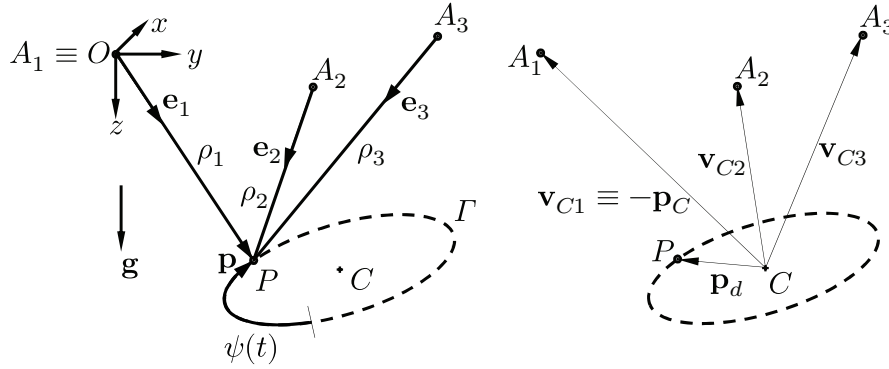


Figure 3.1: (Left) Schematic of a 3-DoF spatial CSPR performing an elliptical motion. (Right) Auxiliary vectors.

Eq. (3.1) represents the most general 3D trajectory defined by sinusoidal functions and can be shown to be an ellipse (or an elliptical arc); see Appendix A.1. Special cases include circles and line segments, either horizontal, vertical or oblique (cases dealt with in [71], [210] and [211]). It should be noted that general elliptical trajectories were first considered in [177]; however, the authors did not consider phase angles nor provided conditions for these trajectories to be feasible.

Said trajectories will now be applied to the 3-cable robot introduced in Subsec. 1.5.1. Note that here the most general location of the cable exit points A_i will be considered, even at different heights, while previous works usually considered only special cases: in [71, 98], for example, the exit points are on a horizontal equilateral triangle, whereas in [210–212] the fixed base is a generic horizontal triangle.

It is convenient to define some auxiliary vectors, that depend on both the architecture and the trajectory, as follows:

$$\mathbf{v}_{Ci} = [x_{Cai}, y_{Cai}, z_{Cai}]^T = \mathbf{a}_i - \mathbf{p}_C \quad (i \in \{1, 2, 3\}) \quad (3.2)$$

$$\boldsymbol{\lambda}_i = [\lambda_{xi}, \lambda_{yi}, \lambda_{zi}]^T = \mathbf{v}_{Cj} \times \mathbf{v}_{Ck} \quad (3.3)$$

These are the position vectors \mathbf{v}_{Ci} from C to A_i (Fig. 3.1), whereas $\boldsymbol{\lambda}_i$ is their cross product; in Eq. (3.3), indexes j and k depend on i as per Eq. (2.4), so for example $\boldsymbol{\lambda}_1 = \mathbf{v}_{C3} \times \mathbf{v}_{C2}$.

As seen in Sec. 2.2, the EE must remain below the plane Π passing through points A_1 , A_2 and A_3 (Fig. 1.3) for Eqs. (2.3) to be valid. Then, trajectory Γ must not intersect Π ; to check this condition, Eq. (3.1) is substituted into Eq. (1.4) which defines Π , thus obtaining

$$Q_0 + Q_s \sin(\psi) + Q_c \cos(\psi) = 0 \quad (3.4)$$

where Q_0 , Q_s and Q_c are as follows:

$$\begin{aligned} Q_0 &= ax_C + by_C + cz_C + d \\ Q_s &= ax_A \cos \phi_x + by_A \cos \phi_y + cz_A \cos \phi_z \\ Q_c &= ax_A \sin \phi_x + by_A \sin \phi_y + cz_A \sin \phi_z \end{aligned} \quad (3.5)$$

Eq. (3.4) can be solved by the tangent half-angle method, by setting $t_n = \tan(\psi/2)$. In this way, a quadratic equation in t_n is found, which must have no solutions for Γ not to intersect Π . Its discriminant must then be negative, so

$$4(Q_s^2 + Q_c^2 - Q_0^2) < 0 \quad (3.6)$$

This is a condition for feasibility that can easily be checked.

3.3 Natural frequency

In [71, 73], it was found that arbitrarily large motions may be achieved, while keeping positive tensions, if the robot moves with a special frequency $\omega_n = \sqrt{g/z_C}$, where z_C is the z coordinate of center C of the trajectory. It will now be shown that there is a similar frequency for the trajectories studied in this chapter.

In analogy to [98], it will be assumed that tensions τ_i are kept proportional to cable lengths ρ_i , which (in theory) can be done by suitably controlling the actuators. The dynamic equilibrium in Eq. (2.1) becomes

$$m\mathbf{g} - \sum_{i=1}^3 k_i(\mathbf{p} - \mathbf{a}_i) = m\ddot{\mathbf{p}} \quad (3.7)$$

where k_i is a “virtual” cable stiffness. Eq. (3.1) can be rewritten as

$$\mathbf{p} = \mathbf{p}_C + \mathbf{c} \cos(\omega t) + \mathbf{s} \sin(\omega t) = \mathbf{p}_C + \mathbf{p}_d \quad (3.8)$$

3. Dynamical trajectories

where $\omega t = \psi$ and ω is the motion frequency. By substituting Eq. (3.8) in Eq. (3.7), one finds

$$m[\mathbf{g} + \omega^2(\mathbf{p} - \mathbf{p}_C)] = \sum_{i=1}^3 k_i(\mathbf{p} - \mathbf{a}_i) \quad (3.9)$$

Here, ω_n is defined as the natural frequency of the second order Ordinary Differential Equation (ODE) in Eq. (3.7), namely $m\omega_n^2 = k_1 + k_2 + k_3 = K$. By setting $\omega = \omega_n$ in Eq. (3.9), the terms in \mathbf{p} cancel out:

$$m\mathbf{g} - K\mathbf{p}_C = -\sum_{i=1}^3 k_i\mathbf{a}_i \quad (3.10)$$

If all three k_i 's are positive and Eq. (3.10) holds, the cable tensions $\tau_i = k_i\rho_i$ are positive, since $\rho_i > 0$. The trajectory may then be realized with $\tau_i = k_i\rho_i$ if and only if Eq. (3.10) is satisfied: this, together with the condition $k_1 + k_2 + k_3 = K$, gives a linear system of equations in the unknowns k_i , which has solution

$$\begin{bmatrix} k_1 & k_2 & k_3 \end{bmatrix} = -\frac{mg}{Q_0} \begin{bmatrix} \lambda_{z1} & \lambda_{z2} & \lambda_{z3} \end{bmatrix} \quad (3.11)$$

where Q_0 was defined in Eq. (3.5). The natural frequency ω_n is then

$$\omega_n = \sqrt{\frac{K}{m}} = \sqrt{-\frac{g(\lambda_{z1} + \lambda_{z2} + \lambda_{z3})}{Q_0}} = \sqrt{\frac{gc}{Q_0}} \quad (3.12)$$

Note that c —given by Eq. (1.5)—is twice the (signed) area of the triangle T_{xy} defined by points $(x_{ai}, y_{ai})^*$; having numbered points A_i in clockwise order (Sec. 2.2), this signed area is negative and so $c < 0$. Also, $\omega_n > 0$, so it must be $Q_0 < 0$. It then follows from Eq. (3.11) that, for the k_1 , k_2 and k_3 to be positive, λ_{zi} must be positive too: it may be shown that this implies that the projection of point C on plane $x - y$ must be within the triangle T_{xy} (see Appendix A.2). This condition and the requirement that Γ must be below Π imply that C has to be within the SEW (which is the set of all points within the convex hull of the A_1 , A_2 and A_3 or below this region).

These results expand those presented in [71, 210, 211], where the authors assumed points A_i 's to have the same z coordinate and Γ to be a circle.

* It is implicitly assumed that plane Π is not vertical, otherwise T_{xy} degenerates into a segment and the SEW vanishes; this is a degenerate architecture that is intuitively avoided for a spatial robot.

3.4 Generic frequency

It is possible to have harmonic motions along a trajectory Γ with a frequency ω different from the frequency ω_n given in Eq. (3.12).

As seen in Ch. 2, the feasibility condition ($\tau_i > 0$ for all cables at every instant) holds if and only if $\mu_i > 0$, where the auxiliary variables μ_i are given by either Eq. (2.3) in Sec. 2.2 (for the robot with point-mass EE) or by Eq. (2.15) in Sec. 2.3 (for the robot with finite size EE). Since working with the μ_i 's leads to generally simpler expressions, these variables will be used in the rest of this chapter[†].

To study the general case, Eq. (3.1) is substituted into Eq. (2.3). Each μ_i can now be written as

$$\mu_i = C_i \cos(\psi) + D_i \sin(\psi) + E_i \quad (3.13)$$

with

$$\begin{aligned} C_i &= C_{i,a} \ddot{\psi} + C_{i,v} \dot{\psi}^2 + C_{i,c} \\ D_i &= D_{i,a} \ddot{\psi} + D_{i,v} \dot{\psi}^2 + D_{i,c} \\ E_i &= E_{i,a} \ddot{\psi} + E_{i,c} \end{aligned} \quad (3.14)$$

having defined the following auxiliary parameters:

$$\begin{aligned} \phi_{xy} &= \phi_x - \phi_y & \phi_{yz} &= \phi_y - \phi_z & \phi_{zx} &= \phi_z - \phi_x \\ \mathbf{n}_e &= \begin{bmatrix} y_A z_A \sin \phi_{yz} & z_A x_A \sin \phi_{zx} & x_A y_A \sin \phi_{xy} \end{bmatrix} \\ \mathbf{p}_{d,c} &= \begin{bmatrix} x_A \cos \phi_x & y_A \cos \phi_y & z_A \cos \phi_z \end{bmatrix} \\ \mathbf{p}_{d,s} &= \begin{bmatrix} x_A \sin \phi_x & y_A \sin \phi_y & z_A \sin \phi_z \end{bmatrix} \end{aligned} \quad (3.15)$$

and

$$\begin{aligned} C_{i,a} &= -\boldsymbol{\lambda}_i \cdot \mathbf{p}_{d,c} & D_{i,a} &= \boldsymbol{\lambda}_i \cdot \mathbf{p}_{d,s} \\ C_{i,v} &= D_{i,a} & D_{i,v} &= -C_{i,a} \\ C_{i,c} &= \mathbf{g} \cdot (\mathbf{p}_{d,s} \times \mathbf{v}_{kj}) & D_{i,c} &= \mathbf{g} \cdot (\mathbf{p}_{d,c} \times \mathbf{v}_{kj}) \\ E_{i,a} &= \mathbf{v}_{kj} \cdot \mathbf{n}_e & E_{i,c} &= g \lambda_{zi} \end{aligned} \quad (3.16)$$

[†] Note that, for the point-mass robot, the indexes i, j, k in μ_i permute as shown in Eq. (2.4), while for the finite-size robot the index pairs (i, j) , (k, l) and (m, n) in μ_{ij} permute as shown in (2.16).

3. Dynamical trajectories

Here, j and k depend on i as per Eq. (2.4) (Eq. (2.16) for the finite-size robot) and \mathbf{n}_e is a vector normal to the plane of the ellipse.

If $\psi = \omega t$, then $\dot{\psi} = \omega$, $\ddot{\psi} = 0$ and $C_i = C_{i,v}\omega^2 + C_{i,c}$, $D_i = D_{i,v}\omega^2 + D_{i,c}$, $E_i = E_{i,c}$. In this case, coefficients C_i , D_i , E_i are constant, once the trajectory Γ has been chosen: C_i and D_i are linear functions of ω^2 , while E_i only depends on g and the position of C . Eq. (3.13) is analogous to one reported in [71] for the special case of circular trajectories (either horizontal or vertical). The definitions in Eq. (3.16) also generalize the ones first provided in [136]; while in [136] the argument of the sine functions was a linear function of time t , here $\psi(t)$ can be a general function of class C^1 .

The extreme values of Eq. (3.13) are

$$\mu_{i,1} = \sqrt{C_i^2 + D_i^2} + E_i, \quad \mu_{i,2} = -\sqrt{C_i^2 + D_i^2} + E_i \quad (3.17)$$

If both extrema are positive, then μ_i is guaranteed to be positive. From Eq. (3.17) it is clear that, if $E_i = \lambda_{zi}g < 0$, then $\mu_{i,2} < 0$, so μ_i will be negative at some point for any value of ω . One then requires $\lambda_{zi} > 0$, which is the condition already found in Sec. 3.3.

Since $\mu_{i,2} < \mu_{i,1}$, it is sufficient to check that $\mu_{i,2} > 0$, so that $E_i > \sqrt{C_i^2 + D_i^2}$. Both sides of this equation are positive, so they may be squared to find $E_i^2 > C_i^2 + D_i^2$. After inserting the definitions of C_i , D_i and E_i in Eq. (3.14), one obtains a fourth degree inequality:

$$\mu_{i,2} > 0 \quad \Leftrightarrow \quad \alpha_i \omega^4 + 2\beta_i \omega^2 + \gamma_i < 0 \quad (3.18)$$

with

$$\begin{aligned} \alpha_i &= C_{i,v}^2 + D_{i,v}^2 \\ \beta_i &= C_{i,c}C_{i,v} + D_{i,c}D_{i,v} \\ \gamma_i &= C_{i,c}^2 + D_{i,c}^2 - E_{i,c}^2 \end{aligned} \quad (3.19)$$

The authors of [71, 210, 211] found ranges of feasible values for ω that guarantee the feasibility of a given circular trajectory, assuming points A_i to be at the same height. It can be assumed that a similar range may be defined in the

broader case considered here, if there is at least one value of ω satisfying condition (3.18); ω_n is indeed one such value, since in this case the trajectory is certainly feasible (see Sec. 3.3).

To find the aforementioned range, one can set $\omega^2 = w$ in Eq. (3.18), thus obtaining a quadratic inequality in w , namely $\alpha_i w^2 + 2\beta_i w + \gamma_i < 0$. Note that, by the definition in Eq. (3.19), $\alpha_i \geq 0$, so $\alpha_i w^2 + 2\beta_i w + \gamma_i = \zeta$ defines a convex parabola in the $w - \zeta$ plane for positive α_i ; the degenerate case $\alpha_i = 0$ will be considered later.

Depending on the sign of $\Delta_i = \beta_i^2 - \alpha_i \gamma_i$, there can be 3 cases:

- (1) $\Delta_i > 0$: there are two values $w_{i,min}$ and $w_{i,max}$ (which in general will be different for the three cables) such that, if $w \in]w_{i,min}, w_{i,max}[$, then $\alpha_i w^2 + 2\beta_i w + \gamma_i < 0$;
- (2) $\Delta_i = 0$: the inequality has a single solution, i.e. $\omega = \omega_n$;
- (3) $\Delta_i < 0$: the inequality has no solutions.

Inequality (3.18) has at least one solution, $\omega = \omega_n$, as long as the trajectory Γ respects the conditions found in Sec. 3.3 (C must be in the SEW and Γ is below Π): under these conditions, Δ_1 , Δ_2 and Δ_3 must be positive (case (1)).

When $\Delta_i > 0$, the values $w_{i,min}$ and $w_{i,max}$ are given by

$$w_{i,min} = \frac{-\beta_i - \sqrt{\Delta_i}}{\alpha_i}, \quad w_{i,max} = \frac{-\beta_i + \sqrt{\Delta_i}}{\alpha_i} \quad (3.20)$$

Recalling that $w = \omega^2 > 0$, there can be the following cases:

- (A) If $w_{i,min}$ and $w_{i,max}$ are ≤ 0 , no value of ω is feasible;
- (B) If $w_{i,min} \leq 0$ and $w_{i,max} > 0$, the range of ω satisfying condition (3.18) is $]0, \sqrt{w_{i,max}}[$;
- (C) If $w_{i,min}$ and $w_{i,max}$ are positive, the condition is $\omega \in]\sqrt{w_{i,min}}, \sqrt{w_{i,max}}[$.

One can finally define three ranges for ω , one for each cable: these ranges are either in the form $]0, \sqrt{w_{i,max}}[$ (case (B)) or in the form $] \sqrt{w_{i,min}}, \sqrt{w_{i,max}} [$ (case (C)), depending on the sign of $w_{i,min}$. The extremes of the range for ω

3. Dynamical trajectories

that ensure positive cable tensions can now be defined as:

$$\begin{aligned}\omega_{min} &= \sqrt{\max\{\max\{w_{i,min}\}, 0\}} \quad , \\ \omega_{max} &= \sqrt{\min\{w_{i,max}\}}\end{aligned}\tag{3.21}$$

Under the conditions in Sec. 3.3 (namely, C is in the SEW and trajectory Γ is below plane II), the condition for feasibility is $\omega_{min} \leq \omega \leq \omega_{max}$. Note that ω_{min} and ω_{max} are defined by explicit algebraic formulas and, thus, they are easy to calculate.

From Eq. (3.21), one can see that ω_{min} might be zero. For ω sufficiently close to zero, the EE moves quasi-statically, so the inertial force is negligible: ω_{min} is then zero if and only if Γ is completely within the SEW (the case $\omega = 0$ will be disregarded, since in this case the robot does not move).

Note that if $\omega = \omega_{min}$ or $\omega = \omega_{max}$, one or more of the cable tensions has a minimum value equal to zero along the trajectory. The conditions above are therefore strict, while those found in [211] are only sufficient (but not strictly necessary): the range for ω found here is therefore larger than that given in [211] (with the exception of horizontal circular trajectories, where the two ranges coincide). In [211], moreover, the authors considered only spatial circular trajectories, which are a subclass of the ellipses studied here.

An interesting particular case is when $z_{a,i} = z_a$ ($i \in \{1, 2, 3\}$), so that cable exit points A_i 's are all at the same height z_a : in this case Eq. (1.5) gives $a = b = 0, d = -c \cdot z_a$, so $Q_0 = c(z_C - z_a)$ and, from Eq. (3.12), $\omega_n = \sqrt{g/(z_C - z_a)}$ [21]. For $\omega = \omega_n$, one obtains (after some simplification) $\mu_i = \lambda_{zi} [g + z_A \omega_n^2 \sin(\omega_n t + \phi_z)]$: this implies $\mu_i \geq 0$ as long as $g \geq z_A \omega_n^2 = \max\{|\ddot{z}|\}$. This condition means that the maximum acceleration along z cannot be greater than g , as expected, and is automatically fulfilled if Γ is below II .

Finally, the degenerate case for which $\alpha_i = 0$ for some i is addressed. Since α_i is a sum of squares, it can be zero only if both squares are zero, namely $C_{i,v} = D_{i,v} = 0$. This is a linear homogeneous system of two equations in the

three unknowns x_A, y_A, z_A : its solutions are in the form

$$\begin{bmatrix} x_A \\ y_A \\ z_A \end{bmatrix} = f_1 \begin{bmatrix} \lambda_{yi} \lambda_{zi} \sin(\phi_{yz}) \\ \lambda_{zi} \lambda_{xi} \sin(\phi_{zx}) \\ \lambda_{xi} \lambda_{yi} \sin(\phi_{xy}) \end{bmatrix} \quad (3.22)$$

where f_1 is any positive scalar. Substituting Eq. (3.22) in Eq. (3.19), one finds that $\beta_i = 0$, too; then, in order to satisfy the inequality in (3.18), the only condition to check is $\gamma_i < 0$, which no longer depends on ω . It can also be proved that $\alpha_i = 0$ if and only if Γ lies on the plane through C , A_j and A_k , with $j, k \neq i$.

Some simulations were also performed to verify the theoretical findings presented above.

Fig. 3.2 shows a harmonic motion along an elliptical trajectory. For the trajectory shown, the method described in [211] gives a range of admissible motion frequencies comprised between $\omega'_{min} = 1.548$ rad/s and $\omega'_{max} = 2.55$ rad/s. By the present approach one finds that the actual endpoints of the admissible range, as defined in Eq. (3.21), are $\omega_{min} = 1.387$ rad/s and $\omega_{max} = 2.75$ rad/s. As expected, the first range is smaller and strictly contained in the second.

Fig. 3.3 shows a plot of the cable tensions τ_i divided by the EE mass m as a function of time, as the EE moves along Γ . Here, the continuous lines correspond to $\omega = \omega'_{max}$, while the dashed ones are for $\omega = \omega_{max}$; this latter case corresponds to a strict limit on the value of ω , so one cable tension reaches zero at one point (while remaining positive otherwise). When $\omega = \omega'_{max}$, the motion period is longer (since $\omega'_{max} < \omega_{max}$) and tensions do not reach the zero value, which shows that the conditions given in [211] are not strict.

It is worth emphasizing that the special frequency ω_n found in Sec. 3.3 does not depend on the motion amplitudes x_A, y_A and z_A , but only on the position of center C with respect to the cable exit points A_i 's. Consider now a series of elliptical trajectories having the same center and phase angles ϕ_x, ϕ_y and ϕ_z , but different oscillation amplitudes: specifically, the latter are given by $x_A = c_A x_{A0}$, $y_A = c_A y_{A0}$ and $z_A = c_A z_{A0}$, where c_A is akin to a size factor that

3. Dynamical trajectories

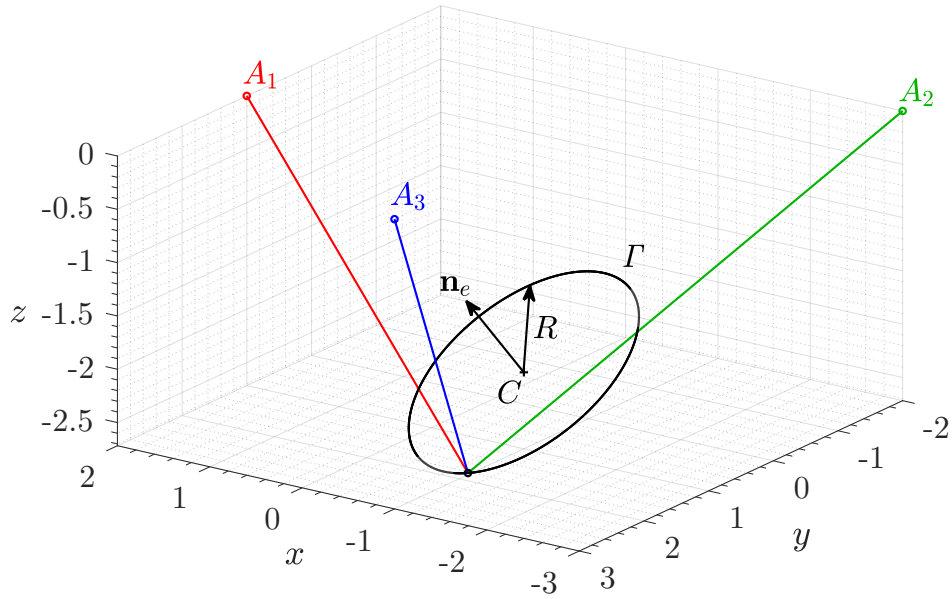


Figure 3.2: An elliptical trajectory Γ with $\mathbf{p}_C = [-1, 1, 2]^T$, $\mathbf{a}_1 = [2, 1, 0]^T$, $\mathbf{a}_2 = [-3, -2, 0]^T$, $\mathbf{a}_3 = [-1, 3, 0]^T$ and lying on a plane normal to $\mathbf{n}_e = [1, 2, 3]^T$. In this special case, the cable exit points A_i 's are all at the same height and the trajectory is a circle with radius $R = 1.2$. The length units are arbitrary.

defines the dimension of the trajectory Γ . Therefore, all trajectories are scaled versions of a “base” trajectory having amplitudes x_{A0} , y_{A0} and z_{A0} (see Fig. 3.4). One thus finds that ω_n is the same for all such trajectories and is always contained in the range of feasible frequencies $[\omega_{min}, \omega_{max}]$ (Fig. 3.5). Even as the size of the trajectory increases, therefore, the motion remains feasible for $\omega = \omega_n$, but the feasible range around ω_n becomes smaller and smaller.

3.5 Variable frequency

The possibility of varying the velocity by which the robot moves along an assigned trajectory will now be studied: in particular, the case where the angle ψ in Eq. (3.1) is a general function of time will be considered. In this case, coefficients C_i , D_i and E_i in Eq. (3.13) are no longer constant. To find the minimum of μ_i , Eq. (3.13) is differentiated with respect to time and the result

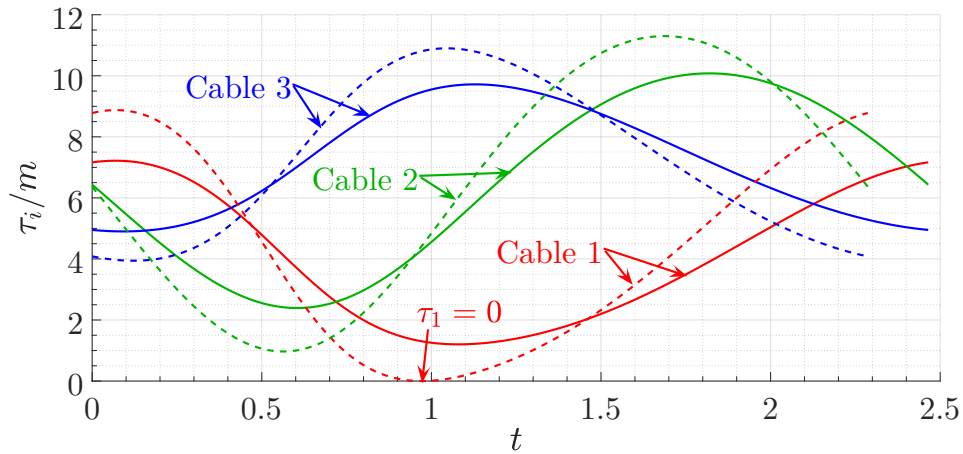


Figure 3.3: The cable tensions divided by the mass of the EE during one period of the trajectory Γ in Fig. 3.2. For each cable, the solid line corresponds to $\omega = \omega'_{max}$, while the dashed line corresponds to $\omega = \omega_{max} > \omega'_{max}$.

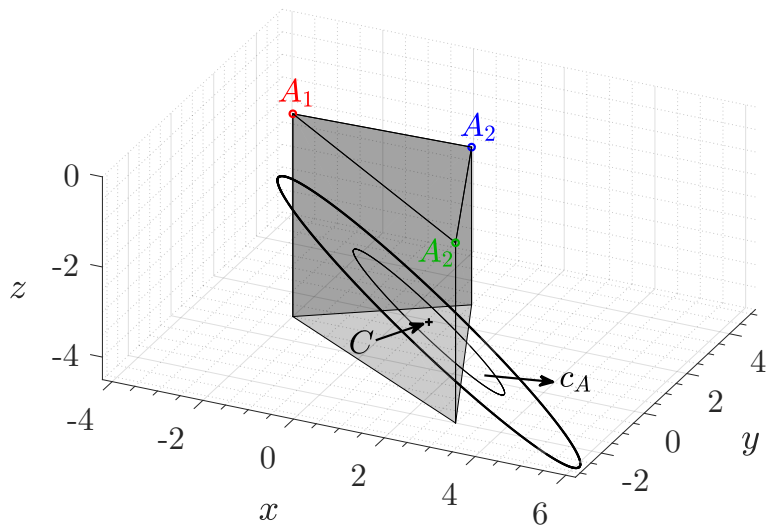


Figure 3.4: A 3D view of a base elliptical trajectory (thinner line) and a scaled up version ($c_A > 1$, thicker line) having the same center C . The SEW is also highlighted as a gray volume (here, the cables are omitted for clarity, cf. Fig. 3.2).

is set to zero. The exact solution of this problem is however complex and (seemingly) unsuitable for real-time applications.

3. Dynamical trajectories

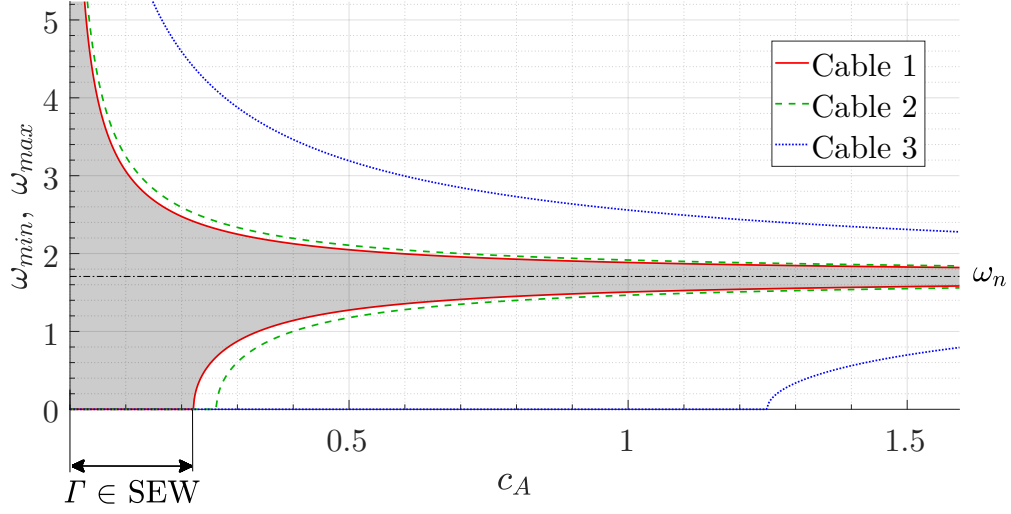


Figure 3.5: Plot of the three different ranges defined for $\omega^2 \in [w_{min}, w_{max}]$, with the range endpoints given by Eq. (3.20). The intersection of the three ranges, which gives the *global* feasible range, is highlighted in gray. If c_A is small enough that the corresponding trajectory Γ is entirely contained in the SEW, then $\omega = 0$ is contained in the admissible range, as seen in Sec. 3.4. In this particular case, the feasible range for cable 1 is strictly contained in the corresponding admissible ranges for cables 2 and 3.

A simpler alternative is to find a lower bound for the extrema of μ_i by interval analysis. If the values of C_i , D_i are kept fixed for assigned values of $\dot{\psi}$ and $\ddot{\psi}$ while varying ψ in Eq. (3.13), one can use the same approach described in Sec. 3.4 to find the minimum of μ_i . It is thus found that

$$\min \{\mu_i\} = -\sqrt{C_i^2 + D_i^2} + E_i \quad (3.23)$$

A sufficient condition for having $\mu_i > 0$ is then

$$E_i > \sqrt{C_i^2 + D_i^2} \quad (3.24)$$

Assuming $E_i > 0$ (this assumption will be verified later on), both sides can be squared to obtain again three biquadratic inequalities, expressed as $\alpha_i \dot{\psi}^4 + 2\beta_i \dot{\psi}^2 + \gamma'_i < 0$. The coefficients α_i and β_i are the same as in Eq. (3.19), while $\gamma'_i = \ddot{\psi}^2 \gamma_{i,\ddot{\psi}} + \gamma_i$ and $\gamma_{i,\ddot{\psi}} = C_{i,v}^2 + D_{i,v}^2 - E_{i,a}^2$.

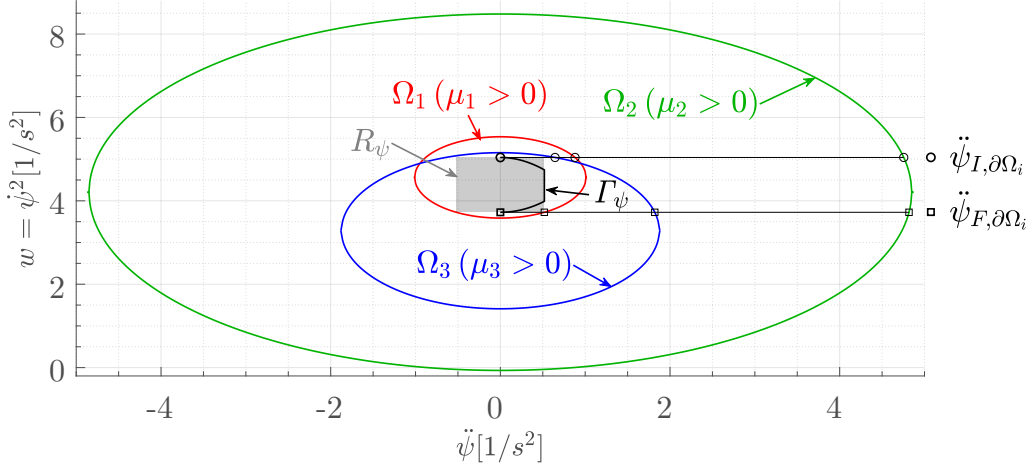


Figure 3.6: Plane $\ddot{\psi} - \dot{\psi}^2$ with the three ellipses Ω_i , rectangle R_ψ (in gray) and curve Γ_ψ (black line). Notice how $R_\psi \in \Omega_1 \cap \Omega_2 \cap \Omega_3$ and $\Gamma_\psi \in R_\psi$.

Setting $w = \dot{\psi}^2$, the parabola defined in the $w - \zeta$ plane by $\alpha_i w^2 + 2\beta_i w + \gamma'_i = \zeta$ shifts along the ζ axis as $\ddot{\psi}$ varies, since the only coefficient that depends on $\ddot{\psi}$ is the constant term. The parabola is convex (see Sec. 3.4), so the range of w satisfying $\alpha_i w^2 + 2\beta_i w + \gamma_i \leq 0$ is given by $[w_{i,min}, w_{i,max}]$, with $w_{i,min}$ and $w_{i,max}$ given by the points of intersection of the parabola with the w axis; the center of this range is $w_{i,c} = -\beta_i/\alpha_i$. Changing $\ddot{\psi}$ leaves the middle point $w_{i,c}$ unaltered, but the width of the admissible range varies, since $\Delta'_i = \beta_i^2 - \alpha_i \gamma'_i = \beta_i^2 - \alpha_i (\ddot{\psi}^2 \gamma_{i,\ddot{\psi}} + \gamma_i) = \Delta_i - \alpha_i \ddot{\psi}^2 \gamma_{i,\ddot{\psi}}$ changes.

It may be proven that, if C is in the SEW (so $\Delta_i > 0$), then $\gamma_{i,\ddot{\psi}} > 0$ (see Appendix A.3). The figure Ω_i defined by all points in the $\ddot{\psi} - w$ plane satisfying $\alpha_i w^2 + 2\beta_i w + \gamma'_i(\ddot{\psi}) \leq 0$ is then an ellipse, symmetrical with respect to the w axis (γ'_i only depends on $\ddot{\psi}^2$; see Fig. 3.6). It can also be proved that, for every point in Ω_i , $E_i > 0$, as required (see Appendix A.3).

Now, a motion law $\psi(t)$ is required, that allows the user to change the motion frequency along Γ from ω_I to ω_F . Here, ω_I and ω_F must be in the admissible range for ω defined in Sec. 3.4. Therefore, one can set $\dot{\psi} = U(t)$ and $\ddot{\psi} = V(t) = dU/dt$, where $U(t)$ is a function of class C^1 defined for $t \in [0, T]$ and T is the transition time from ω_I to ω_F . Also, the boundary conditions

3. Dynamical trajectories

$U(0) = \omega_I$, $U(T) = \omega_F$ and $V(0) = V(T) = 0$ are imposed, together with condition $V(t) \geq 0$ for $t \in [0, T]$, so that the function $U(t)$ is monotonically increasing.

The extreme values of $\dot{\psi}$ are ω_I and ω_F (since U is monotonic), while the extreme value of $|\ddot{\psi}|$ is $\ddot{\psi}_e = \max |V(t)|$. As a consequence, the curve Γ_ψ described in the plane $\ddot{\psi} - \dot{\psi}^2$ during the transition is then entirely contained in a rectangle R_ψ defined by $w_I = \omega_I^2 < w < w_F = \omega_F^2$ and $|\ddot{\psi}| < \ddot{\psi}_e$ (Fig. 3.6).

One then has only to find the minimum time T such that $R_\psi \in \Omega_1 \cap \Omega_2 \cap \Omega_3$. Since the ellipses Ω_i 's are convex, one only has to check that the corners of R_ψ are within all three Ω_i 's. Moreover, since the latter are symmetric with respect to the w axis, one only has to check the two corners of R_ψ with $\ddot{\psi} > 0$, that is, those with coordinates $(\ddot{\psi}_e, w_I)$ and $(\ddot{\psi}_e, w_F)$.

The point $(\ddot{\psi}_{I, \partial\Omega_i}, w_I)$ on the boundary $\partial\Omega_i$ can be found analytically by solving $\alpha_i w_I^2 + 2\beta_i w_I + \gamma_i'(\ddot{\psi}_{I, \partial\Omega_i}) = 0$: see Fig. 3.6, where such points have been marked by squares. Equivalent results (with w_F in place of w_I) can be found for the points $(\ddot{\psi}_{F, \partial\Omega_i}, w_F)$, marked by circles in Fig. 3.6. Finally, one defines a maximum $\ddot{\psi}$ as follows:

$$\ddot{\psi}_{max} = \min \left\{ \begin{array}{l} \ddot{\psi}_{I, \partial\Omega_1}, \ddot{\psi}_{I, \partial\Omega_2}, \ddot{\psi}_{I, \partial\Omega_3}, \\ \ddot{\psi}_{F, \partial\Omega_1}, \ddot{\psi}_{F, \partial\Omega_2}, \ddot{\psi}_{F, \partial\Omega_3} \end{array} \right\} \quad (3.25)$$

If $\ddot{\psi}_e < \ddot{\psi}_{max}$, R_ψ is contained within all Ω_i 's and the transition motion is feasible.

The only issue that is left is to pick a suitable motion law $U(t)$ and find the minimum transition time T . $U(t)$ has to be of class C^1 ; moreover, it would be convenient to choose $U(t)$ such that its first derivative $V(t)$ quickly reaches its maximum value and then remains constant for most of the motion. In this way, the curve Γ_ψ closely follows the borders of rectangle R_ψ , the acceleration is (for most of the motion) only slightly under its maximum prescribed value $\ddot{\psi}_{max}$ and the transition time is reduced: a linear motion law with parabolic blends [24, pp. 62–76] appears to be suitable.

3.6 Transition trajectories

3.6.1 Variable amplitudes

The sinusoidal trajectory defined in Eq. (3.1) has velocity $\dot{\mathbf{p}}$ and acceleration $\ddot{\mathbf{p}}$ that are nonzero at all points (if $\omega \neq 0$), so the robot cannot be in a state of rest. For practical applications, however, the robot has to reach a dynamic state starting from rest and vice versa. For this purpose, transition motions will be defined as follows:

$$\mathbf{p} = \mathbf{p}_C + U(\xi)\mathbf{p}_d \quad (3.26)$$

where \mathbf{p}_C and \mathbf{p}_d are defined as in Sec. 3.3 (here again $\psi = \omega t$, with ω being a constant frequency). $U(\xi)$ is a function of class C^2 and depends on the adimensional variable $\xi = t/T \in [0, 1]$ (with T being the duration of the transition). Eq. (3.26) is a generalization of Eq. (3.1); the former degenerates in the latter when $U(\xi) = 1$ (constant amplitudes).

Having introduced the derivatives $V(\xi) = dU/d\xi$ and $W(\xi) = d^2U/d\xi^2$, the following boundary conditions are set:

$$\begin{cases} U(0) = 0, & U(1) = 1 \\ V(0) = 0, & V(1) = 0 \\ W(0) = 0, & W(1) = 0 \end{cases} \quad (3.27)$$

$U(\xi)$ must be monotonically increasing, so $V(\xi)$ is always positive. With these conditions, the robot starts moving from position $\mathbf{p} = \mathbf{p}_C$ at $t = 0$, when it is at rest ($\dot{\mathbf{p}} = \ddot{\mathbf{p}} = \mathbf{0}$); then the amplitudes of motion along the coordinate axes grow until, at time $t = T$, the trajectory can be blended with the harmonic elliptical motion (ellipse Γ , defined by Eq. (3.26) for $U(\xi) = 1$).

With another choice of boundary conditions (namely, for $U(0) = 1$ and $U(1) = 0$), Eq. (3.26) can be similarly used to slow down a robot moving on an ellipse Γ until it stops in the center C of the ellipse. Moreover, it can be used to connect two ellipses Γ_s and Γ_f , where Γ_f is Γ_s “scaled” by a factor F , so the two ellipses have the same center C and the same phase angles, but

3. Dynamical trajectories

different amplitudes ($x_{Af} = Fx_{As}$ and so on): for this case, one can simply set $U(1) = F \cdot U(0)$. For the sake of brevity, only the first case will be studied here, with $U(0) = 0$ and $U(1) = 1$; the other cases can be studied in a similar way.

Substituting Eq. (3.26) in Eq. (2.3), one obtains

$$\begin{aligned} \mu_i = q_{i,W} \frac{W(\xi)}{T^2} + q_{i,V} \frac{V(\xi)}{T} + q_{i,UV} \frac{U(\xi)V(\xi)}{T} \\ + \underbrace{q_{i,U}U(\xi) + E_i}_{\mu_{i,0}} \end{aligned} \quad (3.28)$$

with

$$\begin{aligned} q_{i,W} &= -\boldsymbol{\lambda}_i \cdot \mathbf{p}_d \\ q_{i,V} &= -2\boldsymbol{\lambda}_i \cdot \dot{\mathbf{p}}_d \\ q_{i,UV} &= 2\omega E_{i,a} \\ q_{i,U} &= C_i \cos(\omega t) + D_i \sin(\omega t) \end{aligned} \quad (3.29)$$

where C_i, D_i are as in Eq. (3.14) and $E_{i,a}$ is defined in Eq. (3.16).

To see whether the so-defined motion is feasible, consider $T \rightarrow \infty$, so that, from Eq. (3.28), $\mu_i \rightarrow \mu_{i,0} = q_{i,U}U(\xi) + E_i$.

The minimum value of $q_{i,U}$ is $q_{i,U,min} = -\sqrt{C_i^2 + D_i^2}$, while the maximum value of U (for $\xi \in [0, 1]$) is $U_{max} = 1$, since U is monotonically increasing from $U(0) = 0$ to $U(1) = 1$. A lower bound for the minimum value of $\mu_{i,0}$ is then $\mu_{i,0,LB} = q_{i,U,min}U_{max} + E_i = -\sqrt{C_i^2 + D_i^2} + E_i = \mu_{i,2}$: this is the minimum value defined in Eq. (3.17), which is positive if the target trajectory Γ is feasible (see Sec. 3.4). Therefore, the transition motion is feasible by taking a sufficiently large value of T , since in this case $\mu_i \approx \mu_{i,0} > \mu_{i,0,LB} > 0$.

It would be clearly of practical interest to know the minimum value of T that guarantees positive cable tensions. In order to find it, one could set the time-derivative of Eq. (3.28) to zero: then, the extrema $\mu_{i,min}$ and $\mu_{i,max}$ of μ_i could be found. Then, one should search for the minimum T such that $\mu_{i,min} > 0$ (for $i = 1, 2, 3$). This method however leads to complex equations

that must be solved numerically; thus, it does not appear suitable for real-time problems.

A simpler alternative will then be adopted here, finding a lower bound for the minimum value of μ_i . The extreme values of $q_{i,W}$ and $q_{i,V}$, which are functions of time, are (see Appendix A.4)

$$\begin{aligned} q_{i,W,e} &= \max \{|q_{i,W}|\} = \|\Phi_i\| \\ q_{i,V,e} &= \max \{|q_{i,V}|\} = 2\omega\|\Phi_i\| \end{aligned} \quad (3.30)$$

with

$$\|\Phi_i\| = \sqrt{C_{i,a}^2 + D_{i,a}^2} \quad (3.31)$$

Also, the following terms are defined: $V_e = \max \{|V(\xi)|\}$, $W_e = \max \{|W(\xi)|\}$ and $(UV)_e = \max \{|U(\xi) \cdot V(\xi)|\}$. Here, all extrema are those found in the interval $\xi \in [0, 1]$ and depend on the chosen function $U(\xi)$. A lower bound for Eq. (3.28) is then

$$\mu_{i,LB} = -q_{i,W,e} \frac{W_e}{T^2} - q_{i,V,e} \frac{V_e}{T} + q_{i,UV} \frac{(UV)_e}{T} + \mu_{i,0,LB} \quad (3.32)$$

if $q_{i,UV} < 0$, and

$$\mu_{i,LB} = -q_{i,W,e} \frac{W_e}{T^2} - q_{i,V,e} \frac{V_e}{T} + \mu_{i,0,LB} \quad (3.33)$$

otherwise. If one sets T such that $\mu_{i,LB} > 0$, then $\mu_i \geq \mu_{i,LB} > 0$ and the trajectory is feasible. $\mu_{i,LB}$ can now be expressed as a function of T :

$$\mu_{i,LB}(T) = \frac{\mu_{i,c} + \mu_{i,T}T + \mu_{i,T^2}T^2}{T^2} = \frac{M_i(T)}{T^2} \leq \mu_i \quad (3.34)$$

with

$$\begin{aligned} \mu_{i,c} &= -q_{i,W,e} W_e \\ \mu_{i,T} &= \begin{cases} -q_{i,V,e} V_e + q_{i,UV} (UV)_e & q_{i,UV} < 0 \\ -q_{i,V,e} V_e & q_{i,UV} \geq 0 \end{cases} \\ \mu_{i,T^2} &= \mu_{i,0,LB} \end{aligned} \quad (3.35)$$

It has already been shown that, if the target trajectory Γ (defined by Eq. (3.26) with $U(\xi) = 1$) is feasible, then $\mu_{i,T^2} = \mu_{i,0,LB} = \mu_{i,2} > 0$. From this it is found

3. Dynamical trajectories

that, if $\mu_{i,LB}(T) = 0$ (which implies $M_i(T) = 0$) has solutions T_{min}, T_{max} , then $\mu_{i,LB}(T) < 0$ for T in the interval $[T_{min}, T_{max}]$ and $\mu_{i,LB}(T) > 0$ otherwise. Moreover, $\mu_{i,c} < 0$ (by definition), so $M_i(0) < 0$ and thus $0 \in [T_{min}, T_{max}]$. The condition for positive μ_i along the trajectory is then

$$T > T_{i,max} = \frac{-\mu_{i,T} + \sqrt{\mu_{i,T}^2 - 4\mu_{i,T^2}\mu_{i,c}}}{2\mu_{i,T^2}} \quad (3.36)$$

Finally, the sufficient (albeit not necessary) condition on T to ensure feasibility is

$$T > \max \{T_{1,max}, T_{2,max}, T_{3,max}\} \quad (3.37)$$

The strategy defined above has a drawback in the limit cases where $\omega = \omega_{min}$ or $\omega = \omega_{max}$ (with $\omega_{min}, \omega_{max}$ defined as in Eq. (3.21)). In such cases one has respectively $\omega^2 = w_{i,min}$ or $\omega^2 = w_{i,max}$, for one $i \in \{1, 2, 3\}$: the corresponding μ_i has then minimum value $\mu_{i,2} = 0$. When this happens, at least one of the cable tensions τ_i reaches zero at some point, while being still greater than zero along the rest of the trajectory (see Fig. 3.3).

However, if $\mu_{i,0,LB} = \mu_{i,2} = 0$, there are no finite values of T that make $\mu_{i,LB} > 0$ (as defined in Eq. (3.34)), since all terms on the right side are negative, except for $\mu_{i,0,LB}$, which is zero. As ω gets close to the limits $\omega_{min}, \omega_{max}$ of the admissible range, at least one of the $T_{i,max}$ approaches $+\infty$ (see Eq. (3.36), where $\mu_{i,T^2} = \mu_{i,0,LB} \rightarrow 0$).

Note that having T approaching $+\infty$ is a mathematical consequence of the conditions found in Eq. (3.37), which are sufficient but not strictly necessary. The actual minimum value of T that makes a given transition trajectory feasible has been numerically found in a series of computational experiments and compared with the minimum defined in Eq. (3.37): it was found that T is acceptably close to the actual minimum when ω is close to the middle of the admissible range $[\omega_{min}, \omega_{max}]$. When instead ω is close to the limits of the range, the minimum value of T to ensure feasibility remains bounded, while the lower bound defined by Eq. (3.37) goes to infinity. This limit can be circumvented in practice by using the frequency changing method introduced in

Sec. 3.5: one might choose an ω which is roughly in the middle of the admissible range for the corresponding elliptical trajectory Γ , move the robot from a rest condition to Γ using the transition trajectory just outlined, and finally change the frequency ω to the desired value.

It is worth considering the special case $\omega_{min} = 0$, which can only happen when Γ is entirely within the SEW (see Sec. 3.4). In such a case, the three $w_{i,min}$ in Eq. (3.21) are negative, μ_{i,T^2} from Eq. (3.36) is positive and the three $T_{i,max}$ remain bounded even if $\omega \rightarrow \omega_{min}$. This case has little practical interest.

3.6.2 Variable center

In this subsection, the possibility of moving the ellipse center will be studied. A new transition trajectory will be defined, based on the original one shown in Eq. (3.1), as follows:

$$\mathbf{p} = [\mathbf{p}_{C,s} + U(\xi)\mathbf{p}_{sf}] + \mathbf{p}_d \quad (3.38)$$

with \mathbf{p}_d as in Sec. 3.3 (where $\psi = \omega t$ and ω is a constant frequency) and $U(\xi)$ being a function of class C^2 in the variable $\xi = t/T$, where T is the duration of the transition.

This is another possible generalization of Eq. (3.1), which smoothly connects two elliptical trajectories Γ_s and Γ_f having the same shape and orientation, but different centers $\mathbf{p}_{C,s}$ and $\mathbf{p}_{C,f}$, with $\mathbf{p}_{sf} = \mathbf{p}_{C,f} - \mathbf{p}_{C,s} = [x_{sf}, y_{sf}, z_{sf}]^T$.

In order to do this, one has to set the boundary conditions seen in Eq. (3.27) and require $V(\xi)$ to be positive for any value of ξ , as already done for the transition motion with variable amplitudes (Subsec. 3.6.1).

Substituting the trajectory Eq. (3.38) in the conditions (2.3), one obtains (after some simplification)

$$\mu_i = \mu_{i,s} + U(\xi)(\mu_{i,f} - \mu_{i,s}) + \frac{W(\xi)}{T^2} q_{i,sf} \quad (3.39)$$

3. Dynamical trajectories

Here, the following variables will be introduced:

$$\begin{aligned}
\mathbf{v}_{Ci,s} &= \mathbf{a}_i - \mathbf{p}_{C,s}, & \mathbf{v}_{Ci,f} &= \mathbf{a}_i - \mathbf{p}_{C,f} \\
\boldsymbol{\lambda}_{i,s} &= [\lambda_{xi,s}, \lambda_{yi,s}, \lambda_{zi,s}]^T & &= \mathbf{v}_{Cj,s} \times \mathbf{v}_{Ck,s} \\
\boldsymbol{\lambda}_{i,f} &= [\lambda_{xi,f}, \lambda_{yi,f}, \lambda_{zi,f}]^T & &= \mathbf{v}_{Cj,f} \times \mathbf{v}_{Ck,f} \\
q_{i,sf} &= (\mathbf{p}_d \times \mathbf{v}_{jk} - \boldsymbol{\lambda}_{i,s}) \cdot \mathbf{p}_{sf}
\end{aligned} \tag{3.40}$$

where again indexes j and k depend on index i (Eq. (2.4)). In Eq. (3.39), $\mu_{i,f}$ and $\mu_{i,s}$ are functions of time and are defined as per Eqs. (3.13) to (3.16), with $\dot{\psi} = \omega$ and $\ddot{\psi} = 0$; here, however, parameters $\lambda_{xi}, \lambda_{yi}, \lambda_{zi}$ in Eq. (3.16) are replaced respectively with $\lambda_{xi,f}, \lambda_{yi,f}, \lambda_{zi,f}$ and $\lambda_{xi,s}, \lambda_{yi,s}, \lambda_{zi,s}$. With these definitions, $\mu_{i,f}$ and $\mu_{i,s}$ correspond to μ_i for the start and target trajectories Γ_s and Γ_f .

Considering Eq. (3.39) and letting $T \rightarrow \infty$, then $\mu_i \rightarrow \mu_{i,s} + U(\xi)(\mu_{i,f} - \mu_{i,s})$; since $U(\xi)$ is required to be monotonically increasing from 0 to 1, then $\mu_i \in [\mu_{i,s}, \mu_{i,f}] \forall t$. If Γ_s and Γ_f are both feasible, then $\mu_{i,s} \geq \mu_{i,2,s} \geq 0$ and $\mu_{i,f} \geq \mu_{i,2,f} \geq 0$, for any t (here, $\mu_{i,2,s}$ and $\mu_{i,2,f}$ correspond to $\mu_{i,2}$ from Eq. (3.17), calculated respectively for Γ_s and Γ_f); then, it can safely be concluded that $\mu_i \geq \min\{\mu_{i,2,s}, \mu_{i,2,f}\} \geq 0$. It can thus be said that if the transition trajectory defined by Eq. (3.38) connects two ellipses that are feasible, the transition itself will be feasible, as long as T is large enough.

At this point it would be useful to find a lower bound on T such that the transition is feasible. As in Subsec. 3.6.1, finding the minimum feasible value T is a complex task that cannot be analytically solved; however, defining a safe lower bound is enough for practical purposes.

For this, reconsider Eq. (3.39), specifically the second term $W(\xi)/T^2 q_{i,sf}$: this is the term that may become negative along the trajectory. The upper and lower extrema of $W(\xi)$ are here denoted as W_{max} and W_{min} ; these are known from the choice of the transition motion $U(\xi)$. Note that, in general, for any function $U(\xi)$ of class C^2 that satisfies the boundary conditions in Eq. (3.27)

it will hold that $W_{min} < 0, W_{max} > 0$. It can then be proved the following:

$$\min \{W(\xi)q_{i,sf}\} \geq \min \left\{ W_{min} \max \{q_{i,sf}\}, \right. \\ \left. W_{max} \min \{q_{i,sf}\} \right\} \quad (3.41)$$

From the definition in Eq. (3.40), $q_{i,sf}$ is a trigonometric function of time (having frequency ω) that can be written as

$$\begin{aligned} q_{i,sf} &= C_{i,sf} \cos(\omega t) + D_{i,sf} \sin(\omega t) + E_{i,sf} \\ C_{i,sf} &= (\mathbf{p}_{d,s} \times \mathbf{v}_{jk}) \cdot \mathbf{p}_{sf} \\ D_{i,sf} &= (\mathbf{p}_{d,c} \times \mathbf{v}_{jk}) \cdot \mathbf{p}_{sf} \\ E_{i,sf} &= -\boldsymbol{\lambda}_{i,s} \cdot \mathbf{p}_{sf} \end{aligned} \quad (3.42)$$

In this expression, the coefficients $C_{i,sf}$, $D_{i,sf}$ and $E_{i,sf}$ are constant; it then follows that the extrema of $q_{i,sf}$ are (cf. Eq. (3.17))

$$\begin{aligned} \max \{q_{i,sf}\} &= E_{i,sf} + \sqrt{C_{i,sf}^2 + D_{i,sf}^2} \\ \min \{q_{i,sf}\} &= E_{i,sf} - \sqrt{C_{i,sf}^2 + D_{i,sf}^2} \end{aligned} \quad (3.43)$$

Going back to Eq. (3.39), its lower bound can now be written as

$$\mu_{i,LB}(T) = \frac{\mu_{i,c} + \mu_{i,T^2}T^2}{T^2} = \frac{M_i(T)}{T^2} \leq \mu_i \quad (3.44)$$

with

$$\begin{aligned} \mu_{i,c} &= \min \{W(\xi)q_{i,sf}\} \leq 0 \\ \mu_{i,T^2} &= \min \{\mu_{i,2,s}, \mu_{i,2,f}\} \geq 0 \end{aligned} \quad (3.45)$$

which replace Eqs. (3.34) and Eq. (3.35). One can be sure that $\mu_{i,T^2} \geq 0$ if the ellipses Γ_s and Γ_f are feasible; the fact that $\mu_{i,c} \leq 0$ can be inferred by observing that in Eq. (3.41) at least one of the two terms is negative, since $W_{min} < 0, W_{max} > 0$, and clearly $\min \{q_{i,sf}\} < \max \{q_{i,sf}\}$.

The considerations in Subsec. 3.6.1 then apply: $\mu_{i,LB}(T) < 0$ if and only if T is in the interval $[T_{min}, T_{max}]$ (with T_{min}, T_{max} being the solutions of $M_i(T) = 0$), since the coefficient μ_{i,T^2} of the quadratic term in $M_i(T)$ is positive; also, $M_i(0) = \mu_{i,c} \leq 0$, so $0 \in [T_{min}, T_{max}]$. The condition for positive μ_i along the trajectory is then

$$T > T_{i,max} = \sqrt{-\frac{\mu_{i,c}}{\mu_{i,T^2}}} \quad (3.46)$$

3. Dynamical trajectories

It may be concluded that a sufficient condition to have positive tensions in the cables along the transition motion is given by Eq. (3.37), with $T_{i,max}$ given by Eq. (3.46).

Note that, if the start and target elliptical trajectories have to be feasible, then it must hold that $\omega \in [\omega_{min,s}, \omega_{max,s}] \cap [\omega_{min,f}, \omega_{max,f}] = [\omega_{min,sf}, \omega_{max,sf}]$, namely, the frequency ω along the transition motion must be in the ranges of admissible frequencies (Eq. (3.21)) both for Γ_s and Γ_f ; clearly here one has to assume that such ranges overlap, otherwise there are no values of ω such that both ellipses are feasible.

As seen in Subsec. 3.6.1, some issues arise when ω is close to the boundaries $\omega_{min,sf}$ or $\omega_{max,sf}$ of the admissible range (given by the intersection of the start and the end range). For example, $\omega = \omega_{min,sf}$ means either $\omega^2 = w_{i,s,min}$ or $\omega^2 = w_{i,f,min}$, for some $i \in \{1, 2, 3\}$ (with $w_{i,s,min}$ and $w_{i,f,min}$ being the values given by Eq. (3.20), for the start and the target ellipse). In such a case, the corresponding μ_{i,T^2} from Eq. (3.45) is zero, since either $\mu_{i,2,f} = 0$ or $\mu_{i,2,s} = 0$, and $T_{i,max}$ is not defined. Again, this is a consequence of using a sufficient, but not strictly necessary condition; the actual minimum value of T remains finite even as $\omega \rightarrow \omega_{min,sf}$. Analogous considerations hold for $\omega \rightarrow \omega_{max,sf}$. The special case $\omega_{min,sf} = 0$ can happen only if both Γ_s and Γ_f are within the SEW and has little practical interest.

To conclude this section on transition trajectories, it is worth remarking that, if the frequency ω of the transition motion (for either the case of variable amplitude or the case of variable center) can be chosen freely, a reasonable approach is to pick $\omega \approx (\omega_{min} + \omega_{max})/2$, with ω_{min} , ω_{max} being the lower and upper endpoints of the range of admissible frequencies. In this way, ω will be the farthest from the endpoints and the transition time can be expected to be close to the actual minimum.

If instead one has to connect two (feasible) elliptical trajectories Γ_s and Γ_f , with assigned frequencies ω_s and ω_f , the transition motions described in this section can be combined with the method shown in Sec. 3.5 to vary the

motion frequency. For example, consider two ellipses Γ_s and Γ_f having the same shape and orientation, but different centers $\mathbf{p}_{C,s}$ and $\mathbf{p}_{C,f}$. Assume that the admissible range of frequencies for Γ_s , $[\omega_{min,s}, \omega_{max,s}]$, overlaps with the admissible range for Γ_f , $[\omega_{min,f}, \omega_{max,f}]$; Γ_s has to be followed with frequency $\omega_s \in [\omega_{min,s}, \omega_{max,s}]$ and Γ_f with frequency $\omega_f \in [\omega_{min,f}, \omega_{max,f}]$ (where in general $\omega_s \neq \omega_f$). An approach to smoothly connect the start and the target trajectory could be divided in three steps, as follows:

- first, change the frequency along Γ_s , from ω_s to $\omega_{sf} \in [\omega_{min,s}, \omega_{max,s}] \cap [\omega_{min,f}, \omega_{max,f}] = [\omega_{min,sf}, \omega_{max,sf}]$; a good approach would be to take $\omega_{sf} \approx (\omega_{min,sf} + \omega_{max,sf}) / 2$.
- then move along the variable-center transition motion defined in the present subsection, with constant frequency ω_{sf} ;
- finally, change the frequency again, moving along Γ_f , from ω_{sf} to ω_f .

Should the admissible frequency ranges for Γ_s and Γ_f have no overlap, one could find an intermediate ellipse Γ_i whose admissible range has nonempty intersections with the admissible ranges for both the start and the end ellipse and then repeat the steps defined above to smoothly connect Γ_s with Γ_i , and Γ_i with Γ_f .

By suitably combining the various motion types described in Secs. 3.4 to 3.6, a great variety of dynamic trajectories can be obtained.

3.7 Experimental results

To validate the theoretical results presented in Secs. 3.3 to 3.6, a series of tests were performed on the CSPR prototypes at the Laboratoire de Robotique of Université Laval (Canada). The results of the experiments can be found in the multimedia attachments (see the list of attachments at page 157), where the dynamic trajectories presented here are performed by both the point-mass robot (Subsec. 3.7.1) and the finite-size robot with special architecture \mathcal{L} (Subsec. 3.7.2). In both cases the robots are clearly moving outside their respective

3. Dynamical trajectories

SEWs while keeping positive tensions in the cables.

The robots used in both experimental sessions are non-engineered prototypes that were meant to be proofs of concept. In any case, it was verified that the desired trajectories were followed with an acceptable degree of accuracy, given the prototypes' limitations.

3.7.1 Experimental results: point-mass EE

The first video (see page 157) shows a point-mass performing, sequentially, the following trajectories:

- (i) a harmonic elliptical trajectory from Sec. 3.2;
- (ii) an elliptical trajectory with variable frequency from Sec. 3.5;
- (iii) a variable-center trajectory from Subsec. 3.6.2.

Before and after each trajectory, a transition motion with variable amplitudes (Subsec. 3.6.1) is performed, to start the robot from rest and bring it back to a rest condition.

The cables remain taut throughout the motion. In parts of the trajectory, however, one or more cables start vibrating: this is due to the limitations of the prototype, since the EE has in fact finite dimensions and the cables' attachment points on it do not coincide: thus, the point-mass model approximation has limited validity and the EE rotates around its CoM. In any case, it was found that the desired trajectories were followed reasonably well.

The first trajectory shown in the video (case (i)) is a simple ellipse with constant frequency (see Sec. 3.4). The robot starts moving with growing amplitudes of oscillation, then reaches the target elliptical trajectory, finally slowing down and going back to a rest condition within the SEW. The 3D depiction of the trajectory is shown in Fig. 3.7; the (calculated) cable tensions along the three parts of the trajectory described are in Fig. 3.8.

After that, the robot performs the variable frequency trajectory (case (ii)).

The robot starts moving with a given frequency $\omega = \omega_{med}$ along a given ellipse, then accelerates and moves with a higher frequency $\omega = \omega_{sup}$, namely at a higher velocity (while remaining on the same ellipse). After that, the frequency is lowered to $\omega = \omega_{inf}$; finally, the frequency is changed again to ω_{med} . Clearly, it must hold $\omega_{min} < \omega_{inf} < \omega_{med} < \omega_{sup} < \omega_{max}$ for the trajectory to be feasible, where $\omega_{min}, \omega_{max}$ are those given by (3.21).

Finally, the third part of the video shows the transition trajectories defined in Sec. 3.6. Again, the robot starts moving from a rest position in the SEW until it reaches a target upper trajectory. After that, a variable center transition is employed, so the robot passes on a lower trajectory. Finally, the dynamic motion is stopped.

The control system of the prototype provides the cable length at every time-step, by using the motor rotations measured by the encoders: by comparing the actual lengths to the desired values set as targets, an average error over the entire motion of about 4.4×10^{-2} mm and a maximum value of 1 mm were found (for the motion in case (i)). By solving the DKP with either the desired or the actual cable lengths, one respectively finds the desired position \mathbf{p}_d (as set in the robot control system) and the actual one \mathbf{p}_e . Comparing \mathbf{p}_d and \mathbf{p}_e along the motion, it was found that the corresponding average and maximum errors $\|d\mathbf{p}\| = \|\mathbf{p}_e - \mathbf{p}_d\|$ in 3D space are respectively 9.5×10^{-1} mm and 7.3 mm (see Fig. 3.9): given that the workspace dimensions are in the order of meters, these errors can be considered to be acceptable.

3.7.2 Experimental results: finite-size EE

In this section, the results of the tests performed on a translational robot, designed according to the conditions that define architecture \mathcal{LR} , will be presented. Specifically, the robot was designed so that the cable attachment points B_i 's define a regular hexagon, with the center of mass P in its center: therefore, the architecture is an instance of architecture \mathcal{L}_2 (Subsec. 1.5.2.1). The cable exit points A_i 's are placed on the sides of an equilateral triangle, as

3. Dynamical trajectories

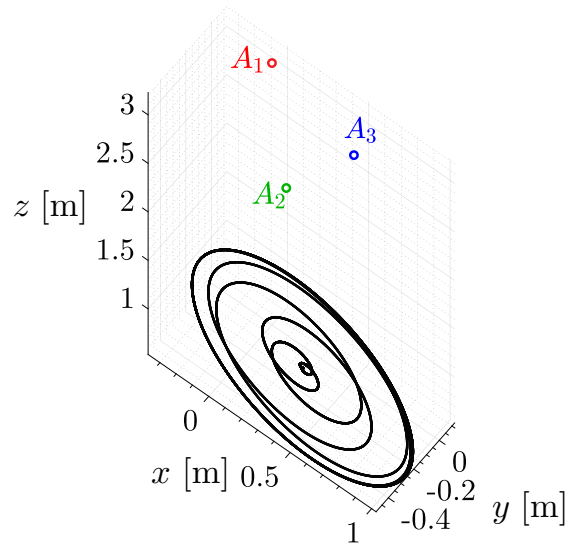


Figure 3.7: Trajectory of the robot during the experiments: first part in attached video (see page 157), simple harmonic elliptical trajectory.

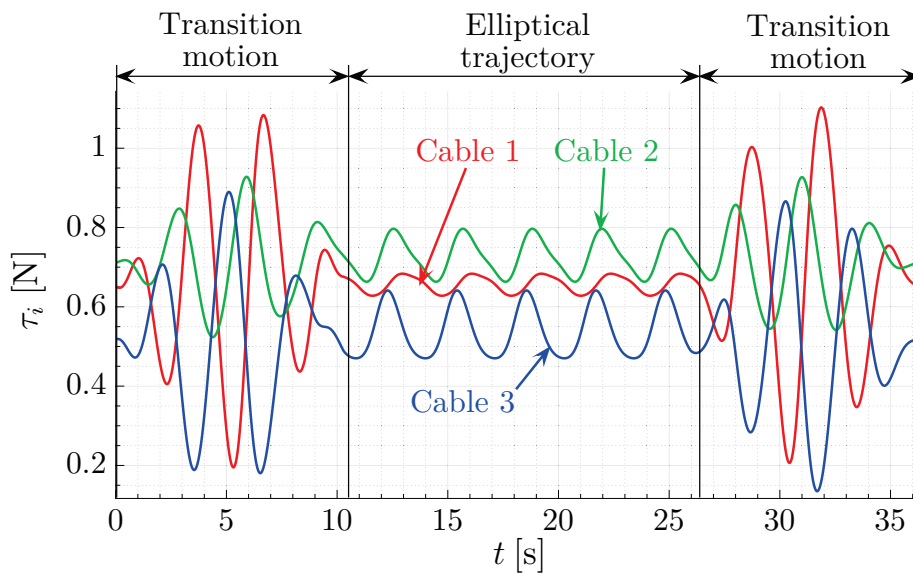


Figure 3.8: Cable tensions along a spatial trajectory.

shown in Fig. 3.10a; as all A_i are on the same plane, this is also an example of architecture \mathcal{R}_1 .

The 6 cables are wound on 3 motorized winches, each moving 2 cables

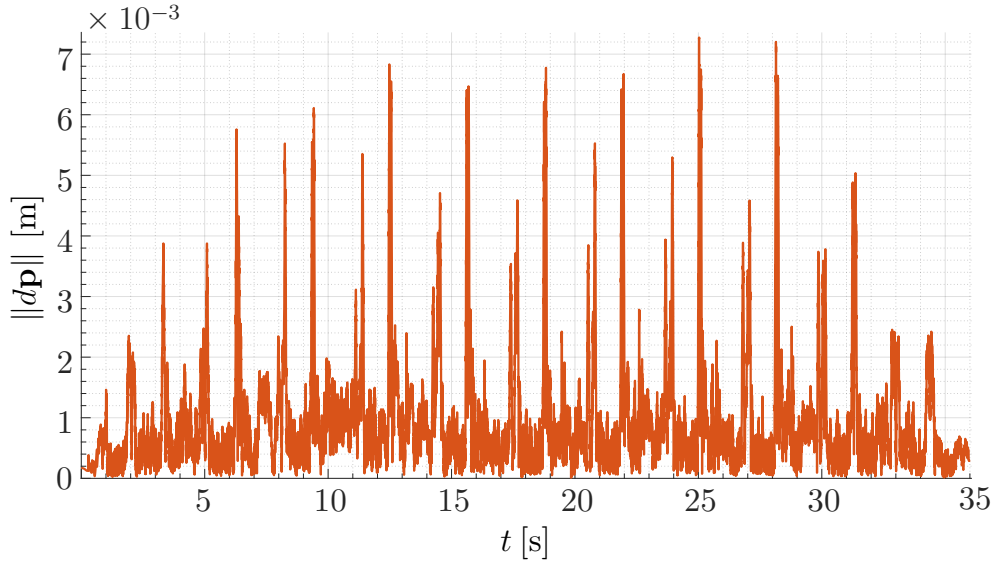


Figure 3.9: Plot of the position error $\|d\mathbf{p}\|$ along part (i) of the motion.

simultaneously. The winches are composed of two coaxial pulleys (both connected to a servomotor) of the same radius; the cables in each parallelogram wind simultaneously on different pulleys, in order to avoid interference between cables. In this way, if the pulley rotates by a given angle, the two cables wind on the pulleys by the same amount (since the winding radius is the same) and thus their lengths remain equal, provided that they were equal at the beginning of the motion. The motor axes pass through the auxiliary points A_{ij}^* 's, and in this case A_i and A_j are symmetrical with respect to A_{ij}^* . The location of the motors and the cable exit points was chosen so as to have a large workspace and avoid cable interference.

The final prototype is shown in Fig. 3.10b and the winches are in Fig. 3.10c. The prototype is controlled via a Simulink model where the user can set the desired trajectory and its parameters; the platform coordinates in Cartesian space are converted in corresponding rotation angles in the joint space by the inverse kinematics. The motors' target positions are then sent to the real-time control system of the robot, based on a PID control loop.

The results can be seen in the attached video (page 157, video 2), showing

3. Dynamical trajectories

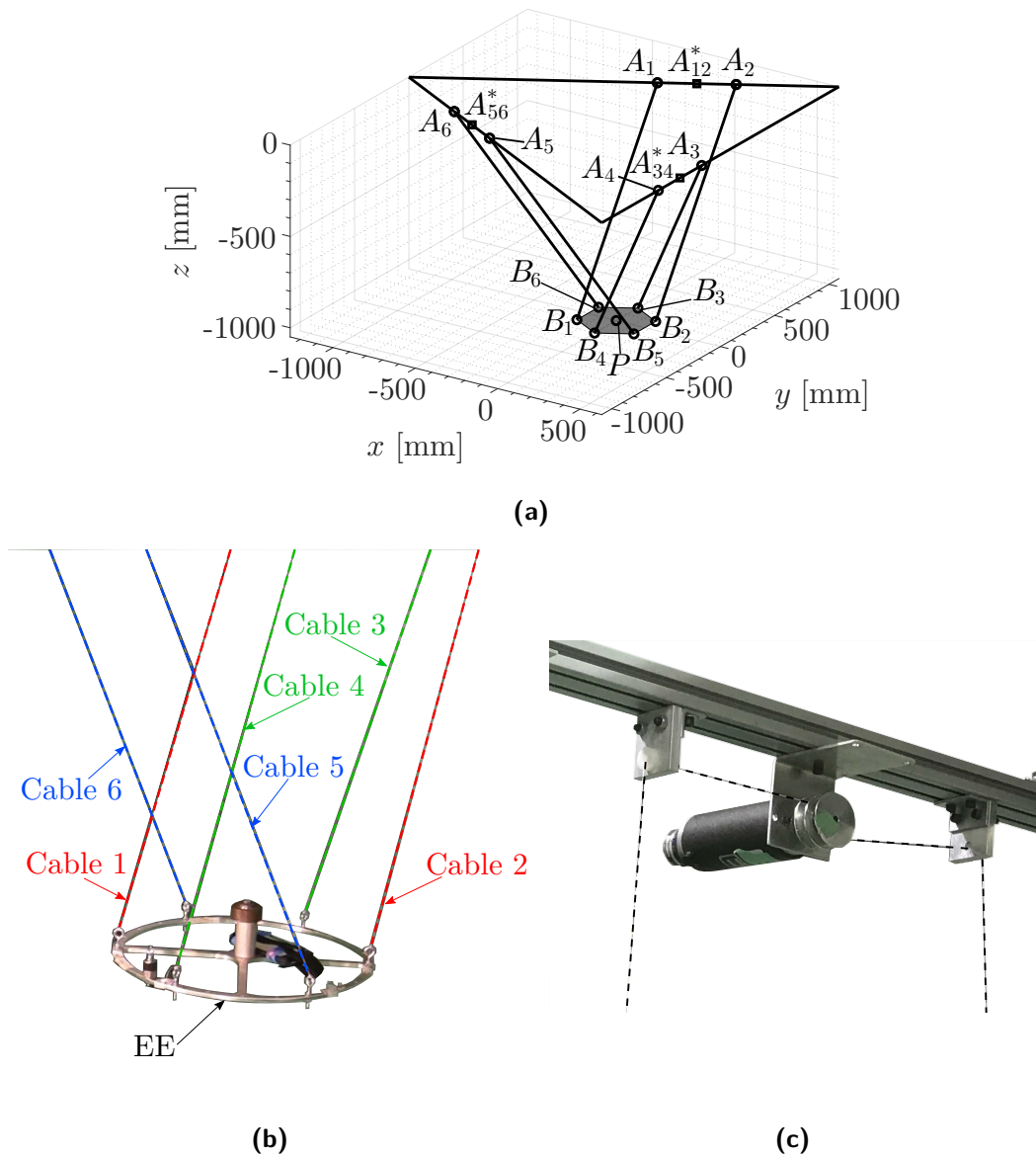
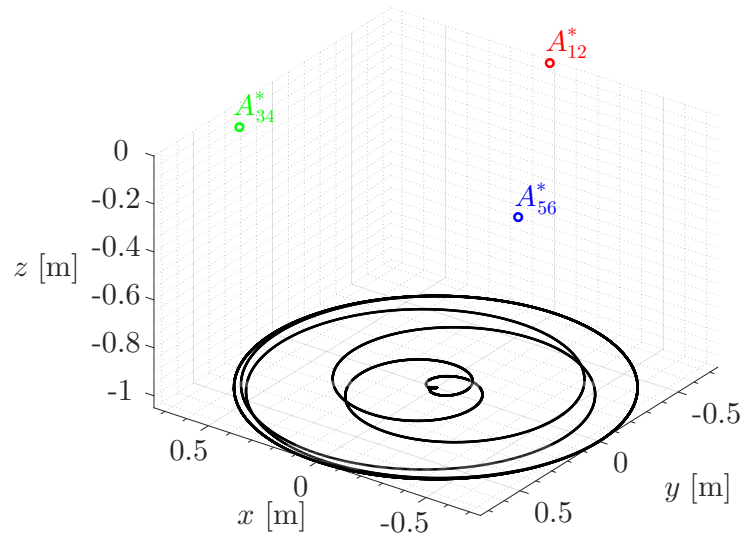
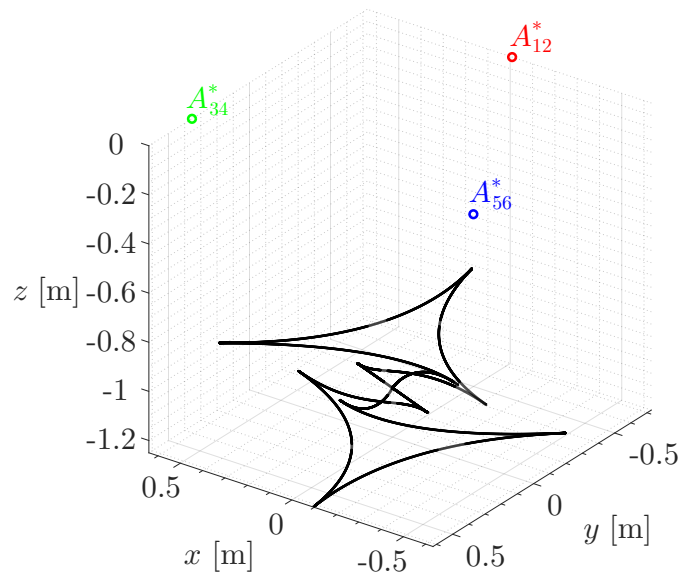


Figure 3.10: (a): a schematic of the prototype in the reference pose. (b): top view of the prototype developed at Université Laval. (c): a photo of one of the robot winches, with two cables (highlighted by dashed lines) coiling on the same pulley.

the robot as it performs two dynamic trajectories; the video shows the robot from two different viewpoints, one frontal and another above the robot. Again, the robot is clearly moving outside the SEW (marked by green lines on the



(a)

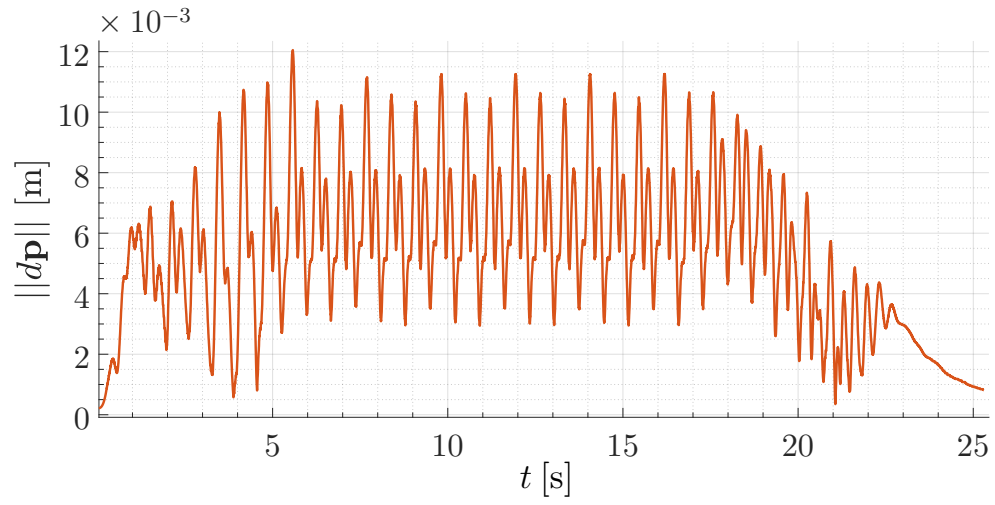


(b)

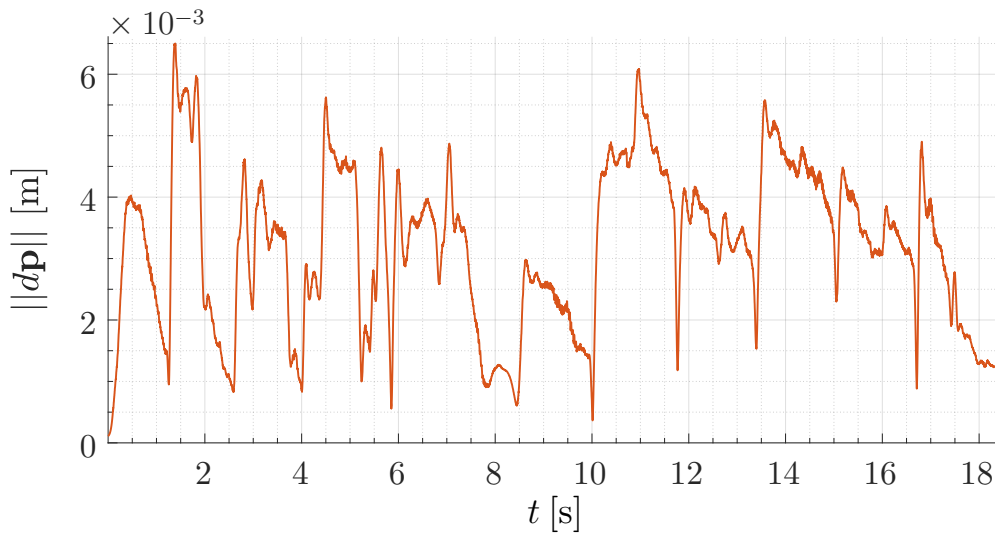
Figure 3.11: (a): 3D plot of the periodic motion. (b): 3D plot of the point-to-point motion.

table shown in the video) while keeping positive cable tensions and maintaining a constant orientation; also, it is easy to see that the cables remain parallel as

3. Dynamical trajectories



(a)



(b)

Figure 3.12: (a): plot of the position error $\|d\mathbf{p}\|$ along the harmonic motion ($\|d\mathbf{p}\|$ is the distance between desired position \mathbf{p}_d and the actual one \mathbf{p}_e).
(b): plot of $\|d\mathbf{p}\|$ along the point-to-point motion.

the robot moves.

The video is divided in two parts:

- (a) First, the robot performs a dynamic *harmonic* trajectory: the robot starts

from rest and oscillates with increasing motion amplitudes until it moves along a horizontal circle centered in the center of the SEW and having a radius larger than the workspace. For this trajectory, ω was chosen as $(\omega_{max} + \omega_{min})/2$, as suggested in Subsec. 3.6.2. After a few cycles, the robot is slowed down to its starting point (see Fig. 3.11a for a 3D plot of the trajectory).

- (b) In the second part, *point-to-point* dynamic motions reaching outside the SEW are performed. At the target points the robot velocity is zero, but not the acceleration (the robot cannot be at rest out of the SEW); here, the method in [98] is used to plan the trajectories (see Fig. 3.11b).

To verify the accuracy of the prototype in tracking the desired trajectory, the method to analyze the position errors used in Subsec. 3.7.1 is applied again here. The forward position kinematics algorithm for the finite-size EE robot [31] is the same as the one for the point-mass EE robot, which simplifies the analysis. The plots of the distance $\|d\mathbf{p}\|$ between the desired and the actual harmonic and point-to-point trajectories are shown in Figs. 3.12a and 3.12b, respectively. The maximum positioning error during the harmonic motion was 1.205×10^{-2} m, with an average error of 5.36×10^{-3} m (respectively 6.5×10^{-3} m and 3.2×10^{-3} m for the point-to-point motion). Considering the limitations of the prototype and that the robot was moving with high accelerations (up to ~ 6.6 m/s² during the tests) in a workspace that is meters wide, these errors can be considered to be acceptable.

To verify that the orientation was constant as the robot moved, the roll, pitch and yaw angles of the platform were recorded during the experiments by using the Inertial Measurement Unit (IMU) in a common smartphone that was secured on the robot platform. An example of the results can be seen in Fig. 3.13: the platform never rotated by more than 3° with respect its start pose, which seems an acceptable error given the approximations in the measurement of the architecture parameters. Such results are compatible with what was observed in [49], where the authors performed a multibody simulation of the dynamic behavior of a CSPR with a cable architecture similar to the

3. Dynamical trajectories

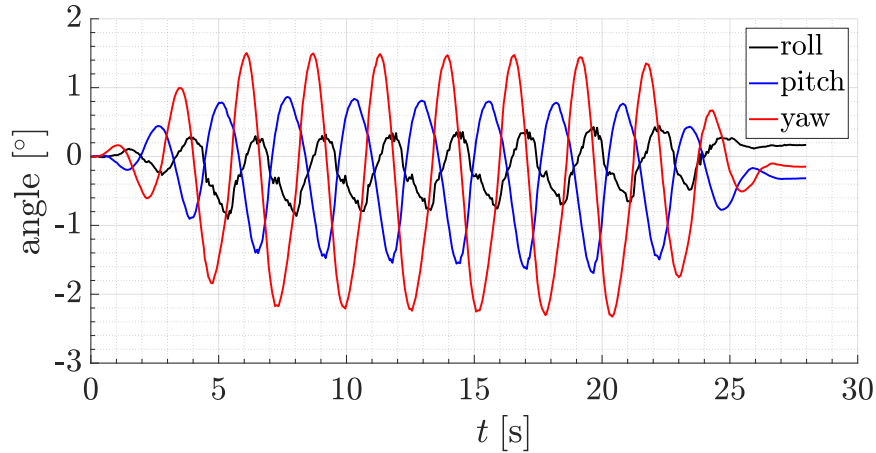


Figure 3.13: Yaw, pitch and roll angles of the robot, as measured by an IMU on the EE, with respect to the start position (where the three angles were set to zero) along a circular horizontal motion (see video, p. 157).

one proposed here (except that the robot only moved in a vertical plane and employed 8 cables, thus being over-constrained), observing a variation of the EE Euler angles not bigger than 1° . Given that in this case the accelerations are an order of magnitude higher and the robot moves outside its SEW, a larger orientation error is to be expected, also considering the very simple mechanical realization of the tested prototype[‡].

3.8 Summary of the chapter

In this chapter a general class of harmonic elliptical trajectories has been defined for a CSPR, modeled as a point-mass EE suspended by three cables. The robot position can be properly controlled, with positive tensions in the cables, even as it moves beyond its static workspace.

[‡] Since a smartphone IMU is not a precision instrument (the Root Mean Square (RMS) error on the orientation angles in dynamic conditions can be up to roughly 2° [139]), the results reported in Fig. 3.13 must not be intended as an accurate quantitative assessment of the orientation error. However, they provide a clear indication that the EE orientation remains reasonably constant.

Transition trajectories were also defined, to perform one of the following:

- change the frequency with which a given ellipse is followed (so as to increase or reduce the motion velocity);
- move the robot from a state of rest to one of the aforementioned harmonic trajectories, or vice versa;
- smoothly connect two elliptical trajectories having the same shape, orientation and center, but different sizes;
- smoothly connect two elliptical trajectories having the same shape, orientation and size, but different centers.

For all aforementioned trajectories conditions for feasibility were defined: the conditions for the harmonic trajectories are necessary and sufficient, whereas the conditions for the transition motions are only sufficient. All conditions are algebraic inequalities that can be verified in a few milliseconds; this makes the proposed work applicable for real-time problems.

The trajectories shown in this chapter expand and generalize previous results [71, 136, 210, 211]. One of the advantages of the proposed trajectories is that there are many parameters that can be chosen; therefore, they provide a greater flexibility during the trajectory planning phase.

It was shown both theoretically and experimentally that the above trajectories can also be applied to a translational robot such as the one presented in Subsec. 1.5.2, provided that the conditions that define architecture \mathcal{L} are respected. If this is not the case, the trajectories presented in this chapter only guarantee that the condition in Eq. (2.15) are respected, so the total tension in each cable pair is positive; to verify that all six cables are in tension, Eq. (2.22) should also be verified. Integrating both Eqs. (2.15) and (2.22) at the trajectory planning stage is left as future work. Note that a method to define purely-translational dynamic trajectories for a robot with finite-size EE controlled by 6 cables was already presented in [100]: however, the architecture proposed in [100] does not take advantage of parallelogram actuation and, thus, it requires 6 motors to be independently controlled. The application

3. Dynamical trajectories

of dynamically feasible trajectories to CSPR with parallelogram actuation is novel: other works have considered the dynamics of such robots [49, 199], but the feasibility of a given trajectory was verified through numerical simulations, which are in general too computationally expensive for real-time application.

As noted in Sec. 1.2, dynamic motions can greatly expand the available workspace for cable-driven systems: instead of moving only within the Static Equilibrium Workspace, the robot can move in the full dynamic workspace [14], in which the former is strictly contained. Practical applications of the dynamic trajectories include recovery of the robot in case of a cable failure [21, 29] or for pick-and-place operations over large workspaces, where the robot reaches a series of target points with zero instantaneous velocity at each point. To perform such pick-and-place operations, a gripper could be applied on the EE, as proposed in [173, 174], given the high rotational stability that was observed in the experiments. Moreover, dynamically feasible trajectories have been proposed for entertainment [177]: a robotic roller coaster could be developed where the passengers ride in a cable-suspended cabin that moves with high accelerations over a wide workspace. Specifically, the translational architecture (Subsec. 1.5.2) could be of interest, as it allows a full control of all translational DoFs of the EE while avoiding rotational motions that in some cases could be distressing for passengers.

With the results presented in this chapter, goal (I) from Sec. 1.2 can be considered fulfilled.

4

Practically feasible motions

To practically achieve the dynamic motions introduced in the previous chapters, singularities and cable interferences must be avoided and conditions on cable lengths must be respected.

4.1 Introduction

Having found the conditions for dynamic feasibility in Ch. 3, one needs to verify that the trajectories thus defined can be followed by a robot such as those presented in Subsecs. 1.5.1 and 1.5.2. Indeed, there are other issues that could limit the motion of a cable-driven robot, besides cables losing tension: for instance, the cables or the EE could interfere with the environment or with each other, the robot could enter a singularity condition, the cable lengths might reach their limits, the motors could be unable to exert the required joint torques, and so on.

This chapter will focus on singularities, cable interference and cable length limits, as these seem to be the most realistic issues that could limit the motion for the prototypes shown in Subsecs. 3.7.1 and 3.7.2. Specifically, the second prototype (having a finite size EE) will be analyzed in detail, as it leads to more complete examples of the potential issues under consideration; the extension to the simpler robot in Subsec. 1.5.1 is straightforward.

4. Practically feasible motions

State of the art

Looking at Eq. (1.1), one sees that in general a given velocity of the EE $\dot{\mathbf{x}}$ corresponds to one and only one set of joint velocities $\dot{\boldsymbol{\theta}}$ (here, only fully-actuated robots are considered). One can thus solve the 1st-order DKP as $\dot{\mathbf{x}} = -\mathbf{F}_x^{-1}\mathbf{F}_\theta\dot{\boldsymbol{\theta}}$ or the 1st-order IKP as $\dot{\boldsymbol{\theta}} = -\mathbf{F}_\theta^{-1}\mathbf{F}_x\dot{\mathbf{x}}$. These problems are significantly easier to solve than their 0th-order counterparts, as they correspond to systems of linear equations, while the function $\mathbf{F}(\boldsymbol{\theta}, \mathbf{x})$ that defines the position relationship yields in general a nonlinear system with multiple solutions (see Subsec. 1.3.2.3).

Solving the 1st-order kinematics requires that matrices \mathbf{F}_x and \mathbf{F}_θ are invertible. When this is not true, the robot is at a singularity. Specifically, by using the notation from [74], one can distinguish the following cases for the singularities of parallel mechanisms:

- *Type 1 singularity*: If \mathbf{F}_θ is singular, its kernel has dimension greater than zero: therefore, there are nonzero joint velocities $\dot{\boldsymbol{\theta}}$ that lead to zero velocity $\dot{\mathbf{x}}$ at the EE (these configurations are also called *dead points*). Also, not all velocity vectors $\dot{\mathbf{x}}$ can be produced: this condition is generally reached when the robot is at a boundary of the workspace (either external or internal). The robot thus loses one or more DoFs, as $\dot{\mathbf{x}}$ cannot be realized if it has a component normal to the workspace boundary.
- *Type 2 singularity*: If \mathbf{F}_x is singular, there are nonzero output velocities $\dot{\mathbf{x}}$ that yield zero joint velocities $\dot{\boldsymbol{\theta}}$: therefore, when all joints are at zero velocity, the EE can still move and the parallel kinematic chain gains one or more DoFs. By the kinematic-static duality [197], this also means that the EE can no longer resist an external wrench.
- *Type 3 singularity*: this occurs when both \mathbf{F}_x and \mathbf{F}_θ are singular and in general requires the robot not only to be at specific poses but also to fulfill special conditions on the architecture.

The literature on the singularities of parallel manipulators is vast [129, pp. 179–213] and even a summary would be beyond the scope of the present

work. Instead, a brief description of the singularities of CDPRs will be presented [161, pp. 125–129].

One of the first works on the topic is [195], where it was proven that cable-driven systems with one EE connected to the fixed frame by several cables have no singularities of Type 1. In general, the study of singularities of cable-driven systems is approached with the tools of classical robot analysis, assuming all cables to be in tension: see for instance [33], where an over-actuated cable-driven robot with parallelogram actuation (conceptually similar to the translational robot here considered) was shown to have no singular poses in the WFW. See also [115], where it was shown (for a class of robots with parallel-cable actuation) that being in a nonsingular pose is a necessary requirement for the robot to be inside the WCW.

The study of singularity poses while taking into account the unilaterality of cable actuation was presented in [205] for a planar, over-constrained robot: it was shown that this manipulator has singularity configurations that are not present in its rigid-link counterpart. The singularities of a 6-cable robot inspired by the Gough-Stewart platform were studied in [153]: it was experimentally shown that the tracking performance of the robot becomes far worse in this case, as a small noise on the measurements of cable lengths yields a large variation on the final robot pose.

Some authors have also developed methods to safely cross the singularities of a parallel manipulator by taking advantage of its dynamic properties. One of the first works on this topic was [92], where the author found dynamic *consistency conditions* that must be fulfilled as the manipulator passes through a singular pose; also, it was shown that the dynamic equations in this case depend on higher order derivatives (beyond the 2nd) of the trajectory. This work was later expanded in [38] where the authors found optimal conditions for singularity crossing and provided results from experimental tests. Recently, the concept of singularity crossing was also applied to a simple CDPR in [212].

4. Practically feasible motions

Chapter description

In this chapter, the following issues will be studied for the translational cable robot introduced in Subsec. 1.5.2:

- The effect of parallel singularities (Sec. 4.2): the singularity loci will be analytically defined and classified according to the standard taxonomy in the literature [51, 217]. Two particular architectures will also be considered (Subsecs. 4.2.1 and 4.2.2) that lead to a particularly simple geometry of the singularity loci; one of these architectures in particular (Subsec. 4.2.2) corresponds to the special case \mathcal{R} presented in Subsec. 1.5.2.2 (see also Fig. 1.6) and has a singularity surface that coincides with plane Π .
- The RW, as defined in Subsec. 1.3.2.3 (see page 17), will be presented for the robot architecture used in the prototype;
- The interference-free workspace (see again p. 17) will be studied by using the tools from [158]. For special architecture \mathcal{R}_1 (see again Subsec. 1.5.2.2 and Fig. 1.6), it will be proven that the zones where interference can occur have an easy geometric interpretation.

Finally, the results of the chapter are summarized in Sec. 4.5, and design guidelines are provided.

4.2 Singularities

In Sec. 2.3 it was assumed that matrix \mathbf{M}_{sup} in Eq. (2.13) is invertible, in order to compute total cable tensions $\boldsymbol{\tau}_{tot}$. However, this is not the case if vectors \mathbf{e}_1 , \mathbf{e}_3 and \mathbf{e}_5 are linearly dependent, in which case the robot reaches a singular configuration.

This condition has a geometric interpretation: since the cable direction vectors $\mathbf{e}_i = (\mathbf{a}_{ij}^* - \mathbf{p}) / \|\mathbf{a}_{ij}^* - \mathbf{p}\|$ go from P to the auxiliary points A_{ij}^* , defined in Subsec. 1.5.2 (page 26), for matrix \mathbf{M}_{sup} to be singular P must be in the plane Π passing through A_{12}^* , A_{34}^* and A_{56}^* . If these three points are on the same line, there are infinite such planes and the robot is always in a singular

configuration: if this degenerate architecture is avoided in the robot design, plane Π is unique. As long as P is not on Π , then, $\boldsymbol{\tau}_{tot}$ is found from Eq. (2.13) through inversion of \mathbf{M}_{sup} .

A second type of singularity emerges when matrix \mathbf{A} in Eq. (2.18) has not full rank, in which case tension ratios cannot be calculated. If either \mathbf{M}_{sup} or \mathbf{A} is singular, matrix \mathbf{M} in Eqs. (2.11) and (2.12) is undefined, since it comprises vectors \mathbf{b}_{ij} 's that depend on cable tensions τ_i 's, which are undefined when the robot is at a singular configuration*. The union of the singularity loci of \mathbf{M}_{sup} and \mathbf{A} provides the complete singularity locus of the manipulator.

Both the singularity given by $\det(\mathbf{M}_{sup}) = 0$ and the one given by $\det(\mathbf{A}) = 0$ are of Type 2). A further classification can also be introduced: by using the definitions from [51, 217], the former defines an *actuation singularity*, while the latter is a *constraint singularity*. Specifically, in the latter case the robot gains an additional freedom: indeed, if \mathbf{A} is re-written as

$$\mathbf{A} = \begin{bmatrix} \mathbf{c}_{12} & \mathbf{c}_{34} & \mathbf{c}_{56} \end{bmatrix} \quad (4.1)$$

with

$$\mathbf{c}_{ij} = (\mathbf{d}_{ij} \times \mathbf{e}_i) \tau_{tot,ij} \quad (4.2)$$

and in Eq. (2.14) the strict inequality holds (i.e. $\tau_{tot,ij} > 0$), \mathbf{A} is singular when \mathbf{c}_{12} , \mathbf{c}_{34} and \mathbf{c}_{56} are coplanar (assuming $\|\mathbf{c}_{ij}\| \neq 0$; the special case $\|\mathbf{c}_{ij}\| = 0$ will be discussed later in this section). However, \mathbf{c}_{ij} has the same direction as the vector \mathbf{n}_{ij} orthogonal to the plane Π_{ij} through A_i , B_i , A_j and B_j (see Sec. 1.5.2), since $\mathbf{d}_{ij} \times \mathbf{e}_i$ is orthogonal to both $\mathbf{d}_{ij} = B_i - B_j$ and \mathbf{e}_i (Fig. 1.5). Therefore, if vectors \mathbf{c}_{ij} 's are coplanar, vectors \mathbf{n}_{ij} 's must be coplanar too: this is the condition where the robot is no longer purely translational and gains a rotational freedom.

The poses where \mathbf{A} is singular are given by

$$\det(\mathbf{A}) = \frac{\tau_{tot,12}\tau_{tot,34}\tau_{tot,56}}{\rho_1\rho_3\rho_5} \{ [\mathbf{d}_{12} \times (\mathbf{a}_{12}^* - \mathbf{p})] \times [\mathbf{d}_{34} \times (\mathbf{a}_{34}^* - \mathbf{p})] \} \cdot [\mathbf{d}_{56} \times (\mathbf{a}_{56}^* - \mathbf{p})] = 0 \quad (4.3)$$

* This is equivalent to matrix $\tilde{\mathbf{M}}$ in the kinetostatic problem (2.9) being singular.

4. Practically feasible motions

Since ρ_i and $\tau_{tot,ij}$ are nonzero, this reduces to finding the roots of the determinant of a matrix $\tilde{\mathbf{A}} = \begin{bmatrix} \mathbf{d}_{12} \times (\mathbf{a}_{12}^* - \mathbf{p}) & \mathbf{d}_{34} \times (\mathbf{a}_{34}^* - \mathbf{p}) & \mathbf{d}_{56} \times (\mathbf{a}_{56}^* - \mathbf{p}) \end{bmatrix}$ whose column vectors depend on position \mathbf{p} . After expanding and simplifying, this turns out to be a 2nd-degree variety in x, y, z , namely a quadric Σ .

In order to obtain an explicit formulation for Σ , some auxiliary parameters can be introduced. First, define the cross products

$$\boldsymbol{\lambda}_{ij,kl} = \mathbf{d}_{ij} \times \mathbf{d}_{kl} \quad (4.4a)$$

$$\boldsymbol{\lambda}_{a,ij} = \mathbf{d}_{ij} \times \mathbf{a}_{ij}^* \quad (4.4b)$$

where indexes i, j, k and l range from 1 to 6, and pairs $i-j$ and $k-l$ denote two different parallelograms of the manipulator. Also, the following cross products are defined:

$$\boldsymbol{\lambda}_{a,ij,kl} = \boldsymbol{\lambda}_{a,ij} \times \boldsymbol{\lambda}_{a,kl} \quad (4.5)$$

and the two matrices

$$\boldsymbol{\Lambda} = \begin{bmatrix} \boldsymbol{\lambda}_{34,56} & \boldsymbol{\lambda}_{56,12} & \boldsymbol{\lambda}_{12,34} \end{bmatrix} \quad (4.6a)$$

$$\boldsymbol{\Lambda}_a = \begin{bmatrix} \boldsymbol{\lambda}_{a,12} & \boldsymbol{\lambda}_{a,34} & \boldsymbol{\lambda}_{a,56} \end{bmatrix} \quad (4.6b)$$

Since a general quadric in space can be expressed as

$$\mathbf{p}_e^T \mathbf{Q} \mathbf{p}_e = 0 \quad (4.7)$$

where $\mathbf{p}_e = [x, y, z, 1]^T$ and \mathbf{Q} is a 4×4 matrix with real coefficients, it can be proven that the quadric defined by $\det(\tilde{\mathbf{A}}) = 0$ has

$$\mathbf{Q} = \begin{bmatrix} \mathbf{Q}_{3,3} & \mathbf{t} \\ \mathbf{t}^T & k_Q \end{bmatrix} \quad (4.8)$$

where the blocks composing \mathbf{Q} are

$$\mathbf{Q}_{3,3} = -\frac{1}{2} \left[\boldsymbol{\Lambda}_a \boldsymbol{\Lambda}^T + \boldsymbol{\Lambda} \boldsymbol{\Lambda}_a^T \right] \quad (4.9a)$$

$$\mathbf{t} = -\frac{1}{2} \left[\mathbf{d}_{12} \times \boldsymbol{\lambda}_{a,34,56} + \mathbf{d}_{34} \times \boldsymbol{\lambda}_{a,56,12} + \mathbf{d}_{56} \times \boldsymbol{\lambda}_{a,12,34} \right] \quad (4.9b)$$

$$k_Q = -\boldsymbol{\lambda}_{a,12,34} \cdot \boldsymbol{\lambda}_{a,56} = -\boldsymbol{\lambda}_{a,34,56} \cdot \boldsymbol{\lambda}_{a,12} = -\boldsymbol{\lambda}_{a,56,12} \cdot \boldsymbol{\lambda}_{a,34} \quad (4.9c)$$

(the three definitions of k_Q are equivalent).

The full singularity locus for the manipulator is then given by $\det(\mathbf{M}_{sup}) \cdot \det(\tilde{\mathbf{A}}) = 0$, where $\det(\mathbf{M}_{sup}) = 0$ gives the plane Π defined in Sec. 1.5.2 and $\det(\tilde{\mathbf{A}}) = 0$ defines the quadric Σ . As a result, the singularity locus is given by a third-degree polynomial in x , y and z . This is coherent with the results reported in [180], where the authors found that the singularity locus of the general Gough-Stewart platform in the Cartesian space (for a given orientation of the platform) is a 3rd-degree polynomial in x , y and z . The manipulator at hand can be seen as a particular type of the Gough-Stewart platform (assuming that all cables are taut) where the orientation of the EE is constant; the remarkable result is that the complex polynomial defined by Eq. (32) and Table 4 of the cited reference [180] can here be factored in two simpler terms of lower degree.

Analogous results were found for the 3-UPU translational manipulator in [82, 154], where the authors distinguished between translational and rotational singularities, showing that, for a specific architecture, the former define a plane and the latter define the union of a plane and a right cylinder. In [81], the author found the singularity locus for Delta-like translational manipulators of general architecture, but provided no explicit formulation of the singularity condition as a function of the platform position. A rigid-link robot with three actuators and three translational DoFs, based on a parallelogram actuation system, was presented in [206]; the present cable-driven architecture is conceptually similar. The singularity conditions of the robot in [206] were studied by assuming a symmetric architecture and by taking into account only translational singularities: it can be shown that the singularity conditions provided in [206] correspond to the plane Π previously defined. Another example can be found in [40], where the authors study a translational robot with three legs, and prove that the singularity surface is given by the union of a quadric and a plane (but in this case there are no constraint singularities, provided that some conditions on the robot architecture are fulfilled).

4. Practically feasible motions

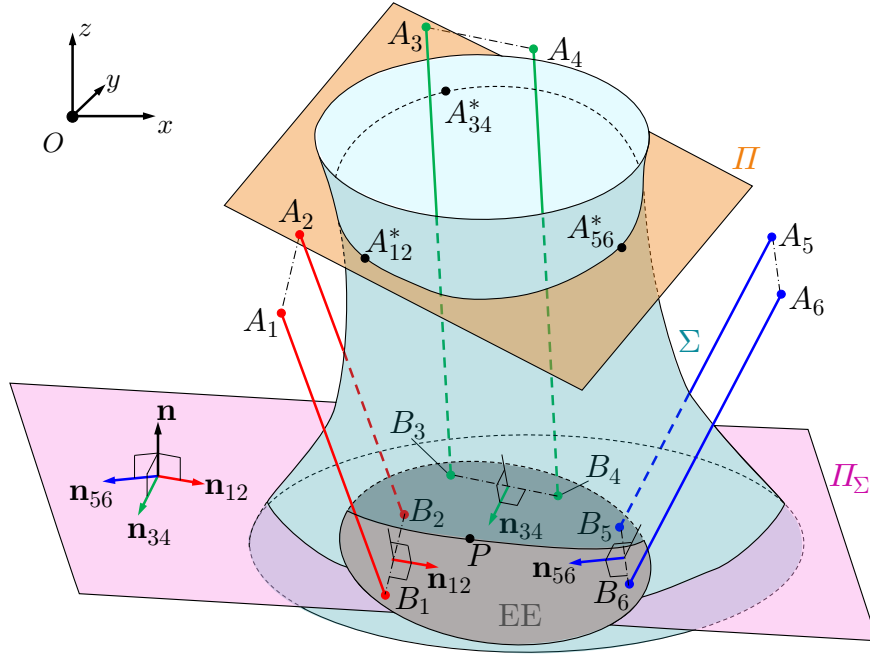


Figure 4.1: The singularity surface Σ for a translational cable-suspended robot with a general architecture.

Fig. 4.1 qualitatively illustrates the singularity surface Σ for the robot at hand. Vector \mathbf{n}_{34} (in green) is orthogonal to the plane Π_{34} passing through cables 3 and 4 (also in green). The same holds for vectors \mathbf{n}_{12} (in red) and \mathbf{n}_{56} (in blue). Since \mathbf{n}_{12} , \mathbf{n}_{34} and \mathbf{n}_{56} are coplanar (i.e. they are parallel to a common plane Π_{Σ}), there is a direction \mathbf{n} , orthogonal to Π_{Σ} , around which the robot is free to rotate.

To help the reader to visualize quadric Σ , note that Σ has the following properties:

- It emerges from Eq. (4.3) that $\det(\mathbf{A}) = 0$ if \mathbf{p} is equal to \mathbf{a}_{12}^* , \mathbf{a}_{34}^* or \mathbf{a}_{56}^* . The three points A_{ij}^* 's are thus contained in Σ .
- Similarly, $\det(\mathbf{A}) = 0$ if $\mathbf{a}_{ij}^* - \mathbf{p}$ is aligned to \mathbf{d}_{ij} , so that the cross product of these two vectors is zero (this corresponds to the case $\|\mathbf{c}_{ij}\| = 0$). Thus, the line r_{ij} defined by $\mathbf{p} = \mathbf{a}_{ij}^* + \beta_{ij}\mathbf{d}_{ij}$, with $\beta_{ij} \in \mathbb{R}$, is contained in Σ ; note that there are in fact three such lines, one for each parallelogram. It

is known from projective geometry that there is one and only one quadric through a given set of three skew lines [88]; the quadric is then either a hyperbolic paraboloid (if the three vectors \mathbf{d}_{ij} are all parallel to a single plane, but not to each other) or a hyperboloid of one sheet (otherwise). If instead the lines are not skew, the quadric may be a cylinder (either elliptic, parabolic or hyperbolic), a cone or the union of two planes (either parallel, intersecting or coincident). The possibility of the quadric being a cylinder can be ruled out by a geometric reasoning: if this were the case, the three lines r_{12} , r_{34} and r_{56} would be parallel, and so would be \mathbf{d}_{12} , \mathbf{d}_{34} and \mathbf{d}_{56} . In this case the three vectors \mathbf{n}_{12} , \mathbf{n}_{34} and \mathbf{n}_{56} would have a common normal, and the robot would be architecturally singular. Accordingly, an architecture with all vectors \mathbf{d}_{ij} 's parallel is a degenerate case to be avoided. In a similar manner, it can be shown that Σ cannot be a cone: this could only happen if lines r_{ij} passed through a common point, but again, this would lead to a singular architecture.

Two special architectures can be identified, that lead to a simplified shape for Σ .

4.2.1 Two \mathbf{d}_{ij} 's are parallel

Consider first the case when vectors \mathbf{d}_{ij} and \mathbf{d}_{kl} are parallel, namely $\mathbf{d}_{ij} = f\mathbf{d}_{kl}$, $f \in \mathbb{R}$. Since $\mathbf{d}_{ij} = \mathbf{b}_i - \mathbf{b}_j = \mathbf{a}_i - \mathbf{a}_j$, this implies that segments $\overline{A_i A_j}$ and $\overline{A_k A_l}$ are parallel too. See Fig. 4.2 for an illustration of a possible implementation, where cables 1 and 2 (resp. 3 and 4) in the same parallelogram are controlled by one spool rotating around an axis parallel to line $A_1 A_2$ (resp. $A_3 A_4$).

If $\mathbf{d}_{ij} = f\mathbf{d}_{kl}$, the polynomial $\det[\tilde{\mathbf{A}}(x, y, z)] = 0$ can be factored out in two linear terms, and Σ degenerates into the union of two planes, $\Pi_{ij,kl,\alpha}$ and $\Pi_{ij,kl,\beta}$. To see this, set (without loss of generality) $\mathbf{d}_{34} = f\mathbf{d}_{12}$ and consider the determinant of $\tilde{\mathbf{A}}$. One obtains

$$\det(\tilde{\mathbf{A}}) = \{[\mathbf{d}_{12} \times (\mathbf{a}_{12}^* - \mathbf{p})] \times [f\mathbf{d}_{12} \times (\mathbf{a}_{34}^* - \mathbf{p})]\} \cdot [\mathbf{d}_{56} \times (\mathbf{a}_{56}^* - \mathbf{p})] \quad (4.10)$$

Consider the quadruple vector product in the curly brackets in Eq. (4.10),

4. Practically feasible motions

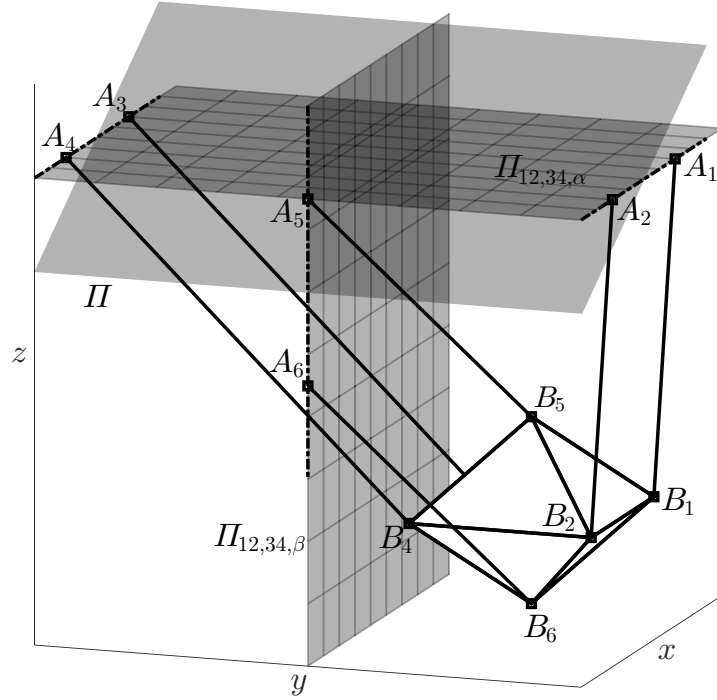


Figure 4.2: A simplified architecture, with the spools of cables 1-2 and 3-4 having parallel axes. The rotational singularity planes $\Pi_{12,34,\alpha}$ and $\Pi_{12,34,\beta}$ are shown with grid lines; the translational singularity plane Π is shown with no grid.

which can be expanded as

$$\begin{aligned}
 & [\mathbf{d}_{12} \times (\mathbf{a}_{12}^* - \mathbf{p})] \times [f\mathbf{d}_{12} \times (\mathbf{a}_{34}^* - \mathbf{p})] \\
 &= -[(\mathbf{a}_{12}^* - \mathbf{p}) \times \mathbf{d}_{12}] \times [f\mathbf{d}_{12} \times (\mathbf{a}_{34}^* - \mathbf{p})] \\
 &= -\{(\mathbf{a}_{12}^* - \mathbf{p}) \cdot [\mathbf{d}_{12} \times (\mathbf{a}_{34}^* - \mathbf{p})]\} f\mathbf{d}_{12} + \{(\mathbf{a}_{12}^* - \mathbf{p}) \cdot [\mathbf{d}_{12} \times f\mathbf{d}_{12}]\} (\mathbf{a}_{34}^* - \mathbf{p}) \\
 &= -\{(\mathbf{a}_{12}^* - \mathbf{p}) \cdot [\mathbf{d}_{12} \times (\mathbf{a}_{34}^* - \mathbf{p})]\} f\mathbf{d}_{12}
 \end{aligned} \tag{4.11}$$

by using known properties of vector products [20, p. 187, Eq. xxxiii] and the obvious fact that $\mathbf{d}_{12} \times f\mathbf{d}_{12} = 0$. Eq. (4.11) can be further simplified as

$$\begin{aligned}
 & -\{(\mathbf{a}_{12}^* - \mathbf{p}) \cdot [\mathbf{d}_{12} \times (\mathbf{a}_{34}^* - \mathbf{p})]\} f\mathbf{d}_{12} = \{(\mathbf{a}_{12}^* - \mathbf{p}) \cdot [(\mathbf{a}_{34}^* - \mathbf{p}) \times \mathbf{d}_{12}]\} f\mathbf{d}_{12} \\
 &= \{[(\mathbf{a}_{12}^* - \mathbf{p}) \times (\mathbf{a}_{34}^* - \mathbf{p})] \cdot \mathbf{d}_{12}\} f\mathbf{d}_{12}
 \end{aligned} \tag{4.12}$$

Finally, this term can be expanded as

$$\begin{aligned} & \{[(\mathbf{a}_{12}^* - \mathbf{p}) \times (\mathbf{a}_{34}^* - \mathbf{p})] \cdot \mathbf{d}_{12}\} f \mathbf{d}_{12} \\ &= \{[\mathbf{a}_{12}^* \times \mathbf{a}_{34}^* - \mathbf{a}_{12}^* \times \mathbf{p} - \mathbf{p} \times \mathbf{a}_{34}^*] \cdot \mathbf{d}_{12}\} f \mathbf{d}_{12} \end{aligned} \quad (4.13)$$

which is recognized as a linear function of the position \mathbf{p} . Substituting Eq. (4.13) in Eq. (4.10) one recognizes the product of two terms that are linear in \mathbf{p} :

$$\det(\tilde{\mathbf{A}}) = \{[\mathbf{a}_{12}^* \times \mathbf{a}_{34}^* - \mathbf{a}_{12}^* \times \mathbf{p} - \mathbf{p} \times \mathbf{a}_{34}^*] \cdot \mathbf{d}_{12}\} \{f \mathbf{d}_{12} \cdot [\mathbf{d}_{56} \times (\mathbf{a}_{56}^* - \mathbf{p})]\} \quad (4.14)$$

Therefore, the singularity surface Σ in this case is the union of two planes. These planes are generally unrelated to the plane Π defined by $\det(\mathbf{M}_{sup}) = 0$.

It can also be proved that:

- Plane $\Pi_{ij,kl,\alpha}$ passes through points A_{ij}^* and A_{kl}^* , whereas $\Pi_{ij,kl,\beta}$ passes through point A_{mn}^* . Here, m and n are the indexes of the two cables in the third parallelogram (in general, \mathbf{d}_{mn} is parallel to neither \mathbf{d}_{ij} nor \mathbf{d}_{kl}).
- Plane $\Pi_{ij,kl,\alpha}$ is orthogonal to vector $f\boldsymbol{\lambda}_{a,kl} - \boldsymbol{\lambda}_{a,ij}$, whereas plane $\Pi_{ij,kl,\beta}$ is orthogonal to both $\boldsymbol{\lambda}_{ij,mn}$ and $\boldsymbol{\lambda}_{kl,mn}$ (which are parallel in this case).

4.2.2 All \mathbf{d}_{ij} 's are parallel to plane Π

Another case of practical interest is found when the three vectors \mathbf{d}_{ij} are all parallel to the plane Π through A_{12}^* , A_{34}^* and A_{56}^* , as in Fig. 4.3 (architecture \mathcal{R} in Fig. 1.6). An example of such a robot is found in [196], where the authors show a design where all points A_i 's are on the same horizontal plane Π , and all points B_i 's are on the horizontal plane through P . Notice that, in the more general architecture \mathcal{R} , neither points A_i 's nor points B_i 's are coplanar (Fig. 4.3).

By choosing, without loss of generality, the fixed coordinate frame $Oxyz$ so that O lies in (and z is normal to) Π , the z components of both points A_{ij}^* 's and vectors \mathbf{d}_{ij} 's are all zero. With these simplifications, $\det(\tilde{\mathbf{A}}) = 0$ becomes

$$\det(\tilde{\mathbf{A}}) = -(\boldsymbol{\Lambda} \boldsymbol{\Lambda}_a^T)_{3,3} z^2 = 0 \quad (4.15)$$

4. Practically feasible motions

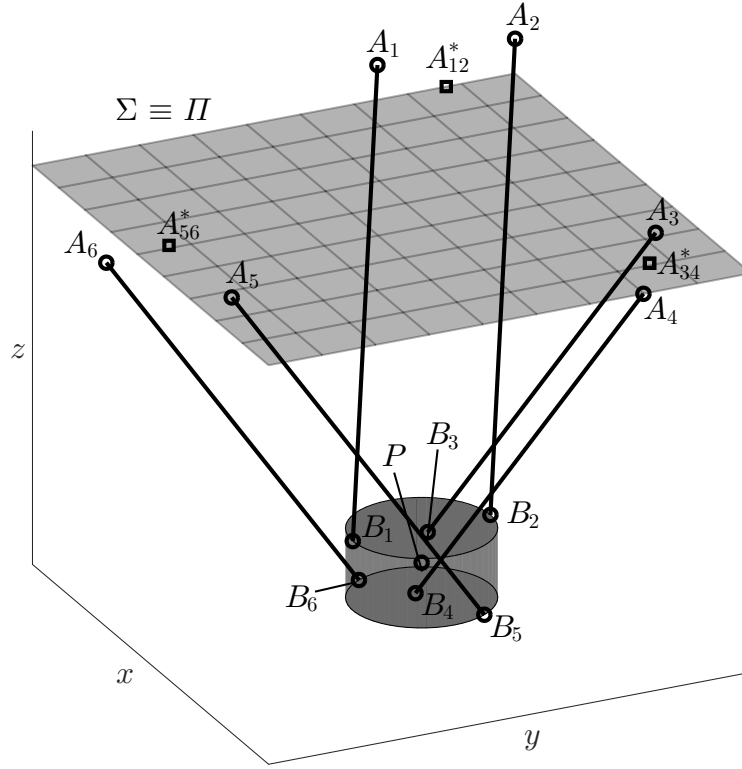


Figure 4.3: A simplified architecture with lines A_1A_2 , A_3A_4 and A_5A_6 parallel to the plane Π through A_{12}^* , A_{34}^* and A_{56}^* .

where $(\cdot)_{3,3}$ denotes the 3rd element on the 3rd row of matrix (\cdot) . Clearly, Σ is in this case a degenerate quadric defined by two coincident planes with $z = 0$, so $\Sigma \equiv \Pi$.

4.3 Reachable workspace

In order to be feasible, dynamic trajectories must satisfy, other than kinematic and kineto-static constraints concerning cable tensionability and singularity avoidance, also physical constraints related to cable extension and interference. With regard to the former issue, the RW is the set of poses that can be reached with cable lengths comprised between a minimum and maximum value, that is, $\rho_i \in [\rho_{min}, \rho_{max}]$, $i = 1, \dots, 6$. Since, for cables i and j belonging to the same parallelogram, $\rho_i = \rho_j = \|\mathbf{a}_{ij}^* - \mathbf{p}\|$, the condition on their length implies that

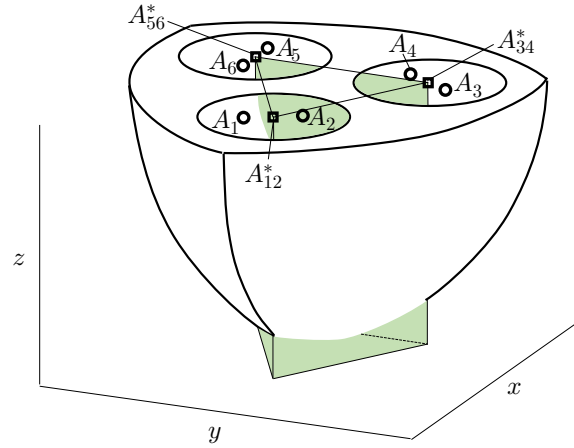


Figure 4.4: SEW (gray prism) and RW (white spherical surfaces) for the robot used in the experiment described in Section 3.7.2. The SEW is a vertical triangular prism with upper vertexes in points A_{12}^* , A_{34}^* and A_{56}^* , as shown in Subsec. 2.3.1. The RW is the volume comprised between three smaller spherical surfaces defined by $\rho_i = \rho_{min}$, three bigger spherical surfaces defined by $\rho_i = \rho_{max}$, and plane Π through points A_{ij}^* .

point P must be comprised within two spheres, centered in A_{ij}^* , and having radii ρ_{min} and ρ_{max} , respectively; therefore, one obtains a RW whose boundaries are spherical surfaces. Fig. 4.4 shows the RW and the SEW for the robot used during the experiments described in Subsec. 3.7.2.

4.4 Cable interference

Another issue to be considered is the possibility of cables interfering with each other, as this limits the workspace (see page 17). Since two cables i and j in a given parallelogram are on parallel lines, they cannot intersect, unless the two lines are actually coincident: in this case A_i , A_j , B_i and B_j are aligned, a condition which is easily ruled out in practice. Consider then two cables i and k from two different parallelograms. In the instant they cross, they must be contained in the same plane; it is worth emphasizing that this condition is necessary, but not sufficient, since cable lines might cross outside the cable span.

4. Practically feasible motions

The problem of defining the interference-free workspace of cable robots when the EE orientation is constant was studied in [127, 158]. In [158], it was shown that cables i and k are coplanar if and only if

$$(\Delta \mathbf{a}_{ki} \times \mathbf{d}_{ki}) \cdot (\mathbf{p} - \mathbf{a}_i + \mathbf{b}_i) = 0 \quad (4.16)$$

where $\Delta \mathbf{a}_{ki} = \mathbf{a}_k - \mathbf{a}_i$. Eq. (4.16) holds in these cases:

- (a) $\|\Delta \mathbf{a}_{ki}\| = 0$ or $\|\mathbf{d}_{ki}\| = 0$, namely if the two attachment points A_i and A_k , or B_i and B_k , coincide. In fact, in this case the two cables cross in the attachment point $A_i = A_k$, or $B_i = B_k$.
- (b) $\Delta \mathbf{a}_{ki}$ is parallel to \mathbf{d}_{ki} , so that $\Delta \mathbf{a}_{ki} \times \mathbf{d}_{ki} = \mathbf{0}$: this is a special architecture in which cables i and k are always coplanar, regardless of the robot position[†].
- (c) $\mathbf{p} - \mathbf{a}_i + \mathbf{b}_i = \mathbf{0}$: since $\mathbf{p} - \mathbf{a}_i + \mathbf{b}_i$ is the vector from A_i to B_i , this can only happen if the i -th cable has zero length.
- (d) $\Delta \mathbf{a}_{ki} \times \mathbf{d}_{ki}$ is orthogonal to $\mathbf{p} - \mathbf{a}_i + \mathbf{b}_i$, which is the general case considered in [158].

Excluding the special cases (a), (b) and (c), Eq. (4.16) defines a plane Ω_{ik} such that, if $P \in \Omega_{ik}$, the cables i and k are coplanar and thus could cross. In order to provide geometric insight to this condition, it is useful to introduce auxiliary points C_{ik} having position vectors $\mathbf{c}_{ik} = \mathbf{a}_i - \mathbf{d}_{ki}$, and auxiliary planes Γ_{ik} passing through C_{ik} , C_{ki} , A_i , and A_k . It can be proven that the plane Ω_{ik} defined by Eq. (4.16) is parallel to Γ_{ik} and passes through A_i^* and A_k^* (note that, since cables i and k are not in the same parallelogram, A_i^* and A_k^* are not coincident).

Consider now special architecture \mathcal{R}_1 (Subsec. 1.5.2.2), with all points A_i 's lying on a plane Γ and all points B_i 's lying on a plane parallel to Γ . In this case, it is easy to see that all points C_{ik} 's also lie on Γ : consequently, all planes Γ_{ik} 's coincide with Γ , and Ω_{ik} coincides with the singularity plane $\Pi \equiv \Sigma$. For a robot such as the one in [196] (which falls in the \mathcal{R}_1 architecture

[†] In this case, the two cables are either always crossing or never crossing, for any position of the robot.

class), then, there can be no cable interference unless the robot is at a singular configuration. This makes such an architecture attractive as the singularity-free workspace and the interference-free workspace are coincident and very simple to visualize: therefore, this architecture was used for the experimental tests. Indeed, the architecture chosen for the experiments falls under both class \mathcal{L}_2 (see Subsec. 3.7.2), so that its kineto-static model can be simplified as seen in Sec. 2.3.1, and class \mathcal{R}_1 , to easily avoid singularities and cable interference loci.

4.5 Summary of the chapter

In this chapter, the properties of the purely-translational CSPRs presented in Subsec. 1.5.2 were investigated. Specifically, the singularity-free workspace, the reachable workspace, and the interference-free workspace were studied, finding in all cases analytical formulations of the corresponding loci. In this way, one can verify that the dynamically feasible trajectories presented in Ch. 3 can actually be followed without losing control of the EE or the cables crossing each other; since all loci have analytical formulas, the feasibility conditions can be verified in real time. Moreover, the special architectures presented in Subsecs. 1.5.2.2 and 1.5.2.3 were shown to have interesting features that allow to greatly simplify the loci defined above.

From the results summarized above, goal (II) from Sec. 1.2 can be considered satisfied.

5

Kinematic performance indexes

in which the effects of errors in the control of actuators are analyzed, and kinematic indexes are proposed that measure how much the robot is sensitive to such errors in a given pose.

5.1 Introduction

Control errors

In Subsec. 1.3.2.3 the modeling method commonly applied in cable robotics (considering taut cables as straight line segments) was presented: assuming a fully-actuated architecture (such as those considered in this work, see Subsecs. 1.5.1 and 1.5.2), the solution of the 0-th order IKP is unique and straightforward to find, while the 0-th order DKP has usually a finite number of solutions.

From the DKP and IKP, one can infer the control algorithms for the robot. However, the control of the actuators cannot be perfect: small errors between the desired joint position $\boldsymbol{\theta}_d$ and the actual one $\boldsymbol{\theta}_e$ will always be present, therefore the real pose \mathbf{x}_e will also be different from the desired one \mathbf{x}_d (see for instance Fig. 3.12).

Consider for example the 6-cable robot in Subsec. 1.5.2: the motion is purely translational only if the two cables in a parallelogram are kept at the same length as the robot moves. In the prototype, this was obtained by having

5. Kinematic performance indexes

the cable pair wind on a common pulley (Fig. 3.10c). However, it is necessary to ensure that the free lengths ρ_i of the cables are pairwise equal as motion starts; since this condition cannot be perfectly guaranteed even with an accurate calibration procedure, the EE starts moving with an initial difference between lengths ρ_i and ρ_j in a pair, thus introducing small errors in the orientation as the robot moves.

For the aforementioned reasons, it is important to study how the platform orientation changes as joint position errors are introduced in cable lengths: one can thus verify whether the robot, for a given architecture or at a given pose, is especially sensitive to such errors. Since in general input joint errors have a known maximum magnitude, which depends on the accuracy of the control system, one can thus find an upper bound on the output error on the robot pose.

State of the art: dexterity and manipulability

There is a very vast literature on *kinematic performance indexes*, which are a way to measure the sensitivity of a robot to small control errors: see for instance [128, 156, 170] and [129, pp. 163–171]. Here, the focus will be on *local* indexes that measure the sensitivity at a given pose, as opposed to *global* indexes that measure the sensitivity over the entire workspace; when global indexes are needed, for example in order to compare different architectures, they are generally defined as the average of local indexes evaluated at a number of different poses.

Most commonly, kinematic performance indexes are based on the *direct Jacobian matrix* $\mathbf{J} = -\mathbf{F}_x^{-1}\mathbf{F}_\theta$, which, for a fully-actuated robot, is defined for any pose where the robot is not at a Type 2 singularity (in which case \mathbf{F}_x is not invertible). The 1st-order DKP can then be written as $\dot{\mathbf{x}} = \mathbf{J}\dot{\boldsymbol{\theta}}$; by considering infinitesimal variations of joint and EE coordinates, one obtains $d\mathbf{x} = \mathbf{J}d\boldsymbol{\theta}$. This relationship maps small actuation errors $d\boldsymbol{\theta} = \boldsymbol{\theta}_d - \boldsymbol{\theta}_e$ to corresponding pose errors $d\mathbf{x} = \mathbf{x}_d - \mathbf{x}_e$. Frequently used indexes based on \mathbf{J} are Yoshikawa's *manipulability index* [208] and the *dexterity index* first proposed in [176].

Yoshikawa’s *manipulability index* [208] is defined as $\mu = \sqrt{\det(\mathbf{J}^T \mathbf{J})}$ and corresponds (up to a constant) to the volume of the *manipulability hyperellipsoid*: this is the projection of the unit hypersphere in the joint space (defined by $\|\boldsymbol{\theta}_d - \boldsymbol{\theta}_e\| = 1$) in the Cartesian space, where the robot Jacobian \mathbf{J} is the projection matrix. In other terms, the hyperellipsoid is the set of all possible pose errors $\|\mathbf{x}_d - \mathbf{x}_e\|$ which correspond to joint errors of unit norm. Thus, μ gives an overall measure of the amplification factor between joint and pose errors. However, it has several drawbacks:

- It does not consider the ellipsoid shape and thus may lead, if used uncritically in the design stage, to highly distorted architectures [43].
- The maximum joint errors are defined based on the Euclidean norm*. This model is not physically realistic [128], as it means that, when the error on one joint is at its maximum, all other joint errors are zero.
- As shown in [103], μ does not depend on the position of the OP P on the EE, which seems counterintuitive and undesirable in practical use.

In [176], the authors propose the *dexterity index* κ as the condition number of the Jacobian matrix, so that $\kappa = \|\mathbf{J}^{-1}\| \|\mathbf{J}\|$. It can be proved from linear algebra [67, pp. 87–88] that κ provides an upper bound on the error amplification between joint and EE coordinates. However, as noted in [43], κ^{-1} provides a lower bound for the error amplification, so that a smaller κ does not lead in general to a better overall performance (the maximum error will decrease, but the minimum error will increase at the same time).

Regarding cable robots in particular, the study of kinematic indexes for a 3D printing CSPR with an architecture similar to the one proposed in Subsec. 1.5.2 (but with six DoFs) was performed in [13], to verify that the maximum position error was within the printing accuracy; an index of kinematic performance for a translational CDPR with parallelogram actuation was also proposed in [213]. Also, in [110] the authors proposed indexes that extend

* Here and in the rest of the thesis, $\|\bullet\|$ corresponds to the 2-norm of \bullet , unless otherwise specified; where confusion may arise due to the use of different norms, this will be equivalently denoted by $\|\bullet\|_2$.

5. Kinematic performance indexes

the concept of dexterity by taking into account the effect of the unilateral constraints set by cables.

A common issue for the indexes presented so far is that they are based on \mathbf{J} , which in general has non-homogeneous units when the robot has both translational and rotational DoFs. Thus, changing the units of measure changes the indexes, while clearly the robot accuracy is constant at a given pose.

This, for instance, is the case of the CSPR presented in Subsec. 1.5.2: the 1-st order DKP is written (at nonsingular poses) as $\mathbf{J}\dot{\boldsymbol{\rho}} = \begin{bmatrix} \mathbf{v}^T & \boldsymbol{\omega}^T \end{bmatrix}^T$, with \mathbf{v} and $\boldsymbol{\omega}$ being the linear and angular velocities of the EE and $\dot{\boldsymbol{\rho}}$ being the 6×1 array of cable velocities. Thus, while the first three rows of \mathbf{J} (corresponding to translational DoFs) have dimensionless entries, the last three (corresponding to unactuated rotational DoFs) have dimension of the inverse of a length.

Several authors have proposed different ways to overcome this issue, but they all introduce some arbitrary choice; indeed, as observed in [155] for a spatial 6-DoF robot, “*this arbitrariness is an unavoidable consequence of the geometry of $SE(3)$* ”, on which “*there is no natural positive-definite metric*” [120]. Some of the proposed methods are:

- To divide the rotational components of \mathbf{J} by a quantity with unit of length [7, 122]. The definition of this length is however arbitrary and it is thus difficult to compare different architectures.
- To analyze the 1-st order kinematics of the robot by the velocities of a set of points on the EE [70, 107]. In this way, \mathbf{J} has homogeneous dimensions, but there is no general criterion to pick such points on the EE.

For the reasons above, the robotics research community has not come to a complete consensus over the choice of such indexes [43], as they all show some drawbacks.

Chapter description

Here, the analysis will start from the *kinematic sensitivity indexes* introduced in [43], which offer the advantages of having a clear physical interpretation and dimensional homogeneity; then, indexes that build and upon the existing literature will be defined (Sec. 5.2).

In Sec. 5.3, the properties of the indexes are presented. Then, in Sec. 5.4, the indexes are applied to the translational CSPR with finite-size EE presented in Subsec. 1.5.2. Though Sec. 5.4 focuses on the translational CSPR (which is a more realistic robot model) the methods here presented could also be applied to the robot with point-mass EE.

Finally, in Sec. 5.5, a way to model *finite errors* on the cable lengths is presented for the translational CSPR.

In the rest of this chapter, the cables are always supposed to be kept in tension by external forces acting on the EE, for example by using the trajectories presented in Ch. 3.

5.2 Definition of sensitivity indexes

To overcome the issues of defining kinematic indexes from a Jacobian matrix \mathbf{J} with nonhomogeneous units, Ref. [43] proposed to separate the pose error $d\mathbf{x}$ into translational ($d\mathbf{p}$) and rotational DoFs ($d\boldsymbol{\phi}$, the vector parallel to the axis of rotation of the mobile frame on the EE—with respect to the fixed frame—and having magnitude equal to the rotation angle). The authors then define two kinematic sensitivity indexes that describe the sensitivity of the robot position and orientation to actuator displacements, as follows:

$$\sigma_{r,q} = \max_{\|d\boldsymbol{\theta}\|_q=1} \|d\boldsymbol{\phi}\|_q \quad (5.1a)$$

$$\sigma_{p,q} = \max_{\|d\boldsymbol{\theta}\|_q=1} \|d\mathbf{p}\|_q \quad (5.1b)$$

5. Kinematic performance indexes

with $\|\bullet\|_q$ being the q -norm ($q \geq 1$) of $(\bullet)^\dagger$.

Among the various kinematic performance indexes seen so far, the latter two provide desirable characteristics:

- they have a well-defined physical meaning, that is, $\max\{\|d\mathbf{p}\|_q\} = \sigma_{p,q} \|d\boldsymbol{\theta}\|_q$ and $\max\{\|d\boldsymbol{\phi}\|_q\} = \sigma_{r,q} \|d\boldsymbol{\theta}\|_q$;
- each of them is consistent in terms of dimensional units (assuming that all joint coordinates have the same units, as is usually the case);
- they do not introduce an arbitrary choice in the definition and thus can be used to compare different architectures;
- $\sigma_{r,q}$ does not depend on the choice of P , but $\sigma_{p,q}$ does (cf. [103]), which corresponds to physical intuition.

In [43], the authors proposed using either the 2-norm or the ∞ -norm in Eqs. (5.1). By setting $q = 2$, they showed that closed-form expressions can be obtained for $\sigma_{r,q}$ and $\sigma_{p,q}$; however, as noted previously, using the 2-norm to bound the joint errors is not realistic [128]. In [43] the possibility of setting $q = \infty$ was also explored; this would be the most physically sound choice for $\|d\boldsymbol{\theta}\|_q$, as this corresponds to limiting the error on each joint's position (for a CDPR, on the cable lengths) to be comprised within ± 1 (in a conveniently defined system of units).

Note, however, that the method proposed in [43] for the case $q = \infty$ calculates sensitivities by solving three linear programming problems for each of the two indexes, at every position of interest for the robot. If one wants to have a clear map of the sensitivities, $\sigma_{r,\infty}$ and $\sigma_{p,\infty}$ ought to be evaluated for a very large number of points in the workspace, so computation becomes impractically long. More importantly, while the ∞ -norm is a sensible choice for measuring the errors in the joint space, it is less meaningful for errors in the Cartesian space; for example, in Eq. (5.1a), this corresponds to taking

[†] Following the notation from [43], this thesis will refer to the q -norm (instead of the p -norm, which is the more common term) to avoid confusion with the subscript p which refers to position.

the largest component (in absolute value) of the rotation vector $d\phi$, whose significance in the robot design does not appear obvious.

In [151] the author proposed to use different norms, defining a kinematic sensitivity index as

$$\mu_{max} = \max_{\|d\theta\|_\infty=1} \|d\mathbf{x}\|_2 \quad (5.2)$$

In this way, the position error $\|d\mathbf{x}\|_2$ measures the Euclidean distance between the desired and actual positions; all errors on the joint coordinates have maximum absolute value 1 and are independent of each other. However, Eq. (5.2) again mixes terms in nonhomogeneous units, if the EE pose \mathbf{x} has both translational and rotational DoFs.

Combining insights from the previous works, kinematic performance indexes are here defined as follows:

$$\sigma_{r,q,s} = \max_{\|d\theta\|_q=1} \|d\phi\|_s \quad (5.3a)$$

$$\sigma_{p,q,s} = \max_{\|d\theta\|_q=1} \|d\mathbf{p}\|_s \quad (5.3b)$$

With this approach, the indexes in Eqs. (5.3) are dimensionally consistent; moreover, by taking $s = 2$ and $q = \infty$, the errors in both the joint and Cartesian space are measured in the most “natural” way. This idea is also reminiscent of [6], where indexes to define an upper bound on the translational displacement $d\mathbf{p}$ of the EE were proposed based on mixed norms; however, the application was different (for path planning of serial robots in presence of obstacles) and the authors used $q = 1$ for ease of computation.

This definition of sensitivity indexes is analogous to the one presented in [171] for planar parallel manipulators with rigid links; later, the same indexes were applied to cable-driven planar robots [102]. Note that, to the best of the author’s knowledge, the properties of the kinematic indexes analyzed in this chapter have not been investigated in the available literature; also, the application of the kinematic indexes to spatial robots with both rotational and translational DoFs is novel.

5.3 Properties of sensitivity indexes

Assuming that the robot under examination is a fully-actuated parallel robot in a non-singular pose, the relationship between joint and Cartesian errors is $d\mathbf{x} = [d\mathbf{p}^T \ d\phi^T]^T = \mathbf{J}d\boldsymbol{\theta} = -\mathbf{F}_x^{-1}\mathbf{F}_\theta d\boldsymbol{\theta}$, as obtained from Eq. (1.1). Note that, using this linear relationship between $d\mathbf{x}$ and $d\boldsymbol{\theta}$, it is implicitly assumed that the errors are very small with respect to the nominal joint coordinates; this assumption will be used throughout the rest of this section and in Sec. 5.4.

The Jacobian matrix can now be divided as follows: $\mathbf{J} = [\mathbf{J}_p^T \ \mathbf{J}_r^T]^T$, where each of the two sub-matrices \mathbf{J}_p and \mathbf{J}_r , corresponding to translational and rotational DoFs respectively, is dimensionally homogeneous. The relationships between small errors in the joint coordinates and in the EE position/orientation then become $d\mathbf{p} = \mathbf{J}_p d\boldsymbol{\theta}$ and $d\phi = \mathbf{J}_r d\boldsymbol{\theta}$.

Eqs. (5.3) can now be rewritten as

$$\sigma_{r,q,s} = \max_{\|d\boldsymbol{\theta}\|_q=1} \|\mathbf{J}_r d\boldsymbol{\theta}\|_s \quad (5.4a)$$

$$\sigma_{p,q,s} = \max_{\|d\boldsymbol{\theta}\|_q=1} \|\mathbf{J}_p d\boldsymbol{\theta}\|_s \quad (5.4b)$$

The kinematic sensitivities used in this section are comprised between 0 and ∞ (since they are defined as vector norms); in fact, they can be zero only if \mathbf{F}_θ does not have full column rank.

Eqs. (5.4) are recognized as equivalent to the definition of a matrix norm $\|\bullet\|_{q,s}$ which is subordinate to vector norms $\|\bullet\|_q$ and $\|\bullet\|_s$ [67]. This result is compatible with the observation from [43] that indexes (5.1) (which are a special case of the more general indexes (5.3)) can be expressed as matrix norms for both serial and parallel manipulators (for the latter, this only holds if the manipulator is not redundantly-actuated or in a singularity configuration). Finally, the proposed indexes can be computed (outside a parallel Type 2

singularity) as follows:

$$\sigma_{r,q,s} = \|\mathbf{J}_r\|_{q,s} \quad (5.5a)$$

$$\sigma_{p,q,s} = \|\mathbf{J}_p\|_{q,s} \quad (5.5b)$$

Calculating the kinematic sensitivities from matrix norms avoids having to solve the (generally nonlinear) convex optimization problem defined by Eqs. (5.3). Matrix norms can sometimes be easily computed from closed-form expressions, such as if $q = s = \infty$; however, no such formulas exist for the general case. Indeed, it was proven in [86] that even the problem of *approximating* (up to a given relative error) the $\|\bullet\|_{\infty,s}$ matrix norm is NP-hard for any $1 \leq s < \infty$, meaning that no known algorithm can do so in polynomial time. NP-hard problems thus become quickly intractable as the size of the input (in this case, the matrix whose norm must be computed) grows. In the case at hand, the input size corresponds to the size of matrices \mathbf{J}_r , \mathbf{J}_p : NP-hardness could then be a problem if these matrices are large, for example for a multi-link manipulator with a large number of DoFs. On the other hand, if one considers 6-DoF, fully-actuated manipulators such as the translational robot studied in this thesis, the calculation time is not an issue. Indeed, the maximum of $\|\mathbf{J}d\boldsymbol{\theta}\|_s$ in the hypercube defined by $\|d\boldsymbol{\theta}\|_\infty = 1$ must occur, for any matrix \mathbf{J} , at a vector $d\boldsymbol{\theta} \in \{-1, 1\}^{n_A}$ (where n_A is the number of actuators), that is, each element of $d\boldsymbol{\theta}$ must be either 1 or -1 (since the maximum over a polytope of a q -norm is attained at some vertex [26]). Therefore, it is only necessary to evaluate $\|\mathbf{J}d\boldsymbol{\theta}\|_s$ in 2^{n_A} points; since usually in parallel robots $n_A \leq 6$, the computation times are in fact still reasonable[‡]. If a multi-link manipulator (such as the one in [6], which has ten DoFs) has to be analyzed, the problem of calculating the matrix norms grows exponentially with the number of actuators; in this case, one might use the results from [181], which provide approximate lower and upper bounds that can be efficiently computed.

Some of the interesting features of the kinematic indexes defined in [43]

[‡] The computation time can also be reduced by noting that $\|\mathbf{J}d\boldsymbol{\theta}\|_s = \|\mathbf{J}(-d\boldsymbol{\theta})\|_s$, therefore it is not necessary to check both $d\boldsymbol{\theta}$ and $-d\boldsymbol{\theta}$. One can thus halve the search space, for instance, by only considering the vectors $d\boldsymbol{\theta} \in \{-1, 1\}^{n_A}$ whose first element is positive.

5. Kinematic performance indexes

still apply to the indexes employed in this thesis. For instance, such indexes provide upper bounds on the EE displacement and rotation under joint errors of known maximum absolute value $d\theta_{max}$, that is, $\|d\mathbf{p}\|_s \leq \sigma_{p,\infty,s}d\theta_{max}$ and $\|d\phi\|_s \leq \sigma_{r,\infty,s}d\theta_{max}$, as follows from the properties of matrix norms [20, p. 553, Eq. (9.4.4)]. Furthermore, these bounds are tight, meaning that there is at least one vector $d\theta$ such that the corresponding position or rotation error reaches its maximum value. These properties descend immediately from the general properties of matrix norms.

It is also worth exploring the effect of changing the mobile reference frame on the EE. Suppose that indexes (5.3) have been computed for a robot at a certain pose and with respect to a coordinate frame A defined by $Px_Ay_Az_A$. One might ask how the proposed indexes change if computed with respect to a different reference frame B defined by $Qx_By_Bz_B$. Let $\mathbf{d} = P - Q$ (see Fig. 5.1) and \mathbf{R}_{BA} be the rotation matrix from A to B . If $d\mathbf{p}$ and $d\mathbf{q}$ are the infinitesimal displacements of P and Q respectively, then $d\mathbf{q} = d\mathbf{p} + \mathbf{d} \times d\phi$, and thus the infinitesimal displacements expressed in B are

$$\begin{bmatrix} \{d\phi\}_B \\ \{d\mathbf{q}\}_B \end{bmatrix} = \begin{bmatrix} \mathbf{R}_{BA} & \mathbf{0} \\ \{\tilde{\mathbf{d}}\}_B \mathbf{R}_{BA} & \mathbf{R}_{BA} \end{bmatrix} \begin{bmatrix} \{d\phi\}_A \\ \{d\mathbf{p}\}_A \end{bmatrix} \quad (5.6)$$

where $\tilde{\mathbf{d}}$ is the skew-symmetric matrix associated with vector \mathbf{d} such that $\tilde{\mathbf{d}}\mathbf{w} = \mathbf{d} \times \mathbf{w}$ for any vector $\mathbf{w} \in \mathbb{R}^3$. This is called the *adjoint transformation* [141]. Calculating $\sigma_{r,q,s}$ in frame B leads to $\{\sigma_{r,q,s}\}_B = \max_{\|d\theta\|_q=1} \|\mathbf{R}_{BA}\{d\phi\}_A\|_s$. From this expression, one can see that $\{\sigma_{r,q,s}\}_B = \{\sigma_{r,q,s}\}_A$ if either $\mathbf{R}_{BA} = \mathbf{I}$, so that frames A and B have the same orientation, or $s = 2$, since \mathbf{R}_{BA} is an *orthogonal* matrix, which thus preserves the 2-norm of a vector. The translational sensitivity instead becomes $\{\sigma_{p,q,s}\}_B = \max_{\|d\theta\|_q=1} \|\{\tilde{\mathbf{d}}\}_B \mathbf{R}_{BA}\{d\phi\}_A + \mathbf{R}_{BA}\{d\mathbf{p}\}_A\|_s$, from which it can be seen that in general $\{\sigma_{p,q,s}\}_B \neq \{\sigma_{p,q,s}\}_A$ even if $\mathbf{R}_{BA} = \mathbf{I}$. This is consistent with physical intuition: the rotation angle $\|d\phi\|_2$ of the EE remains the same if observed from different reference frames, while the displacement of different OPs on the platform is generally different (cf. [43], where similar results were obtained for the indexes defined therein—but assuming only a change of OP).

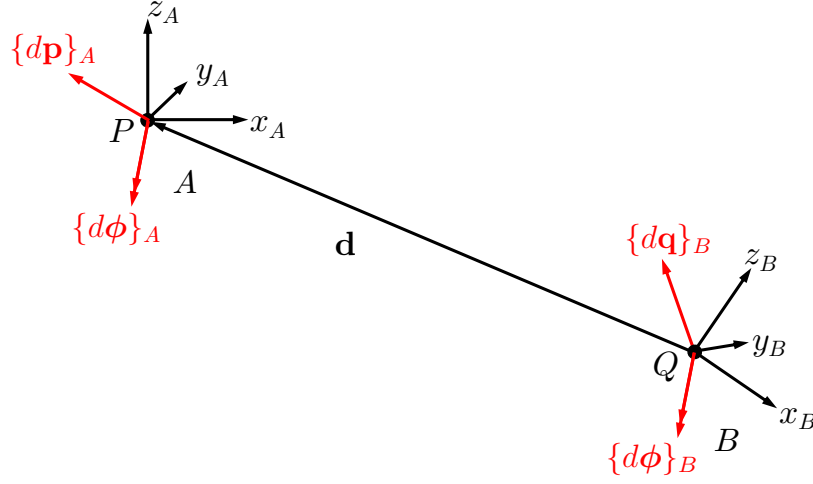


Figure 5.1: A small displacement $d\mathbf{p}$ and a small rotation $d\phi$ expressed in two different coordinate frames.

One might also be interested in comparing the proposed indexes with the ones provided by previous literature. The most natural comparison is against the kinematic sensitivities in [43]. It can be proven that

$$\|\mathbf{J}\|_{\infty,2}/\sqrt{n} \leq \|\mathbf{J}\|_2 \leq \|\mathbf{J}\|_{\infty,2} \quad (5.7a)$$

$$\|\mathbf{J}\|_{\infty,2}/\sqrt{m} \leq \|\mathbf{J}\|_{\infty} \leq \|\mathbf{J}\|_{\infty,2} \quad (5.7b)$$

for any $m \times n$ matrix \mathbf{J} , including \mathbf{J}_p and \mathbf{J}_r (see Appendix A.5).

Considering a non-redundant parallel robot outside a singularity pose, the indexes from [43] can be computed with the matrix norms $\|\bullet\|_{\infty}$ and $\|\bullet\|_2$; this implies $\sigma_{p,\infty,2}/\sqrt{6} \leq \sigma_{p,2} \leq \sigma_{p,\infty,2}$ and $\sigma_{p,\infty,2}/\sqrt{3} \leq \sigma_{p,\infty} \leq \sigma_{p,\infty,2}$ (note that in this case the matrices \mathbf{J}_p and \mathbf{J}_r are 3×6). Similar inequalities can be written for the rotational sensitivity index. This shows that the proposed indexes provide bounds for the ones already established in the literature.

It is worth observing that Eqs. (5.4) are not valid when the robot is in a Type 2 singularity, in which case $\mathbf{J} = -\mathbf{F}_x^{-1}\mathbf{F}_\theta$ is not defined. In this case, it is convenient to divide $\mathbf{F}_x = [\mathbf{F}_{x,p} \ \mathbf{F}_{x,\phi}]$ in dimensionally consistent submatrices. Eq. (1.1) can now be rewritten (again in terms of infinitesimal variations

5. Kinematic performance indexes

instead of time derivatives) as

$$\mathbf{F}_{x,p}d\mathbf{p} + \mathbf{F}_{x,\phi}d\phi = -\mathbf{F}_\theta d\theta \quad (5.8)$$

From this expression, one can prove the following[§] (see Appendix A.5):

- if $\mathfrak{R}(\mathbf{F}_{x,p}) \cap \mathfrak{R}(\mathbf{F}_{x,\phi}) = \{\mathbf{0}\}$ and $\mathbf{F}_{x,p}$ does not have full column rank, while $\mathbf{F}_{x,\phi}$ does, then $\sigma_{p,q,s} = \infty$, while $\sigma_{r,q,s}$ remains finite;
- if $\mathfrak{R}(\mathbf{F}_{x,p}) \cap \mathfrak{R}(\mathbf{F}_{x,\phi}) = \{\mathbf{0}\}$ and $\mathbf{F}_{x,\phi}$ does not have full column rank, while $\mathbf{F}_{x,p}$ does, then $\sigma_{r,q,s} = \infty$, while $\sigma_{p,q,s}$ remains finite;
- in all other cases of Type 2 singularity, both $\sigma_{r,q,s}$ and $\sigma_{p,q,s}$ go to infinity.

This shows how the proposed indexes are also useful to distinguish between a translational singularity, in which case the robot can have an uncontrolled displacement $d\mathbf{p}$ and thus $\sigma_{p,q,s} = \infty$, and a rotational singularity, where the uncontrolled DoF is a rotation $d\phi$.

Finally, it is to be noted that the proposed indexes are *not* matrix norms when the manipulator is redundantly-actuated [43]. In this case not every vector of joint displacements $d\theta$ that respects condition $\|d\theta\|_q = 1$ has a corresponding pose displacement $d\mathbf{x}$ that solves the kinematic equation $\mathbf{F}_x d\mathbf{x} = -\mathbf{F}_\theta d\theta$ (as noted for a planar robot in [171]). However, using the matrix norms in Eqs. (5.5) still provides an upper bound on the kinematic sensitivity indexes from Eqs. (5.3), as the function to be maximized is the same (but the search space is smaller in the redundantly-constrained case).

5.4 Application to translational robot

The indexes defined in the previous section are now applied to the analysis of the translational CSPR described in Subsec. 1.5.2.

Due to kinematic–static duality [197], the Jacobian can be obtained from matrix $\tilde{\mathbf{M}}$ (introduced in Eq. (2.10)): one thus has $\mathbf{J} = \tilde{\mathbf{M}}^{-T}$.

A remarkable aspect of the translational robot studied here is that, unlike

[§] Here, $\mathfrak{R}(\mathbf{F})$ denotes the range of matrix \mathbf{F} , that is, the linear span of its columns.

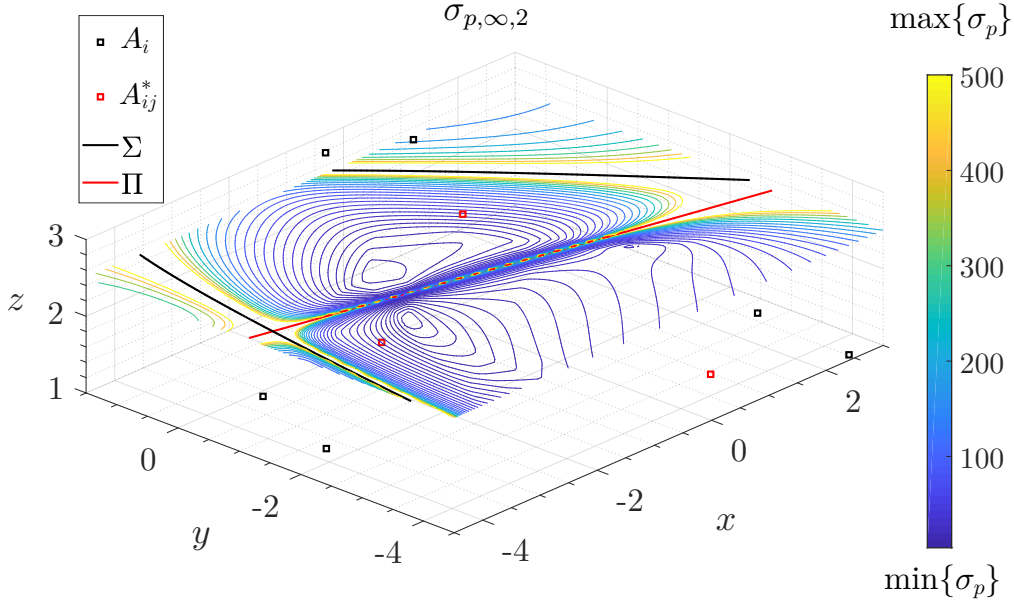


Figure 5.2: The translational kinematic sensitivity $\sigma_{p,\infty,2}$ calculated at a reference height z_r . The fixed cable attachment points are represented as squares (the EE and the cables are not shown). Notice how $\sigma_{p,\infty,2}$ reaches very high values (in yellow, see the colorbar) close to the singularity quadric Σ (whose intersection with the plane $z = z_r$ is indicated by a black line) and also close to the singularity plane Π (whose intersection is in red). Length unit is arbitrary.

most parallel manipulators, it has a direct Jacobian that can be calculated analytically; indeed, one finds

$$\mathbf{J}_p = \frac{1}{\det(\mathbf{M}_{sup})\pi_A} \begin{bmatrix} \mathbf{J}_{p,1} & \mathbf{J}_{p,2} & \mathbf{J}_{p,3} & \mathbf{J}_{p,4} & \mathbf{J}_{p,5} & \mathbf{J}_{p,6} \end{bmatrix} \quad (5.9a)$$

$$\mathbf{J}_r = \frac{1}{\pi_A} \begin{bmatrix} \mathbf{J}_{r,1} & -\mathbf{J}_{r,1} & \mathbf{J}_{r,3} & -\mathbf{J}_{r,3} & \mathbf{J}_{r,5} & -\mathbf{J}_{r,5} \end{bmatrix} \quad (5.9b)$$

where π_A , $\mathbf{J}_{p,i}$ and $\mathbf{J}_{r,i}$ ($i = 1, \dots, 6$) are defined in Appendix A.6 and $\mathbf{M}_{sup} = [\mathbf{e}_1 \ \mathbf{e}_3 \ \mathbf{e}_5]$ was introduced in Sec. 2.3 (Eqs. (2.12) and (2.13)). When the robot approaches a rotational singularity, $\det(\mathbf{A}) \rightarrow 0$, so $\pi_A \rightarrow 0$ (as shown in Appendix A.6); from Eqs. (5.9), all elements in matrices \mathbf{J}_r and \mathbf{J}_p go to infinity. Since kinematic sensitivities are defined from the norms of said matrices, $\sigma_{p,q,s} \rightarrow \infty$ and $\sigma_{r,q,s} \rightarrow \infty$. Also, as the robot approaches a translational singularity, $\det(\mathbf{M}_{sup})$ goes to zero, the elements of \mathbf{J}_p go to infinity, and so does

5. Kinematic performance indexes

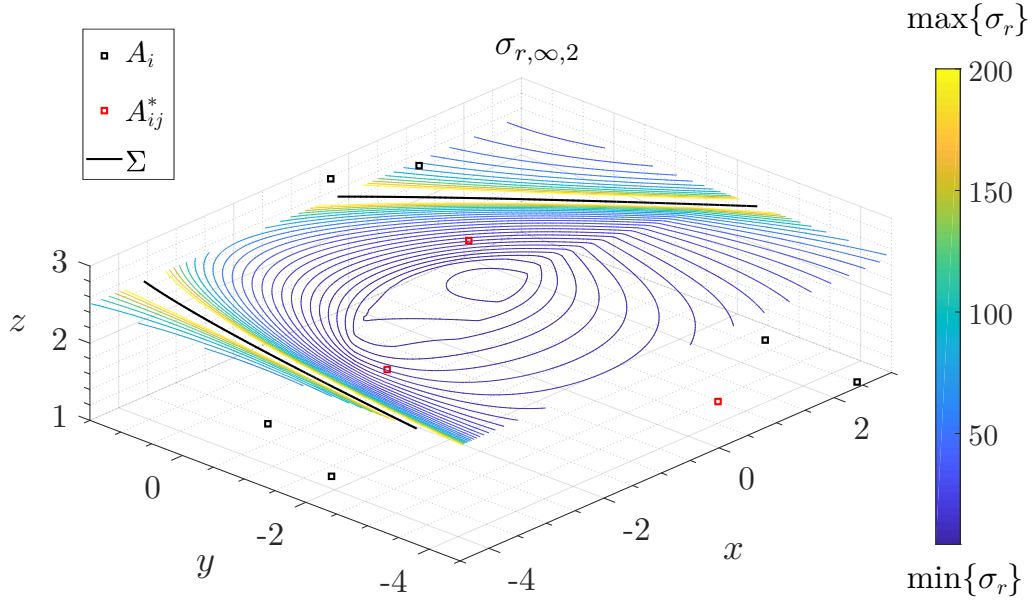


Figure 5.3: Same as Fig. 5.2, but for the rotational kinematic sensitivity $\sigma_{r,\infty,2}$. In this case, the index remains finite in the translational singularity Π .

$\sigma_{p,q,s}$, while $\sigma_{r,q,s}$ remains finite.

Figs. 5.2 and 5.3 show respectively the contour curves of $\sigma_{p,\infty,2}$ and $\sigma_{r,\infty,2}$, calculated numerically at a given height $z = z_r$, for an example architecture. As expected, the sensitivities become very high close to the singularity quadric Σ (introduced in Sec. 4.2) and to the singularity plane Π defined in Subsec. 1.5.2. In particular, both indexes tend to infinity close to Σ ; meanwhile, $\sigma_{p,\infty,2}$ tends to infinity close to Π , while $\sigma_{r,\infty,2}$ remains finite, so the rotational singularity (in Σ) and the translational one (in Π) are partially decoupled.

In Subsec. 2.3.1 it was found that, if P is in the intersection of segments $\overline{B_1B_2}$, $\overline{B_3B_4}$ and $\overline{B_5B_6}$ (special architecture \mathcal{L}), the dynamic equations (2.8) can be greatly simplified.

It can also be shown that for this architecture \mathbf{J}_p is definite as long as \mathbf{M}_{sup} is invertible, so $\sigma_{p,\infty,2}$ remains finite everywhere except at a translational singularity: the two singularities are thus completely decoupled (see Appendix A.7).

A further specialization of this architecture happens when P is on the midpoint of segments $\overline{B_i B_j}$ (special architecture \mathcal{L}_1 from Subsec. 1.5.2.1): this choice appears sensible from an engineering point of view, as it leads to having equal tensions in the two cables of each parallelogram (see again Subsec. 2.3.1) and thus balanced forces on the actuated spools. In this case, the matrices in Eqs. (5.9) simplify as

$$\mathbf{J}_p = \frac{\mathbf{M}_{sup}^{-T}}{2} \begin{bmatrix} 1 & 1 & 0 & 0 & 0 & 0 \\ 0 & 0 & 1 & 1 & 0 & 0 \\ 0 & 0 & 0 & 0 & 1 & 1 \end{bmatrix} \quad (5.10a)$$

$$\mathbf{J}_r = \frac{\check{\mathbf{A}}^{-T}}{2} \begin{bmatrix} 1 & -1 & 0 & 0 & 0 & 0 \\ 0 & 0 & 1 & -1 & 0 & 0 \\ 0 & 0 & 0 & 0 & 1 & -1 \end{bmatrix} \quad (5.10b)$$

with $\check{\mathbf{A}}$ as defined in Appendix A.6. The sensitivities can then be directly calculated as $\sigma_{r,\infty,2} = \|\check{\mathbf{A}}^{-T}\|_{\infty,2}$ and $\sigma_{p,\infty,2} = \|\mathbf{M}_{sup}^{-T}\|_{\infty,2}$, as can be proven from the $\|\bullet\|_{\infty,2}$ -norm definition (see Appendix A.7); this further reduces the computational expense, as the matrices involved have a smaller size.

Furthermore, in this case \mathbf{J}_p (and thus $\sigma_{p,\infty,2}$) only depends on position, but not on vectors \mathbf{b}_i : the positional sensitivity is thus independent of the EE size (measured by the largest distance from any of the attachment points B_i to P). As for the $\sigma_{r,\infty,2}$, it can be proven that, for a given size of the EE, it is minimized when the three segments $\overline{B_i B_j}$ are of equal length; in this condition, $\sigma_{r,\infty,2}$ is inversely proportional to the EE size (see Appendix A.7). This suggests that, in order to optimize the rotational sensitivity and thus have a better chance of preventing rotations on the platform, one should pick all B_i 's at the same distance from P and that this distance should be the largest compatible with size and weight constraints, which also corresponds to physical intuition.

These results, together with the ones from Ch. 4, suggest designing the EE such that the attachment points B_i are on a circle, with its center on P , and to position all fixed cable exit points A_i on a plane parallel to the platform

5. Kinematic performance indexes

plane; in this way, the singularity surfaces degenerate in a single plane passing through points A_i 's (Subsec. 4.2.2). Also, as seen in Sec. 4.4, in this case there is no risk of cable interference, unless the robot is at a singularity. This is the principle used in the design of the robot prototype in Subsec. 3.7.2. The final result is an architecture similar to the one in [196].

For the robot whose architecture has points A_i 's and B_i 's on horizontal planes, it seems interesting to separate the sensitivities along the $x-y$ axes and along z . To do this, the matrices in \mathbf{J} in Eqs. (5.9) can be further subdivided as $\mathbf{J}_p = [\mathbf{J}_{p,xy}^T \quad \mathbf{J}_{p,z}^T]^T$ and $\mathbf{J}_r = [\mathbf{J}_{r,xy}^T \quad \mathbf{J}_{r,z}^T]^T$, with $\mathbf{J}_{p,xy}$ and $\mathbf{J}_{r,xy}$ being 2×6 matrices, and $\mathbf{J}_{p,z}$, $\mathbf{J}_{r,z}$ being 6-element row vectors. Then, one can define four separate sensitivity “sub-indexes” as $\sigma_{r,xy,\infty,2} = \|\mathbf{J}_{r,xy}\|_{\infty,2}$, $\sigma_{p,xy,\infty,2} = \|\mathbf{J}_{p,xy}\|_{\infty,2}$, $\sigma_{r,z,\infty,2} = \|\mathbf{J}_{r,z}\|_{\infty,2}$ and $\sigma_{p,z,\infty,2} = \|\mathbf{J}_{p,z}\|_{\infty,2}$.

From the definition of the $\|\bullet\|_{\infty,2}$ -norm, these sub-indexes are correlated to the ones defined in Eq. (5.3) as follows (Appendix A.7):

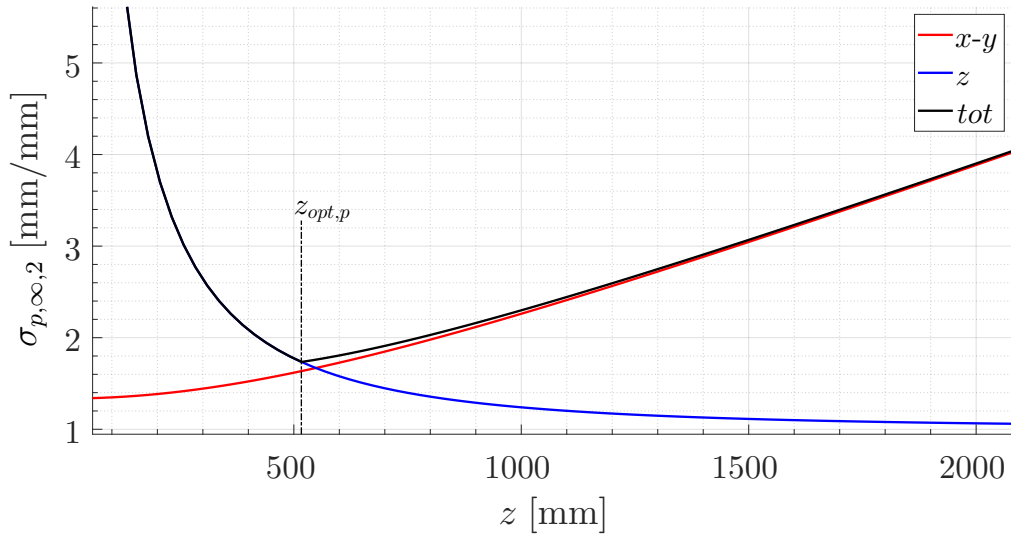
$$\max\{\sigma_{r,xy,\infty,2}, \sigma_{r,z,\infty,2}\} \leq \sigma_{r,\infty,2} \leq \sqrt{\sigma_{r,xy,\infty,2}^2 + \sigma_{r,z,\infty,2}^2} \quad (5.11a)$$

$$\max\{\sigma_{p,xy,\infty,2}, \sigma_{p,z,\infty,2}\} \leq \sigma_{p,\infty,2} \leq \sqrt{\sigma_{p,xy,\infty,2}^2 + \sigma_{p,z,\infty,2}^2} \quad (5.11b)$$

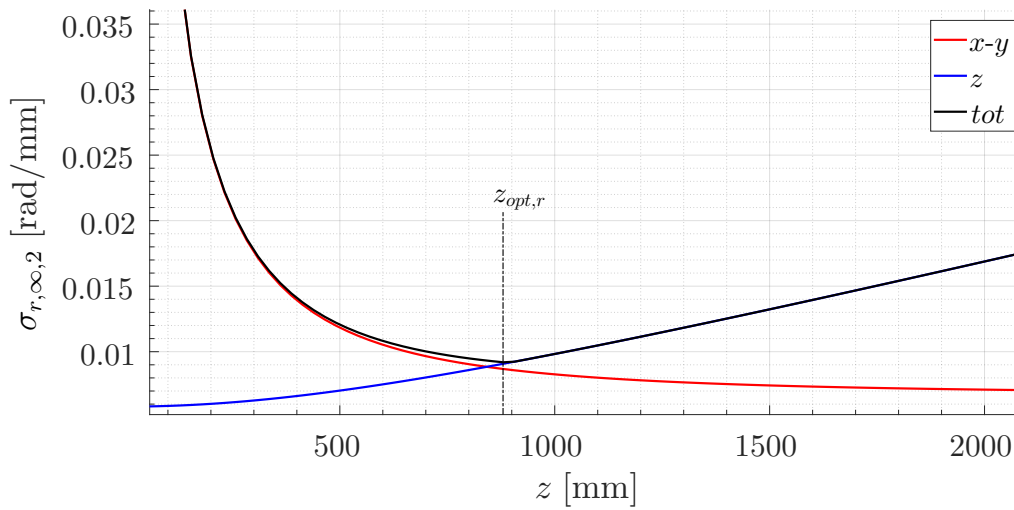
The results, for the robot used in the experimental tests (Subsec. 3.7.2), are shown in Fig. 5.4 where sensitivities are plotted as a function of z .

The results can be thus explained:

- $z \rightarrow \infty$: $\sigma_{r,z,\infty,2}$ increases, as the vectors \mathbf{n}_{ij} normal to the planes Π_{ij} through each parallelogram (Fig. 1.5) become approximately horizontal and thus close to being linearly dependent: therefore, the ability of the robot to prevent rotations around the z axis is reduced. As the cables become almost vertical, a motion of the platform in the horizontal $x-y$ plane causes only a small change in the cable lengths: therefore, $\sigma_{p,xy,\infty,2}$ also increases.
- $z \rightarrow 0$: all planes Π_{ij} 's coalesce in a single horizontal plane (the singularity plane Π through points A_{ij}^* 's), so the rotation along the vertical direction is blocked, but the platform can rotate along the x and y axes,



(a)



(b)

Figure 5.4: The rotational (a) and translational (b) sensitivities, calculated at $x = y = 0$, as functions of z , for the architecture used in the tests (Subsec. 3.7.2). Note that both sensitivities go to infinity as $z \rightarrow 0$ (close to the singularity plane $\Pi \equiv \Sigma$) and for $z \rightarrow \infty$; $\sigma_{r,\infty,2}$ and $\sigma_{p,\infty,2}$ have a minimum respectively at $z = z_{opt,r}$ and at $z = z_{opt,p}$.

5. Kinematic performance indexes

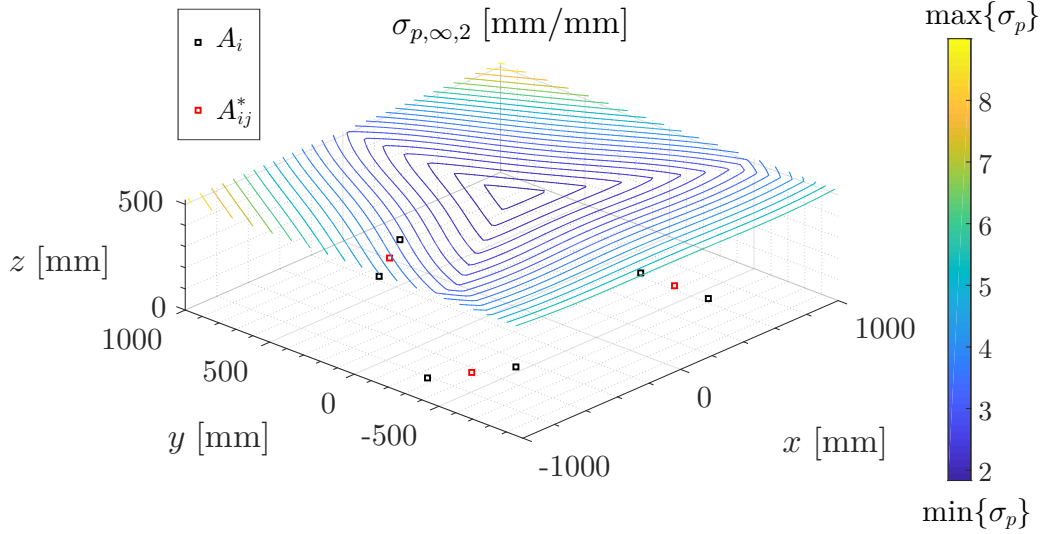


Figure 5.5: The translational kinematic sensitivity for the 6-cable robot prototype, at a height $z_{opt,p}$.

thus $\sigma_{r,xy,\infty,2} \rightarrow \infty$. Also, it can be seen that when P is on Π all cables are horizontal: the robot cannot move in plane Π , but it can have an infinitesimal motion in a direction normal to Π without changing the cable lengths. Therefore, $\sigma_{p,z,\infty,2}$ goes to infinity, too.

Figs. 5.4 suggest that there is an optimal interval of z where both indexes $\sigma_{p,\infty,2}$ and $\sigma_{r,\infty,2}$ are generally smaller, between $z = z_{opt,p}$ (where the translational sensitivity is minimal) and $z = z_{opt,r}$ (where $\sigma_{r,\infty,2}$ is lowest). Therefore, one may argue that the robot may move somewhere in between $z_{opt,p}$ and $z_{opt,r}$, depending on whether it is more important to have an accurate position or an accurate orientation. Given that in the present case $\sigma_{r,\infty,2}$ does not change much around $z_{opt,r}$, while the variation of $\sigma_{p,\infty,2}$ in the neighborhood of $z_{opt,p}$ is steeper, keeping $z \approx z_{opt,p}$ during the motion appears as a sensible choice for an accurate horizontal positioning.

Contour line plots of the sensitivity indexes for the prototype are displayed in Figs. 5.5 and 5.6. Note that the indexes are smaller towards the center of the workspace: this indicates that the robot will be more accurate (both in

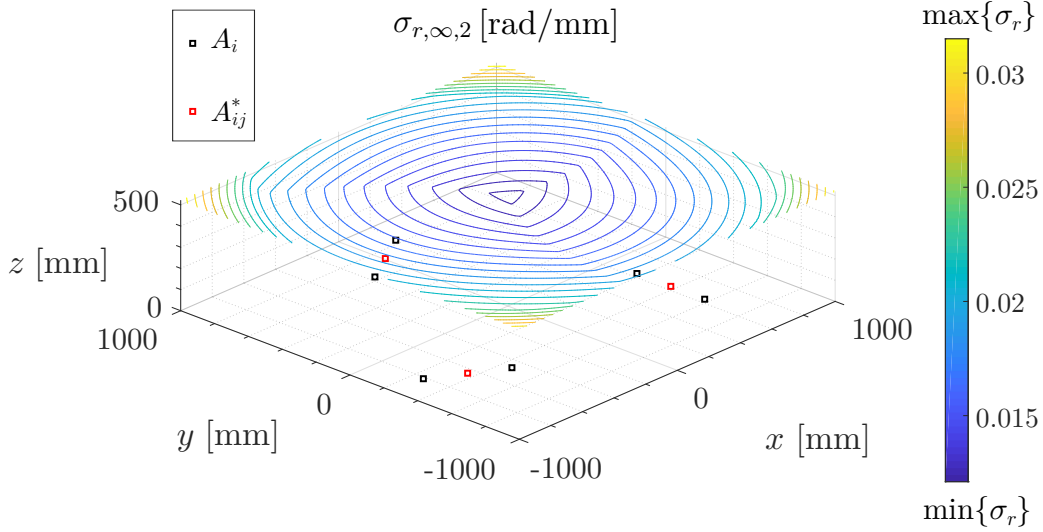


Figure 5.6: As in Fig. 5.5, for the rotational sensitivity. Note that here the indexes always remain finite, as there is no singularity in the workspace below the plane defined by $z = 0$.

terms of position and orientation) close to the center and less so the more it moves close to the boundaries of the SEW (or even beyond said boundaries, using the dynamical trajectories from Ch. 3). This indicates that a trade-off must be considered when designing dynamic trajectories: these can enlarge the zone where the robot can work, but at the expense of a reduced accuracy.

Note also the 120° symmetry of the plots in Figs. 5.5 and 5.6, as expected due to the symmetry of the robot itself (where points A_{ij}^* 's are approximately on the vertexes of an equilateral triangle).

Finally, the sensitivity indexes have been validated by comparing them against the positioning error observed during the experimental tests (Subsec. 3.7.2). Fig. 5.7 shows again the position error from Fig. 3.12a and compares it with the maximum position error given by the kinematic sensitivity index $\sigma_{p,\infty,2}$. In Fig. 5.7, the position error (orange line) is obtained by solving the DKP with both the desired and the actual cable lengths and calculating the distance $\|d\mathbf{p}\|_2$ between the desired and actual position. Multiplying the position sensitivity $\sigma_{p,\infty,2}$ by the norm of the error on the cable lengths $\|d\boldsymbol{\rho}\|_\infty$

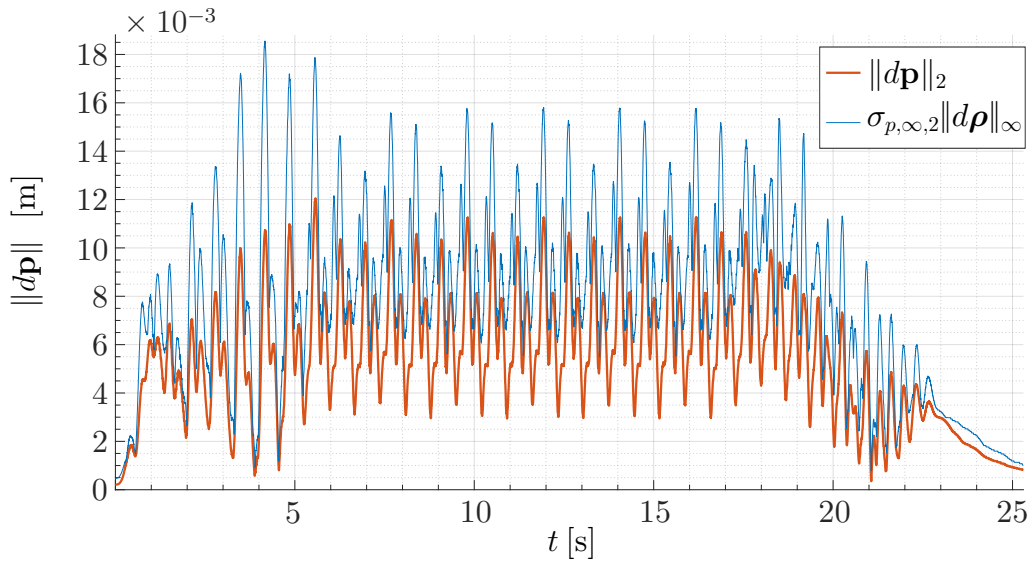


Figure 5.7: Plot of the position error $\|d\mathbf{p}\|_2$ for the translational cable robot during the periodic motion (a) described in Subsec. 3.7.2 (orange line, see Fig. 3.12a) and the estimated maximum error (blue line) given by the position sensitivity (calculated along the same trajectory).

(calculated at each time-step) provides an upper bound (blue line) on the position error: indeed, it can be observed from the figure that the maximum error obtained with the sensitivity index is always larger than the actual error. This confirms that $\sigma_{p,\infty,2}$ provides a useful upper bound to the error amplification between the joint and the Cartesian coordinates. It is worth noting that $\|d\mathbf{p}\|_2$ is obtained by solving a nonlinear DKP, while $\sigma_{p,\infty,2}$ was calculated assuming a linear relationship between $d\boldsymbol{\rho}$ and $d\mathbf{p}$: the clear correlation between the two plots in Fig. 5.7 suggests that this assumption (which is closer to the truth, the smaller the errors on the cable lengths are) is in fact valid.

5.5 Parallelogram planarity error

The previous section dealt with the effect of *infinitesimal* errors on the actuators. Suppose now that the edges $A_iA_jB_jB_i$ in the cable pair $i-j$ (that should ideally define a parallelogram) are no longer coplanar: this could be due, for

example, to a (finite) error on the cable lengths, an error in the architecture parameters or an error in the way the robot was assembled at the initial stage. Note that even if cables i and j have the same length (and so do the segments $\overline{A_i A_j}$ and $\overline{B_i B_j}$), points A_i , A_j , B_i and B_j might not be coplanar, so they do not form a parallelogram and do not properly constrain platform rotations: this situation is here referred to as a *planarity error* in one or more parallelograms. Starting from an initial position I with a planarity error, this error could grow uncontrolled as the robot moves to final position F ; moreover, the rotation matrix \mathbf{R} between the fixed and the mobile frame will not remain constant (as the robot is no longer purely translational).

In order to verify whether a parallelogram planarity error may cause a serious problem for the translational manipulator at hand, a series of numerical simulations were run before the tests described in Subsec. 3.7.2. In these simulations, it was assumed that errors were only in the cable lengths ρ_i (architecture parameters, such as the positions of points A_i 's in the fixed frame, can be measured when the robot is at rest with high precision): each cable length could thus be controlled up to a finite uncertainty $\pm\Delta\rho$ [¶], which is assumed to be the same for all cables.

The scheme of the numerical simulations is as follows.

- (1) In the first step, the IKP is solved for the robot in ideal conditions (that is, with no planarity errors in the parallelograms) at poses I and F , thus obtaining the corresponding cable lengths $\rho_{i,I}$ and $\rho_{i,F}$.
- (2) To simulate what happens when the robot moves from I to F , two approaches are adopted:
 - (a) One can imagine that the maximum errors $\Delta\rho$ are introduced all at once with the robot in the final position F , and thus solve the DKP where each cable length is $\rho_i \in [\rho_{i,F} - \Delta\rho, \rho_{i,F} + \Delta\rho]$. The initial

¶ In the numerical simulations here described, $\Delta\rho$ was $\approx 20 - 30$ mm, which is the order of magnitude of the errors in the robot calibration procedure used for the tests in Subsec. 3.7.2; while still small with respect to the robot size, this error is no longer clearly infinitesimal with respect to the cable lengths.

5. Kinematic performance indexes

guess for the solver is the desired final position F . Note that, when rotations are no longer locked, a 6-cable robot is equivalent to a Gough-Stewart platform of general architecture (assuming that all cables are in tension) and the DKP can have up to 40 solutions [58, 90]. Since ρ_i can assume any value within $\rho_{i,F} - \Delta\rho$ and $\rho_{i,F} + \Delta\rho$, n_ρ equally spaced values within this interval were taken, and the DKP was solved for each of the n_ρ^6 possible combinations of the cable lengths. Finally, the solution with the highest value of the pose error^{||} was taken as the worst case scenario. This combinatorial approach of checking all possible combinations of errors on the cable lengths is similar to the one used in [198], but in that paper the authors assume for simplicity that the highest error on the platform pose is obtained when all cables have an error equal to its maximum absolute value (an assumption that is only valid for infinitesimal errors): therefore, they only check the 2^6 combinations given by $\rho_i = \rho_{i,F} \pm \Delta\rho$. Here instead $n_\rho > 2$ possible lengths are considered for each cable.

- (b) One can choose to set errors $\Delta\rho$ in initial position I and solve the DKP with cable lengths $\rho_i \in [\rho_{i,I} - \Delta\rho, \rho_{i,I} + \Delta\rho]$, so that the robot has an initial planarity error and the EE can in fact rotate. Then the robot is moved from I to F , by discretizing the motion in n intermediate steps; the ideal cable length at the k -th step is $\rho_{i,k} = \rho_{i,I} + k(\rho_{i,F} - \rho_{i,I})/n$. The DKP is solved at every step, with the actual cable length at the k -th step being $\rho_i \in [\rho_{i,k} - \Delta\rho, \rho_{i,k} + \Delta\rho]$, again for each of the n_ρ^6 possible combinations of the cable lengths

^{||} To measure the error on the pose with respect to the ideal case, the following strategy was adopted: define the center of the platform as the point B_C with coordinates (in the mobile frame) given by $\sum_{i=1}^6 \mathbf{b}_i/6$; then, take the three B_i 's who are farthest from B_C (without loss of generality, assume that these are B_1, B_2 and B_3). The error on the platform pose can now be defined as $\sum_{i=1}^3 \|\mathbf{p} + \mathbf{R}\mathbf{b}_i - \mathbf{b}_{i,e}\|/3$, with $(\mathbf{p} + \mathbf{R}\mathbf{b}_i)$ and $\mathbf{b}_{i,e}$ being respectively the ideal position of B_i and the real one (in the fixed frame). The idea of defining the pose of a robot with the position of three points on the EE is taken from [70].

(see point (a)); the solution with the highest value of the error on the pose is retained. Here, however, three different starting guesses are taken:

- (i) the “ideal” solution (zero error on the cable lengths);
- (ii) the solution from the previous step $k - 1$;
- (iii) the “opposite” solution with respect to the one given by the previous step: if the solution found at step $k - 1$ had cable lengths $\rho_{i,k-1} \pm \Delta\rho_{i,k-1}$, solve the DKP with $\rho_{i,k-1} \mp \Delta\rho_{i,k-1}$, and use the resulting pose as yet another starting guess.

In this way one might likely catch more than one possible solution: the appearance of multiple solutions in the 6-dimensional space of possible cable lengths would indicate a potential risk. In that case, the robot may switch from one solution where the six cables define (at least approximately) three parallelograms to another solution which is farther from the theoretical one; from then on, the planarity error could become uncontrolled as the robot keeps moving.

If the planarity error were an issue, one would expect the two solutions for the final position, found by using either procedure (a)—applying all errors at the end of motion—or (b)—applying all errors at the beginning, so that the robot is no longer purely translational, and let the system evolve—not to be the same in the two cases; if otherwise the two solutions were identical or reasonably close, the architecture may be considered *stable*, in the sense that a small initial planarity error does not grow uncontrolled as the robot moves. This is exactly what was observed in the numerical simulations and shows that the architecture proposed is robust with respect to planarity errors in the parallelograms.

A more complete study would require using interval analysis [22, 102] to solve the DKP at each step from I to F and for each combination of the errors on the cable lengths, so as to be sure to find all possible solutions with errors on the cable lengths smaller than $\Delta\rho$. This approach is left for a future study. In any case, the experiments performed (see Subsec. 3.7.2) seem to confirm

what the above simulations suggested: the platform appeared in fact to be very stable against uncontrolled rotations.

5.6 Summary of the chapter

In this chapter, the effect of control errors on the robot motion has been studied.

The proposed indexes for kinematic performance follow the guidelines indicated in [156]: they are defined everywhere in the workspace (including singularities), have clearly definite lower and upper bounds (0 and ∞ , respectively in Type 1 or Type 2 singularities) and avoid combining terms with inconsistent units. Also, the dependency of the indexes on the choice of the coordinate frame on the EE is clear and consistent with design expectations. The main drawback of such indexes is that they do not generally have an analytical, closed-form expression, as recommended in [156]; however, they can still be computed in a very short time for most manipulators.

Proposed applications of the study presented in this chapter are:

- to optimize the trajectory connecting a start and a target pose: different trajectories can be compared by integrating the sensitivity indexes along each trajectory. Lower kinematic sensitivities denote in general a better trajectory, in the sense that the control errors will have a lower impact on the positioning accuracy of the EE.
- to compare different robot architectures: a global sensitivity index can be computed by integrating each index in the robot workspace. Then, an optimal architecture can be found as the one that has the lowest overall sensitivity in the desired workspace.

It could be the case that the kinematic sensitivities cannot be optimized independently: for example, one might have to compare two different architectures \mathcal{A} and \mathcal{B} , where \mathcal{A} has a better overall translational sensitivity $\sigma_{p,q,s}$ but \mathcal{B} is superior in terms of rotational sensitivity $\sigma_{r,q,s}$. While in some cases

the most important index is defined by the application (e.g., for simple pick-and-place operations an accurate control on the EE position would be more important than controlling the orientation), in general one needs to combine the two indexes in a meaningful way. A common approach for multi-objective optimization is to define a global objective function as a weighted sum of each objective [170], but this inevitably introduces an arbitrariness in the choice of weights and again combines quantities with different units. A more appropriate approach is *Pareto optimization* [37, 56], where many different solutions are obtained and *dominated* ones (that is, the ones that are “worse” than other solutions in terms of every objective function) are discarded. With two objectives (such as minimizing $\sigma_{p,q,s}$ and $\sigma_{r,q,s}$) one thus obtains a boundary of possible solutions that optimize either the first or the second objective and various combinations in between; finally, the designer can pick the best compromise for the application at hand. Applying Pareto optimization to the design of a translational cable robot such as the one studied in this thesis is left as future work.

6 Stiffness modeling and measuring

in which the effect of mechanical compliance in the robot is modeled and the global stiffness is measured by using appropriate indexes.

6.1 Stiffness modeling

As seen in Ch. 5, an accurate control of the EE of a parallel robot depends on the robot's control system. However, even if actuators could provide a perfect control of joint coordinates, the platform would still be not in its desired pose: indeed, all components have been so far modeled as perfectly rigid, but in fact some compliance is inevitable under the effect of external loads. The robot, then, will have a displacement with respect to its “unloaded” pose, an effect that ought to be taken into account for a complete physical model of the robot: this effect is especially important in cable robots, as cables can have a large mechanical compliance.

Therefore, in this chapter a model of the compliance for the translational cable-driven robot (Subsec. 1.5.2) will be developed, to show how external forces/torques on the EE cause displacements and/or rotations on the platform. Indeed, the property of purely-translational motion for the robot under exam was proven under the assumption of massless and infinitely stiff cables [31]. The first assumption is reasonable for most CDPRs, such as the

6. Stiffness modeling and measuring

prototype used in experimental tests (Subsec. 3.7.2), given that very thin cables were used; however, the compliance of the actuation system cannot be disregarded. Like Ch. 5, this chapter will focus on the 6-cable robot; a model of the simpler, 3-cable robot (Subsec. 1.5.1) could be promptly derived with the tools presented in this chapter.

Once the compliance model of the robot has been established, it is helpful to provide the designer with a measure of how much the EE pose can change under external loads. Indeed, the stiffness of a given mechanism is posture-dependent and is in general defined by a number of stiffness parameters whose combined effect cannot be easily visualized. Therefore, this chapter will also consider *stiffness indexes* that give a global measure of the stiffness at a given pose.

State of the art

Many authors have considered the effect of flexibility on the control of parallel robots in general and CDPRs in particular: this chapter will mostly focus on the latter, as a full review of the literature on the stiffness of parallel robots [129, pp. 266–273] would be out of the scope of this thesis.

One of the first works on the stiffness of CDPRs is [55], where the stiffness of a 6-cable robot in a suspended configuration is studied. The *stiffness matrix* for general cable robots was found in [17], where the authors modeled the cables as massless linear springs with fixed attachment points. In [195], the definition of a *workspace with stiffness conditions* was introduced as the set of poses where the minimum eigenvalue of said stiffness matrix is greater than a certain value (set by the designer, according to application requirements). The effect of using a nonlinear stiffness model for cables was studied in [101], while the effect of cable mass on stiffness is considered in [147]. In [185], the authors included the effect of pulley motion in the stiffness modeling: in this way, the cable attachment points on the fixed frame can move, following the motion of the pulley. The application of stiffness modeling to the vibration analysis of CDPRs was presented in [57]: here, the authors found that the

effect of transversal vibrations in cables was negligible when compared to the effect of axial vibrations. The effect of the torsional stiffness in the cables was considered in [144]. Finally, the possibility of varying the stiffness matrix of a cable robot at a given pose, by introducing *variable stiffness elements* in series with the cables, was explored in [207].

After establishing the stiffness model of a cable robot, e.g. with the methods from [17], it is useful to see how it varies throughout the workspace, to see if there are poses where compliance is excessively high. Also, the stiffness matrix varies depending on the architecture parameters: this should be taken into account when comparing different design options. Since the stiffness of a spatial robot is (usually) described by a matrix \mathbf{K}_g , it is hard to visualize its variation; thus, it is helpful to define stiffness indexes, which give a measure of the global stiffness at a certain pose.

Various stiffness indexes were proposed in the literature, depending on the stiffness matrix \mathbf{K}_g . See for instance:

- [23], where the indexes are the *minimum singular value* and the *determinant*;
- [62], where the indexes are the *minimum* and *maximum eigenvalues*;
- [119], where the *condition number* is used;
- [65], where the index is a *weighted sum* of the diagonal entries in \mathbf{K}_g , or [37], where the *diagonal entries* in \mathbf{K}_g^{-1} are used instead.

For a review of the state of the art on this topic, see [42, 170].

A common issue for such indexes is that they combine quantities in non-homogeneous units: thus, they depend on measure units, which complicates their use. This issue is analogous to the one regarding the measures of kinematic sensibility derived from the non-homogeneous Jacobian matrix \mathbf{J} (see Ch. 5). In [159], the author overcomes this issue by defining *equivalent* translational and rotational stiffness matrices (in homogeneous units); a similar approach was used in [188], where the authors define unit-homogenized matrices from the eigenvectors of sub-blocks of \mathbf{K}_g . Some authors instead propose to

6. Stiffness modeling and measuring

divide the stiffness matrix by a *characteristic length* to obtain a dimensionally-homogeneous matrix [118, 147]. Some authors instead [53] consider two separate eigenvalue problems, each depending only on sub-blocks of the stiffness matrix. Yet another approach is found in [204], where the authors studied a translational spatial robot and proposed a stiffness index defined as the inverse of the virtual work of an external unit wrench against the elastic forces. These stiffness indexes however lack an immediate physical interpretation or introduce arbitrary definitions (either in the characteristic length or in the direction of the external wrench).

Chapter description

This chapter will focus on the stiffness of the 6-cable robot against external wrenches. By modeling cables as linear springs, relevant properties of the stiffness matrix will be proven (Sec. 6.1.1); it is found that, under a specific architecture (\mathcal{L}_1 , from Subsec. 1.5.2.1), the stiffness matrix can be considerably simplified. Then, a physically consistent measure of the manipulator's rotational and translational stiffnesses at a given pose will be provided (Subsec. 6.2) and mapped within the workspace for the 6-cable robot (Subsec. 6.3).

6.1.1 Stiffness matrix

This section presents the derivation of the *Cartesian* stiffness matrix \mathbf{K}_g that relates the external wrench \mathbf{W}_e to the corresponding pose variation*, such that $\mathbf{W}_e = \mathbf{K}_g \begin{bmatrix} d\mathbf{p}^T & d\boldsymbol{\phi}^T \end{bmatrix}^T$. Here, it is convenient to divide \mathbf{K}_g in 3×3 blocks as

$$\mathbf{K}_g = \begin{bmatrix} \mathbf{K}_{F,p} & \mathbf{K}_{F,\phi} \\ \mathbf{K}_{M,p} & \mathbf{K}_{M,\phi} \end{bmatrix} \quad (6.1)$$

* This implies assuming that the elastic displacements are small, as is usually done, otherwise the wrench-twist relationship cannot be linearized by a stiffness matrix. In other words, one assumes that the robot stiffness is large enough that a *finite* wrench \mathbf{W}_e causes a pose variation (given by displacement $d\mathbf{p}$ and rotation $d\boldsymbol{\phi}$) due to the elastic elongations in the cables that is very small (thus, almost infinitesimal), as is usually done in structure mechanics.

Since $\mathbf{W}_e = [\mathbf{F}_e^T, \mathbf{M}_e^T]^T$, the external force and torque are obtained as

$$\mathbf{F}_e = \mathbf{K}_{F,p}d\mathbf{p} + \mathbf{K}_{F,\phi}d\boldsymbol{\phi} \quad (6.2a)$$

$$\mathbf{M}_e = \mathbf{K}_{M,p}d\mathbf{p} + \mathbf{K}_{M,\phi}d\boldsymbol{\phi} \quad (6.2b)$$

The stiffness of cable-driven manipulators was first studied in [17, 18], where the authors provided a general expression of the stiffness matrix; the same formulas will be used here.

It is assumed that the robot's compliance is concentrated in cables, while the EE and the frame are perfectly rigid; this approach is called the *Virtual Joint Method (VJM)* [188] and is the one most commonly employed for parallel manipulators. Introduce now the stiffnesses k_i of cables, modeled as massless linear springs; this is the commonly used model in the stiffness analysis of CDPRs and was numerically justified in [57]. The stiffness of a cable is generally written as $k_i = (ES)/\rho_i$, where E is the elastic modulus of the cable (which depends on the cable material) and S is its effective cross-section; a review of values of E for different cable materials is reported in [161, p. 115, Tab. 3.6]. Here, it is assumed that all cables are equal in composition and section, as it is usually the case, so the stiffness only varies with length ρ_i . Furthermore, with this assumption, two cables in the same parallelogram have the same stiffness[†]. Then, one can introduce $\mathbf{K}_l = \text{diag}(k_1, \dots, k_6)$ as the stiffness matrix in the *joint* space, such that $\boldsymbol{\tau} = \mathbf{K}_l d\boldsymbol{\rho}$.

One can also introduce a *preload* tension τ_{0i} due to an initial wrench \mathbf{W}_0 ; from Eq. (2.9), it holds $\tilde{\mathbf{M}}\boldsymbol{\tau}_0 = \mathbf{W}_0$, with $\boldsymbol{\tau}_0$ being the vector of the preload tensions in cables. In general, preloading should be taken into account, as confirmed experimentally in [3, 55], where it was shown that the effect of an initial preloading is to increase the platform stiffness.

[†] Some authors lump in k_i both the physical stiffness of the cable and the “virtual” stiffness k_c of the control loop (such as the proportional coefficient in a PID control scheme). This effect can be included by redefining $1/k_i = \rho_i/(ES) + 1/k_c$ as the stiffness of two springs in series; the stiffness of two cables in the same parallelogram is still equal in this case, if the stiffnesses k_c of the corresponding control algorithms are the same.

6. Stiffness modeling and measuring

From [17, 18], the Cartesian stiffness matrix can be written as the sum of three matrices:

$$\mathbf{K}_g = \mathbf{K}_e + \mathbf{K}_s + \mathbf{K}_f \quad (6.3)$$

The first matrix \mathbf{K}_e can be written as

$$\mathbf{K}_e = \tilde{\mathbf{M}}\mathbf{K}_l\tilde{\mathbf{M}}^T = \sum_{i=1}^6 k_i \begin{bmatrix} \mathbf{e}_i\mathbf{e}_i^T & \mathbf{e}_i\mathbf{e}_i^T\tilde{\mathbf{b}}_i^T \\ \tilde{\mathbf{b}}_i\mathbf{e}_i\mathbf{e}_i^T & \tilde{\mathbf{b}}_i\mathbf{e}_i\mathbf{e}_i^T\tilde{\mathbf{b}}_i^T \end{bmatrix} \quad (6.4)$$

where $\tilde{\mathbf{b}}_i$ is the cross-product matrix associated with vector \mathbf{b}_i (see Ch. 5). \mathbf{K}_e is called the *elastic* stiffness, that is, the stiffness that is only due to cables' compliance; if there is no preloading, $\mathbf{K}_g = \mathbf{K}_e$ [175]. The other two matrices instead depend on preloading and together they compose the *antagonistic* stiffness $\mathbf{K}_s + \mathbf{K}_f$; these are expressed as

$$\mathbf{K}_s = \sum_{i=1}^6 \frac{\tau_{0i}}{\rho_i} \begin{bmatrix} \mathbf{I} - \mathbf{e}_i\mathbf{e}_i^T & (\mathbf{I} - \mathbf{e}_i\mathbf{e}_i^T)\tilde{\mathbf{b}}_i^T \\ \tilde{\mathbf{b}}_i(\mathbf{I} - \mathbf{e}_i\mathbf{e}_i^T) & \tilde{\mathbf{b}}_i(\mathbf{I} - \mathbf{e}_i\mathbf{e}_i^T)\tilde{\mathbf{b}}_i^T \end{bmatrix} \quad (6.5a)$$

$$\mathbf{K}_f = -\sum_{i=1}^6 \tau_{0i} \begin{bmatrix} \mathbf{0} & \mathbf{0} \\ \mathbf{0} & \tilde{\mathbf{e}}_i\tilde{\mathbf{b}}_i \end{bmatrix} \quad (6.5b)$$

These two matrices are linearly dependent on the initial cable tensions τ_{0i} . Note that \mathbf{K}_e and \mathbf{K}_s are symmetric, while \mathbf{K}_f contains skew-symmetric terms.

From here onwards, it will be assumed that all cables remain in tension under both \mathbf{W}_0 and \mathbf{W}_e (where \mathbf{W}_e is the wrench that is added to \mathbf{W}_0), so that each contributes to the total robot's stiffness. In this case, the 6-cable CSPR is equivalent to a classic Gough-Stewart platform; the stiffness matrices then correspond to the ones found in [186] (when setting legs' masses to zero), where the authors also proved that the skew-symmetric matrix \mathbf{K}_f is zero if the initial wrench \mathbf{W}_0 is a pure force.

Eqs. (6.4) and (6.5) will now be specialized for the 6-cable translational manipulator (Subsec. 1.5.2), where vectors \mathbf{e}_i , cable lengths ρ_i and stiffnesses k_i are pairwise equal. Specifically, the special architecture \mathcal{L}_1 from Subsec. 1.5.2.1

will be considered, as this was the one selected for the prototype (Subsec. 3.7.2): here, $\mathbf{b}_j = -\mathbf{b}_i$ (and thus $\tilde{\mathbf{b}}_j = -\tilde{\mathbf{b}}_i$) for two cables i, j in the same parallelogram. In this case, it also holds $\tau_{0i} = \tau_{0j}$ for any initial wrench \mathbf{W}_0 (see Subsec. 2.3.1). Consider now the terms in the upper-right 3×3 block of \mathbf{K}_e (which corresponds to $\mathbf{K}_{F,\phi}$ in Eq. (6.1)) due to cables i and j ; from (6.4) one has

$$k_i \mathbf{e}_i \mathbf{e}_i^T \tilde{\mathbf{b}}_i^T + k_j \mathbf{e}_j \mathbf{e}_j^T \tilde{\mathbf{b}}_j^T = k_i \mathbf{e}_i \mathbf{e}_i^T \tilde{\mathbf{b}}_i^T + k_i \mathbf{e}_i \mathbf{e}_i^T (-\tilde{\mathbf{b}}_i^T) = \mathbf{0} \quad (6.6)$$

Since this result holds for all three cable pairs (i, j) , the sum is zero; given that \mathbf{K}_e is symmetric, its lower-left 3×3 block (corresponding to $\mathbf{K}_{M,p}$) is zero, too, thus the elastic stiffness matrix is block diagonal. For \mathbf{K}_s , the sum in the upper-right block for cables i, j becomes

$$\begin{aligned} \frac{\tau_{0i}}{\rho_i} (\mathbf{I} - \mathbf{e}_i \mathbf{e}_i^T) \tilde{\mathbf{b}}_i^T + \frac{\tau_{0j}}{\rho_j} (\mathbf{I} - \mathbf{e}_j \mathbf{e}_j^T) \tilde{\mathbf{b}}_j^T = \\ \frac{\tau_{0i}}{\rho_i} (\mathbf{I} - \mathbf{e}_i \mathbf{e}_i^T) \tilde{\mathbf{b}}_i^T + \frac{\tau_{0i}}{\rho_i} (\mathbf{I} - \mathbf{e}_i \mathbf{e}_i^T) (-\tilde{\mathbf{b}}_i)^T = \mathbf{0} \end{aligned} \quad (6.7)$$

Again, the sum in the upper-right block (and thus also the sum in the lower-left one) is zero. Finally, the sum in the lower-right block in matrix \mathbf{K}_f is, for i, j in the same parallelogram,

$$-\tau_{0i} \tilde{\mathbf{e}}_i \tilde{\mathbf{b}}_i - \tau_{0j} \tilde{\mathbf{e}}_j \tilde{\mathbf{b}}_j = -\tau_{0i} \tilde{\mathbf{e}}_i \tilde{\mathbf{b}}_i - \tau_{0i} \tilde{\mathbf{e}}_i (-\tilde{\mathbf{b}}_i)^T = \mathbf{0} \quad (6.8)$$

For the architecture \mathcal{L}_1 proposed, one can thus conclude the following:

- the Cartesian stiffness matrix \mathbf{K}_g is symmetric even under the effect of preloading due to any initial wrench \mathbf{W}_0 , as the matrix \mathbf{K}_f containing skew-symmetric terms is zero;
- the stiffness matrix is *block diagonal*, so $\mathbf{K}_{F,\phi} = \mathbf{K}_{M,p} = \mathbf{0}$. Thus the elastic equilibrium equation (6.2) can be *decoupled* between the rotational and translational degrees of freedom: a pure external force \mathbf{F}_e leads to a pure displacement $d\mathbf{p}$ and a pure external torque \mathbf{M}_e leads to a pure rotation $d\phi$. This does not hold in general for parallel manipulators: see for instance [8, 219], where it was shown that a symmetric stiffness matrix can be decoupled in this way with a coordinate change if and only if the coupling blocks $\mathbf{K}_{F,\phi} = \mathbf{K}_{M,p}^T$ are singular, which is not generally

6. Stiffness modeling and measuring

the case. See also [120], where the author showed that, for a generic symmetric stiffness matrix, $\mathbf{K}_{F,\phi}$ and $\mathbf{K}_{M,p}$ can be made diagonal (but still nonzero) with a coordinate change.

This shows that the given architecture leads to a simpler form of the stiffness matrix, for which the study of elastic equilibrium becomes easier.

6.2 Stiffness indexes

The aim of this section is to evaluate the stiffness of the manipulator throughout the workspace, thus checking where stiffness reaches its extreme values. For this, one needs to define an index which gives a measure of the global stiffness at a given pose. Based on the idea from [43], a distinction is made between rotational and translational DoFs, thus obtaining multiple indexes with physically consistent units. One can define the Cartesian *compliance* matrix as

$$\mathbf{G}_g = \mathbf{K}_g^{-1} = \begin{bmatrix} \mathbf{G}_{p,F} & \mathbf{G}_{p,M} \\ \mathbf{G}_{\phi,F} & \mathbf{G}_{\phi,M} \end{bmatrix} \quad (6.9)$$

This can be obtained by inverting matrix \mathbf{K}_g provided by Eq. (6.3)[‡]; alternatively, if there is no preloading, elastic compliance is easily found as $\mathbf{G}_g = \mathbf{K}_e^{-1} = \mathbf{J}\mathbf{K}_l^{-1}\mathbf{J}^T$ (inverting the diagonal matrix \mathbf{K}_l is computationally immediate and \mathbf{J} is already known from Ch. 5). Unless otherwise specified, matrices \mathbf{K}_g and \mathbf{G}_g are assumed to be invertible.

Using the compliance matrix, the displacement due to an external wrench can be found as:

$$d\mathbf{p} = \mathbf{G}_{p,F}\mathbf{F}_e + \mathbf{G}_{p,M}\mathbf{M}_e \quad (6.10a)$$

$$d\phi = \mathbf{G}_{\phi,F}\mathbf{F}_e + \mathbf{G}_{\phi,M}\mathbf{M}_e \quad (6.10b)$$

[‡] The blocks in Eq. (6.9) are *not*, in general, the inverses of the blocks in Eq. (6.1); for architecture \mathcal{L}_1 , however, $\mathbf{G}_{p,F} = \mathbf{K}_{F,p}^{-1}$ and $\mathbf{G}_{\phi,M} = \mathbf{K}_{M,\phi}^{-1}$, since the stiffness matrix is block diagonal.

(compare with Eq. (6.2)). Following the approach used in Ch. 5 (compare with Eq. (5.3)) the following indexes can now be proposed:

$$\kappa_{p,F,q,s} = \max_{\|\mathbf{F}_e\|_q=1} \|d\mathbf{p}\|_s \quad (\text{for } \mathbf{M}_e = \mathbf{0}) \quad (6.11a)$$

$$\kappa_{p,M,q,s} = \max_{\|\mathbf{M}_e\|_q=1} \|d\mathbf{p}\|_s \quad (\text{for } \mathbf{F}_e = \mathbf{0}) \quad (6.11b)$$

$$\kappa_{\phi,F,q,s} = \max_{\|\mathbf{F}_e\|_q=1} \|d\phi\|_s \quad (\text{for } \mathbf{M}_e = \mathbf{0}) \quad (6.11c)$$

$$\kappa_{\phi,M,q,s} = \max_{\|\mathbf{M}_e\|_q=1} \|d\phi\|_s \quad (\text{for } \mathbf{F}_e = \mathbf{0}) \quad (6.11d)$$

Substituting Eqs. (6.10) in the above definitions, one obtains more convenient expressions of the indexes as matrix norms[§]:

$$\kappa_{p,F,q,s} = \max_{\|\mathbf{F}_e\|_q=1} \|\mathbf{G}_{p,F}\mathbf{F}_e\|_s = \|\mathbf{G}_{p,F}\|_{q,s} \quad (6.12a)$$

$$\kappa_{p,M,q,s} = \max_{\|\mathbf{M}_e\|_q=1} \|\mathbf{G}_{p,M}\mathbf{M}_e\|_s = \|\mathbf{G}_{p,M}\|_{q,s} \quad (6.12b)$$

$$\kappa_{\phi,F,q,s} = \max_{\|\mathbf{F}_e\|_q=1} \|\mathbf{G}_{\phi,F}\mathbf{F}_e\|_s = \|\mathbf{G}_{\phi,F}\|_{q,s} \quad (6.12c)$$

$$\kappa_{\phi,M,q,s} = \max_{\|\mathbf{M}_e\|_q=1} \|\mathbf{G}_{\phi,M}\mathbf{M}_e\|_s = \|\mathbf{G}_{\phi,M}\|_{q,s} \quad (6.12d)$$

These indexes are defined based on the compliance matrix, unlike the stiffness indexes proposed in the previously cited works (see page 120): thus, the lower the indexes, the higher the robot's stiffness. For this, they can be more accurately called *compliance indexes*. From the definition of matrix norms, these indexes are nonnegative real numbers: a zero index is obtained only for an ideal rigidity.

The definition in Eqs. (6.11) are valid for any $\|\bullet\|_{q,s}$ -norm; practically, the most reasonable choice appears to be $q = s = 2$. In this way, the indexes define the effect of forces/torques of known maximum magnitude in terms of the magnitude of the corresponding displacement/rotation. From here onwards, then, it will be implicitly assumed that $q = s = 2$, and the subscripts q and s in the indexes will be dropped, to simplify notation. With these definitions,

[§] Note that, even if $\mathbf{G}_{p,M} = \mathbf{G}_{\phi,F}^T$, the indexes $\kappa_{p,M,q,s}$ and $\kappa_{\phi,F,q,s}$ may not be equal, as the norm of a matrix is in general not invariant after transposition.

6. Stiffness modeling and measuring

the indexes proposed here correspond to the inverses of the indexes proposed in [202], where said indexes were applied to the stiffness analysis of a planar manipulator (under the assumption of a symmetric stiffness matrix). Other dimensionally homogeneous indexes have been proposed in the past: for instance, Ref. [84] proposes the index $1/\sqrt[3]{\det \mathbf{G}_{p,F}}$, whereas in [106] the Frobenius norm of the same sub-block is used. Finally, in [200], the authors define translational and rotational stiffnesses as the 2-norms of the vectors that contain the eigenvalues of $\mathbf{K}_{F,p}$ and $\mathbf{K}_{M,\phi}$. However, these indexes lack an immediate physical interpretation, therefore they will not be employed here.

The compliance indexes used here share some of the desirable characteristics of the sensitivity indexes from [43]:

- They have a well-defined physical meaning: for example, suppose the external wrench acting on the platform is a pure force whose magnitude is known to be at most F_e . Then, the total displacement of the platform will be at most $\kappa_{p,F,q}F_e$ and the rotation angle will be at most $\kappa_{\phi,F,q}F_e$; a similar reasoning holds if the wrench is a pure torque. These upper limits on the displacement and the rotation angle are strict, so they cannot be replaced with smaller values.
- Each index is dimensionally consistent; for instance, the units of measure of $\kappa_{p,F,q}$ are a displacement divided by a force, which is coherent with measuring a linear compliance. Moreover, the indexes do not require arbitrary choices in their definition.

6.3 Application to robot A: stiffness maps

The stiffness indexes previously defined are applied to the translational 6-cable robot (again assuming constant orientation, as done in Sec. 5.4 for the kinematic indexes). These indexes are evaluated with the robot at different positions in the workspace, to identify zones where the stiffness can be dangerously low (compare with [69], where the indexes plotted across the workspace were the diagonal elements of matrix \mathbf{K}_g).

6.3. Application to robot A: stiffness maps

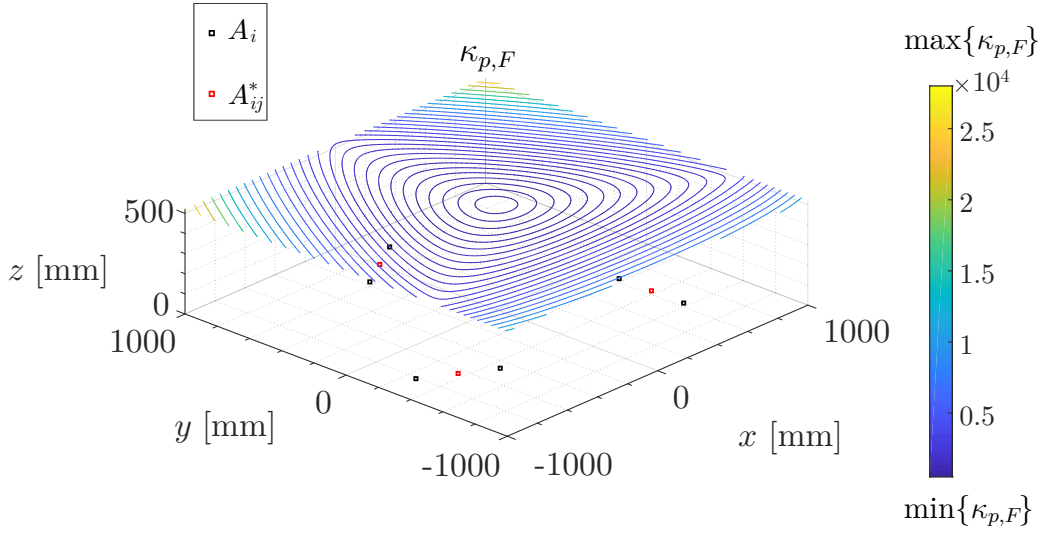


Figure 6.1: The stiffness index $\kappa_{p,F}$ for the 6-cable robot prototype, at a height $z_{opt,p} \approx 510\text{mm}$ (see Fig. 5.4a).

In the graphs presented hereafter, the preloading in the cables is set to zero: indeed, as the robot is not over-constrained, the preloading can only come from the gravitational force on the EE (which is considered to be in static conditions). Given that the weight of the EE is small, the effect of preloading forces can be safely disregarded. With the above assumption, $\mathbf{K}_g = \mathbf{K}_e$.

To calculate \mathbf{K}_g (and thus the compliance indexes), it is necessary to define the cable stiffnesses $k_i = (ES)/\rho_i$, which depend on the cable material and section. Unfortunately, as observed in [160], mechanical performance figures such as Young's modulus cannot be easily specified, especially for cables made by synthetic fibers. Due to the lack of available data, the product (ES) was set to 1 in arbitrary units. In any case, this does not change the qualitative behavior of compliance indexes: since \mathbf{K}_e depends linearly on the cable stiffnesses k_i (see Eq. (6.4)), multiplying all stiffness by a different value of (ES) implies dividing the indexes by the same value. Therefore, it is still possible to compare different robot poses or different architectures.

The results are shown in Figs. 6.1 and 6.2: as expected, the compliance is higher as the robot moves away from the center of the workspace. Therefore,

6. Stiffness modeling and measuring

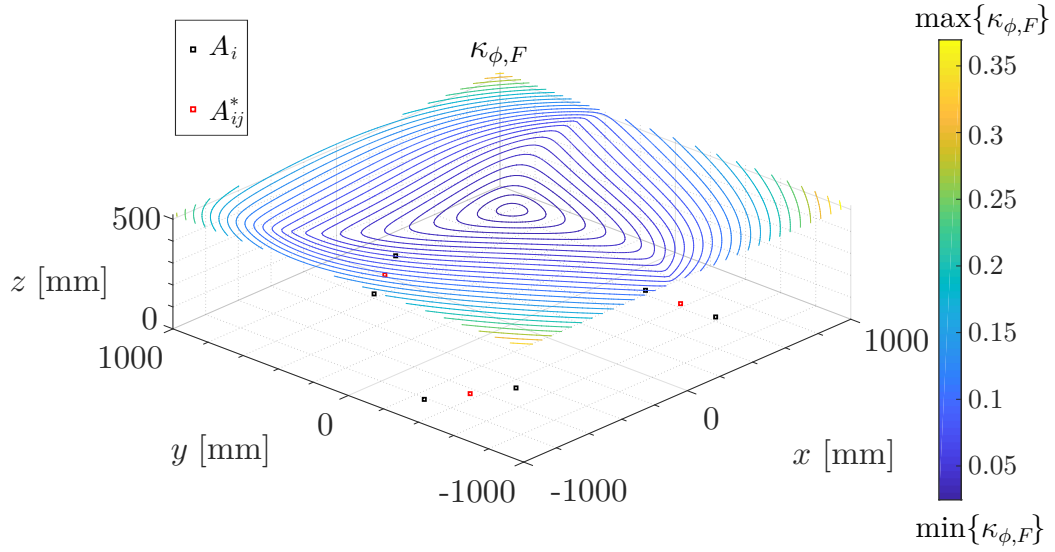


Figure 6.2: As in Fig. 6.1, for the stiffness index $\kappa_{\phi,M}$.

for accurate positioning of the EE, it is preferable to have the robot close to the center of the SEW. In this case, too, there is an apparent 120° symmetry in the plots of the indexes, which reflects the rotational symmetry of the robot architecture itself. Here, it was not necessary to compute the indexes $\kappa_{\phi,F}$ and $\kappa_{p,M}$: given that the prototype has architecture \mathcal{L}_1 , the stiffness matrices $\mathbf{K}_{\phi,F}$ and $\mathbf{K}_{p,M}$ are zero (see Sec. 6.1.1) and so are the corresponding matrices $\mathbf{G}_{\phi,F}$ and $\mathbf{G}_{p,M}$, therefore $\kappa_{\phi,F} = \kappa_{p,M} = 0$.

6.4 Summary of the chapter

This chapter presented the stiffness modeling of the translational cable robot studied in this thesis. Salient properties of the stiffness matrix were investigated and it was shown that the special architecture \mathcal{L}_1 introduced in Subsec. 1.5.2.1 leads to an especially simple stiffness model. This further justifies the interest in this architecture.

Compliance indexes have been proposed and their properties were briefly investigated; exemplifying plots of said indexes were provided, that show the variation of the indexes across the workspace, for the prototype used in the

tests.

As a note on future work, the behavior of the stiffness indexes nearby singularities ought to be investigated. Indeed, as noted in [83] for a Gough-Stewart platform with elastic legs, a singularity of the Jacobian matrix \mathbf{J} does not imply a singularity of the stiffness matrix \mathbf{K} , nor vice versa. Therefore, it would be interesting to define the conditions in which the stiffness indexes reach their minimum and maximum values (0 and ∞ , respectively) and analyze how such behavior is related to the various types of singularities defined in Ch. 4.

The stiffness indexes defined here could be also integrated in an architecture multi-objective optimization as outlined in Sec. 5.6, to improve the stiffness and the accuracy of the robot at the same time. It would be especially useful to evaluate how the stiffness indexes correlate with the accuracy indexes defined in Eqs. (5.3): if two of the indexes are found to be strongly correlated with each other, only one of them could be considered as an objective for optimization and the other one will be (almost) optimized as well. This would allow the dimensionality of the problem and thus its computational complexity to be reduced.

With the results from this chapter and the previous Ch. 5, goal (III) defined in Sec. 1.2 can be considered satisfied.

7

Conclusions

in which the usefulness of the work presented in this thesis, its potential applications and the opportunities for future work are summarized.

7.1 Conclusions

This thesis considered the dynamic behavior of cable-suspended parallel robots and the possibility of defining motions that allow them to move outside their static workspace, by taking advantage of the inertial and gravitational forces acting on the EE. While this opportunity has been explored before, in this work the goal was to expand the idea of dynamically feasible motions in order to make said trajectories more general and at the same time easier to apply in practice. Major limits for the practical applications of dynamic trajectories have been identified as the risk of kinematic singularities and cable interference. The kinematic accuracy and the effect of elastic deflections were also taken into account, by developing indexes that measure these properties across the workspace.

One of the guiding principles of this work was to use analytical methods as much as possible. In this way, the results provided by modeling can be presumably computed in real time and thus have a larger scope of application, e.g. if dynamic trajectories are to be applied in the recovery of cable robots after a cable failure, as suggested in Sec. 3.8. In these cases, the time required

7. Conclusions

to define a recovery strategy becomes of paramount importance, since a cable failure cannot be predicted. Moreover, providing analytical descriptions of the feasibility conditions can be useful to provide the designer with a clearer picture of the advantages and disadvantages of his/her design choices.

Throughout the thesis, two cable robots have been considered in particular: a 3-cable CSPR and a 6-cable robot. These models were chosen because, though simple, they include many of the issues encountered in the design of cable-actuated parallel manipulators. These two models are also linked, in the sense that the dynamic analysis of the simpler 3-cable robot can be extended to the more realistic model with 6 cables, provided that some conditions on the architecture are fulfilled. For the 6-cable robot, a number of special architectures with useful and distinctive features have been found.

A series of experimental tests with both a 3-cable and a 6-cable prototype confirmed the theoretical results: the robots can move inside and outside their respective SEWs while keeping the cables in tension. Moreover, for the translational robot, it was observed that the orientation remains stable when the robot moves, as desired.

7.2 Future work

While the work presented in this thesis can be seen as a useful advancement towards the understanding of CDPR dynamics and the application of dynamic effects in the control of cable-driven systems, a number of research questions remain open. Ideas for future work regarding the topics of single chapters have been outlined in Secs. 5.6 and 6.4.

A broader issue would be to generalize the motions defined in Ch. 3 to consider how to connect various trajectories (for instance, elliptical arcs such as those defined in Sec. 3.2) in a piecewise motion: this would be especially useful for pick-and-place operation, where point-to-point motions are commonly used. It would be especially useful to define trajectories that allow the robot to reach

points that are not coplanar (note that the elliptical trajectories defined in Sec. 3.2 are spatial motions that remain constrained in a plane).

One of the interesting features of the 6-DoF cable robot studied in this thesis is that its Jacobian can be written analytically. Therefore, it is possible to obtain the cable tensions in analytical form when the external force is known. It is conjectured that in this way one could generalize the method seen for the 3-cable robot in Sec. 3.4 and define general feasibility conditions for the translational cable robot, without any special condition on its architecture. Given the complexity of the analytical Jacobian, however, this appears a difficult task that is left as a future work.

In the thesis, cable tensions were assumed to never reach a dangerous level that could damage or break the cables and that the motors are always capable of providing the required tensions. Excessively high tensions could however become a problem if the robot moves with very high dynamics, such that the inertial force becomes substantial, or if the robot goes close to the singularity zone (for parallel systems, if the manipulator is close to a kinematic singularity of Type 2, the forces/torques in the actuators can become very high). Guaranteeing that maximum tensions are below a required threshold τ_{max} along a dynamic motion is left as a future work.

All robots considered in this work are fully-constrained, as for these systems the inverse dynamics problem becomes especially easy. Dynamically feasible trajectories for over-constrained systems were proposed in [178], while under-constrained systems were tackled in [91]. However, these works could be usefully extended with the methods presented in this thesis, to define a broader class of applicability for these trajectories.

Finally, it would be useful to consider the dynamic capabilities of the cable actuation systems: in the thesis it was assumed that these robots can reach any prescribed velocity/acceleration, while in fact any real motor has limits on its maximum speed and torque. Considering the complex interplay between the motions of all actuators, taking into account these effects requires defining

7. Conclusions

some measure of the maximum speed and acceleration that can be reached by the EE at each position, similar to what was done for traditional parallel mechanisms in [151]. This, too, is left as a future work.

A

Proofs

A.1 Proof of properties in Sec. 3.2.

Let $x'y'$ be a coordinate plane with origin O' in the center C of an ellipse and the coordinate axes directed along the principal axes (see Fig. A.1). The parametric equations of the ellipse in plane $x'y'$ are

$$\mathbf{p}' = \begin{bmatrix} x' \\ y' \\ z' \end{bmatrix} = \begin{bmatrix} A \cos(\psi) \\ B \sin(\psi) \\ 0 \end{bmatrix} \quad (\text{A.1})$$

with A, B being the semi-major and semi-minor axes.

By applying the coordinate transformation $\mathbf{p} = \mathbf{R}\mathbf{p}' + \mathbf{p}_C$, where $\mathbf{R} = (r_{ij}) \in \mathbb{R}^{3 \times 3}$ is the rotation matrix from $O'x'y'z'$ to $Oxyz$ and $\mathbf{p}_C = [x_C, y_C, z_C]^T$ is the position vector of C in $Oxyz$, one still obtains an ellipse, since this transformation corresponds to a rigid motion. From Eq. (A.1) the x coordinate can be expanded as

$$x = r_{11}A \cos(\psi) + r_{12}B \sin(\psi) + x_C \quad (\text{A.2})$$

An amplitude x_A and a phase angle ϕ_x are now defined as

$$\begin{aligned} x_A &= \sqrt{r_{11}^2 A^2 + r_{12}^2 B^2} \\ \phi_x &= \text{atan}_2 \left(\frac{r_{11}A}{x_A}, \frac{r_{12}B}{x_A} \right) \end{aligned} \quad (\text{A.3})$$

A. Proofs

and, by factoring x_A in Eq. (A.2), one obtains

$$\begin{aligned}
 x &= x_A \left[\frac{r_{11}A}{x_A} \cos(\omega t) + \frac{r_{12}B}{x_A} \sin(\omega t) \right] + x_C \\
 &= x_A [\sin(\phi_x) \cos(\omega t) + \cos(\phi_x) \sin(\omega t)] + x_C \\
 &= x_A \sin(\omega t + \phi_x) + x_C
 \end{aligned} \tag{A.4}$$

which is equivalent to the expression for x given by Eq. (3.1); the same proof applies for the y and z coordinates. Note that, by following the same steps backwards, it can also be shown that all trajectories defined by Eq. (3.1) are, indeed, ellipses.

It is also worth noting that, in Eq. (3.1), one could subtract a phase angle ϕ_d from each of the arguments of the sine functions and still obtain the same ellipse. For instance, by setting $\phi_d = \phi_x$, one obtains

$$\begin{bmatrix} x \\ y \\ z \end{bmatrix} = \begin{bmatrix} x_C \\ y_C \\ z_C \end{bmatrix} + \begin{bmatrix} x_A \sin(\psi) \\ y_A \sin(\psi - \phi_{xy}) \\ z_A \sin(\psi + \phi_{zx}) \end{bmatrix} \tag{A.5}$$

where ϕ_{xy} and ϕ_{zx} have been defined in Eqs. (3.15). Thus, $9 - 1 = 8$ independent parameters (two phase angles, the coordinates of center C and the three motion amplitudes x_A, y_A, z_A) are needed to geometrically define an elliptical trajectory, plus the frequency ω .

A.2 Proof of properties in Sec. 3.3

Here the results mentioned in Sec. 3.3 about the admissible zone for the center C of the trajectory will be proven.

To give the inequalities $\lambda_{zi} > 0$, $i \in \{1, 2, 3\}$ a geometric interpretation, consider for instance the first one: from the definitions in Eqs. (1.3), (3.2) and (3.3), one can obtain λ_{z1} as a function of C , namely

$$\lambda_{z1}(x_C, y_C) = y_{a23}x_C - x_{a23}y_C + (x_{a3}y_{a2} - x_{a2}y_{a3}) > 0 \tag{A.6}$$

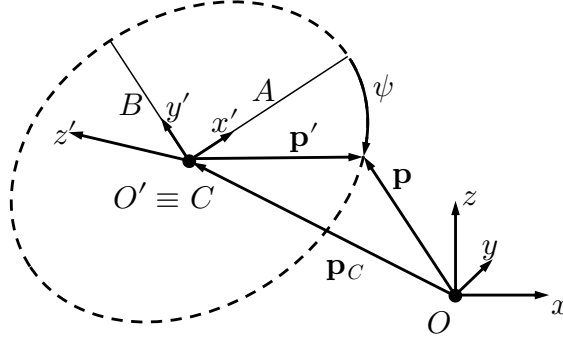


Figure A.1: Scheme of the ellipse in a “local” ($O'x'y'z'$) and “global” ($Oxyz$) coordinate frame.

This is recognized as a linear inequality in two variables defining a half-plane in the $x_C - y_C$ plane, the border of which is the line l_1 defined by $\lambda_{z1}(x_C, y_C) = 0$. One then finds that $\lambda_{z1}(x_{a2}, y_{a2}) = \lambda_{z1}(x_{a3}, y_{a3}) = 0$; moreover, $\lambda_{z1}(x_{a1}, y_{a1}) = -c > 0$. l_1 , then, passes through the projections of A_2 and A_3 on plane $x - y$ (which are vertexes of triangle T_{xy}) and the half plane defined by $\lambda_{z1} > 0$ contains the remaining vertex of T_{xy} (the projection of A_1), together with all points on the same side of said vertex with respect to l_1 .

Similar results can be found when checking that λ_{z2} and λ_{z3} are both greater than zero. The intersection of the three half-planes thus defined is the triangle T_{xy} ; if (x_C, y_C) is within T_{xy} , then, all three inequalities are satisfied.

A.3 Proof of properties in Sec. 3.5

First, it is useful to prove that

$$C_{i,v}D_{i,c} - C_{i,c}D_{i,v} = E_{i,a}E_{i,c} \quad (\text{A.7})$$

By substituting the definitions in Eq. (3.16) into Eq. (A.7), one finds, after some simplification,

$$\begin{aligned} C_{i,v}D_{i,c} - C_{i,c}D_{i,v} - E_{i,a}E_{i,c} &= -g_{x_A y_A}(\mathbf{v}_{kj} \cdot \boldsymbol{\lambda}_i) \sin(\phi_{xy}) \\ &= -g_{x_A y_A}[\mathbf{v}_{kj} \cdot (\mathbf{v}_{Cj} \times \mathbf{v}_{Ck})] \sin(\phi_{xy}) \end{aligned} \quad (\text{A.8})$$

A. Proofs

where the definition of $\boldsymbol{\lambda}_i$ from Eq. (3.3) was used in the last identity. Now, looking at the definitions in Eq. (3.2) and Eq. (1.3), it can be seen that the three vectors $\mathbf{v}_{kj} = \mathbf{a}_j - \mathbf{a}_k$, $\mathbf{v}_{Cj} = \mathbf{a}_j - \mathbf{p}_C$ and $\mathbf{v}_{Ck} = \mathbf{a}_k - \mathbf{p}_C$ are all contained in the same plane, passing through points C , A_j and A_k : thus, the triple vector product $\mathbf{v}_{kj} \cdot (\mathbf{v}_{Cj} \times \mathbf{v}_{Ck})$ is zero, which proves Eq. (A.7).

By substituting Eq. (3.19) into $\Delta_i = \beta_i^2 - \alpha_i \gamma_i$ as defined in Sec. 3.4, and simplifying, one obtains

$$\begin{aligned} \Delta_i &= (C_{i,v}^2 + D_{i,v}^2)E_{i,c}^2 - (C_{i,v}D_{i,c} - C_{i,c}D_{i,v})^2 \\ &= (C_{i,v}^2 + D_{i,v}^2 - E_{i,a}^2)E_{i,c}^2 = \gamma_{i,\ddot{\psi}}E_{i,c}^2 \end{aligned} \quad (\text{A.9})$$

where Eq. (A.7) has been used in the last equality. If the center C of the elliptical trajectory under consideration is in the SEW, then $\Delta_i > 0$ (see Sec. 3.4) and thus $\gamma_{i,\ddot{\psi}} = C_{i,v}^2 + D_{i,v}^2 - E_{i,a}^2 > 0$.

To prove that Ω_i is an ellipse in the $\ddot{\psi} - w$ plane, consider first its boundary $\partial\Omega_i$, as defined by $\alpha_i w^2 + 2\beta_i w + \gamma_i'(\ddot{\psi}) = \alpha_i w^2 + 2\beta_i w + \ddot{\psi}^2 \gamma_{i,\ddot{\psi}} + \gamma_i = 0$. This is a quadratic curve in the $\ddot{\psi} - w$ plane; to verify that it is an ellipse, it is useful to define

$$\begin{aligned} \Delta_{\Omega,i} &= \begin{vmatrix} \gamma_{i,\ddot{\psi}} & 0 & 0 \\ 0 & \alpha_i & \beta_i \\ 0 & \beta_i & \gamma_i \end{vmatrix} \\ J_{\Omega,i} &= \begin{vmatrix} \gamma_{i,\ddot{\psi}} & 0 \\ 0 & \alpha_i \end{vmatrix} \\ I_{\Omega,i} &= \gamma_{i,\ddot{\psi}} + \alpha_i \end{aligned} \quad (\text{A.10})$$

As known from plane geometry, Ω_i is an ellipse if and only if $\Delta_{\Omega,i} \neq 0$, $J_{\Omega,i} > 0$ and $\Delta_{\Omega,i}/I_{\Omega,i} < 0$. It is easy to see that $\Delta_{\Omega,i} = \gamma_{i,\ddot{\psi}}(\alpha_i \gamma_i - \beta_i^2) = -\gamma_{i,\ddot{\psi}}\Delta_i < 0$ since it has been assumed that the center of the trajectory is in the SEW, so that $\Delta_i > 0$ and consequently $\gamma_{i,\ddot{\psi}} > 0$.

Assume first $\alpha_i > 0$: in this case $J_{\Omega,i} = \gamma_{i,\ddot{\psi}}\alpha_i > 0$ and also $I_{\Omega,i} > 0$, so the conditions that define an ellipse are fulfilled.

If instead $\alpha_i = 0$ (remember that $\alpha_i \geq 0$), then $\beta_i = 0$, as stated in Sec. 3.4.

Also, recall that in this case the trajectory is contained in the plane through points C , A_j and A_k , so $E_{i,a} = \mathbf{v}_{kj} \cdot \mathbf{n}_e = 0$, since $\mathbf{v}_{kj} = \mathbf{a}_j - \mathbf{a}_k$ is contained in this plane while \mathbf{n}_e is the vector normal to the plane containing the trajectory. Thus, $\gamma_{i,\psi} = C_{i,v}^2 + D_{i,v}^2 - E_{i,a}^2 = \alpha_i - E_{i,a}^2 = 0$ and the condition that defines Ω_i degenerates to $\gamma_i < 0$: if this condition is satisfied, then Ω_i coincides with the whole plane $\ddot{\psi} - w$.

When $\ddot{\psi}$ becomes large enough, the admissible range of w degenerates into a single point; this happens for

$$\ddot{\psi}^2 = \ddot{\psi}_{i,e}^2 = \Delta_i / (\alpha_i \gamma_{i,\psi}) \quad (\text{A.11})$$

as can be seen by setting $\Delta'_i = \Delta_i - \alpha_i \ddot{\psi}^2 \gamma_{i,\psi} = 0$ and solving for $\ddot{\psi}^2$. The admissible area Ω_i is then contained within the limits $-\ddot{\psi}_{i,e} < \ddot{\psi} < \ddot{\psi}_{i,e}$.

It has been previously required (in Sec. 3.5) that $E_i > 0$; it can now be shown that this is in fact the case for every point in Ω_i . Indeed, Eq. (3.14) yields

$$E_i = E_{i,a} \ddot{\psi}^2 + E_{i,c} > 0 \Rightarrow \begin{cases} \ddot{\psi} > \ddot{\psi}_{i,l}, & E_{i,a} > 0 \\ \ddot{\psi} < \ddot{\psi}_{i,l}, & E_{i,a} < 0 \end{cases} \quad (\text{A.12})$$

with

$$\ddot{\psi}_{i,l} = -E_{i,c} / E_{i,a}, \quad \begin{cases} \ddot{\psi}_{i,l} < 0, & E_{i,a} > 0 \\ \ddot{\psi}_{i,l} > 0, & E_{i,a} < 0 \end{cases} \quad (\text{A.13})$$

Here, the property that $E_{i,c} = \lambda_{zi} g > 0$ when C is in the SEW (see Sec. 3.3) has been used. From Eqs. (A.12) and (A.13), it is found that if $|\ddot{\psi}| < |\ddot{\psi}_{i,l}|$ then $E_i > 0$, as desired. However, Ω_i is strictly contained in the range thus found, since $|\ddot{\psi}_{i,e}| < |\ddot{\psi}_{i,l}|$. This is seen by squaring both sides of the inequality and using the definitions from Eqs. (A.11) and (A.13):

$$\ddot{\psi}_{i,e}^2 < \ddot{\psi}_{i,l}^2 \Rightarrow \frac{\gamma_{i,\psi} E_{i,c}^2}{\gamma_{i,\psi} (C_{i,v}^2 + D_{i,v}^2)} < \frac{E_{i,c}^2}{E_{i,a}^2} \quad (\text{A.14})$$

where the equivalent definition of Δ_i from Eq. (A.9) and the definition of α_i from Eq. (3.19) have been used. After simplification, this finally reduces to $C_{i,v}^2 + D_{i,v}^2 - E_{i,a}^2 = \gamma_{i,\psi} > 0$, which has already been proved.

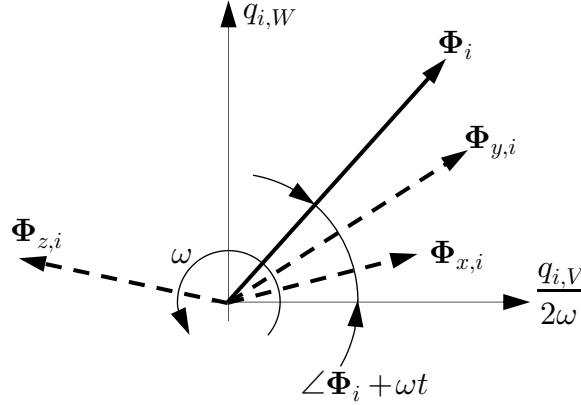


Figure A.2: The vectors $\Phi_{x,i}$, $\Phi_{y,i}$ and $\Phi_{z,i}$, with their sum Φ_i , rotate in the $q_{i,V}/(2\omega) - q_{i,W}$ plane at angular velocity ω .

A.4 Proof of properties in Subsec. 3.6.1

To find the extreme values of $q_{i,W}$ and $q_{i,V}$, which depend on t , remember that a sinusoidal function having frequency ω can be seen as the projection along a fixed line of a phase vector rotating with angular velocity ω . Note that $q_{i,W}$ and $q_{i,V}$ from Subsec. 3.6.1 are defined respectively as sums of sinusoidal and cosinusoidal functions (see Eq. (3.29), where λ_i is a constant vector, and $\mathbf{p}_d, \dot{\mathbf{p}}_d$ from Eq. (3.1) are respectively a sine and a cosine function of angle $\psi = \omega t$). Thus, they can be expressed as the projections of a rotating phase vector Φ_i along two orthogonal axes (here it is convenient to consider $q_{i,V}/(2\omega)$ instead of $q_{i,V}$ for dimensional homogeneity), with $\Phi_i = \Phi_{x,i} + \Phi_{y,i} + \Phi_{z,i}$ (see Fig. A.2) and where such vectors have the following magnitudes and phases:

$$\begin{aligned} \|\Phi_{x,i}\| &= |x_A \lambda_{xi}|, \quad \angle \Phi_{x,i} = \phi_x + \pi/2[1 + \text{sgn}(\lambda_{xi})] \\ \|\Phi_{y,i}\| &= |y_A \lambda_{yi}|, \quad \angle \Phi_{y,i} = \phi_y + \pi/2[1 + \text{sgn}(\lambda_{yi})] \\ \|\Phi_{z,i}\| &= |z_A \lambda_{zi}|, \quad \angle \Phi_{z,i} = \phi_z + \pi/2[1 + \text{sgn}(\lambda_{zi})] \end{aligned} \quad (\text{A.15})$$

(here, $\angle(\bullet)$ denotes the phase angle). Then one has $q_{i,V}/(2\omega) = \|\Phi_i\| \cos(\angle \Phi_i + \omega t)$ and $q_{i,W} = \|\Phi_i\| \sin(\angle \Phi_i + \omega t)$, which can be verified by substitution. From this, the extrema in Eq. (3.30) are proved.

The components of Φ_i , in the $q_{i,V}/(2\omega) - q_{i,W}$ plane, are respectively

$\|\Phi_{x,i}\| \cos(\angle \Phi_{x,i}) + \|\Phi_{y,i}\| \cos(\angle \Phi_{y,i}) + \|\Phi_{z,i}\| \cos(\angle \Phi_{z,i})$ and $\|\Phi_{x,i}\| \sin(\angle \Phi_{x,i}) + \|\Phi_{y,i}\| \sin(\angle \Phi_{y,i}) + \|\Phi_{z,i}\| \sin(\angle \Phi_{z,i})$; these are respectively $C_{i,a}$ and $D_{i,a}$, which again can be found by substitution. This proves Eq. (3.31).

A.5 Proof of properties in Sec. 5.3

It is known from the properties of vector q -norms that the following holds for any $\mathbf{x} \in \mathbb{R}^n$ [67, p. 69]:

$$0 \leq \|\mathbf{x}\|_2 / \sqrt{n} \leq \|\mathbf{x}\|_\infty \leq \|\mathbf{x}\|_2 \leq \|\mathbf{x}\|_\infty \sqrt{n} \quad (\text{A.16})$$

It then holds

$$\frac{\|\mathbf{J}\mathbf{x}\|_\infty}{\|\mathbf{x}\|_\infty} \leq \frac{\|\mathbf{J}\mathbf{x}\|_2}{\|\mathbf{x}\|_\infty} \leq \frac{\sqrt{m}\|\mathbf{J}\mathbf{x}\|_\infty}{\|\mathbf{x}\|_\infty} \quad (\text{A.17a})$$

$$\frac{\|\mathbf{J}\mathbf{x}\|_2}{\|\mathbf{x}\|_2} \leq \frac{\|\mathbf{J}\mathbf{x}\|_2}{\|\mathbf{x}\|_\infty} \leq \frac{\|\mathbf{J}\mathbf{x}\|_2}{\|\mathbf{x}\|_2 / \sqrt{n}} \quad (\text{A.17b})$$

respectively applying inequalities (A.16) on the numerator and on the denominator of $\|\mathbf{J}\mathbf{x}\|_2 / \|\mathbf{x}\|_\infty$ (for the second inequality in (A.17a), note that $\mathbf{J}\mathbf{x}$ has m terms).

The definition of subordinate matrix norms from [67, p. 72] is reported here:

$$\|\mathbf{J}\|_{q,s} = \sup_{\mathbf{x} \neq \mathbf{0}} \frac{\|\mathbf{J}\mathbf{x}\|_s}{\|\mathbf{x}\|_q}, \quad \mathbf{J} \in \mathbb{R}^{m \times n} \quad (\text{A.18})$$

Considering the supremum of each term in inequalities (A.17), the inequalities (5.7) are proven (to simplify notation, here $\|\bullet\|_{q,q}$ is noted $\|\bullet\|_q$).

Regarding the claims in Sec. 5.3 on the behavior of the indexes near singularities, the proof of the statements on page 104 is proven in the following (see Tab. A.1 for a diagram of the possible cases).

A. Proofs

$\exists \mathbf{f} \in \mathfrak{R}(\mathbf{F}_{x,p}) \cap \mathfrak{R}(\mathbf{F}_{x,\phi})$ $\mathbf{f} \neq \mathbf{0}$ (A)	$\mathfrak{R}(\mathbf{F}_{x,p}) \cap \mathfrak{R}(\mathbf{F}_{x,\phi}) = \{\mathbf{0}\}$ (B)		
$\sigma_{r,q,s} \rightarrow \infty, \sigma_{p,q,s} \rightarrow \infty$	$\text{rank}(\mathbf{F}_{x,\phi}) = 3$ (1)	$\text{rank}(\mathbf{F}_{x,\phi}) < 3$ (2)	
	$\text{rank}(\mathbf{F}_{x,p}) = 3$ (1)	$\sigma_{p,q,s}$ finite $\sigma_{r,q,s}$ finite	$\sigma_{p,q,s}$ finite $\sigma_{r,q,s} \rightarrow \infty$
	$\text{rank}(\mathbf{F}_{x,p}) < 3$ (2)	$\sigma_{p,q,s} \rightarrow \infty$ $\sigma_{r,q,s}$ finite	$\sigma_{p,q,s} \rightarrow \infty$ $\sigma_{r,q,s} \rightarrow \infty$

Table A.1: Schematic of the possibilities for a Type 2 singularity.

The possible cases are:

(A) There is a nonzero vector \mathbf{f} which belongs at the same time to $\mathfrak{R}(\mathbf{F}_{x,p})$ and to $\mathfrak{R}(\mathbf{F}_{x,\phi})$. In this case, there must be nonzero vectors $d\mathbf{p}, d\phi \in \mathbb{R}^3$ such that $\mathbf{f} = \mathbf{F}_{x,p}d\mathbf{p} = \mathbf{F}_{x,\phi}d\phi$; setting $d\mathbf{x} = [d\mathbf{p}^T \ d\phi^T]^T$, one has $\mathbf{F}_x d\mathbf{x} = \mathbf{f} - \mathbf{f} = \mathbf{0}$, so matrix \mathbf{F}_x clearly cannot have full column rank. Eq. (5.8) in general must have at least one solution $d\mathbf{p} = d\mathbf{p}_0$, $d\phi = d\phi_0$, $d\theta = d\theta_0$ having $d\theta_0 \neq \mathbf{0}$ (unless $\mathbf{F}_x = \mathbf{0}$, which is easily ruled out in practice). This equation can be normalized by dividing by $\|d\theta_0\|_q$: one has $\mathbf{F}_{x,p}d\hat{\mathbf{p}}_0 + \mathbf{F}_{x,\phi}d\hat{\phi}_0 = -\mathbf{F}_\theta d\hat{\theta}_0$, where $d\hat{\mathbf{p}}_0 = d\mathbf{p}_0/\|d\theta_0\|_q$, $d\hat{\phi}_0 = d\phi_0/\|d\theta_0\|_q$ and $d\hat{\theta}_0 = d\theta_0/\|d\theta_0\|_q$. The “base” solution defined by $d\hat{\mathbf{p}}_0$, $d\hat{\phi}_0$ and $d\hat{\theta}_0$ fulfills at the same time Eq. (5.8) and the condition $\|d\hat{\theta}_0\|_q = 1$. Combining this solution with the $d\mathbf{x}$ previously found, one gets $\mathbf{F}_{x,p}(d\hat{\mathbf{p}}_0 + \lambda d\mathbf{p}) + \mathbf{F}_{x,\phi}(d\hat{\phi}_0 - \lambda d\phi) = -\mathbf{F}_\theta d\hat{\theta}_0$, which is yet another solution of Eq. (5.8) that respects the bound on the norm of $d\theta$; note that λ can be any real number. In this case, the norm of the position displacement is $\|d\mathbf{p}\|_s = \|d\hat{\mathbf{p}}_0 + \lambda d\mathbf{p}\|_s \leq \|d\hat{\mathbf{p}}_0\|_s + \lambda \|d\mathbf{p}\|_s$, which can clearly be made as large as desired by taking a large enough λ : therefore, the translational sensitivity $\sigma_{p,q,s}$ goes to infinity. A similar reasoning holds for the translational sensitivity $\sigma_{r,q,s}$.

(B) The case in which the subspaces spanned respectively by the columns

of $\mathbf{F}_{x,p}$ and of $\mathbf{F}_{x,\phi}$ have no intersection (besides the null vector) can be subdivided in 4 sub-cases:

- (B.1.1) If both $\mathbf{F}_{x,p}$ and $\mathbf{F}_{x,\phi}$ have full rank, matrix $\mathbf{F}_x = \begin{bmatrix} \mathbf{F}_{x,p} & \mathbf{F}_{x,\phi} \end{bmatrix}$ also has full column rank and the robot is not in a Type 2 singularity; to see this, note that $\mathfrak{R}(\mathbf{F}_{x,p}) \cap \mathfrak{R}(\mathbf{F}_{x,\phi}) = \{\mathbf{0}\}$ implies $\text{rank}(\mathbf{F}_x) = \text{rank}(\mathbf{F}_{x,p}) + \text{rank}(\mathbf{F}_{x,\phi}) = 6$ [20, p. 121, Fact (2.11.4)]. Therefore, the sensitivity indexes can be written as matrix norms (see Eqs. (5.5)), as long as the robot is not redundantly-actuated.
- (B.1.2) If $\mathbf{F}_{x,\phi}$ has full rank, but $\mathbf{F}_{x,p}$ doesn't, one can find a vector $d\mathbf{p}^*$ for which $\mathbf{F}_{x,p}d\mathbf{p}^* = \mathbf{0}$. In general, it is possible to find at least one “base” solution $d\mathbf{p} = d\hat{\mathbf{p}}_0$, $d\phi = d\hat{\phi}_0$ and $d\theta = d\hat{\theta}_0$ for Eq. (5.8) that satisfies $\|d\hat{\theta}_0\|_q = 1$ (see previous point (A)). Combining this solution with $d\mathbf{p}^*$, an class of infinitely many solutions can be found in the form $\mathbf{F}_{x,p}(d\hat{\mathbf{p}}_0 + \lambda d\mathbf{p}^*) + \mathbf{F}_{x,\phi}d\hat{\phi}_0 = -\mathbf{F}_\theta d\hat{\theta}_0$ where the norm of the displacement $d\hat{\mathbf{p}}_0 + \lambda d\mathbf{p}^*$ can be made as large as desired: therefore, $\sigma_{p,q,s}$ tends to infinity in this case, too.

To see that $\sigma_{r,q,s}$ remains finite (even if the robot is in a singularity) consider again Eq. (5.8), rearrange and take the norm of both sides: one obtains $\|\mathbf{F}_\theta d\theta\|_s = \| -(-\mathbf{F}_{x,p}d\mathbf{p}) + \mathbf{F}_{x,\phi}d\phi \|_s$. It must be $\|\mathbf{F}_{x,\phi}d\phi - (-\mathbf{F}_{x,p}d\mathbf{p})\|_s \geq \|\mathbf{F}_{x,\phi}d\phi - (-\mathbf{F}_{x,p}d\mathbf{p})\|_2 / \sqrt{n}$ (where n is the number of rows in both $\mathbf{F}_{x,p}$ and $\mathbf{F}_{x,\phi}$): this can be proven from the general properties of matrix q -norms (see [20, p. 545, Eq. (9.1.6)] and [67, p. 69, Eq. (2.2.6)]. Now, vector $\mathbf{F}_{x,p}d\mathbf{p}$ belongs to the subspace $\mathfrak{R}(\mathbf{F}_{x,p})$, while in general vector $\mathbf{F}_{x,\phi}d\phi$ doesn't; call \mathbf{P}_p the *projector matrix* onto $\mathfrak{R}(\mathbf{F}_{x,p})$, a $n \times n$ symmetric matrix (which exists and is unique, see [20, p. 175, Fact (3.5.1)]) such that $\mathfrak{R}(\mathbf{P}_p) = \mathfrak{R}(\mathbf{F}_{x,p})$ and $\mathbf{P}_p\mathbf{P}_p = \mathbf{P}_p$. Then, $\|\mathbf{F}_{x,\phi}d\phi - (-\mathbf{F}_{x,p}d\mathbf{p})\|_2 \geq \|\mathbf{F}_{x,\phi}d\phi - \mathbf{P}_p\mathbf{F}_{x,\phi}d\phi\|_2$, as $\mathbf{P}_p\mathbf{F}_{x,\phi}d\phi$ is the best approximation to $\mathbf{F}_{x,\phi}d\phi$ over the subspace $\mathfrak{R}(\mathbf{F}_{x,p})$. Finally, the set of vectors $\mathbf{F}_\theta d\theta$

with $\|d\boldsymbol{\theta}\|_q = 1$ is bounded, as the set of possible $d\boldsymbol{\theta}$'s is itself bounded [20, p. 571, Fact (9.8.1)]: therefore, there exists an $f_{max} > 0$ such that $f_{max} \geq \|\mathbf{F}_\theta d\boldsymbol{\theta}\|_s$ for any $d\boldsymbol{\theta}$. Taken together, these facts imply $f_{max} \geq \|(\mathbf{F}_{x,\phi} - \mathbf{P}_p \mathbf{F}_{x,\phi}) d\boldsymbol{\phi}\|_2 / \sqrt{n}$. Suppose the matrix $\mathbf{F}_{x,\phi} - \mathbf{P}_p \mathbf{F}_{x,\phi}$ does not have full column rank: there must then be a nonzero vector $d\boldsymbol{\phi}^*$ such that $(\mathbf{F}_{x,\phi} - \mathbf{P}_p \mathbf{F}_{x,\phi}) d\boldsymbol{\phi}^* = \mathbf{0}$. However, this implies that the vector $\mathbf{F}_{x,\phi} d\boldsymbol{\phi}^*$ in the subspace $\mathfrak{R}(\mathbf{F}_{x,\phi})$ also belongs to $\mathfrak{R}(\mathbf{P}_p) = \mathfrak{R}(\mathbf{F}_{x,p})$, against the original assumption (B)—see again Tab. A.1. Therefore, $\mathbf{F}_{x,\phi} - \mathbf{P}_p \mathbf{F}_{x,\phi}$ has full rank and thus there exists a strictly positive real \hat{l} such that $\|(\mathbf{F}_{x,\phi} - \mathbf{P}_p \mathbf{F}_{x,\phi}) d\boldsymbol{\phi}\|_2 \geq \hat{l} \|d\boldsymbol{\phi}\|_2$ [20, p. 579, Fact (9.8.43)]. Finally, this proves that $f_{max} \sqrt{n} / \hat{l} \geq \|d\boldsymbol{\phi}\|_2$, so $\|d\boldsymbol{\phi}\|_2$ (and thus $\sigma_{r,q,s}$) remains bounded.

(B.2.1) If $\mathbf{F}_{x,p}$ has full rank, but $\mathbf{F}_{x,\phi}$ doesn't, then $\sigma_{r,q,s} \rightarrow \infty$ while $\sigma_{p,q,s}$ remains finite. The proof is conceptually identical to the one for case (B.1.2) and will not be repeated here.

(B.2.2) If $\mathbf{F}_{x,p}$ and $\mathbf{F}_{x,\phi}$ both have rank less than 3, a reasoning similar to the one seen for cases (A) and (B.1.2) shows that it is possible to find vectors in the form $d\hat{\mathbf{p}}_0 + \lambda d\mathbf{p}^*$ (where $d\hat{\mathbf{p}}_0$ is part of a “base” solution to Eq. (5.8), λ is any scalar and $d\mathbf{p}^*$ is in the kernel of $\mathbf{F}_{x,p}$) that have arbitrarily large norm. Therefore, $\sigma_{p,q,s} \rightarrow \infty$; similarly, one can prove that $\sigma_{r,q,s} \rightarrow \infty$.

A.6 Full expressions of quantities in Sec. 5.4

Here some of the variables from Sec. 5.4 will be defined. First, introduce

$$\boldsymbol{\lambda}_{e,ij} = \mathbf{e}_i \times \mathbf{e}_j, \quad \boldsymbol{\pi}_i = \mathbf{e}_i \times \mathbf{b}_i, \quad \boldsymbol{\pi}_{ij} = \boldsymbol{\pi}_i - \boldsymbol{\pi}_j \quad (\text{A.19})$$

from which one also gets

$$\det(\mathbf{M}_{sup}) = \det \left(\begin{bmatrix} \mathbf{e}_1 & \mathbf{e}_3 & \mathbf{e}_5 \end{bmatrix} \right) = \mathbf{e}_1 \times \mathbf{e}_3 \cdot \mathbf{e}_5 \quad (\text{A.20a})$$

$$\det(\mathbf{A}) = -\tau_{tot,12} \tau_{tot,34} \tau_{tot,56} \underbrace{\boldsymbol{\pi}_{12} \times \boldsymbol{\pi}_{34} \cdot \boldsymbol{\pi}_{56}}_{\boldsymbol{\pi}_A} \quad (\text{A.20b})$$

A.6. Full expressions of quantities in Sec. 5.4

so $\det(\mathbf{A}) = 0$ if and only if $\boldsymbol{\pi}_A = 0$, as stated in Sec. 5.4. Then, define

$$\mathbf{J}_{p,1} = + \boldsymbol{\lambda}_{e,51}(\boldsymbol{\pi}_{56} \cdot \boldsymbol{\pi}_3 \times \boldsymbol{\pi}_4) + \boldsymbol{\lambda}_{e,13}(\boldsymbol{\pi}_{34} \cdot \boldsymbol{\pi}_6 \times \boldsymbol{\pi}_5) \quad (\text{A.21a})$$

$$+ \boldsymbol{\lambda}_{e,35}(\boldsymbol{\pi}_2 \cdot \boldsymbol{\pi}_{56} \times \boldsymbol{\pi}_{34})$$

$$\mathbf{J}_{p,2} = - \mathbf{J}_{p,1} - \boldsymbol{\lambda}_{e,35}(\boldsymbol{\pi}_{12} \cdot \boldsymbol{\pi}_{56} \times \boldsymbol{\pi}_{34}) \quad (\text{A.21b})$$

$$\mathbf{J}_{p,3} = + \boldsymbol{\lambda}_{e,13}(\boldsymbol{\pi}_{12} \cdot \boldsymbol{\pi}_5 \times \boldsymbol{\pi}_6) + \boldsymbol{\lambda}_{e,35}(\boldsymbol{\pi}_{56} \cdot \boldsymbol{\pi}_2 \times \boldsymbol{\pi}_1) \quad (\text{A.21c})$$

$$+ \boldsymbol{\lambda}_{e,51}(\boldsymbol{\pi}_4 \cdot \boldsymbol{\pi}_{12} \times \boldsymbol{\pi}_{56})$$

$$\mathbf{J}_{p,4} = - \mathbf{J}_{p,3} - \boldsymbol{\lambda}_{e,51}(\boldsymbol{\pi}_{34} \cdot \boldsymbol{\pi}_{12} \times \boldsymbol{\pi}_{56}) \quad (\text{A.21d})$$

$$\mathbf{J}_{p,5} = + \boldsymbol{\lambda}_{e,35}(\boldsymbol{\pi}_{34} \cdot \boldsymbol{\pi}_1 \times \boldsymbol{\pi}_2) + \boldsymbol{\lambda}_{e,51}(\boldsymbol{\pi}_{12} \cdot \boldsymbol{\pi}_4 \times \boldsymbol{\pi}_3) \quad (\text{A.21e})$$

$$+ \boldsymbol{\lambda}_{e,13}(\boldsymbol{\pi}_6 \cdot \boldsymbol{\pi}_{34} \times \boldsymbol{\pi}_{12})$$

$$\mathbf{J}_{p,6} = - \mathbf{J}_{p,5} - \boldsymbol{\lambda}_{e,13}(\boldsymbol{\pi}_{56} \cdot \boldsymbol{\pi}_{34} \times \boldsymbol{\pi}_{12}) \quad (\text{A.21f})$$

and

$$\mathbf{J}_{r,1} = \boldsymbol{\pi}_{56} \times \boldsymbol{\pi}_{34}, \quad \mathbf{J}_{r,3} = \boldsymbol{\pi}_{12} \times \boldsymbol{\pi}_{56}, \quad \mathbf{J}_{r,5} = \boldsymbol{\pi}_{34} \times \boldsymbol{\pi}_{12} \quad (\text{A.22})$$

for the general case.

If P is on the midpoint of segments $\overline{B_i B_j}$, as in the special architecture \mathcal{L}_1 introduced in Sec. 1.5.2.1, it holds $\mathbf{b}_j = -\mathbf{b}_i$, so from (A.19) one has $\boldsymbol{\pi}_j = -\boldsymbol{\pi}_i$ and thus $\boldsymbol{\pi}_{ij} = 2\boldsymbol{\pi}_i$ and $\boldsymbol{\pi}_i \times \boldsymbol{\pi}_j = 0$ for each pair of cables i, j in the same parallelogram. Eqs. (A.21) and (A.22) simplify as

$$\mathbf{J}_{p,1} = -4\boldsymbol{\lambda}_{e,35}(\boldsymbol{\pi}_1 \cdot \boldsymbol{\pi}_5 \times \boldsymbol{\pi}_3) = \mathbf{J}_{p,2} \quad (\text{A.23a})$$

$$\mathbf{J}_{p,3} = -4\boldsymbol{\lambda}_{e,51}(\boldsymbol{\pi}_3 \cdot \boldsymbol{\pi}_1 \times \boldsymbol{\pi}_5) = \mathbf{J}_{p,4} \quad (\text{A.23b})$$

$$\mathbf{J}_{p,5} = -4\boldsymbol{\lambda}_{e,13}(\boldsymbol{\pi}_5 \cdot \boldsymbol{\pi}_3 \times \boldsymbol{\pi}_1) = \mathbf{J}_{p,6} \quad (\text{A.23c})$$

and

$$\mathbf{J}_{r,1} = 4\boldsymbol{\pi}_5 \times \boldsymbol{\pi}_3, \quad \mathbf{J}_{r,3} = 4\boldsymbol{\pi}_1 \times \boldsymbol{\pi}_5, \quad \mathbf{J}_{r,5} = 4\boldsymbol{\pi}_3 \times \boldsymbol{\pi}_1 \quad (\text{A.24})$$

Also, from (A.20), one gets $\boldsymbol{\pi}_A = 8\boldsymbol{\pi}_1 \times \boldsymbol{\pi}_3 \cdot \boldsymbol{\pi}_5$. One can also define matrix $\check{\mathbf{A}} = [\boldsymbol{\pi}_1, \boldsymbol{\pi}_3, \boldsymbol{\pi}_5]$, from which the rotational kinematic sensitivity for architecture \mathcal{L}_1 (as seen in Sec. 5.4) can be derived.

A.7 Proof of properties in Sec. 5.4

Regarding the computation of $\sigma_{p,\infty,2} = \max \|\mathbf{J}_p d\boldsymbol{\theta}\|_2$ (for $\|d\boldsymbol{\theta}\|_\infty = 1$) for special architecture \mathcal{L}_1 (see page 107), recall that the maximum of $\|\mathbf{J}_p d\boldsymbol{\theta}\|_2$ must occur for a vector $d\boldsymbol{\theta}$ whose entries are all equal to either $+1$ or -1 , that is, $d\boldsymbol{\theta} \in \{-1, 1\}^6$. Multiplying the second matrix in Eq. (5.10a) for any such vector, the resultant is a 3×1 vector whose entries are any combination (with repetitions) $+2, 0$ or -2 ; considering the $1/2$ factor in (5.10a), one then seeks the maximum of $\|\mathbf{M}_{sup}^{-T} d\boldsymbol{\theta}\|_2$ for $d\boldsymbol{\theta} \in \{-1, 0, 1\}^3$. Since this set contains $\{-1, 1\}^3$, where the maximum value $\|\mathbf{M}_{sup}^{-T}\|_{\infty,2}$ of $\|\mathbf{M}_{sup}^{-T} d\boldsymbol{\theta}\|_2$ must occur for $\|d\boldsymbol{\theta}\|_\infty = 1$, it follows $\sigma_{p,\infty,2} = \|\mathbf{J}_p\|_{\infty,2} = \|\mathbf{M}_{sup}^{-T}\|_{\infty,2}$, as desired; a similar reasoning applies to $\sigma_{r,\infty,2} = \|\mathbf{J}_r\|_{\infty,2} = \|\check{\mathbf{A}}^{-T}\|_{\infty,2}$.

The decoupling between rotational and translational singularities can be explained in a geometrical fashion, as follows.

- If P is on Π , the equivalent 3-cable robot with attachment points in A_{ij}^* (Sec. 2.3) is in a singular position, with all three cables in the same plane Π : thus, it can have an infinitesimal translation $d\mathbf{p}$ in a direction normal to Π without changing the cable lengths and $\sigma_{p,q,s}$ tends to infinity. However, the rotation is still controlled, as the three vectors \mathbf{n}_{ij} are in general not coplanar in this configuration (Sec. 4.2): therefore, $\sigma_{r,q,s}$ is finite.
- If $\det(\mathbf{A}) = 0$, so that P is on Σ , then $\sigma_{r,q,s} \rightarrow \infty$, as expected: there is an uncontrolled rotation $d\boldsymbol{\phi}$ even when the cable lengths are fixed. Still, the behavior of $\sigma_{p,q,s}$ ought to be explained.

First, consider a point O on the EE in the plane Π_{ij} through one of the parallelograms (Fig. A.3). The line r_O parallel to the vectors of cable direction $\mathbf{e}_i = \mathbf{e}_j$ and passing through O meets the segment $\overline{B_i B_j}$ at point B_O . Due to the geometry of the parallelogram leg, B_O , as all points on $\overline{B_i B_j}$, has a velocity \mathbf{v}_{B_O} whose component $\mathbf{v}_{B_O \Pi}$ in Π_{ij} is normal to \mathbf{e}_i ; the component of \mathbf{v}_{B_O} not contained in this plane will be denoted as $\mathbf{v}_{B_O, n}$ and is normal to Π_{ij} (and thus to \mathbf{e}_i , which is in Π_{ij}). Thus, $\mathbf{v}_{B_O} =$

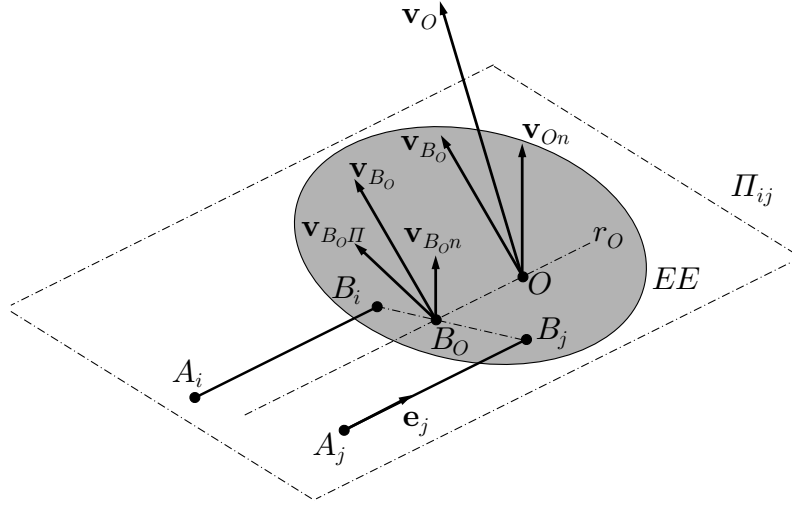


Figure A.3: A section (in gray) of the EE through plane Π_{ij} containing one parallelogram. Point O is on the EE, on line r_O (parallel to cables $i - j$).

$\mathbf{v}_{B_{On}} + \mathbf{v}_{B_{O\Pi}}$ is normal to \mathbf{e}_i , since it is the sum of two components that are both normal to \mathbf{e}_i . Since the attachment points B_i can be modeled as spherical joints, O can only rotate around $\overline{B_i B_j}$, so the relative velocity \mathbf{v}_{O_n} of O with respect to B_O is normal to Π_{ij} and thus to \mathbf{e}_i . The absolute velocity $\mathbf{v}_O = \mathbf{v}_{O_n} + \mathbf{v}_{B_O}$ of O , being the sum of two velocities both normal to \mathbf{e}_i , has thus zero component along the direction of the cables.

This goes to show that any point on the EE in one of the planes Π_{ij} has zero velocity along the corresponding vector \mathbf{e}_i . Consider now the point P : for architecture \mathcal{L} , P is on $\overline{B_1 B_2}$, $\overline{B_3 B_4}$ and $\overline{B_5 B_6}$ and thus on the intersection of Π_{12} , Π_{34} and Π_{56} . P must have zero velocity along $\mathbf{e}_1 = \mathbf{e}_2$, $\mathbf{e}_3 = \mathbf{e}_4$ and $\mathbf{e}_5 = \mathbf{e}_6$: these three vectors span the whole of \mathbb{R}^3 (unless they are coplanar, in which case $\mathbf{M}_{sup} = 0$ and the robot is in the translational singularity seen in Sec. 4.2) and therefore P has zero velocity. This goes to show that in a rotational singularity, a robot with architecture \mathcal{L} can have no translation if the cables are kept at a constant length: therefore, $\sigma_{p,q,s}$ is finite.

It will now be proven that, as stated on page 107, the index $\sigma_{r,\infty,2}$ reaches its smallest value when the distances $b_i = \|\mathbf{b}_i\|_2$ from P to B_i are at their

A. Proofs

largest value, for any robot pose. First, notice that the norm of vectors $\boldsymbol{\pi}_i$ from Eqs. (A.19) can be written as

$$\pi_i = \|\mathbf{e}_i \times \mathbf{b}_i\|_2 = \underbrace{\|\mathbf{e}_i\|_2}_{=1} \|\mathbf{b}_i\|_2 \sin(\angle(\mathbf{e}_i, \mathbf{b}_i)) = b_i \sin(\angle(\mathbf{e}_i, \mathbf{b}_i)) \quad (\text{A.25})$$

where $\angle(\mathbf{e}_i, \mathbf{b}_i)$ is the angle between vectors \mathbf{e}_i and \mathbf{b}_i (which clearly does not depend on b_i). The inverse transpose of matrix $\check{\mathbf{A}} = [\pi_1 \hat{\boldsymbol{\pi}}_1 \quad \pi_3 \hat{\boldsymbol{\pi}}_3 \quad \pi_5 \hat{\boldsymbol{\pi}}_5]$ (where $\hat{\boldsymbol{\pi}}_i = \boldsymbol{\pi}_i/\pi_i$) can then be written as a function of lengths b_i , namely $\check{\mathbf{A}}^{-T}(b_1, b_3, b_5) = [\mathbf{l}_1/b_1 \quad \mathbf{l}_3/b_3 \quad \mathbf{l}_5/b_5]$, where vectors \mathbf{l}_i are as follows:

$$\mathbf{l}_i = \frac{\hat{\boldsymbol{\pi}}_m \times \hat{\boldsymbol{\pi}}_k}{\det([\hat{\boldsymbol{\pi}}_1 \quad \hat{\boldsymbol{\pi}}_3 \quad \hat{\boldsymbol{\pi}}_5]) \sin(\angle(\mathbf{e}_i, \mathbf{b}_i))} \quad (\text{A.26})$$

where indexes i, m and k permute as in Eq. (2.16). The aspect to note here is that vectors \mathbf{l}_i do not depend on b_i .

It remains to be proven that the norm of matrix $\check{\mathbf{A}}^{-T}$ has a minimum when the distances b_i are at their maximum. For this, it will first be proven that, for any $\mathbf{A}, \mathbf{B} \in \mathbb{R}^{n \times n}$ and all $q, s, t \in [1, \infty]$, it holds

$$\|\mathbf{AB}\|_{q,t} \leq \|\mathbf{A}\|_{s,t} \|\mathbf{B}\|_{q,s} \quad (\text{A.27})$$

Indeed, this is a direct consequence of a known result of induced norms [20, p. 553, Eq. (9.4.5)].

Now, consider the rotational sensitivity when all b_i 's in $\check{\mathbf{A}}^{-T}$ are set to their maximum value b_{max} , which in general depends on size and weight considerations (assuming this maximum value is the same for b_1, b_3 and b_5). Since it holds $\check{\mathbf{A}}^{-T}(b_{max}, b_{max}, b_{max}) = \check{\mathbf{A}}^{-T}(b_1, b_3, b_5) \text{diag}([b_1/b_{max}, b_3/b_{max}, b_5/b_{max}])$, applying the inequality in (A.27)—with $q = \infty, s = \infty, t = 2$ —one obtains $\|\check{\mathbf{A}}^{-T}(b_{max}, b_{max}, b_{max})\|_{\infty,2} \leq \|\check{\mathbf{A}}^{-T}(b_1, b_3, b_5)\|_{\infty,2} \max\{b_1/b_{max}, b_3/b_{max}, b_5/b_{max}\} \leq \|\check{\mathbf{A}}^{-T}(b_1, b_3, b_5)\|_{\infty,2} = \sigma_{r,\infty,2}$ (the second inequality follows from the fact that $b_i/b_{max} \in [0, 1]$). Therefore, $\|\check{\mathbf{A}}^{-T}(b_{max}, b_{max}, b_{max})\|_{\infty,2}$ is the minimum value of the rotational sensitivity, as it was required to prove.

Regarding the claim on the sub-indexes introduced in page 108, a more general property will be proven here: for any $\mathbf{J} = [\mathbf{J}_s^T \quad \mathbf{J}_i^T]^T$, where $\mathbf{J}_s \in$

$\mathbb{R}^{m_s \times n}$, $\mathbf{J}_i \in \mathbb{R}^{m_i \times n}$, it holds

$$\max\{\|\mathbf{J}_s\|_{\infty,2}, \|\mathbf{J}_i\|_{\infty,2}\} \leq \|\mathbf{J}\|_{\infty,2} \leq \sqrt{\|\mathbf{J}_s\|_{\infty,2}^2 + \|\mathbf{J}_i\|_{\infty,2}^2} \quad (\text{A.28})$$

of which inequalities (5.11) are direct consequences. Moreover, Eq. (A.28) also correlates the index μ_{max} from [151] to the general indexes proposed in this thesis: from the respective definitions in Eqs. (5.2) and (5.3), it also follows $\max\{\sigma_{r,\infty,2}, \sigma_{p,\infty,2}\} \leq \mu_{max} \leq \sqrt{\sigma_{r,\infty,2}^2 + \sigma_{p,\infty,2}^2}$.

To prove inequalities (A.28), first notice that, for any $d\boldsymbol{\theta} \in \mathbb{R}^n$,

$$\|\mathbf{J}d\boldsymbol{\theta}\|_2 = \left\| \begin{bmatrix} \mathbf{J}_s d\boldsymbol{\theta} \\ \mathbf{0} \end{bmatrix} + \begin{bmatrix} \mathbf{0} \\ \mathbf{J}_i d\boldsymbol{\theta} \end{bmatrix} \right\|_2 \quad (\text{A.29})$$

Using the fact that the two vectors in the second term are orthogonal (as their dot product is zero) and from the properties of the Euclidean norm [20, p. 564, Eq. *viii*)], it then follows

$$\|\mathbf{J}d\boldsymbol{\theta}\|_2 = \sqrt{\|\mathbf{J}_s d\boldsymbol{\theta}\|_2^2 + \|\mathbf{J}_i d\boldsymbol{\theta}\|_2^2} \quad (\text{A.30})$$

Now, the norm $\|\mathbf{J}\|_{\infty,2}$ is the maximum value of $\|\mathbf{J}d\boldsymbol{\theta}^*\|_2$, achieved at some $m \times 1$ vector $d\boldsymbol{\theta}^*$ (with $m = m_s + m_i$) for which $\|d\boldsymbol{\theta}^*\|_{\infty} = 1$. From (A.30), it follows $\|\mathbf{J}d\boldsymbol{\theta}^*\|_2 = \sqrt{\|\mathbf{J}_s d\boldsymbol{\theta}^*\|_2^2 + \|\mathbf{J}_i d\boldsymbol{\theta}^*\|_2^2} \leq \sqrt{\|\mathbf{J}_s\|_{\infty,2}^2 + \|\mathbf{J}_i\|_{\infty,2}^2}$ (using the fact that $\|\mathbf{J}_s d\boldsymbol{\theta}^*\|_2 \leq \|\mathbf{J}_s\|_{\infty,2}$ and $\|\mathbf{J}_i d\boldsymbol{\theta}^*\|_2 \leq \|\mathbf{J}_i\|_{\infty,2}$, for any $d\boldsymbol{\theta}^*$ having $\|d\boldsymbol{\theta}^*\|_{\infty} = 1$). The second inequality in (A.28) then follows. To prove the first inequality, notice that it must be $\|\mathbf{J}_s\|_{\infty,2} = \|\mathbf{J}_s d\boldsymbol{\theta}_s^*\|_2$ for some $d\boldsymbol{\theta}_s^*$ having $\|d\boldsymbol{\theta}_s^*\|_{\infty} = 1$. Then, again by (A.30), it must be $\|\mathbf{J}d\boldsymbol{\theta}_s^*\|_2 = \sqrt{\|\mathbf{J}_s d\boldsymbol{\theta}_s^*\|_2^2 + \|\mathbf{J}_i d\boldsymbol{\theta}_s^*\|_2^2} \geq \|\mathbf{J}_s d\boldsymbol{\theta}_s^*\|_2 = \|\mathbf{J}_s\|_{\infty,2}$. Since, for any $d\boldsymbol{\theta}_s^*$ having unitary ∞ -norm, it holds $\|\mathbf{J}\|_{\infty,2} \geq \|\mathbf{J}d\boldsymbol{\theta}_s^*\|_2$, it follows $\|\mathbf{J}\|_{\infty,2} \geq \|\mathbf{J}_s\|_{\infty,2}$; the fact that $\|\mathbf{J}\|_{\infty,2} \geq \|\mathbf{J}_i\|_{\infty,2}$ can be proved analogously.

List of figures

Figure 1.1	A comparison of serial and parallel robots.	4
Figure 1.2	Schematic of the robot.	15
Figure 1.3	Schematic of a 3-DoF spatial CSPR and the corresponding auxiliary vectors.	23
Figure 1.4	A 6-cable CDPR with 3 translational DoFs.	25
Figure 1.5	The planar parallelogram formed by cables i and j	26
Figure 1.6	A general schematic of the possible special architectures for the translational robot.	28
Figure 2.1	The planar parallelogram formed by cables i and j (cf. Fig. 1.5).	33
Figure 2.2	Scheme of the special architecture.	37
Figure 3.1	Schematic of a 3-DoF spatial CSPR and the corresponding auxiliary vectors.	44
Figure 3.2	An elliptical trajectory to be performed by one of the example robot architectures.	52
Figure 3.3	The cable tensions divided by the mass of the end effector during one period of the trajectory.	53
Figure 3.4	A 3D view of a base elliptical trajectory and a scaled version with the same center C . The SEW is also highlighted.	53
Figure 3.5	Plot of the three different frequency ranges (one for each cable).	54

List of figures

Figure 3.6	Plane $\ddot{\psi} - \dot{\psi}^2$ with the three ellipses Ω_i , rectangle R_ψ and curve Γ_ψ	55
Figure 3.7	Trajectory of the robot during the experiments: first part in attached video, simple harmonic elliptical trajectory. . .	68
Figure 3.8	Cable tensions along a spatial trajectory.	68
Figure 3.9	Plot of the position error $\ d\mathbf{p}\ $ along part (i) of the motion.	69
Figure 3.10	A schematic of the robot in the reference pose, a view of the prototype and a photo of one of the winches.	70
Figure 3.11	(a): 3D plot of the periodic motion. (b): 3D plot of the point-to-point motion.	71
Figure 3.12	Plot of the position error along the harmonic and along the point-to-point motion.	72
Figure 3.13	Yaw, pitch and roll angles of the robot, with respect to the start position along a circular horizontal motion. . . .	74
Figure 4.1	The singularity surface Σ for a translational cable-suspended robot with a general architecture.	84
Figure 4.2	A simplified architecture, with the spools of cables 1-2 and 3-4 having parallel axes.	86
Figure 4.3	A simplified architecture with lines A_1A_2 , A_3A_4 and A_5A_6 parallel to the plane Π through A_{12}^* , A_{34}^* and A_{56}^*	88
Figure 4.4	Static-equilibrium workspace and reachable workspace for the robot used in the experiment described in Subsec. 3.7.2.	89
Figure 5.1	A small displacement $d\mathbf{p}$ and a small rotation $d\phi$ expressed in two different coordinate frames.	103
Figure 5.2	The translational kinematic sensitivity $\sigma_{p,\infty,2}$ calculated at a reference height z_r	105
Figure 5.3	Same as Fig. 5.2, but for the rotational kinematic sensitivity $\sigma_{r,\infty,2}$	106

Figure 5.5	The translational kinematic sensitivity for the 6-cable robot prototype, at a height $z_{opt,p}$	110
Figure 5.6	As in Fig. 5.5, for the rotational sensitivity.	111
Figure 5.7	Plot of the position error $\ d\mathbf{p}\ _2$ for the translational cable robot during a periodic motion.	112
Figure 6.1	The stiffness index $\kappa_{p,F}$ for the 6-cable robot prototype, at a height $z_{opt,p} \approx 510\text{mm}$ (see Fig. 5.4a).	129
Figure 6.2	As in Fig. 6.1, for the stiffness index $\kappa_{\phi,M}$	130
Figure A.1	Scheme of the ellipse in a “local” ($O'x'y'z'$) and “global” ($Oxyz$) coordinate frame.	139
Figure A.2	The vectors $\Phi_{x,i}$, $\Phi_{y,i}$ and $\Phi_{z,i}$, with their sum Φ_i , rotate in the $q_{i,V}/(2\omega) - q_{i,W}$ plane at angular velocity ω	142
Figure A.3	A section (in gray) of the EE through plane Π_{ij} containing one parallelogram.	149

List of video attachments

The video attachments are available at the links below.

Video #	Link	Page
1	https://www.youtube.com/watch?v=14TUFrG0Zk0	66
2	https://bit.ly/2N4xL1o	69

List of symbols and acronyms

List of Symbols

Symbol	Description
\mathcal{L}	A special robot architecture in which the CoM P is on segments $\overline{B_1B_2}$, $\overline{B_3B_4}$ and $\overline{B_5B_6}$ through the mobile cable attachment points (Subsec. 1.5.2.1)
\mathcal{L}_1	A special case of architecture \mathcal{L} where the CoM P is on the <i>midpoint</i> of segments $\overline{B_iB_j}$ (Subsec. 1.5.2.1)
\mathcal{L}_2	A further specialization of architecture \mathcal{L}_1 where all three segments $\overline{B_1B_2}$, $\overline{B_3B_4}$ and $\overline{B_5B_6}$ have the same length (Subsec. 1.5.2.1)
\mathcal{R}	A special robot architecture in which the three vectors \mathbf{d}_{12} , \mathbf{d}_{34} and \mathbf{d}_{56} are parallel to the plane Π through points A_{12}^* , A_{34}^* and A_{56}^* (Subsec. 1.5.2.2)
\mathcal{R}_1	A special case of architecture \mathcal{R}_1 in which all the fixed attachment points A_i are coplanar (Subsec. 1.5.2.2)
\mathcal{LR}	The final architecture chosen for the prototype, an combination of the conditions for both architecture \mathcal{L}_2 and \mathcal{R}_1 (Subsec. 1.5.2.3)

List of Acronyms

Acronym	Description
AGV	Automated Guided Vehicle
CDPR	Cable-Driven Parallel Robot
CoM	Center of Mass
CSPR	Cable-Suspended Parallel Robot
DGP	Direct Geometrico-static Problem

List of Acronyms

Acronym	Description
DKP	Direct-Kinematics Problem
DoF	Degree of Freedom
EE	End-Effector
IGP	Inverse Geometrico-static Problem
IKP	Inverse-Kinematics Problem
IMU	Inertial Measurement Unit
ODE	Ordinary Differential Equation
OP	Operation Point
RMS	Root Mean Square
RW	Reachable Workspace
SEW	Static Equilibrium Workspace
VJM	Virtual Joint Method
WCW	Wrench-Closure Workspace
WFW	Wrench-Feasible Workspace

Acknowledgments

I would like to extend my sincere thanks to my supervisor, Prof. Marco Carri-cato, who guided my work during the three years of my PhD and shared with me his great technical and professional expertise.

I must also thank Prof. Vincenzo Parenti Castelli as the coordinator of the GRAB (Group of Robotics, Automation and Articular Biomechanics) at the University of Bologna, where I have spent my PhD studentship, and the other esteemed researchers at GRAB (prof. Rocco Vertechy, asst. prof. Nicola Sancisi, dr. Michele Conconi) who have provided me with valuable suggestions about my work.

I must also thank prof. Paolo Negrini of the Department of Mathematics at the University of Bologna for enlightening conversations about the mathematical aspects of my work, especially on the matrix norms discussed on Ch. 5.

Special thanks also go to my colleagues Chen, Claudio, Edoardo, Francesco, Giacomo, Giulio, Luca, Stefano and Troy, with whom I have worked these years.

I would like to thank my colleagues, the other PhD students at the Department of Industrial Engineering at the University of Bologna, for suggestions and for the opportunity of sharing our ideas.

During my PhD, I have spent a period of study abroad at Université Laval (Québec, Canada), under the supervision of Prof. Clément Gosselin, who has given me the opportunity to further my research in an international context and has provided me with his valuable guidance: I take the opportunity to thank him here. Of the team at the Laboratoire de Robotique at Université Laval, I would especially like to thank Prof. Xiaoling Jiang for her insightful remarks on the dynamics of cable-suspended robots, Mr. Simon Foucault and Mr. Jordan Longval for their help during the experimental campaign detailed

Acknowledgments

in Sec. 3.7, Mr. André Gallant for his help on the video editing (see page 157) and Dr. Dinh-Son Vu for helpful discussions on the general setup of the translational cable robot and on the issue of cable interference (Sec. 4.4). My thanks also go to all the other colleagues and friends at the Laboratoire de Robotique who have given me precious ideas and suggestions.

I must also mention Mr. Emanuele Dall’Ospedale and Mrs. Elena Stagni for technical and editorial support during the thesis writing process.

Finally, my gratitude goes to my family and all my friends, for their support throughout my studies.

Copyright notice

Some of the images and content presented in Chapters 2 to 4 have been reprinted with permission from:

- Springer Nature Customer Service Centre GmbH: Springer, *Cable-Driven Parallel Robots - Proceedings of the Third International Conference on Cable-Driven Parallel Robots*, “Dynamically-Feasible Elliptical Trajectories for Fully Constrained 3-DOF Cable-Suspended Parallel Robots”, G. Mottola, C. Gosselin and M. Carricato, © (2018), (doi: https://doi.org/10.1007/978-3-319-61431-1_19) [136]
- American Society of Mechanical Engineers (ASME): ASME, *Journal of Mechanisms and Robotics*, “Dynamically Feasible Periodic Trajectories for Generic Spatial Three-Degree-of-Freedom Cable-Suspended Parallel Robots”, G. Mottola, C. Gosselin and M. Carricato, volume 10, number 3, © (2018), (doi: https://doi.org/10.1007/978-3-319-61431-1_19) [137]
- Elsevier: *Mechanism and Machine Theory*, “Dynamically feasible motions of a class of purely-translational cable-suspended parallel robots”, G. Mottola, C. Gosselin and M. Carricato, volume 132, © (2019), (doi: <https://doi.org/10.1016/j.mechmachtheory.2018.10.017>) [138]

In reference to Springer Nature GmbH, ASME and Elsevier copyrighted

material which is used with permission in this thesis, Springer Nature GmbH, ASME and Elsevier do not endorse any of the University of Bologna's products or services.

Giovanni Mottola

Bologna, Italy

February 13, 2019

References

- [1] G. Abbasnejad and M. Carricato. Direct geometrico-static problem of underconstrained cable-driven parallel robots with n cables. *IEEE Trans. Robot.*, 31(2):468–478, 2015. doi:[10.1109/TRO.2015.2393173](https://doi.org/10.1109/TRO.2015.2393173).
- [2] J. Albus, R. Bostelman, and N. Dagalakis. The NIST Robocrane. *J. of Rob. Syst.*, 10(5):709–724, 1993. doi:[10.1002/rob.4620100509](https://doi.org/10.1002/rob.4620100509).
- [3] G. Alici and B. Shirinzadeh. Enhanced stiffness modeling, identification and characterization for robot manipulators. *IEEE Trans. Robot.*, 21(4): 554–564, 2005. doi:[10.1109/TRO.2004.842347](https://doi.org/10.1109/TRO.2004.842347).
- [4] A. Alikhani, S. Behzadipour, S. Vanini, and A. Alasty. Workspace analysis of a three DOF cable-driven mechanism. *ASME J. Mech. Rob.*, 1(4):041005, 2009. doi:[10.1115/1.3204255](https://doi.org/10.1115/1.3204255).
- [5] A. Alikhani, S. Behzadipour, A. Alasty, and S. Vanini. Design of a large-scale cable-driven robot with translational motion. *Robotics and Computer-Integrated Manufacturing*, 27(2):357–366, 2011. doi:[10.1016/j.rcim.2010.07.019](https://doi.org/10.1016/j.rcim.2010.07.019).
- [6] B. An, J. Kim, and F. C. Park. An adaptive stepsize RRT planning algorithm for open-chain robots. *IEEE Robot. Autom. Lett.*, 3(1):312–319, 2018. doi:[10.1109/LRA.2017.2745542](https://doi.org/10.1109/LRA.2017.2745542).
- [7] J. Angeles. The design of isotropic manipulator architectures in the presence of redundancies. *Int. J. Rob. Res.*, 11(3):196–201, 1992. doi:[10.1177/027836499201100303](https://doi.org/10.1177/027836499201100303).
- [8] J. Angeles. On the nature of the Cartesian stiffness matrix. *Ingeniería mecánica, tecnología y desarrollo*, 3(5):163–170, 2010. doi:[10.1007/s11465-010-0023-z](https://doi.org/10.1007/s11465-010-0023-z).

References

- [9] M. Arsenault and C. M. Gosselin. Kinematic, static and dynamic analysis of a planar 2-DOF tensegrity mechanism. *Mech. Mach. Theory*, 41(9): 1072–1089, 2006. doi:[10.1016/j.mechmachtheory.2005.10.014](https://doi.org/10.1016/j.mechmachtheory.2005.10.014).
- [10] M. Bamdad, F. Taheri, and N. Abtahi. Dynamic analysis of a hybrid cable-suspended planar manipulator. In *Proc. of the IEEE 2015 ICRA*, pages 1621–1626, Seattle, USA, 2015. doi:[10.1109/ICRA.2015.7139405](https://doi.org/10.1109/ICRA.2015.7139405).
- [11] L. Barbazza, F. Oscari, S. Minto, and G. Rosati. Trajectory planning of a suspended cable driven parallel robot with reconfigurable end effector. *Robotics and Computer-Integrated Manufacturing*, 48:1–11, 2017. doi:[10.1016/j.rcim.2017.02.001](https://doi.org/10.1016/j.rcim.2017.02.001).
- [12] L. Barbazza, D. Zanotto, G. Rosati, and S. K. Agrawal. Design and optimal control of an underactuated cable-driven micro-macro robot. *IEEE Robot. Autom. Lett.*, 2(2):896–903, 2017. doi:[10.1109/LRA.2017.2651941](https://doi.org/10.1109/LRA.2017.2651941).
- [13] E. Barnett and C. M. Gosselin. Large-scale 3D printing with a cable-suspended robot. *Additive Manufacturing*, 7:27–44, 2015. doi:[10.1016/j.addma.2015.05.001](https://doi.org/10.1016/j.addma.2015.05.001).
- [14] G. Barrette and C. M. Gosselin. Determination of the dynamic workspace of cable-driven planar parallel mechanisms. *ASME J. Mech. Des.*, 127(2):242–248, 2005. doi:[10.1115/1.1830045](https://doi.org/10.1115/1.1830045).
- [15] S. Behzadipour and A. Khajepour. A new cable-based parallel robot with three degrees of freedom. *Multibody System Dynamics*, 13(4):371–383, 2005. doi:[10.1007/s11044-005-3985-6](https://doi.org/10.1007/s11044-005-3985-6).
- [16] S. Behzadipour and A. Khajepour. Cable-based robot manipulators with translational degrees of freedom. In *Industrial Robotics: Theory, Modelling and Control*, pages 211–236. IntechOpen, 2006. doi:[10.5772/5035](https://doi.org/10.5772/5035).
- [17] S. Behzadipour and A. Khajepour. Stiffness of cable-based parallel manipulators with application to stability analysis. *ASME J. Mech. Des.*, 128(1):303–310, 2006. doi:[10.1115/1.2114890](https://doi.org/10.1115/1.2114890).

-
- [18] S. Behzadipour and M. Azadi Sohi. Antagonistic stiffness in cable-driven mechanisms. In *Proc. of the 2007 IFToMM World Congress*, Besançon, France, 2007.
- [19] S. Behzadipour, R. Dekker, A. Khajepour, and E. Chan. DeltaBot: a new cable-based ultra high speed robot. In *Proc. of the ASME 2003 IMECE*, pages 533–537, Washington D.C., USA, 2003. doi:[10.1115/IMECE2003-41470](https://doi.org/10.1115/IMECE2003-41470).
- [20] D. S. Bernstein. *Matrix mathematics: theory, facts, and formulas*. Princeton University Press, 2009.
- [21] A. Berti, M. Gouttefarde, and M. Carricato. Dynamic recovery of cable-suspended parallel robots after a cable failure. In J. Lenarčič and J.-P. Merlet, editors, *Advances in Robot Kinematics*, pages 337–344. Springer International Publishing, Grasse, France, 2016. doi:[10.1007/978-3-319-56802-7_35](https://doi.org/10.1007/978-3-319-56802-7_35).
- [22] A. Berti, J.-P. Merlet, and M. Carricato. Solving the direct geometrico-static problem of underconstrained cable-driven parallel robots by interval analysis. *Int. J. Rob. Res.*, 35(6):723–739, 2016. doi:[10.1177/0278364915595277](https://doi.org/10.1177/0278364915595277).
- [23] S. Bhattacharya, H. Hatwal, and A. Ghosh. On the optimum design of Stewart platform type parallel manipulators. *Robotica*, 13(2):133–140, 1995. doi:[10.1017/S026357470001763X](https://doi.org/10.1017/S026357470001763X).
- [24] L. Biagiotti and C. Melchiorri. *Trajectory planning for automatic machines and robots*. Springer Science & Business Media, 2008. doi:[10.1007/978-3-540-85629-0](https://doi.org/10.1007/978-3-540-85629-0).
- [25] L. Blanchet and J.-P. Merlet. Interference detection for cable-driven parallel robots (CDPRs). In *2014 IEEE/ASME Int. Conf. on Advanced Intelligent Mechatronics*, pages 1413–1418, Besançon, France, 2014. doi:[10.1109/AIM.2014.6878280](https://doi.org/10.1109/AIM.2014.6878280).
-

References

- [26] H. L. Bodlaender, P. Gritzmann, V. Klee, and J. Van Leeuwen. Computational complexity of norm-maximization. *Combinatorica*, 10(2):203–225, 1990. doi:[10.1007/BF02123011](https://doi.org/10.1007/BF02123011).
- [27] C. Bonivento, A. Eusebi, C. Melchiorri, M. Montanari, and G. Vassura. WireMan: a portable wire manipulator for touch-rendering of bas-relief virtual surfaces. In *Proc. of the 8th Int. Conf. on Advanced Robotics*, pages 13–18, Monterey, USA, 1997. doi:[10.1109/ICAR.1997.620155](https://doi.org/10.1109/ICAR.1997.620155).
- [28] P. H. Borgstrom, N. P. Borgstrom, M. J. Stealey, B. Jordan, G. S. Sukhatme, M. A. Batalin, and W. J. Kaiser. Design and implementation of NIMS3D, a 3-D cabled robot for actuated sensing applications. *IEEE Trans. Robot.*, 25(2):325–339, 2009. doi:[10.1109/TRO.2009.2012339](https://doi.org/10.1109/TRO.2009.2012339).
- [29] G. Boschetti, C. Passarini, and A. Trevisani. A strategy for moving cable driven robots safely in case of cable failure. In G. Boschetti and A. Gasparetto, editors, *Advances in Italian Mechanism Science*, volume 47 of *Mechanisms and Machine Science*, pages 203–211. Springer, Vicenza, Italy, 2017. doi:[10.1007/978-3-319-48375-7_22](https://doi.org/10.1007/978-3-319-48375-7_22).
- [30] P. Bosscher and I. Ebert-Uphoff. Wrench-based analysis of cable-driven robots. In *Proc. of the IEEE 2004 ICRA*, volume 5, pages 4950–4955, New Orleans, USA, 2004. doi:[10.1109/ROBOT.2004.1302502](https://doi.org/10.1109/ROBOT.2004.1302502).
- [31] P. Bosscher, R. Williams, and M. Tummino. A concept for rapidly-deployable cable robot search and rescue systems. In *Proc. of the ASME 2005 IDETC/CIE*, pages 589–598, Long Beach, USA, 2005. doi:[10.1115/DETC2005-84324](https://doi.org/10.1115/DETC2005-84324).
- [32] P. Bosscher, A. Riechel, and I. Ebert-Uphoff. Wrench-feasible workspace generation for cable-driven robots. *IEEE Trans. Robot.*, 22(5):890–902, 2006. doi:[10.1109/TRO.2006.878967](https://doi.org/10.1109/TRO.2006.878967).
- [33] P. Bosscher, R. Williams, L. Bryson, and D. Castro-Lacouture. Cable-suspended robotic contour crafting system. *Automation in construction*, 17(1):45–55, 2007. doi:[10.1016/j.autcon.2007.02.011](https://doi.org/10.1016/j.autcon.2007.02.011).

-
- [34] R. Bostelman, A. Jacoff, and R. Bunch. Delivery of an advanced double-hull ship welding system using robocrane. In *3rd international ICSC IIA/SOCO*, 1999.
- [35] R. V. Bostelman, J. S. Albus, R. E. Graham, and G. Pilgrim. Robocrane and EMMA applied to waste storage tank remediation. In *American Nuclear Society 7th Topical Meeting on Robotics and Remote Systems*, volume 2, pages 708–713, Augusta, USA, 1997.
- [36] S. Bouchard, C. M. Gosselin, and B. Moore. On the ability of a cable-driven robot to generate a prescribed set of wrenches. *ASME J. Mech. Rob.*, 2(1):011010, 2010. doi:[10.1115/1.4000558](https://doi.org/10.1115/1.4000558).
- [37] B. Bounab. Multi-objective optimal design based kineto-elastostatic performance for the DELTA parallel mechanism. *Robotica*, 34(2):258–273, 2016. doi:[10.1017/S0263574714001416](https://doi.org/10.1017/S0263574714001416).
- [38] S. Briot and V. Arakelian. Optimal force generation in parallel manipulators for passing through the singular positions. *Int. J. Rob. Res.*, 27(8):967–983, 2008. doi:[10.1177/0278364908094403](https://doi.org/10.1177/0278364908094403).
- [39] T. Bruckmann, W. Lalo, K. Nguyen, and B. Salah. Development of a storage retrieval machine for high racks using a wire robot. In *Proc. of the ASME 2012 IDETC/CIE*, pages 771–780, Chicago, USA, 2012. doi:[10.1115/DETC2012-70389](https://doi.org/10.1115/DETC2012-70389).
- [40] M. Callegari and M. Tarantini. Kinematic analysis of a novel translational platform. *ASME J. Mech. Des.*, 152(2):308–315, 2003. doi:[10.1115/1.1563637](https://doi.org/10.1115/1.1563637).
- [41] P. Campbell, P. Swaim, and C. J. Thompson. CharlotteTM robot technology for space and terrestrial applications. *SAE transactions*, pages 641–648, 1995.
- [42] G. Carbone and M. Ceccarelli. Comparison of indices for stiffness performance evaluation. *Frontiers of Mech. Eng. in China*, 5(3):270–278, 2010. doi:[10.1007/s11465-010-0023-z](https://doi.org/10.1007/s11465-010-0023-z).
-

References

- [43] P. Cardou, S. Bouchard, and C. Gosselin. Kinematic-sensitivity indices for dimensionally nonhomogeneous Jacobian matrices. *IEEE Trans. Robot.*, 26(1):166–173, 2010. doi:[10.1109/TRO.2009.2037252](https://doi.org/10.1109/TRO.2009.2037252).
- [44] M. Carricato. Direct geometrico-static problem of underconstrained cable-driven parallel robots with three cables. *ASME J. Mech. Rob.*, 5(3):031008, 2013. doi:[10.1115/1.4024293](https://doi.org/10.1115/1.4024293).
- [45] M. Carricato. Inverse geometrico-static problem of underconstrained cable-driven parallel robots with three cables. *ASME J. Mech. Rob.*, 5(3):031002, 2013. doi:[10.1115/1.4024291](https://doi.org/10.1115/1.4024291).
- [46] M. Carricato and J.-P. Merlet. Stability analysis of underconstrained cable-driven parallel robots. *IEEE Trans. Robot.*, 29(1):288–296, 2013. doi:[10.1109/TRO.2012.2217795](https://doi.org/10.1109/TRO.2012.2217795).
- [47] M. Carricato and V. Parenti Castelli. Singularity-free fully-isotropic translational parallel mechanisms. *Int. J. Rob. Res.*, 21(2):161–174, 2002. doi:[10.1177/027836402760475360](https://doi.org/10.1177/027836402760475360).
- [48] M. Carricato and V. Parenti Castelli. On the topological and geometrical synthesis and classification of translational parallel mechanisms. In *11th World Congress in Mechanism and Machine Science*, pages 1624–1628, Tianjin, China, 2004.
- [49] G. Castelli, E. Ottaviano, and P. Rea. A Cartesian cable-suspended robot for improving end-users’ mobility in an urban environment. *Robotics and Computer-Integrated Manufacturing*, 30(3):335–343, 2014. doi:[10.1016/j.rcim.2013.11.001](https://doi.org/10.1016/j.rcim.2013.11.001).
- [50] R. Clavel. Device for the movement and positioning of an element in space, 1990. URL patents.google.com/patent/US4976582A.
- [51] M. Conconi and M. Carricato. A new assessment of singularities of parallel kinematic chains. *IEEE Trans. Robot.*, 25(4):757–770, 2009. doi:[10.1109/TRO.2009.2020353](https://doi.org/10.1109/TRO.2009.2020353).

-
- [52] L. L. Cone. Skycam-an aerial robotic camera system. *Byte*, 10(10), 1985.
- [53] E. Courteille, D. Deblaise, and P. Maurine. Design optimization of a Delta-like parallel robot through global stiffness performance evaluation. In *Proc. of the IEEE/RSJ 2009 IROS*, pages 5159–5166, 2009. doi:[10.1109/IROS.2009.5353906](https://doi.org/10.1109/IROS.2009.5353906).
- [54] D. Cunningham and H. H. Asada. The Winch-Bot: A cable-suspended, under-actuated robot utilizing parametric self-excitation. In *Proc. of the IEEE 2009 ICRA*, pages 1844–1850, Kobe, Japan, 2009. doi:[10.1109/ROBOT.2009.5152378](https://doi.org/10.1109/ROBOT.2009.5152378).
- [55] N. Dagalakis, J. Albus, B. Wang, J. Unger, and J. Lee. Stiffness study of a parallel link robot crane for shipbuilding applications. *ASME J. Offshore Mech. Arct. Eng.*, 111(3):183–193, 1989. doi:[10.1115/1.3257146](https://doi.org/10.1115/1.3257146).
- [56] K. Deb. *Multi-objective optimization using evolutionary algorithms*. Wiley, 2005.
- [57] X. Diao and O. Ma. Vibration analysis of cable-driven parallel manipulators. *Multibody System Dynamics*, 21(4):347–360, 2009. doi:[10.1007/s11044-008-9144-0](https://doi.org/10.1007/s11044-008-9144-0).
- [58] P. Dietmaier. The Stewart-Gough platform of general geometry can have 40 real postures. In J. Lenarčič and M. L. Husty, editors, *Advances in Robot Kinematics: Analysis and Control*, pages 7–16. Springer, Salzburg, Austria, 1998. doi:[10.1007/978-94-015-9064-8_1](https://doi.org/10.1007/978-94-015-9064-8_1).
- [59] P. Dion-Gauvin and C. M. Gosselin. Trajectory planning for the static to dynamic transition of point-mass cable-suspended parallel mechanisms. *Mech. Mach. Theory*, 113:158–178, 2017. doi:[10.1016/j.mechmachtheory.2017.03.003](https://doi.org/10.1016/j.mechmachtheory.2017.03.003).
- [60] P. Dion-Gauvin and C. M. Gosselin. Dynamic point-to-point trajectory planning of a three-DOF cable-suspended mechanism using the hypocycloid curve. *IEEE Trans. Mechatronics*, 34(3):1–10, 2018. doi:[10.1109/TMECH.2018.2840051](https://doi.org/10.1109/TMECH.2018.2840051).
-

References

- [61] I. Ebert-Uphoff and P. A. Voglewede. On the connections between cable-driven robots, parallel manipulators and grasping. In *Proc. of the IEEE 2004 ICRA*, volume 5, pages 4521–4526, New Orleans, USA, 2004. doi:[10.1109/ROBOT.2004.1302430](https://doi.org/10.1109/ROBOT.2004.1302430).
- [62] B. El-Khasawneh and P. Ferreira. Computation of stiffness and stiffness bounds for parallel link manipulators. *Int. J. Mach. Tools*, 39(2):321–342, 1999. doi:[10.1016/S0890-6955\(98\)00039-X](https://doi.org/10.1016/S0890-6955(98)00039-X).
- [63] S. Fang, D. Franitza, M. Torlo, F. Bekes, and M. Hiller. Motion control of a tendon-based parallel manipulator using optimal tension distribution. *IEEE Trans. Mechatronics*, 9(3):561–568, 2004. doi:[10.1109/TMECH.2004.835336](https://doi.org/10.1109/TMECH.2004.835336).
- [64] L. Gagliardini, S. Caro, M. Gouttefarde, and A. Girin. Discrete reconfiguration planning for cable-driven parallel robots. *Mech. Mach. Theory*, 100:313–337, 2016. doi:[10.1016/j.mechmachtheory.2016.02.014](https://doi.org/10.1016/j.mechmachtheory.2016.02.014).
- [65] Z. Gao, D. Zhang, and Y. Ge. Design optimization of a spatial six degree-of-freedom parallel manipulator based on artificial intelligence approaches. *Robotics and Computer-Integrated Manufacturing*, 26(2):180–189, 2010. doi:[10.1016/j.rcim.2009.07.002](https://doi.org/10.1016/j.rcim.2009.07.002).
- [66] M. Gobbi, G. Mastinu, and G. Previati. A method for measuring the inertia properties of rigid bodies. *Mechanical Systems and Signal Processing*, 25(1):305–318, 2011. doi:[10.1016/j.mechmachtheory.2005.10.014](https://doi.org/10.1016/j.mechmachtheory.2005.10.014).
- [67] G. Golub and C. Van Loan. *Matrix computations*. Johns Hopkins University Press, 2013.
- [68] J. Gorman, K. Jablokow, and D. Cannon. The cable array robot: theory and experiment. In *Proc. of the IEEE 2001 ICRA*, volume 3, pages 2804–2810, Seoul, South Korea, 2001. doi:[10.1109/ROBOT.2001.933047](https://doi.org/10.1109/ROBOT.2001.933047).
- [69] C. M. Gosselin. Stiffness mapping for parallel manipulators. *IEEE Trans. Robot. Autom.*, 6(3):377–382, 1990. doi:[10.1109/70.56657](https://doi.org/10.1109/70.56657).

-
- [70] C. M. Gosselin. The optimum design of robotic manipulators using dexterity indices. *Robotics and Autonomous Systems*, 9(4):213–226, 1992. doi:[10.1016/0921-8890\(92\)90039-2](https://doi.org/10.1016/0921-8890(92)90039-2).
- [71] C. M. Gosselin. Global planning of dynamically feasible trajectories for three-DOF spatial cable-suspended parallel robots. In T. Bruckmann and A. Pott, editors, *Cable-Driven Parallel Robots*, pages 3–22. Springer, Stuttgart, Germany, 2013. doi:[10.1007/978-3-642-31988-4_1](https://doi.org/10.1007/978-3-642-31988-4_1).
- [72] C. M. Gosselin. Cable-driven parallel mechanisms: state of the art and perspectives. *Mechanical Engineering Reviews*, 1(1), 2014. doi:[10.1299/mer.2014dsm0004](https://doi.org/10.1299/mer.2014dsm0004).
- [73] C. M. Gosselin, P. Ren, and S. Foucault. Dynamic trajectory planning of a two-dof cable-suspended parallel robot. In *Proc. of the IEEE 2012 ICRA*, pages 1476–1481, Saint Paul, USA, 2012. doi:[10.1109/ICRA.2012.6224683](https://doi.org/10.1109/ICRA.2012.6224683).
- [74] C. M. Gosselin and J. Angeles. Singularity analysis of closed-loop kinematic chains. *IEEE Trans. Robot.*, 6(3):281–290, 1990. doi:[10.1109/70.56660](https://doi.org/10.1109/70.56660).
- [75] C. M. Gosselin and S. Foucault. Dynamic point-to-point trajectory planning of a two-DOF cable-suspended parallel robot. *IEEE Trans. Robot.*, 30(3):728–736, 2014. doi:[10.1109/TRO.2013.2292451](https://doi.org/10.1109/TRO.2013.2292451).
- [76] VE Gough. Universal tyre test machine. In *Proc. of the FISITA 9th Int. Technical Congress*, pages 117–137, London, 1962, 1962.
- [77] M. Gouttefarde and C. M. Gosselin. Analysis of the wrench-closure workspace of planar parallel cable-driven mechanisms. *IEEE Trans. Robot.*, 22(3):434–445, 2006. doi:[10.1109/TRO.2006.870638](https://doi.org/10.1109/TRO.2006.870638).
- [78] M. Gouttefarde, J.-P. Merlet, and D. Daney. Determination of the wrench-closure workspace of 6-DOF parallel cable-driven mechanisms. In J. Lenarčič and B. Roth, editors, *Advances in Robot Kinematics*, pages
-

References

- 315–322. Springer, Ljubljana, Slovenia, 2006. doi:[10.1007/978-1-4020-4941-5_34](https://doi.org/10.1007/978-1-4020-4941-5_34).
- [79] M. Gouttefarde, D. Daney, and J.-P. Merlet. Interval-analysis-based determination of the wrench-feasible workspace of parallel cable-driven robots. *IEEE Trans. Robot.*, 27(1):1–13, 2011. doi:[10.1109/TRO.2010.2090064](https://doi.org/10.1109/TRO.2010.2090064).
- [80] M. Gouttefarde, J.-F. Collard, N. Riehl, and C. Baradat. Geometry selection of a redundantly actuated cable-suspended parallel robot. *IEEE Trans. Robot.*, 31(2):501–510, 2015. doi:[10.1109/TRO.2015.2400253](https://doi.org/10.1109/TRO.2015.2400253).
- [81] R. Di Gregorio. Determination of singularities in Delta-like manipulators. *Int. J. Rob. Res.*, 23(1):89–96, 2004. doi:[10.1177/0278364904039689](https://doi.org/10.1177/0278364904039689).
- [82] R. Di Gregorio and V. Parenti Castelli. Mobility analysis of the 3-UPU parallel mechanism assembled for a pure translational motion. *ASME J. Mech. Des.*, 124(2):259–264, 2002. doi:[10.1115/1.1471530](https://doi.org/10.1115/1.1471530).
- [83] M. Griffis and J. Duffy. Global stiffness modeling of a class of simple compliant couplings. *Mech. Mach. Theory*, 28(2):207–224, 1993. doi:[10.1016/0094-114X\(93\)90088-D](https://doi.org/10.1016/0094-114X(93)90088-D).
- [84] Y. Guo, H. Dong, and Y. Ke. Stiffness-oriented posture optimization in robotic machining applications. *Robotics and Computer-Integrated Manufacturing*, 35:69–76, 2015. doi:[10.1016/j.rcim.2015.02.006](https://doi.org/10.1016/j.rcim.2015.02.006).
- [85] M. Hassan and A. Khajepour. Optimization of actuator forces in cable-based parallel manipulators using convex analysis. *IEEE Trans. Robot.*, 24(3):736–740, 2008. doi:[10.1109/TRO.2008.919289](https://doi.org/10.1109/TRO.2008.919289).
- [86] J. M. Hendrickx and A. Olshevsky. Matrix p -norms are NP-hard to approximate if $p \neq 1, 2, \infty$. *SIAM J. Matrix Anal. & Appl.*, 31(5):2802–2812, 2010. doi:[10.1137/09076773X](https://doi.org/10.1137/09076773X).

-
- [87] T. Heyden and C. Woernle. Dynamics and flatness-based control of a kinematically undetermined cable suspension manipulator. *Multibody System Dynamics*, 16(2):155, 2006. doi:[10.1007/s11044-006-9023-5](https://doi.org/10.1007/s11044-006-9023-5).
- [88] D. Hilbert and S. Cohn-Vossen. *Geometry and the imagination*. Chelsea Publishing Company, 1952.
- [89] M. M. Horoub, M. Hassan, and M. A. Hawwa. Workspace analysis of a Gough-Stewart type cable marine platform subjected to harmonic water waves. *Mech. Mach. Theory*, 120:314–325, 2018. doi:[10.1016/j.mechmachtheory.2017.09.001](https://doi.org/10.1016/j.mechmachtheory.2017.09.001).
- [90] M. Husty. An algorithm for solving the direct kinematics of general Stewart-Gough platforms. *Mech. Mach. Theory*, 31(4):365–379, 1996. doi:[10.1016/0094-114X\(95\)00091-C](https://doi.org/10.1016/0094-114X(95)00091-C).
- [91] E. Idà, A. Berti, T. Bruckmann, and M. Carricato. Rest-to-rest trajectory planning for planar underactuated cable-driven parallel robots. In C. M. Gosselin, P. Cardou, T. Bruckmann, and A. Pott, editors, *Cable-Driven Parallel Robots*, pages 207–218. Springer, Québec, Canada, 2018. doi:[10.1007/978-3-319-61431-1_18](https://doi.org/10.1007/978-3-319-61431-1_18).
- [92] S. K. Ider. Inverse dynamics of parallel manipulators in the presence of drive singularities. *Mech. Mach. Theory*, 40(1):33–44, 2005. doi:[10.1016/j.mechmachtheory.2004.05.007](https://doi.org/10.1016/j.mechmachtheory.2004.05.007).
- [93] M. H. Irvine. *Cable structures*, volume 17 of *MIT Press Series in Structural Mechanics*. MIT Press, 1981.
- [94] S. C. Jacobsen, J. E. Wood, D. Knutti, and K. B. Biggers. The UTAH/MIT dextrous hand: work in progress. *Int. J. Rob. Res.*, 3(4): 21–50, 1984. doi:[10.1177/027836498400300402](https://doi.org/10.1177/027836498400300402).
- [95] S. C. Jacobsen, H. Ko, E. K. Iversen, and C. C. Davis. Antagonistic control of a tendon driven manipulator. In *Proc. of the IEEE 1989 ICRA*, pages 1334–1339, Scottsdale, USA, 1989. doi:[10.1109/ROBOT.1989.100165](https://doi.org/10.1109/ROBOT.1989.100165).
-

References

- [96] J. W. Jeong, S. H. Kim, and Y. K. Kwak. Kinematics and workspace analysis of a parallel wire mechanism for measuring a robot pose. *Mech. Mach. Theory*, 34(6):825–841, 1999. doi:[10.1016/S0094-114X\(98\)00080-9](https://doi.org/10.1016/S0094-114X(98)00080-9).
- [97] X. Jiang and C. M. Gosselin. Dynamically feasible trajectories for three-DOF planar cable-suspended parallel robots. In *Proc. of the ASME 2014 IDETC/CIE*, Buffalo, USA, 2014. doi:[10.1115/DETC2014-34419](https://doi.org/10.1115/DETC2014-34419).
- [98] X. Jiang and C. M. Gosselin. Dynamic point-to-point trajectory planning of a three-DOF cable-suspended parallel robot. *IEEE Trans. Robot.*, 32(6):1550–1557, 2016. doi:[10.1109/TRO.2016.2597315](https://doi.org/10.1109/TRO.2016.2597315).
- [99] X. Jiang, E. Barnett, and C. M. Gosselin. Dynamic point-to-point trajectory planning beyond the static workspace for six-DOF cable-suspended parallel robots. *IEEE Trans. Robot.*, 34(3):1–13, 2018. doi:[10.1109/TRO.2018.2794549](https://doi.org/10.1109/TRO.2018.2794549).
- [100] X. Jiang, E. Barnett, and C. M. Gosselin. Periodic trajectory planning beyond the static workspace for 6-DOF cable-suspended parallel robots. *IEEE Trans. Robot.*, 34(3):1–13, 2018. doi:[10.1109/TRO.2018.2819668](https://doi.org/10.1109/TRO.2018.2819668).
- [101] S. Kawamura, H. Kino, and C. Won. High-speed manipulation by using parallel wire-driven robots. *Robotica*, 18(1):13–21, 2000. doi:[10.1017/S0263574799002477](https://doi.org/10.1017/S0263574799002477).
- [102] S. A. Khalilpour, A. Z. Loloie, H. D. Taghirad, and M. T. Masouleh. Feasible kinematic sensitivity in cable robots based on interval analysis. In T. Bruckmann and A. Pott, editors, *Cable-Driven Parallel Robots*, pages 233–249. Springer, Stuttgart, Germany, 2013. doi:[10.1007/978-3-642-31988-4_15](https://doi.org/10.1007/978-3-642-31988-4_15).
- [103] W. A. Khan and J. Angeles. The kinetostatic optimization of robotic manipulators: the inverse and the direct problems. *ASME Journal of Mechanical Design*, 128(1):168–178, 2006. doi:[10.1115/1.2120808](https://doi.org/10.1115/1.2120808).

-
- [104] M. Khosravi and H. Taghirad. Dynamic modeling and control of parallel robots with elastic cables: singular perturbation approach. *IEEE Trans. Robot.*, 30(3):694–704, 2014. doi:[10.1109/TRO.2014.2298057](https://doi.org/10.1109/TRO.2014.2298057).
- [105] D. J. Kim, W. K. Chung, and Y. Youm. Geometrical approach for the workspace of 6-DOF parallel manipulators. In *Proc. of the IEEE 1997 ICRA*, volume 4, pages 2986–2991, Albuquerque, USA, 1997. doi:[10.1109/ROBOT.1997.606741](https://doi.org/10.1109/ROBOT.1997.606741).
- [106] J. Kim, F. C. Park, S. J. Ryu, J. Kim, J. C. Hwang, C. Park, and C. C. Iurascu. Design and analysis of a redundantly actuated parallel mechanism for rapid machining. *IEEE Trans. Robot. Autom.*, 17(4):423–434, 2001. doi:[10.1109/70.954755](https://doi.org/10.1109/70.954755).
- [107] S.-G. Kim and J. Ryu. New dimensionally homogeneous Jacobian matrix formulation by three end-effector points for optimal design of parallel manipulators. *IEEE Transactions on Robotics and Automation*, 19(4):731–737, 2003. doi:[10.1109/TRA.2003.814496](https://doi.org/10.1109/TRA.2003.814496).
- [108] X. Kong and C. M. Gosselin. Kinematics and singularity analysis of a novel type of 3-CRR 3-DOF translational parallel manipulator. *Int. J. Rob. Res.*, 21(9):791–798, 2002. doi:[10.1177/02783649020210090501](https://doi.org/10.1177/02783649020210090501).
- [109] K. Kozak, Q. Zhou, and J. Wang. Static analysis of cable-driven manipulators with non-negligible cable mass. *IEEE Trans. Robot.*, 22(3):425–433, 2006. doi:[10.1109/TRO.2006.870659](https://doi.org/10.1109/TRO.2006.870659).
- [110] R. Kurtz and V. Hayward. Dexterity measures with unilateral actuation constraints: the $n + 1$ case. *Advanced robotics*, 9(5):561–577, 1994. doi:[10.1163/156855395X00148](https://doi.org/10.1163/156855395X00148).
- [111] P. Lafourcade, M. Llibre, and C. Reboulet. Design of a parallel wire-driven manipulator for wind tunnels. In *Proceedings of the Workshop on Fundamental Issues and Future Research Directions for Parallel Mechanisms and Manipulators*, pages 187–194, Quebec City, Canada, 2002.
-

References

- [112] S. Landsberger and T. Sheridan. A minimal, minimal linkage: the tension-compression parallel link manipulator. In *Robotics, mechanics and manufacturing systems*, pages 81–88. Elsevier, 1993. doi:[10.1016/B978-0-444-89700-8.50017-8](https://doi.org/10.1016/B978-0-444-89700-8.50017-8).
- [113] D. Lau and D. Oetomo. Conditions on the cable-routing matrix for wrench closure of multilink cable-driven manipulators. *ASME J. Mech. Des.*, 138(3):032303, 2016. doi:[10.1115/1.4032402](https://doi.org/10.1115/1.4032402).
- [114] D. Lau, D. Oetomo, and S. K. Halgamuge. Generalized modeling of multilink cable-driven manipulators with arbitrary routing using the cable-routing matrix. *IEEE Trans. Robot.*, 29(5):1102–1113, 2013. doi:[10.1109/TRO.2013.2264866](https://doi.org/10.1109/TRO.2013.2264866).
- [115] T. Le, H. Dobashi, and K. Nagai. Kinematical and static force analysis on redundant drive wire mechanism with velocity constraint modules to reduce the number of actuators. *Robomech*, 3(1):1–22, 2016. doi:[10.1186/s40648-016-0057-z](https://doi.org/10.1186/s40648-016-0057-z).
- [116] D. Lee. Automated all-weather cargo transfer system, 1992. URL patents.google.com/patent/US5154561A.
- [117] S. Lefrançois and C. M. Gosselin. Point-to-point motion control of a pendulum-like 3-DOF underactuated cable-driven robot. In *Proc. of the IEEE 2010 ICRA*, pages 5187–5193, Anchorage, USA, 2010. doi:[10.1109/ROBOT.2010.5509656](https://doi.org/10.1109/ROBOT.2010.5509656).
- [118] Y. Li and Q. Xu. GA-based multi-objective optimal design of a planar 3-DOF cable-driven parallel manipulator. In *Proc. of the IEEE 2006 ROBIO*, pages 1360–1365, Kunming, China, 2006. doi:[10.1109/ROBIO.2006.340127](https://doi.org/10.1109/ROBIO.2006.340127).
- [119] X. J. Liu, Z. L. Jin, and F. Gao. Optimum design of 3-DOF spherical parallel manipulators with respect to the conditioning and stiffness indices. *Mech. Mach. Theory*, 35(9):1257–1267, 2000. doi:[10.1016/S0094-114X\(99\)00072-5](https://doi.org/10.1016/S0094-114X(99)00072-5).

-
- [120] J. Lončarić. Normal forms of stiffness and compliance matrices. *IEEE J. Rob. Automation*, 3(6):567–572, 1987. doi:[10.1109/JRA.1987.1087148](https://doi.org/10.1109/JRA.1987.1087148).
- [121] J. Longval and C. M. Gosselin. Dynamic trajectory planning and geometric design of a two-DOF translational cable-suspended planar parallel robot using a parallelogram cable loop. In *Proc. of the ASME 2018 IDETC/CIE*, page 10, Québec, Canada, 2018.
- [122] O. Ma and J. Angeles. Optimum architecture design of platform manipulator. In *Proc. of the 5th Int. Conf. on Advanced Robotics*, pages 19–22, Pisa, Italy, 1991. doi:[10.1109/ICAR.1991.240404](https://doi.org/10.1109/ICAR.1991.240404).
- [123] K. Maeda, S. Tadokoro, T. Takamori, M. Hiller, and R. Verhoeven. On design of a redundant wire-driven parallel robot WARP manipulator. In *Proc. of the IEEE 1999 ICRA*, volume 2, pages 895–900, Detroit, USA, 1999. doi:[10.1109/ROBOT.1999.772403](https://doi.org/10.1109/ROBOT.1999.772403).
- [124] A. Martin, S. Caro, and P. Cardou. Geometric determination of the cable-cylinder interference regions in the workspace of a cable-driven parallel robot. In C. M. Gosselin, P. Cardou, T. Bruckmann, and A. Pott, editors, *Cable-Driven Parallel Robots*, pages 117–127. Springer, Québec, Canada, 2018. doi:[10.1007/978-3-319-61431-1_11](https://doi.org/10.1007/978-3-319-61431-1_11).
- [125] C. Melchiorri and G. Vassura. Mechanical and control features of the University of Bologna Hand version 2. In *Proc. of the IEEE/RSJ 1992 IROS*, volume 1, pages 187–193, Raleigh, USA, 1992. doi:[10.1109/IROS.1992.587320](https://doi.org/10.1109/IROS.1992.587320).
- [126] J.-P. Merlet. Determination of 6D workspaces of Gough-type parallel manipulator and comparison between different geometries. *Int. J. Rob. Res.*, 18(9):902–916, 1999. doi:[10.1177/02783649922066646](https://doi.org/10.1177/02783649922066646).
- [127] J.-P. Merlet. Analysis of the influence of wires interference on the workspace of wire robots. In J. Lenarčič and C. Galletti, editors, *On Advances in Robot Kinematics*, pages 211–218. Springer, Sestri Levante, Italy, 2004. doi:[10.1007/978-1-4020-2249-4_23](https://doi.org/10.1007/978-1-4020-2249-4_23).
-

References

- [128] J.-P. Merlet. Jacobian, manipulability, condition number, and accuracy of parallel robots. *ASME J. Mech. Rob.*, 128(1):199–206, 2006. doi:[10.1115/1.2121740](https://doi.org/10.1115/1.2121740).
- [129] J.-P. Merlet. *Parallel robots*, volume 128 of *Solid mechanics and its applications*. Springer, 2006. doi:[10.1007/1-4020-4133-0](https://doi.org/10.1007/1-4020-4133-0).
- [130] J.-P. Merlet. Kinematics of the wire-driven parallel robot MARIONET using linear actuators. In *Proc. of the IEEE 2008 ICRA*, pages 3857–3862, Pasadena, USA, 2008. doi:[10.1109/ROBOT.2008.4543803](https://doi.org/10.1109/ROBOT.2008.4543803).
- [131] J.-P. Merlet. Wire-driven parallel robot: open issues. In V. Padois, P. Bidaud, and O. Khatib, editors, *Romansy 19–Robot Design, Dynamics and Control*, pages 3–10. Springer, Paris, France, 2013. doi:[10.1007/978-3-7091-1379-0_1](https://doi.org/10.1007/978-3-7091-1379-0_1).
- [132] J.-P. Merlet, C. M. Gosselin, and N. Mouly. Workspaces of planar parallel manipulators. *Mech. Mach. Theory*, 33(1-2):7–20, 1998.
- [133] N. Michael, J. Fink, and V. Kumar. Cooperative manipulation and transportation with aerial robots. *Autonomous Robots*, 30(1):73–86, 2011. doi:[10.1007/s10514-010-9205-0](https://doi.org/10.1007/s10514-010-9205-0).
- [134] A. Ming and T. Higuchi. Study on multiple degree-of-freedom positioning mechanism using wires (part 1)-Concept, design and control. *International Journal of the Japan Society for Precision Engineering*, 28(2): 131–138, 1994.
- [135] M. Morris and M. Shoham. Applications and theoretical issues of cable-driven robots. In *Florida Conf. on Recent Advances on Robots*, pages 1–29, Boca Raton, USA, 2009.
- [136] G. Mottola, C. M. Gosselin, and M. Carricato. Dynamically feasible elliptical trajectories for fully constrained 3-DOF cable-suspended parallel robots. In C. M. Gosselin, P. Cardou, T. Bruckmann, and A. Pott, editors, *Cable-Driven Parallel Robots*, pages 221–230. Springer, Québec, Canada, 2018. doi:[10.1007/978-3-319-61431-1_19](https://doi.org/10.1007/978-3-319-61431-1_19).

-
- [137] G. Mottola, C. M. Gosselin, and M. Carricato. Dynamically feasible periodic trajectories for generic spatial three-degree-of-freedom cable-suspended parallel robots. *ASME J. Mech. Rob.*, 10(3):031004, 2018. doi:[10.1115/1.4039499](https://doi.org/10.1115/1.4039499).
- [138] G. Mottola, C. M. Gosselin, and M. Carricato. Dynamically feasible motions of a class of purely-translational cable-suspended parallel robots. *Mech. Mach. Theory*, 132:193–206, 2019. doi:[10.1016/j.mechmachtheory.2018.10.017](https://doi.org/10.1016/j.mechmachtheory.2018.10.017).
- [139] Q. Mourcou, A. Fleury, C. Franco, F. Klopčič, and N. Vuillerme. Performance evaluation of smartphone inertial sensors measurement for range of motion. *Sensors*, 15(9):23168–23187, 2015. doi:[10.3390/s150923168](https://doi.org/10.3390/s150923168).
- [140] J. Murayama, L. Bougrila, Y. Luo, K. Akahane, S. Hasegawa, B. Hirsbrunner, and M. Sato. SPIDAR G&G: a two-handed haptic interface for bimanual VR interaction. In *Proceedings of EuroHaptics*, volume 2004, pages 138–146, 2004.
- [141] R. M. Murray, Z. Li, and S. S. Sastry. *A mathematical introduction to robotic manipulation*. CRC press, 1994. URL www.cds.caltech.edu/~murray/books/MLS/.
- [142] S. K. Mustafa and S. K. Agrawal. On the force-closure analysis of n-DOF cable-driven open chains based on reciprocal screw theory. *IEEE Trans. Robot.*, 28(1):22–31, 2012. doi:[10.1109/TRO.2011.2168170](https://doi.org/10.1109/TRO.2011.2168170).
- [143] S. K. Mustafa, W. B. Lim, G. Yang, S. H. Yeo, W. Lin, and S. K. Agrawal. Cable-driven robots. In A. Y. C. Nee, editor, *Handbook of manufacturing engineering and technology*, pages 2169–2228. Springer, 2015. doi:[10.1007/978-1-4471-4670-4_101](https://doi.org/10.1007/978-1-4471-4670-4_101).
- [144] M. Nahon, G. Gilardi, and C. Lambert. Dynamics/control of a radio telescope receiver supported by a tethered aerostat. *J. of Guidance, Control, and Dynamics*, 25(6):1107–1115, 2002. doi:[10.2514/2.4990](https://doi.org/10.2514/2.4990).
-

References

- [145] R. Nan, D. Li, C. Jin, Q. Wang, L. Zhu, W. Zhu, H. Zhang, Y. Yue, and L. Qian. The five-hundred-meter aperture spherical radio telescope (FAST) project. *International Journal of Modern Physics D*, 20(6):989–1024, 2011. doi:[10.1142/S0218271811019335](https://doi.org/10.1142/S0218271811019335).
- [146] T. Narayanan, R. S. Vishnu, R. R. Bhavani, and V. Vashista. A cable driven parallel robot for coconut farm. In *Proc. of the IEEE 2017 ICACCI*, pages 864–870, Udupi, India, 2017. doi:[10.1109/ICACCI.2017.8125950](https://doi.org/10.1109/ICACCI.2017.8125950).
- [147] D. Nguyen and M. Gouttefarde. Stiffness matrix of 6-DOF cable-driven parallel robots and its homogenization. In J. Lenarčič and O. Khatib, editors, *Advances in Robot Kinematics*, pages 181–191. Springer, 2014. doi:[10.1007/978-3-319-06698-1_20](https://doi.org/10.1007/978-3-319-06698-1_20).
- [148] D. Q. Nguyen and M. Gouttefarde. Study of reconfigurable suspended cable-driven parallel robots for airplane maintenance. In *Proc. of the IEEE/RSJ 2014 IROS*, pages 1682–1689, 2014. doi:[10.1109/IROS.2014.6942781](https://doi.org/10.1109/IROS.2014.6942781).
- [149] S. Oh, K. Mankala, S. K. Agrawal, and J. S. Albus. A dual-stage planar cable robot: dynamic modeling and design of a robust controller with positive inputs. *ASME J. Mech. Des.*, 127(4):612–620, 2005. doi:[10.1115/1.1899689](https://doi.org/10.1115/1.1899689).
- [150] S.-R. Oh, J.-C. Ryu, and S. K. Agrawal. Dynamics and control of a helicopter carrying a payload using a cable-suspended robot. *ASME J. Mech. Des.*, 128(5):1113–1121, 2006. doi:[10.1115/1.2218882](https://doi.org/10.1115/1.2218882).
- [151] K. C. Olds. Global indices for kinematic and force transmission performance in parallel robots. *IEEE Trans. Robot.*, 31(2):494–500, 2015. doi:[10.1109/TRO.2015.2398632](https://doi.org/10.1109/TRO.2015.2398632).
- [152] I. J. Oppenheim and W. O. Williams. Tensegrity prisms as adaptive structures. In *Proc. of Symp. on Adaptive Structures and Material Systems*, volume 54, pages 113–120, 1997.

-
- [153] E. Ottaviano and M. Ceccarelli. Numerical and experimental characterization of singularities of a six-wire parallel architecture. *Robotica*, 25(3): 315–324, 2006. doi:[10.1017/S0263574706003110](https://doi.org/10.1017/S0263574706003110).
- [154] V. Parenti Castelli, R. Di Gregorio, and F. Bubani. Workspace and optimal design of a pure translation parallel manipulator. *Meccanica*, 35(3):203–214, 2000. doi:[10.1023/A:1010359523780](https://doi.org/10.1023/A:1010359523780).
- [155] M. K. Park and J. W. Kim. Kinematic manipulability of closed chains. In J. Lenarčič and V. Parenti Castelli, editors, *Recent Advances in Robot Kinematics*, pages 99–108, Portoroz, Slovenia, 1996. Springer. doi:[10.1007/978-94-009-1718-7_10](https://doi.org/10.1007/978-94-009-1718-7_10).
- [156] S. Patel and T. Sobh. Manipulator performance measures—a comprehensive literature survey. *J. of Intelligent and Robotic Systems*, 77(3–4): 547–570, 2015. doi:[10.1007/s10846-014-0024-y](https://doi.org/10.1007/s10846-014-0024-y).
- [157] S. Perreault and C. M. Gosselin. Cable-driven parallel mechanisms: application to a locomotion interface. *ASME J. Mech. Des.*, 130(10): 102301, 2008. doi:[10.1115/1.2965607](https://doi.org/10.1115/1.2965607).
- [158] S. Perreault, P. Cardou, C. M. Gosselin, and M. Otis. Geometric determination of the interference-free constant-orientation workspace of parallel cable-driven mechanisms. *ASME J. Mech. Rob.*, 2(3):031016, 2010. doi:[10.1115/1.4001780](https://doi.org/10.1115/1.4001780).
- [159] V. Portman. Stiffness evaluation of machines and robots: minimum collinear stiffness value approach. *ASME J. Mech. Rob.*, 3(1):011015, 2011. doi:[10.1115/1.4003444](https://doi.org/10.1115/1.4003444).
- [160] A. Pott. Influence of pulley kinematics on cable-driven parallel robots. In J. Lenarčič and M. Husty, editors, *Latest Advances in Robot Kinematics*, pages 197–204. Springer, Innsbruck, Austria, 2012. doi:[10.1007/978-94-007-4620-6_25](https://doi.org/10.1007/978-94-007-4620-6_25).
-

References

- [161] A. Pott. *Cable-driven parallel robots: theory and application*, volume 120 of *Springer Tracts in Advanced Robotics*. Springer, 2018. doi:[10.1007/978-3-319-76138-1](https://doi.org/10.1007/978-3-319-76138-1).
- [162] A. Pott, C. Meyer, and A. Verl. Large-scale assembly of solar power plants with parallel cable robots. In *41st Int. Symp. Robotics and 6th German Conf. Robotics*, pages 1–6, Munich, Germany, 2010.
- [163] A. Pott, H. Mütterich, W. Kraus, V. Schmidt, P. Miermeister, and A. Verl. IPAnema: a family of cable-driven parallel robots for industrial applications. In T. Bruckmann and A. Pott, editors, *Cable-Driven Parallel Robots*, pages 119–134. Springer, Stuttgart, Germany, 2013. doi:[10.1007/978-3-642-31988-4_8](https://doi.org/10.1007/978-3-642-31988-4_8).
- [164] J. Pusey, A. Fattah, S. K. Agrawal, and E. Messina. Design and workspace analysis of a 6–6 cable-suspended parallel robot. *Mech. Mach. Theory*, 39(7):761–778, 2004. doi:[10.1016/j.mechmachtheory.2004.02.010](https://doi.org/10.1016/j.mechmachtheory.2004.02.010).
- [165] S. Qian, B. Zi, W. Shang, and Q. Xu. A review on cable-driven parallel robots. *Chinese Journal of Mechanical Engineering*, 31(1), 2018. doi:[10.1186/s10033-018-0267-9](https://doi.org/10.1186/s10033-018-0267-9).
- [166] T. Rasheed, P. Long, D. Marquez-Gamez, and S. Caro. Tension distribution algorithm for planar mobile cable-driven parallel robots. In C. M. Gosselin, P. Cardou, T. Bruckmann, and A. Pott, editors, *Cable-Driven Parallel Robots*, pages 268–279. Springer, Québec, Canada, 2018. doi:[10.1007/978-3-319-61431-1_23](https://doi.org/10.1007/978-3-319-61431-1_23).
- [167] A. T. Riechel and I. Ebert-Uphoff. Force-feasible workspace analysis for underconstrained point-mass cable robots. In *Proc. of the IEEE 2004 ICRA*, volume 5, pages 4956–4962, New Orleans, USA, 2004. doi:[10.1109/ROBOT.2004.1302503](https://doi.org/10.1109/ROBOT.2004.1302503).
- [168] R. G. Roberts, T. Graham, and T. Lippitt. On the inverse kinematics, statics, and fault tolerance of cable-suspended robots.

-
- J. of Rob. Syst.*, 15(10):581–597, 1998. doi:[10.1002/\(SICI\)1097-4563\(199810\)15:10<581::AID-ROB4>3.0.CO;2-P](https://doi.org/10.1002/(SICI)1097-4563(199810)15:10<581::AID-ROB4>3.0.CO;2-P).
- [169] G. Rosati, P. Gallina, and S. Masiero. Design, implementation and clinical tests of a wire-based robot for neurorehabilitation. *IEEE Transactions on Neural Systems and Rehabilitation Engineering*, 15(4):560–569, 2007. doi:[10.1109/TNSRE.2007.908560](https://doi.org/10.1109/TNSRE.2007.908560).
- [170] A. Rosyid, B. El-Khasawneh, and A. Alazzam. Kinematic performance measures and optimization of parallel kinematics manipulators: a brief review. In E. G. Hurtado, editor, *Kinematics*, pages 1–22. InTech, 2017. doi:[10.5772/intechopen.71406](https://doi.org/10.5772/intechopen.71406).
- [171] M. H. Saadatzi, M. T. Masouleh, H. D. Taghirad, C. M. Gosselin, and P. Cardou. Geometric analysis of the kinematic sensitivity of planar parallel mechanisms. *Transactions of the Canadian Society for Mechanical Engineering*, 35(4):477–490, 2011. doi:[10.1139/tcsme-2011-0028](https://doi.org/10.1139/tcsme-2011-0028).
- [172] O. Saber. A spatial translational cable robot. *ASME J. Mech. Rob.*, 7(3):031006, 2015. doi:[10.1115/1.4028287](https://doi.org/10.1115/1.4028287).
- [173] O. Saber and H. Zohoor. Workspace analysis of a cable-suspended robot with active-passive cables. In *Proc. of the ASME 2005 IDETC/CIE*, Portland, USA, 2013. doi:[10.1115/DETC2013-12646](https://doi.org/10.1115/DETC2013-12646).
- [174] O. Saber, S. Abyaneh, and H. Zohoor. A cable-suspended robot with a novel cable based end effector. In *Proc. of the ASME 2010 ESDA*, pages 799–808, Istanbul, Turkey, 2010. doi:[10.1115/ESDA2010-25312](https://doi.org/10.1115/ESDA2010-25312).
- [175] J. Salisbury. Active stiffness control of a manipulator in Cartesian coordinates. In *Proc. of the 1980 IEEE CDC*, pages 95–100, 1980. doi:[10.1109/CDC.1980.272026](https://doi.org/10.1109/CDC.1980.272026).
- [176] J. K. Salisbury and J. J. Craig. Articulated hands: force control and kinematic issues. *Int. J. Rob. Res.*, 1(4):4–17, 1982. doi:[10.1177/027836498200100102](https://doi.org/10.1177/027836498200100102).
-

References

- [177] V. Schmidt, W. Kraus, W. Y. Ho, J. Seon, A. Pott, J. Park, and A. Verl. Extending dynamic trajectories of cable-driven parallel robots as a novel robotic roller coaster. In *45th Int. Symp. Robotics and 8th German Conf. Robotics*, pages 367–373, Munich, Germany, 2014.
- [178] Z. Shao, T. Li, X. Tang, L. Tang, and H. Deng. Research on the dynamic trajectory of spatial cable-suspended parallel manipulators with actuation redundancy. *Mechatronics*, 49:26–35, 2018. doi:[10.1016/j.mechatronics.2017.11.001](https://doi.org/10.1016/j.mechatronics.2017.11.001).
- [179] M. Shoham. Twisting wire actuator. *ASME J. Mech. Des.*, 127(3):441–445, 2005. doi:[10.1115/1.1866156](https://doi.org/10.1115/1.1866156).
- [180] B. Mayer St-Onge and C. M. Gosselin. Singularity analysis and representation of the general Gough-Stewart platform. *Int. J. Rob. Res.*, 19(3):271–288, 2000. doi:[10.1177/02783640022066860](https://doi.org/10.1177/02783640022066860).
- [181] D. Steinberg. Computation of matrix norms with applications to robust optimization. Master’s thesis, Technion-Israel University of Technology, 2005. URL www2.isye.gatech.edu/~nemirovs/Daureen.pdf.
- [182] D. Stewart. A platform with six degrees of freedom. *Proceedings of the Institution of Mechanical Engineers*, 180(1):371–386, 1965. doi:[10.1243/PIME_PROC_1965_180_029_02](https://doi.org/10.1243/PIME_PROC_1965_180_029_02).
- [183] E. Stump and V. Kumar. Workspaces of cable-actuated parallel manipulators. *ASME J. Mech. Des.*, 128(1):159–167, 2006. doi:[10.1115/1.2121741](https://doi.org/10.1115/1.2121741).
- [184] D. Surdilovic and R. Bernhardt. STRING-MAN: a new wire robot for gait rehabilitation. In *Proc. of the IEEE 2004 ICRA*, volume 2, pages 2031–2036, New Orleans, USA, 2004. doi:[10.1109/ROBOT.2004.1308122](https://doi.org/10.1109/ROBOT.2004.1308122).
- [185] D. Surdilovic, J. Radojicic, and J. Krüger. Geometric stiffness analysis of wire robots: a mechanical approach. In T. Bruckmann and A. Pott,

-
- editors, *Cable-Driven Parallel Robots*, pages 389–404. Springer, Berlin, Germany, 2013. doi:[10.1007/978-3-642-31988-4_24](https://doi.org/10.1007/978-3-642-31988-4_24).
- [186] M. M. Svinin, S. Hosoe, and M. Uchiyama. On the stiffness and stability of Gough-Stewart platforms. In *Proc. of the IEEE 2001 ICRA*, pages 3268–3273, Seoul, South Korea, 2001. doi:[10.1109/ROBOT.2001.933122](https://doi.org/10.1109/ROBOT.2001.933122).
- [187] S. Tadokoro, Y. Murao, M. Hiller, R. Murata, H. Kohkawa, and T. Matsushima. A motion base with 6-DOF by parallel cable drive architecture. *IEEE Trans. Mechatronics*, 7(2):115–123, 2002. doi:[10.1109/TMECH.2002.1011248](https://doi.org/10.1109/TMECH.2002.1011248).
- [188] A. Taghvaeipour, J. Angeles, and L. Lessard. On the elastostatic analysis of mechanical systems. *Mech. Mach. Theory*, 58:202–216, 2012. doi:[10.1016/j.mechmachtheory.2012.07.011](https://doi.org/10.1016/j.mechmachtheory.2012.07.011).
- [189] L. Tang, X. Tang, X. Jiang, and C. M. Gosselin. Dynamic trajectory planning study of planar two-dof redundantly actuated cable-suspended parallel robots. *Mechatronics*, 30:187–197, 2015. doi:[10.1016/j.mechatronics.2015.07.005](https://doi.org/10.1016/j.mechatronics.2015.07.005).
- [190] X. Tang. An overview of the development for cable-driven parallel manipulator. *Advances in Mechanical Engineering*, 6, 2014. doi:[10.1155/2014/823028](https://doi.org/10.1155/2014/823028).
- [191] A. Trevisani. Underconstrained planar cable-direct-driven robots: A trajectory planning method ensuring positive and bounded cable tensions. *Mechatronics*, 20:113–127, 2010. doi:[10.1016/j.mechatronics.2009.09.011](https://doi.org/10.1016/j.mechatronics.2009.09.011).
- [192] A. Trevisani. Experimental validation of a trajectory planning approach avoiding cable slackness and excessive tension in underconstrained translational planar cable-driven robots. In T. Bruckmann and A. Pott, editors, *Cable-Driven Parallel Robots*, pages 23–39. Springer, Stuttgart, Germany, 2013. doi:[10.1007/978-3-642-31988-4_2](https://doi.org/10.1007/978-3-642-31988-4_2).
-

References

- [193] A. Trevisani. Planning of dynamically feasible trajectories for translational, planar, and underconstrained cable-driven robots. *Journal of Systems Science and Complexity*, 26(5):695–717, 2013. doi:[10.1007/s11424-013-3175-1](https://doi.org/10.1007/s11424-013-3175-1).
- [194] L.-W. Tsai. Kinematics of a three-dof platform with three extensible limbs. In J. Lenarčič and V. Parenti Castelli, editors, *Recent Advances in Robot Kinematics*, pages 401–410. Springer, Portoroz, Slovenia, 1996. doi:[10.1007/978-94-009-1718-7_40](https://doi.org/10.1007/978-94-009-1718-7_40).
- [195] R. Verhoeven, M. Hiller, and S. Tadokoro. Workspace, stiffness, singularities and classification of tendon-driven Stewart platforms. In J. Lenarčič and M. L. Husty, editors, *Advances in Robot Kinematics: Analysis and Control*, pages 105–114. Springer, Salzburg, Austria, 1998. doi:[10.1007/978-94-015-9064-8_11](https://doi.org/10.1007/978-94-015-9064-8_11).
- [196] D.-S. Vu, E. Barnett, A. Zaccarin, and C. M. Gosselin. On the design of a three-DOF cable-suspended parallel robot based on a parallelogram arrangement of the cables. In C. M. Gosselin, P. Cardou, T. Bruckmann, and A. Pott, editors, *Cable-Driven Parallel Robots*, pages 319–330. Springer, Québec, Canada, 2018. doi:[10.1007/978-3-319-61431-1_27](https://doi.org/10.1007/978-3-319-61431-1_27).
- [197] K. Waldron and K. Hunt. Series-parallel dualities in actively coordinated mechanisms. *Int. J. Rob. Res.*, 10(5):473–480, 1991. doi:[10.1177/027836499101000503](https://doi.org/10.1177/027836499101000503).
- [198] R. Williams, J. Albus, and R. Bostelman. 3D cable-based Cartesian metrology system. *J. of Field Robotics*, 21(5):237–257, 2004. doi:[10.1002/rob.20012](https://doi.org/10.1002/rob.20012).
- [199] R. Williams, M. Xin, and P. Bosscher. Contour-crafting-cartesian-cable robot system: dynamics and controller design. In *Proc. of the ASME 2008 IDETC/CIE*, pages 39–45, New York, USA, 2008. doi:[10.1115/DETC2008-49480](https://doi.org/10.1115/DETC2008-49480).

-
- [200] R. Williams, M. Xin, and P. Bosscher. Contour-crafting-cartesian-cable robot system concepts: workspace and stiffness comparisons. In *Proc. of the ASME 2008 IDETC/CIE*, pages 31–38, New York, USA, 2008. doi:[10.1115/DETC2008-49478](https://doi.org/10.1115/DETC2008-49478).
- [201] Y. Wischnitzer, N. Shvalb, and M. Shoham. Wire-driven parallel robot: permitting collisions between wires. *Int. J. Rob. Res.*, 27(9):1007–1026, 2008. doi:[10.1177/0278364908095884](https://doi.org/10.1177/0278364908095884).
- [202] B. Xu, T. Li, and Jun J. Wu. A method of stiffness analysis of parallel mechanisms. In *International Conference on Intelligent Robotics and Applications*, pages 562–570, 2009. doi:[10.1007/978-3-642-10817-4_56](https://doi.org/10.1007/978-3-642-10817-4_56).
- [203] M. Yamamoto, N. Yanai, and A. Mohri. Trajectory control of incompletely restrained parallel-wire-suspended mechanism based on inverse dynamics. *IEEE Trans. Robot.*, 20(5):840–850, 2004. doi:[10.1109/TRO.2004.829501](https://doi.org/10.1109/TRO.2004.829501).
- [204] S. J. Yan, S. K. Ong, and A. Y. C. Nee. Stiffness analysis of parallelogram-type parallel manipulators using a strain energy method. *Robotics and Computer-Integrated Manufacturing*, 37(2):13–22, 2016. doi:[10.1016/j.rcim.2015.05.004](https://doi.org/10.1016/j.rcim.2015.05.004).
- [205] G. Yang, S. H. Yeo, and C. B. Pham. Kinematics and singularity analysis of a planar cable-driven parallel manipulator. In *Proc. of the IEEE/RSJ 2014 IROS*, volume 4, pages 3835–3840, Sendai, Japan, 2004. doi:[10.1109/IROS.2004.1390012](https://doi.org/10.1109/IROS.2004.1390012).
- [206] Y. Yang, W. Zhang, H. Pu, and Y. Peng. A class of symmetrical 3T, 3T-1R, and 3R mechanisms with parallel linear motion elements. *ASME J. Mech. Rob.*, 10(5):051016, 2018. doi:[10.1115/1.4040885](https://doi.org/10.1115/1.4040885).
- [207] S. H. Yeo, G. Yang, and W. B. Lim. Design and analysis of cable-driven manipulators with variable stiffness. *Mech. Mach. Theory*, 69:230–244, 2013. doi:[10.1016/j.mechmachtheory.2013.06.005](https://doi.org/10.1016/j.mechmachtheory.2013.06.005).
-

References

- [208] T. Yoshikawa. Analysis and control of robot manipulators with redundancy. In *Proc. of the 1st Int. Symp. on Robotics Research*, pages 735–747, Bretton Woods, USA, 1983.
- [209] D. Zanotto, G. Rosati, and S. K. Agrawal. Modeling and control of a 3-DOF pendulum-like manipulator. In *Proc. of the IEEE 2011 ICRA*, pages 3964–3969, Shanghai, P.R.C., 2011. doi:[10.1109/ICRA.2011.5980198](https://doi.org/10.1109/ICRA.2011.5980198).
- [210] N. Zhang and W. Shang. Dynamic trajectory planning of a 3-DOF under-constrained cable-driven parallel robot. *Mech. Mach. Theory*, 98:21–35, 2016. doi:[10.1016/j.mechmachtheory.2015.11.007](https://doi.org/10.1016/j.mechmachtheory.2015.11.007).
- [211] N. Zhang, W. Shang, and S. Cong. Geometry-based trajectory planning of a 3-3 cable-suspended parallel robot. *IEEE Trans. Robot.*, 33(2):484–491, 2016. doi:[10.1109/TRO.2016.2631591](https://doi.org/10.1109/TRO.2016.2631591).
- [212] N. Zhang, W. Shang, and S. Cong. Dynamic trajectory planning for a spatial 3-DoF cable-suspended parallel robot. *Mech. Mach. Theory*, 122:177–196, 2018. doi:[10.1016/j.mechmachtheory.2017.12.023](https://doi.org/10.1016/j.mechmachtheory.2017.12.023).
- [213] Z. Zhang, Z. Shao, L. Wang, and A. Shih. Optimal design of a high-speed pick-and-place cable-driven parallel robot. In C. M. Gosselin, P. Cardou, T. Bruckmann, and A. Pott, editors, *Cable-Driven Parallel Robots*, pages 340–352. Springer, Québec, Canada, 2018. doi:[10.1007/978-3-319-61431-1_29](https://doi.org/10.1007/978-3-319-61431-1_29).
- [214] B. Zi, B. Duan, J. Du, and H. Bao. Dynamic modeling and active control of a cable-suspended parallel robot. *Mechatronics*, 18(1):1–12, 2008. doi:[10.1016/j.mechatronics.2007.09.004](https://doi.org/10.1016/j.mechatronics.2007.09.004).
- [215] B. Zi, H. Sun, and D. Zhang. Design, analysis and control of a winding hybrid-driven cable parallel manipulator. *Robotics and Computer-Integrated Manufacturing*, 48:196–208, 2017. doi:[10.1016/j.rcim.2017.04.002](https://doi.org/10.1016/j.rcim.2017.04.002).

- [216] J. Zitzewitz, G. Rauter, R. Steiner, A. Brunschweiler, and R. Riener. A versatile wire robot concept as a haptic interface for sport simulation. In *Proc. of the IEEE 2009 ICRA*, pages 313–318, Kobe, Japan, 2009. doi:[10.1109/ROBOT.2009.5152219](https://doi.org/10.1109/ROBOT.2009.5152219).
- [217] D. Zlatanov, R. Fenton, and B. Benhabib. A unifying framework for classification and interpretation of mechanism singularities. *ASME J. Mech. Des.*, 117(4):566–572, 1995. doi:[10.1115/1.2826720](https://doi.org/10.1115/1.2826720).
- [218] N. Zoso and C. M. Gosselin. Point-to-point motion planning of a parallel 3-DOF underactuated cable-suspended robot. In *Proc. of the IEEE 2012 ICRA*, pages 2325–2330, Saint Paul, USA, 2012. doi:[10.1109/ICRA.2012.6224598](https://doi.org/10.1109/ICRA.2012.6224598).
- [219] T. Zou and J. Angeles. The decoupling of the Cartesian stiffness matrix in the design of microaccelerometers. *Multibody System Dynamics*, 34(1):1–21, 2015. doi:[10.1007/s11044-014-9408-9](https://doi.org/10.1007/s11044-014-9408-9).